19950206 090

DEPARTMENT OF THE AIR FOR
AIR UNIVERSITY

AIR FORCE INSTITUTE OF TECHNOLOGY

Wright-Patterson Air Force Base, Ohio

AN EXPERIMENTAL INVESTIGATION OF THE
TIME-DEPENDENT SEPARATION OF TANGENT
BODIES IN SUPERSONIC FLOW

DISSERTATION

Neal Anthony Mosbarger
Captain, USAF

AFIT/DS/AA/94-7

AN EXPERIMENTAL INVESTIGATION OF THE TIME-DEPENDENT SEPARATION OF TANGENT BODIES IN SUPERSONIC FLOW

DISSERTATION

Presented to the Faculty of the School of Engineering

of the Air Force Institute of Technology

Air University

In Partial Fulfillment of the

Requirements for the Degree of

Doctor of Philosophy

Neal Anthony Mosbarger, B.S., M.S.

Captain, USAF

December, 1994
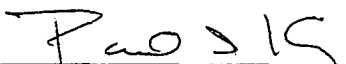
AN EXPERIMENTAL INVESTIGATION OF THE TIME-DEPENDENT SEPARATION OF TANGENT BODIES IN SUPERSONIC FLOW

Neal Anthony Mosbarger, B.S., M.S.

Captain, USAF

Approved:

_____   _____
Paul I. King, Chairman   1 Dec 94

_____   _____
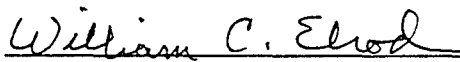William P. Baker   1 Dec 94

_____   _____
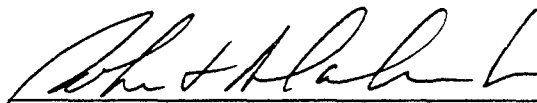Milton E. Franke   1 Dec 94

_____   _____
William C. Elrod, Dean's Representative   1 Dec 94

_____
Robert A. Calico, Jr.
Dean, Graduate School of Engineering

Acknowledgements

Table of Contents

List of Figures

x

xiii

List of Tables

List of Symbols

a   Speed of sound (m/sec)

AOA   Angle of attack (deg.)

CFD   Computational fluid dynamics

C_p Pressure coefficient

CTS   Captive trajectory support

d   Linear dimension (cm)

D   Wedge-store width (6.35 cm)

F   Froude number

g   Gravity constant

$\vec{l}$ Unit tangent vector

M   Mach number

$\vec{n}$ Unit normal vector

p   pressure (N/m^2)

P_w Surface pressure (N/m^2)

P_∞ Freestream static pressure (N/m^2)

P   Normalized pressure (P_w/P_∞)

$\vec{q}$ Velocity vector (m/sec)

R   Transducer radial position normalized radius length (4.93 cm)

t   Time (sec)

v Store velocity (m/sec)

V   Flow velocity (m/sec)

X   Axial distance (cm)

X_{LE} Distance downstream of leading edge normalized by plate length, 20.3 cm.

X/YE   Axial distance normalized by ogive maximum radius, 1.91 cm.

X/c   External tank normalized axial distance

Y   Separation distance between wedge-store and stationary model (cm)

YE	Ogive maximum radius (1.91 cm)
Y/D	Normalized separation distance
Z	Plate Span distance normalized by plate width, 20.3 cm.
α_e	Effective AOA or effective wedge angle (deg.)
α_u	Induced AOA or induced wedge angle (deg.)
β	Shock wave angle (deg.)
δ	Deflection angle (deg.)
ε	Geometric AOA or geometric wedge angle (deg.)
γ	Specific heat ratio
λ	Scaling factor
ψ	Transducer orientation on ogive (deg.)
ϕ	Transducer orientation on plate (deg.)
ρ	Density (kg/m^3)
θ	Pitch divergence (deg.)

Subscripts

∞	Freestream
1	Upstream of shock wave
2	Downstream of shock wave

Abstract

An experimental, time-dependent separation of tangent bodies was performed in a supersonic wind tunnel (Mach 1.5 and 1.9) to investigate the significance of transient effects and the suitability of using steady-state assumptions to predict a dynamic separation event. The model configurations consisted of two bodies placed in a near tangent position. A stationary body, a plate or ogive, was instrumented to obtain dynamic surface pressures, while a second body, a wedge attached to an air cylinder, was plunged in a constrained motion away from and towards the stationary model. (Steady-state, inviscid numerical and experimental results were used to evaluate the surface pressures on the stationary body induced by shock waves between the bodies.)

Three-dimensional flow expansion around the edge of the wedge reduced the strength of the shock waves and created a region of low pressure, near freestream static, on body surfaces between the incident and reflection shock waves. The dynamic motion of the wedge did not significantly affect the shock wave development between the bodies, and steady-state corrections that accounted for the motion-induced wedge angle were appropriate for predicting the time-dependent surface pressures induced by the incident shock wave. However, unsteady pressures due to motion of the wedge were evident when the separation distances were less than 20% of the wedge width.

The expansion flow and unsteady piston induced pressure magnitudes are exacerbated when flat-sided bodies are separated from a near tangent position, such as might occur with aircraft configured with conformal carriages and angular shaped stores.

AN EXPERIMENTAL INVESTIGATION OF THE TIME-DEPENDENT SEPARATION OF TANGENT BODIES IN SUPERSONIC FLOW

I. Introduction

The supersonic flow around an aircraft with externally mounted stores is complex involving viscous flow, shock waves, and mutual aerodynamic interference. An understanding of the initial store separation phase is complicated by the time dependency of the dynamic event. Until the mid-1980s, store trajectory prediction methods were simplified with steady-state assumptions. Since the separation velocity of the store is significantly less than the freestream velocity, it was assumed that for a given store position the time-dependency could be accounted for by the introduction of an induced angle of attack into the steady-state calculations. A steady-state assumption implies that the flow is instantaneously developed for each store position during a store separation event. However, until this investigation the steady-state assumption had not been tested experimentally, particularly for the initial separation phase of tangent bodies. This lack of experimental verification has been a concern since numerical comparisons of steady-state and time-dependent separation simulations indicate differences in the store aerodynamic coefficients and flow field characteristics [Mendenhall, 1988]. Thus, one objective of this study was to quantify the differences between steady-state and time-dependent separations of tangent bodies in a supersonic flow, and suggest the form of a suitable angle-of-attack correction for use in predicting time-dependent separation events.

1.1 Separation of Tangent Bodies.

The proposed investigation of the dynamic effects associated with the initial phase of separating tangent bodies directly supports the need for low drag and low observable characteristics involved in integrating aircraft and store configurations. Modern methods of drag reduction include streamlining the integration of the external stores by eliminating large pylons and placing the stores in contact with the aircraft surface, with tangent store carriages on the wings and conformal carriages on the fuselage. As aircraft drag is reduced through innovative design, and supersonic flight with external stores extends into a target area supersonic store release must be considered. Preliminary tests of a conformal carriage on the Navy F-4B validated the concept of a store release in supersonic flight [Epstein, 1988]. With the conformal configuration the integrated aircraft and store drag was reduced 60% and the aircraft range extended nearly 50%. The store carriage transport envelope was increased from Mach 1.1 to 1.8, and successful store separations were demonstrated at Mach 1.2, 1.4, and 1.6. Other current inventory aircraft such as the U. K. Tornado and the U.S. F-14, F-15E, and F-16F are also beginning to adopt conformal and tangent store carriages.

Although a majority of store separation flight tests and studies involved with specific aircraft programs are classified and not publicly available, there are a few reported tests that acknowledge flight test and trajectory prediction discrepancies. One such flight test was the jettison of an empty JP233 low altitude airfield attack system from the inboard underwing port pylon of the Royal Air Force Buccaneer aircraft (British Aerospace) in straight and level flight [Wood, 1988]. The low speed (Mach 0.45) flight test resulted in a store-to-aircraft collision, when after release, the empty dispenser impacted the wing leading edge removing the wing Pitot tube before yawing outboard and colliding with the wing tip. The comparison of experimental, computational, and flight test data are shown in Fig. 1.1. The displacement of the store center-of-gravity (cg) is in the aircraft axis system represented by X, Y, and Z

respectively. Roll, pitch, and yaw divergence are represented by ϕ, θ, and ψ respectively. The experimental results (identified as light body, i.e., free drop, and Aircraft Research Association two sting rig (ARA TSR) in Fig. 1.1) matched only the first 0.2 seconds of the flight test. After 0.2 seconds large combined pitch and yaw angular motions exceeded the mechanical limits of the TSR system. Both computational methods shown (RAENEAR and TSPARV) failed to predict the store-to-aircraft collision impart due to under-predicting the magnitude of the pitch divergence (θ). Further computational work carried out by BAe Brough [Wood, 1988] revealed that the margin between a collision and clearance was highly dependent upon the initial pitch rate of the store at the end of the ejector stroke.

The store behavior and trajectory are very sensitive to initial conditions. If the initial rotation rate (pitch, roll, or yaw) of the store is large (e.g., the store tip is displaced at a rate greater than the separation rate of the store cg away from the aircraft), then the store is likely to impact the nearest section of the aircraft. Store-to-pylon collisions are the most common type and impact usually occurs within 200ms of store ejection [Arnold and Epstein, 1986]. Although this type of store collision is the least hazardous to the aircraft, the store itself can be damaged, such as the bending or breaking of fins, resulting in an erratic trajectory and a target miss of several thousand feet. A fairly common store-to-rack collision occurs when a store is released from the bottom position of a Triple Ejector Rack (TER) used on most USAF fighter aircraft. Store-to-TER collisions begin around 450 KCAS and the probability of collision grows as the aircraft flight speed increases. At 550 KCAS, blunt nose stores, such as the CBU-24/58 series, exhibit a violent nose down pitching moment that usually results in a collision with the TER [Arnold and Epstein, 1986].

A store nose-up pitching moment is another scenario that can cause a store-to-pylon collision. When a flat sided store is released from a tangent configuration in supersonic flight a flow expansion about the store edge, downstream of the initial shock wave, may induce a pressure trough near the nose of the store and encourage

a nose up moment. This pressure trough will be discussed further in Chapter 5, Results.

The initial goal of all store separation system designs and aircraft integration efforts is to pass the ejected store quickly through the aircraft flow field to attain the stable repeatable trajectory necessary for consistently hitting a selected target. As speeds increase, the aircraft flow field becomes the dominant influence on the store trajectory. Any store that lingers in the aircraft flow field can have enormous forces generated on it, forces severe enough to raise 500 to 1000 pound stores up and over the aircraft. At supersonic speeds induced shock waves add to the complexity of the flow field, and flow discontinuities may cause a store to become unstable. This was demonstrated in a Two Sting Rig wind tunnel test of submunitions released from a carrier rocket system [Wood, 1988]. The submunition experienced a reduction in forebody lift as it passed through the conical bow shock initiated by the rocket. As the submunition crossed the shock wave with a negative pitch angle, it became unstable due to the loss of forebody lift not compensated for on the aftbody.

The dynamic contribution to a store separation event is not well understood and has been neglected during the store design phase primarily due to the lack of sufficient experimental dynamic data [Mendenhall, 1988]. Understanding how a dynamic flow affects the force and moment coefficients is needed for two basic reasons. First, problems still abound in store separation predictions during the store design phase. Accurate predictions are needed to ensure flight safety and identify the repeatable stable trajectory necessary for hitting a target. Second, computational tools are being developed to account for time dependent flowfields, and comparisons between steady-state and time-dependent numerical separation simulations reveal unresolved differences in the aerodynamic coefficients in both magnitude and phase.

Since the majority of store trajectory predictions are made with semi-empirical methods based on steady-state experimental data, the strength and weakness of the different wind tunnel techniques that support these prediction methods are reviewed

next. Thereafter, time-dependent numerical investigations with comparisons between steady-state and time-dependent store separation simulation are presented.

1.2 Wind Tunnel-Supported Trajectory Prediction Methods.

There are primarily three wind tunnel methods used to determine store separation characteristics: the Captive Trajectory Support (CTS), the Grid Survey, and the Free Drop [Carman, et.al, 1980], [Keen, 1985]. None of these methods, however, provide time-dependent data needed to evaluate the unsteady dynamics of a store separation event.

The CTS incorporates a dual-sting arrangement with the aircraft model mounted on one sting, and the store model mounted on a second sting capable of moving with six degrees of freedom. An internal balance is used to measure the aerodynamic forces and moments on the store for a fixed position and orientation with respect to the aircraft. The aerodynamic coefficients along with the store mass, moments of inertia, and center of gravity are substituted into the equations of motion and solved with an on line computer to predict the store motion relative to the aircraft for a given time increment. This procedure is repeated at each new predicted position until a desired distance between the store and aircraft is attained.

The primary advantage of the CTS is the ability to measure forces and moments on the store as a function of its orientation and relative position to the aircraft. The disadvantage of the CTS is two-fold. First, the CTS is a static experimental method. Thus, while calculations for the next store position from the current fixed store attitude include an assumed induced angle of attack to account for the linear and angular motion of the store, the actual flow field dynamics are not simulated. Second, CTS testing cannot be used for near tangent configurations or unstable stores that have a large rotation rate in pitch, yaw, or roll because model-to-model collisions must be avoided.

In the grid survey method the aerodynamic forces and moments on a store influenced by an aircraft flow field are measured in a wind tunnel at preselected positions (a volume grid). Interference coefficients for the store are obtained by subtracting the freestream aerodynamic coefficients of the store from those measured near the aircraft. Trajectory calculations are then made by combining the interference coefficients with the measured freestream aerodynamic coefficients as a function of angle of attack (AOA) to obtain the "best" total aerodynamic coefficients for the store [Schindel, 1975].

Since the grid survey method is configuration dependent, each aircraft and store combination is unique and extrapolations to other configurations are not possible. Thus, the grid survey method is most often used for developmentally mature stores since a change in store design invalidates the previously obtained aerodynamic data base. The disadvantages of the grid survey method are similar to those of the CTS. The induced effects of the linear and angular motion of the store are not measured (due to the steady-state nature of the method), but must be estimated. In addition, force and moment measurements for unstable stores are a time consuming endeavor since the grid survey method requires a finer grid spacing to account for the rapidly changing attitude of the store.

The free drop, also known as the dynamic drop method, is a step closer to simulating an actual store separation in a wind tunnel. The free drop is a qualitative method using photography to record the trajectory of a released scaled store model, and obviously has the advantage of recording the net effects of a time changing flow field relative to the store. Unfortunately, the test does not provide force and moment coefficients or flow field information for use in other semi-empirical trajectory prediction methods or design analysis. Furthermore, for accurate trajectories the free drop method requires adherence to aerodynamic scaling laws, but conflicting requirements force the test engineer to choose the most important scaling laws based on experience and judgment. It is not possible to match all the parameters

(freestream velocity, Mach number, or gravity effect [Schindel, 1975]); thus, he must choose to ignore the least important parameter. The following brief description of the free drop scaling laws is given to highlight the difficulties and limitations of store separation simulations at supersonic flight conditions.

The objective of the free drop is to simulate the aerodynamic forces on a store and the inertial response of the store to these forces. One of three scaling laws must be chosen before designing a scale model and wind tunnel test: Froude, heavy, or light. In the Froude method the wind tunnel freestream velocity and model scaling must maintain the hydrodynamic Froude number (F):

$$F = \frac{V_\infty}{\sqrt{gd}} \tag{1.1}$$

where V_∞ is the freestream velocity, d is a linear dimension of the body, and g the gravitational constant. This scaling principle accounts for gravity and inertia forces which are important for free-moving bodies. Thus for a reduced scale model, d', (where prime variables are scaled for wind tunnel testing)

$$d' = d\lambda \tag{1.2}$$

where $\lambda \leq 1.0$, the freestream wind tunnel velocity must also be reduced as shown below [Carman, 1980]:

$$V'_\infty = V_\infty\sqrt{\lambda} \tag{1.3}$$

and

$$F = \frac{V'_\infty}{\sqrt{gd'}} = \frac{V_\infty\sqrt{\lambda}}{\sqrt{gd\lambda}} \tag{1.4}$$

The Froude method is a valid approach for full scale flight conditions at low subsonic speeds. However, at compressible freestream flight conditions the aerodynamic forces would not be comparable to those obtained on the wind tunnel scaled model at reduced tunnel velocities. Therefore, at compressible flight speeds the developed

"heavy" and "light" Mach scaling techniques must be used to insure an aerodynamic match.

To insure compressible aerodynamic similarity, the "heavy" Mach scaling method calls for Mach number equality ($M'_\infty = M_\infty$). The term "heavy" comes from the fact that the mass of the heavy scaled model is greater than the mass of the Froude scaled model. The model mass is found by keeping the aerodynamic forces scaled in proportion to the force of gravity, and using the relationship that the aerodynamic forces are also proportional to the model area and the freestream dynamic pressure. Although the heavy scaling satisfies the compressible and aerodynamic force similarities, Mach number equality occurs at the expense of the velocity ratio simulation (store separation velocity, v/freestream velocity, V_∞). A supersonic wind tunnel test with an incorrect freestream velocity will cause the store to have the wrong induced angle of attack ($\alpha_u = \arctan \frac{v}{V_\infty}$). Thus, model trajectories will exhibit exaggerated angular amplitudes and linear motions because of the dependency of aerodynamic coefficients on the store angle of attack.

Light scaling is the other Mach scaling method used when angular responses and velocity ratios are important. The "light" scaling term comes from the equality of the mass ratio with the Froude scaling method. To retain the proper velocity ratio in a compressible freestream, light scaling assumes the gravitational constant of the model scale may be arbitrarily increased as follows:

$$g' = g \frac{(V'_\infty/V_\infty)^2}{\lambda} \tag{1.5}$$

Unless the gravitational force on the store can be artificially increased, such as using a magnetic field, then in reality the vertical acceleration will be deficient and the vertical displacement of the store too small.

In general, the free drop method gives the investigator qualitative dynamic information of the store separation event that is not available in the steady-state

CTS and grid survey methods. However, there are additional disadvantages in the free drop method beyond the previous mentioned lack of force measurements that cannot be overlooked [Carman, 1980]:

1. There is some loss in store configuration detail due to testing a smaller scale model.

2. It is difficult to simultaneously have the correct model inertia, weight, and center of gravity.

3. Only straight and level flight of the aircraft can be simulated.

(In a time-dependent experiment with constrained store motion an accounting for inertial or gravitational effects is not required. Thus, the scaling laws need not be included in the present experiment as will be discussed later.)

1.3 Time-Dependent Numerical Simulations.

Trajectory predictions dependent upon steady-state aerodynamic coefficients have correlated well with some flight tests. However, when problems do arise in flight test the most common cause is under-predicted rotation rates. Since the store trajectory is sensitive to initial conditions, improvements in the determination of the dynamic effects on the store during the initial separation phase would increase the accuracy of the trajectory predictions. Recent developments in Computational Fluid Dynamics (CFD) have addressed the initial time-dependent conditions with some success [Dougherty, et al., 1985], [Dougherty and Kuan, 1989], [Meakin and Suhs, 1989], [Dougherty and Kuan, 1990]. However, there are significant differences found between the steady-state and time-dependent numerical solutions for equivalent store separation simulations. The results are disconcerting because it is currently unknown if the differences between the steady-state and time-dependent simulations correspond to physical flows, and if transient effects exist, whether the differences

would significantly alter the predicted store trajectories based on steady-state wind tunnel data.

Belk, Janus, and Whitfield [Belk, et al., 1985] compared time-dependent and steady-state numerical solutions for three stores all having the same effective angle of attack (α_e) (the sum of the geometric (ε) and the motion induced (α_u) angle of attack) along a preselected vertical trajectory in a supersonic freestream, Mach 1.41. The authors solved the three-dimensional unsteady Euler equations on a time-dependent computational grid for the case of a store, a 12% thick parabolic body of revolution, separating from a reflection plate as illustrated in Fig. 1.2. (The reflection plate reflects the shock wave emanating from the store but does not initiate a shock wave.)

The numerical simulation included three cases: one steady-state and two time-dependent, but all with identical effective angles of attack. The steady-state case set the store at a fixed angle of attack of 3 degrees ($\varepsilon = 3.0°$, $\alpha_u = 0.0°$) for the different separation distances simulated. The time-dependent simulations started with the store at a fixed position (a distance of 10% of the store length away from the plate) in a uniform flow field of V_∞, and then impulsively plunged the store away from the plate at a predetermined constant velocity, v. The time-dependent cases had a slow ($\varepsilon = 2.0°$, $\alpha_u = 1.0°$) and a fast separation ($\varepsilon = 0.0°$, $\alpha_u = 3.0°$). In general, the store and plate surface pressures for the three cases differed markedly for separation distances less than 30% of the store length. Some of the specific details follow.

The pressure coefficients, C_p , along the surface of the store nearest the plate were determined for various vertical Y-separation locations (normalized by the store length). The store surface C_p results due to the differences only in the fixed geometric angle of attack ($\varepsilon = 0.0°, 2.0°$, and $3.0°$) prior to the motion of the store from its initial position, Y = 0.1007, are shown in Fig. 1.3a. The shock wave initiated by the nose of the store reflects off the plate surface and impinges on the store resulting in

an induced pressure peak near X = 0.20. As expected, the store orientation that creates the greatest flow deflection, $\varepsilon = 0$, has the highest nose surface pressure before and after the reflected shock.

When the impulsive separation begins (Fig. 1.3b), the moving stores ($\alpha_u \neq 0$) experience a sudden decrease in C_p over the entire surface. As the separation distance increases, Fig.'s 1.3c and 1.3d, the time-dependent C_p values approximate the steady-state values upstream of the reflected shock. However, there is still some disagreement downstream of the reflected shock, where it is seen that the reflected shock-induced pressure peaks for the dynamic cases lag the steady-state case throughout the separation event. "Lag" refers to the greater separation distance needed for the time-dependent shock-induced pressure peak to occur at the same X-location along the surface of the store as in the steady-state case. In other words, the steady-state shock-induced pressure is greater and occurs downstream of the time-dependent case for an equivalent separation distance. Thus, there are differences between equivalent steady-state and time-dependent store separation simulations in magnitude and phase during the initial near-touch stage of the store separation event.

The plate surface pressure coefficients under the above conditions are shown in Fig. 1.4. Before separation (Fig. 1.4a) the C_p differences are due solely to the initial steady-state geometric angles of attack, and the incident shock wave induced pressure peak occurs near X = 0.15 for all cases. As the separation distance increases between the store and plate the shock-induced pressure peak decreases in magnitude and moves downstream as shown in Fig.'s 1.4b, c, and d. However, as with the store, the time-dependent shock-induced pressure rise occurs upstream of the steady-state solution. Therefore, both bodies, store and plate, experience different pressure distributions due solely to the type of analysis performed, steady-state versus time-dependent.

A similar comparison study of time-dependent and steady-state computational results was performed by Meakin [Meakin, 1990] who developed a time-accurate

method for simulating multiple body three-dimensional viscous flows with arbitrary grid combinations, body shapes, and relative motion between grid systems. His objective was to determine the transient aerodynamic forces on the space shuttle during various stages of its ascent. As Meakin states, "Transient effects loom in importance because they cannot be quantified with confidence apriori." The two space shuttle configurations simulated were the isolated external tank (ET) and the solid rocket booster (SRB) separation during the nominal ascent of the shuttle vehicle from subsonic to transonic conditions. Meakin notes that an experimental grid survey data base did exist for the shuttle booster separation. However, this data base does not include any transient effects because of the steady-state nature of the wind tunnel test. In Meakin's study, the transient effects were quantified by a time-dependent and steady-state numerical simulation comparison.

The flow about the isolated external tank was numerically simulated for a nominal ascent as it accelerated from Mach 0.8 to 1.023. Surface C_p distributions for the ET are shown in Fig. 1.5 at Mach 1.023. The flow development of the time-dependent case differs from the corresponding steady-state case especially downstream of the minimum pressure location near $X/c=0.7$. Meakin noted that the flow development in the accelerating case lags slightly behind the development of the flow at a steady-state Mach number. For example, the onset and demise of separated flow regimes in the time-dependent simulations occurred at higher Mach numbers than where steady-state simulations indicated separation should exist.

In the second case study of a two-dimensional SRB separation, the companion steady-state computation was made by "freezing" the SRBs at their time-dependent $t = 1300\Delta t$ position, $\Delta t = 0.0024$, (i.e., SRB positions were fixed and the acceleration was zero) and continuing the computations for 2,000 more time steps. A comparison of Mach contours between the dynamic and quasi-steady results is shown in Fig. 1.6. At $t = 1300\Delta t$, the aerodynamic loads on the SRB predicted by the steady-state method (Fig. 1.6b) exceed the time-dependent predicted loads by

approximately 10 and 30 percent for the forces and moments respectively. As with the isolated external tank, the transient flow field of the time-dependent simulation lags the steady-state solution. Although the author fails to discuss the possible cause of the lagging transient flow development, there does appear to be a correlation with the formation of shock waves since the lag effect was found to be most significant in the regions of shock wave development and movement.

Both Belk [Belk, et al., 1985] and Meakin's [Meakin, 1990] CFD simulations showed that near the shock waves the time-dependent values were reduced in magnitude (pressure and aerodynamic coefficients) and lagged in phase (location of the shock wave) compared to the equivalent steady-state solution. Presently, there is no consensus on why these transient lags occur in the numerical simulations, or if the transient effects significantly affect separation conditions. Furthermore, before this present study, there were no time-dependent experimental data that could address the differences found between the time-dependent and steady-state CFD solutions.

1.4   Research Objectives.

As can be inferred from this review of store separation techniques, it is nearly impossible to obtain quantified measurements of the dynamic contributions that occur during a time-dependent store separation event with conventional techniques. Yet, dynamic data is critical during the near-touch phase of separation for flight safety, target accuracy, and determination of the initial conditions needed for analytical trajectory prediction methods. (The "near-touch phase" describes the time during the separation event that the store is within half a body length from the aircraft.) Therefore, this experimental investigation will focus on the initial phase of a time-dependent separation of two tangent bodies in a supersonic flow. The objective of this experimental investigation was to determine the validity of the steady-state assumptions used to make predictions on time-dependent separation events involving shock waves, to quantify the dynamic contributions, and to es-

tablish a time-dependent data base. As shown later in the Results chapter, this experimental investigation found that while there is no significant time-dependent pressure effect associated with a shock wave passage, unsteady pressures were found for time-dependent separation distances less than 20% of the store width.

An understanding of why comparisons of numerical time-dependent and steady-state solutions of supposedly equivalent separation events differ in magnitude and phase has become an important issue as advances in time-dependent CFD methods begin to play a larger role in store separation trajectory predictions and design analysis. Although the new CFD methods are time-dependent, the aerodynamic data base for specific store configurations and the semi-empirical methods will continue to depend upon steady-state wind tunnel data for the near future. Determination of the aerodynamic time-dependent effects would aid corrections to semi-empirical trajectory prediction methods, identify marginal store and aircraft configurations early in the design phase, and improve time-dependent CFD methods.

The experimental approach in this work involved two bodies placed in a near-tangent position and dynamically separated in a constrained motion. The stationary body (either a plate or an ogive) was instrumented to obtain dynamic surface pressures. The second body (a wedge) was attached to an air cylinder and impulsively plunged in a predetermined vertical motion away from (separation) or towards (closure) the stationary model similar to Belk's numerical simulation of a reflection plate and a parabolic store [Belk, et al., 1985]. The plate and wedge configuration simulated a wing and store separation, and henceforth, the wedge will be referred to as the wedge-store. The ogive and wedge-store were used to investigate the movement of an oblique shock wave intersecting a conical-shaped shock wave. The time-dependent surface pressures associated with shock wave pattern between the two bodies were measured on the stationary body during the dynamic motion of the wedge-store. Steady-state numerical and experimental (i.e., measurements made with the wedge-store at fixed positions) analyses were used to evaluate the basic characteristics of the

flow between the two bodies. Analysis of the time-dependent experimental data was used to evaluate the use of steady-state assumptions to predict the time-dependent influences of the moving shock wave.

The remainder of this report is divided into six chapters: Background, Equipment, Experimental and Numerical Methods, Results, Discussion of Results, and Conclusions. Chapter 2, Background, includes a discussion of shock wave development and interactions that may be encountered during store separation events. Chapter 3, Equipment, includes a description of the experimental configuration: facility, models, instrumentation, and data acquisition. In Chapter 4, Experimental and Numerical Methods, the experimental procedures used for collecting and reducing wind tunnel data are explained. In addition, the CFD method used to simulate the steady-state configuration of a wedge-store and plate is given. Chapter 5, Results, the data is presented with a discussion of the flow field structures responsible for the key surface pressure characteristics. Comparisons are also made between steady-state results, differing time-dependent events, prediction results, and CFD solutions. Finally, Chapter 6 will include a summary of the investigation results, and Chapter 7, Conclusions, will be a discussion of the implications of the investigation for existing store separation prediction methods and design concerns for conformal and tangent carriage configurations.

1.5 Scope of Effort.

This investigation of a time-dependent separation of tangent bodies in a supersonic flow required a programmatic approach which included acquiring funds for instrumentation, designing and fabricating models, and securing Wright Laboratory wind tunnel and computational (CRAY) support. The investigation task sequence is as follows:

1. Secured a $20,000 grant from the Air Force Office of Scientific Research for the purchase of instrumentation and data acquisition equipment.

2. Designed and calibrated a pneumatic apparatus for simulating a time-dependent store motion.

3. Designed and instrumented two stationary models: plate and ogive.

4. Designed three wedge-stores.

5. Designed a model support (center sting) which remains in use at the trisonic tunnel.

6. Tested models in Wright Laboratory trisonic tunnel. Acquired steady and unsteady data that provide time-dependent pressure histories which was previously unavailable from store separation literature.

7. Wrote data reduction and time-dependent prediction computer programs used to analyze experimental data.

8. Ran a three-dimensional Euler program to simulate an experimental, steady-state, plate and wedge-store configuration.

1.6 Major Findings.

The following list identifies the major findings of this investigation.

1. The incident shock wave initiated by the wedge-store is not significantly affected by the time-dependent motion of the wedge-store.

2. Time-dependent surface pressures on the stationary models may be predicted from a quasi-steady, store-separation database or from another time-dependent, store-separation database with a different effective angle of attack.

3. Time-dependent, piston like effects (increased pressure magnitude of the pressure profile plateau region) exist during the wedge-store closure motion for separation distances less than 20% of the store width.

4. The flow expansion about the edge of the wedge-store creates a low pressure region near the nose of the store that may provide the mechanism to produce

a pitch-up moment. Flow expansion and low surface pressures are predictable characteristics which must be accounted for in the design of low drag and low observable stores.

II. Background

One primary focus of this investigation was to determine the magnitude of unsteady effects on the shock wave induced by the moving store; specifically, to determine how shock waves induced by stores with different time-dependent separation histories differ in impingement location and strength and whether these differences can be analytically predicted by introducing an effective angle of attack into the calculations. There were several experimental and analytical difficulties in this investigation regarding the application of steady-state assumptions to the time-dependent separation of near tangent bodies. For example, one desirable wind tunnel test would be an experimental duplication of Belk, Janus, and Whitfield's [Belk, et al., 1985] time-dependent numerical simulation where the moving stores are maintained at the same effective angle of attack, yielding a clear identification of the unsteady effects. Unfortunately, there is no physical step function (Equation 2.1) that can be applied to the store to give it an instantaneous constant velocity.

$$v(t) = \left\{ \begin{array}{ll} v_1 & t \geq 0 \\ 0 & t < 0 \end{array} \right\} \tag{2.1}$$

Although each separation event can have the same geometric angle of attack, ε (relative position with respect to the freestream), the induced (α_u) and therefore the effective angle of attack (α_e), will change with the varying store velocity.

The analytical difficulties are directly attributed to the size limitations of the wind tunnel models. There are two factors that limited the size of the wind tunnel models: the cross sectional area of the test section, and the aerodynamic and inertial constraints of a moving store. To avoid choking the supersonic test section, the entire wind tunnel model frontal blockage area must be no more than approximately 3% of the test section area. The aerodynamic and inertial constraints restrict the mass and surface area of the moving store. Thus, the wedge shaped store used in this

experiment had a finite width, and in a supersonic flow, the finite width wedge-store introduces edge effects that induce a rotational three-dimensional flow downstream of the attached shock wave, complicating the post-test data analyses.

The remaining sections of this chapter will include a discussion of the assumptions and fluid dynamic properties needed for developing a two-dimensional method for predicting the surface pressures induced on a stationary body positioned near a moving wedge-store in a supersonic flow. Section 2.1.1, includes a description on how the induced and the resulting effective angle of attack are used to calculate (with two-dimensional, steady-state assumptions) the shock wave angle associated with a moving wedge-store. Two-dimensional assumptions infer that an irrotational flow crossing a shock wave remains irrotational. Thus, the rationale for using a irrotational perturbation method within a known rotational flowfield is examined in Section 2.1.2. The final sub-section of Section 2.1 includes a discussion of the expected pressure effects induced by the motion of the wedge-store. In Section 2.2, the shock wave interactions expected to be produced during wind tunnel testing (i.e., oblique-conical interaction and oblique-curved surface reflection) are explained.

2.1 Shock Wave Perturbation Predictions.

Downstream of a three-dimensional curved shock wave the flow exhibits complex, rotational characteristics and a non-uniform entropy distribution [Pai, 1952]. This type of flow is governed by nonlinear differential equations that can only be solved with numerical techniques. Although a complete analytical solution for the flow downstream of a three-dimensional shock wave is not possible, an estimation of the flow field parameters may be made for a small change in the shock-wave strength (perturbation) when the initial solution is known. Thus, to determine experimentally the unsteady effects of a perturbed shock wave associated with a tangent body separation it was necessary to limit the area of investigation and make assumptions that would allow the use of analytical methods.

An analytical solution for the flow properties immediately behind a three-dimensional curved shock can be determined with the standard shock relationship equations based on the freestream Mach normal to a small element area dS (planar approximation) around a point P on a known shock wave shape [Anderson, 1990]. In this investigation the shape of the shock wave was determined for steady-state configurations by experimental and steady-state numerical simulations. Since the investigation was directed towards differences between separation events, the assumptions were concerned with how and when induced angle-of-attack perturbations could be used to predict changes in the shock wave position and strength. These assumptions were as follows:

1. Since non-axisymmetric stores are finite in width, they initiate curved shock waves primarily in the spanwise direction. The flow downstream of the wedge-store induced shock wave is rotational and three-dimensional.

2. The first order perturbation to the flow field occurs in the store plane of motion. The moving wedge-store primarily deflects the flow two-dimensionally. The perturbed velocity is parallel to the wedge motion and directly affects the attached shock wave angle and strength.

3. The initial shock wave attached to the wedge-store has the characteristics of a two-dimensional shock wave for most of the wedge width near the wedge surface and for a distance between the wedge-store and the plate not to exceed the wedge width. The intersection of the wedge-store motion plane, that which includes the wedge-store axial centerline, and the initial attached (S_i) shock wave is nearly a straight line (Fig. 2.1).

The primary effect induced by a moving wedge-store is the change in the strength and angle of the attached shock wave. The first assumption identifies the flow downstream of the attached shock wave as three-dimensional and rotational. However, the remaining assumptions limit the flow perturbations to a plane across

a nearly straight shock wave. Thus, it is assumed that the motion of the store introduces an irrotational perturbation into a rotational flow field downstream of the initial shock wave. The characteristics of the perturbed attached shock wave may be divided into two components: the position (or location) of the shock wave front and the strength of the shock wave.

2.1.1 <u>Shock Wave Impingement.</u> A moving store has an associated induced angle of attack, α_u, defined by

$$\alpha_u = \arctan \frac{v}{V_\infty} \qquad (2.2)$$

where v is the velocity of the store and V_∞ the freestream velocity. The total effective angle of attack (α_e) of a store during the separation motion is the sum of the geometric (ε) and induced (α_u) angle of attack.

$$\alpha_e = \varepsilon + \alpha_u \qquad (2.3)$$

Since the store was a wedge aligned with the freestream, a direct analogy may be made between the wedge angle and the store angle of attack. Henceforth, the geometric (ε) and induced (α_u) angles of attack will be referred to as the geometric wedge angle and the induced wedge angle, respectively (Fig. 2.2). In a similar manner the total effective angle of attack is now referred to as the total effective wedge angle, α_e.

A separation motion ($-v$) will decrease the effective wedge angle (α_e); whereas, a closure motion ($+v$) will increase α_e. The assumption that the attached shock wave is two-dimensional in nature and nearly straight allows the changes in the shock wave angle (β) to be predicted from the Mach number, shock angle, and deflection angle relationship [Zucrow and Hoffman, 1976]. With reference to the wedge-store the

deflection angle is equivalent to the effective wedge angle.

$$\frac{1}{\tan \alpha_e} = \left(\frac{\gamma + 1}{2} \frac{M^2}{M^2 (\sin \beta)^2 - 1} - 1\right) \tan \beta \tag{2.4}$$

(The specific heat ratio, γ, is equal to 1.4.) Equation 2.4 indicates that an increase in the effective wedge angle at a constant Mach number (M) will increase the shock wave angle. As illustrated in Fig. 2.3, an increased shock wave angle, with the wedge-store fixed in space, will shift the shock impingement location (X_{sh}) upstream on the plate. Conversely, if the wedge-store moves in a constrained vertical motion perpendicular to the freestream, and the associated shock wave passage is recorded for a selected point (i.e, a pressure transducer) on the plate surface as a function of the wedge-store position, then the passing shock wave occurs at greater separation distances for increasing α_e (Fig. 2.4).

2.1.2 Irrotational Perturbation. Once the shock wave position has been predicted, the gas properties downstream of the shock wave must be determined. Beforehand, however, the physical reasonability and solution feasibility should be shown for an irrotational perturbation induced into a rotational flow field. Thus, beginning with the inviscid isentropic flow assumption one would have the following equations:

Isentropic relationship

$$p\rho^{-\gamma} = const \tag{2.5}$$

Continuity equation

$$\frac{1}{a^2}\frac{Dp}{Dt} + \rho div\vec{q} = 0 \tag{2.6}$$

Momentum equation

$$\frac{D\vec{q}}{Dt} = -\frac{1}{\rho}\vec{\nabla}p \tag{2.7}$$

where p is the pressure, ρ is density, and $\vec{q}$ is the velocity vector. The momentum and continuity equations are nonlinear, but can be linearized by making a small

perturbation approximation and neglecting second order terms. One may assume the flow downstream of the initial attached shock wave is nearly at rest relative to a moving coordinate axis such that the velocity and velocity derivatives are small. If the variables with the o subscript represent the average values of the flow and the prime variables the perturbation values, then the linear approximation of Equations 2.6 and 2.7 respectively are

$$\frac{1}{a_\circ^2}p'_t + \rho_\circ div\vec{q} = 0 \tag{2.8}$$

$$\vec{q_t} = -\vec{\nabla}(\frac{p'}{\rho_\circ}) \tag{2.9}$$

such that $\vec{q}$ includes the perturbations and any initial nonuniformities. Since there was no rotational restriction on the initial flow downstream of the shock wave, one cannot assume $\vec{q}$ to be the gradient of a function. One can assume that $\vec{q}$ has the following form [Sears, 1954]:

$$\vec{q}(x,y,z,t) = \vec{\nabla}\Phi(x,y,z,t) + \vec{q_1}(x,y,z) \tag{2.10}$$

where $\Phi = -\int(\frac{p'}{\rho_\circ})dt$ is the irrotational-induced perturbation and $\vec{q_1}(x,y,z)$ is the initial rotational velocity distribution. As shown in Equation 2.10 the initial vorticity is not disturbed by small perturbations. Thus, irrotational perturbations across a planar shock wave may be determined and added to the wedge-store induced rotational flow downstream of the attached shock wave.

2.1.3 <u>Piston Effects.</u> The inviscid assumption is not valid for small wedge-store separation distances due to the friction between the model surfaces and the fluid moving through a small cross sectional area. A supersonic flow with friction decelerates to a sonic velocity as illustrated by the well known Fanno curve [Anderson, 1990]. Thus, for a range of separation distances where viscous effects dominate, the shock wave pattern between the two-bodies is confined near the leading edge of the wedge-store. Hence, the region downstream of the wedge-store leading edge is not signifi-

cantly affected by shock wave perturbations, but could be influenced by the motion of the wedge-store. For small separation distances it is anticipated that the motion of the wedge-store will impart a velocity to the flow and induce a surface pressure change on the stationary body (plate or ogive). Since the constrained vertical motion of the wedge-store is similar to a piston motion, the perturbed surface pressure induced by the wedge-store is referred to as a piston effect.

The closure motion of the wedge-store induces a vertical velocity $(+v)$ toward the surface of the stationary body, and the wedge-store separation motion induces a vertical velocity $(-v)$ away from the stationary body surface. From the perspective of the stationary body, the closure motion induces a compression wave and the separation motion induces an expansion wave. The resulting force on the stationary body surface due to the change in the fluid motion is determined by applying Newton's second law of motion: force is equal to the time rate of momentum. The wave fronts travel at a velocity equal to the local sonic value, a_o. After a time δt, the wave fronts with a unit area "A" have traveled a distance $a_o \delta t$ and include a mass of air equal to $\rho_o a_o \delta t A$ [Heaslet and Lomax, 1949]. The force on the plate due to the compression wave is

$$F \delta t = (\rho_o a_o \delta t A)(v) \tag{2.11}$$

Since this force is due to only the linear motion of the particles, the force per unit area is interpreted as the pressure above the static pressure

$$\frac{F}{A} = p - p_o = \rho_o a_o v \tag{2.12}$$

For store separation the resulting expansion wave reduces the surface pressure by an equivalent pressure magnitude. Equation 2.12 was also derived by Lamb [Lamb, 1932] through a relationship between the kinetic energy of the wave and the work done on the body surface.

2.2 Shock Wave Interactions.

An oblique-conical shock interaction is commonly produced by external store-wing combinations. In general, the conical shock is generated by a store which is often a body of revolution, while the wing initiates a two-dimensional planar oblique shock. The oblique-conical shock interaction may entail unsteady flow as the shock interference transitions from a regular to an irregular (Mach shock) interaction along the intersection line of the two shock waves. In this study, the shock wave interaction associated with the tangent separation of the wedge-store and ogive partially simulates an oblique-conical shock interference.

A rotational, viscous, three-dimensional flow field is produced downstream of an oblique-conical shock interaction, and the flow field solution is not attainable with analytical methods. However, the flow perturbation immediately downstream of the interaction can be determined in a manner similar to how the flow perturbation immediately downstream of the attached shock wave was determined in the wedge-store and plate configuration. Since the shock waves are the primary structure of the flow field about the wedge-store and ogive configuration, much can be learned from an inviscid study of this shock interaction. The analytical approach presented by Yin and Aihara [Yin and Aihara, 1990] describes a method of reducing a three-dimensional shock interaction problem to two dimensions. This method is applicable to the intersection of oblique and conical shock waves and the impingement of shock waves on a plane or curved surface. Marconi [Marconi, 1983] used a similar numerical method to determine the boundary conditions at the cross-sectional triple point and associated contact surface. His numerical study of the reflection of a conical shock on a plane surface compared well with experimental data, and supports the application of this analytical method for the wedge-store and ogive configuration study.

2.2.1 Oblique-Conical Shock Wave Interaction. The oblique-conical shock interaction shown in Fig. 2.5 [Yin and Aihara, 1990] has the reference axis attached

to the apex of the conical shock. β_w is the shock wave angle between the $X - Z$ plane and the oblique shock. The unit vector normal to the oblique shock is defined on the downstream side of the shock.

$$\vec{n}_w = \sin(\beta_w)\hat{i} - \cos(\beta_w)\hat{j} \tag{2.13}$$

The conical shock is represented by a simple cone with a unit normal also downstream of the shock directed towards the X-axis

$$\vec{n}_c = \sin(\beta_c)\hat{i} + \cos(\beta_c)\cos(\phi)\hat{j} - \cos(\beta_c)\sin(\phi)\hat{k} \tag{2.14}$$

where β_c is the cone angle and ϕ is defined as the angle in the $Y - Z$ plane between the negative Y-axis and a point on the conical shock surface. The intersection of the cone and plane is an ellipsoid (L) whose unit tangent vector $(\vec{l})$ is defined at every point by the surface normal vectors (Fig. 2.5).

$$\vec{l} = \frac{\vec{n}_w \times \vec{n}_c}{\mid \vec{n}_w \times \vec{n}_c \mid} \tag{2.15}$$

This intersection line is used as a reference to decompose the velocity vectors and incorporate the Rankine-Hugoniot conditions to solve for all the flow parameters immediately downstream of the shock interaction.

The shock intersection in the vicinity of point P on L can be estimated by planar surfaces, Fig. 2.6. On each of the four shock surfaces the unit normal vectors are also normal to L as defined above in Equation 2.15. If plane D passes through point P perpendicular to $\vec{l}$, the velocity vector upstream of the interaction can be decomposed into vectors normal and parallel to the line L such that the velocity vector normal to L lies in the D plane. The velocity vector upstream of the shock wave is identified with a subscript 1 and the downstream velocity vector with a

subscript 2. Then the upstream velocity component parallel to $\vec{l}$ at P is

$$\vec{V_{1l}} = (\vec{V_1} \cdot \vec{l})\vec{l} \qquad (2.16)$$

The velocity vector normal to $\vec{l}$ at P lies in the D plane and is given by

$$\vec{V_{1r}} = \vec{V_1} - \vec{V_{1l}} \qquad (2.17)$$

It is well known from momentum principles for oblique shocks that the velocity vector tangent to the shock surface is unchanged across a shock wave.

$$\vec{V_{1t}} = \vec{V_{2t}} = \vec{V_t} \qquad (2.18)$$

Similarly, when any $\vec{V}$ is decomposed into $\vec{V_r}$ and $\vec{V_l}$ (Fig. 2.6) the velocity vector along L will also remain unchanged such that

$$\vec{V_{1l}} = \vec{V_{2l}} = ... = \vec{V_l} \qquad (2.19)$$

The thermodynamic properties immediately downstream of the shock intersection can be calculated for all regions near the line of intersection with the two-dimensional shock theory and the normal component of $\vec{V_{1r}}$ to either the conical or oblique shock waves in the D plane, Fig. 2.7. Of course, if the intersection line is normal to the freestream flow ($\phi = 0°$), the problem is reduced to the classic two-dimensional shock wave intersection.

Once the oncoming flow in the D plane is decomposed into $\vec{V_t}$ and $V_{1n}\vec{n} = (\vec{V_{1r}} \cdot \vec{n})\vec{n}$ the velocity downstream of the shock wave ($\vec{V_2}$) may be found. Using the relationship that the tangential velocity components remain unchanged across the shock wave the difference between the upstream and downstream velocities in the D

plane may be written as

$$\vec{V_{1r}} - \vec{V_{2r}} = (V_{1n} - V_{2n})\vec{n}$$ (2.20)

From the Prandtl relationship for an oblique shock

$$\vec{V_{1n}} \cdot \vec{V_{2n}} = a^{*2} - \frac{\gamma - 1}{\gamma + 1}V_t^2$$ (2.21)

one can get

$$\vec{V_{2r}} = \vec{V_{1r}} - \frac{2}{\gamma + 1}\left[1 - \frac{a_1^2}{V_{1n}^2}\right]V_{1n}\vec{n}$$ (2.22)

and

$$\vec{V_2} = \vec{V_{2r}} + \vec{V_l}$$ (2.23)

where a^* and a_1 are the critical speed of sound and the speed of sound of the oncoming flow respectively.

2.2.2 <u>Reflection of Oblique Shock on Curved Surface.</u> The reflection of an oblique shock wave on a curved solid surface, such as the wedge-store induced shock wave impinging on the ogive, is another shock wave interaction that may be analyzed by the method outlined by Yin [Yin and Aihara, 1990]. For instance, if one considers the planar shock wave intersecting a cylindrical body as shown in Fig. 2.8, at any point P along the intersection line, the initial flow field configuration may be defined by the following vectorial relationships:

$$\vec{V_1} = (V_1, 0, 0)$$ (2.24)

$$\vec{n_w} = (sin\beta, -cos\beta, 0)$$ (2.25)

$$\vec{n_c} = (0, -cos\psi, sin\psi)$$ (2.26)

and

$$\vec{l} = \frac{\vec{n_c} \times \vec{n_w}}{|\vec{n_c} \times \vec{n_w}|}$$ (2.27)

2-11

where $\vec{n_w}$ is the unit normal vector to the oblique shock wave, $\vec{n_c}$ is a unit outward normal vector to the cylindrical surface, and $\vec{V_1}$ is the velocity vector upstream of the shock wave.

To reduce this to a two-dimensional shock wave analysis, the oncoming flow velocity must be decomposed in the direction of $\vec{l}$:

$$\vec{V_{1l}} = \left(\vec{V_1} \cdot \vec{l}\right) \vec{l} \tag{2.28}$$

$$\vec{V_{1r}} = \vec{V_1} - \vec{V_{1l}} \tag{2.29}$$

The velocity downstream of the incident shock wave may be determined from Equations 2.22 and 2.23.

Once the initial shock wave intersects with and reflects from the cylinder, the reflection shock wave must turn the flow away from the surface the same amount as the incident shock wave turned the flow into the surface. The angle at which $\vec{V_2}$ is directed towards the surface is

$$\delta = \arccos \frac{\vec{V_2} \cdot \vec{n_c}}{|\vec{V_2}||\vec{n_c}|} - \frac{\pi}{2} \tag{2.30}$$

With the thermodynamic properties upstream of the reflection shock wave and the deflection angle known, the flow immediately downstream of the shock wave impingement may be determined.

The previous sections provided the background necessary for developing an analytical, two-dimensional method for predicting the surface pressures induced by a moving initial shock wave and wedge-store. The discussion covered how the induced wedge angle will be used to predict a two-dimensional shock wave angle, and how the inferred irrotational perturbation across a shock wave was a reasonable estimation of the shock wave changes as the irrotational perturbation did not disturb the initial vorticity downstream of a suspected three-dimensional shock wave. A

prediction method for the surface pressures induced by the piston motion of the wedge-store was also developed. In the next chapter, the details of the experimental setup are explained, and Chapter 4, Experimental and Numerical Methods, will include a description of how the analytical background discussed in this chapter will be implemented into the prediction programs.

III. Equipment

3.1 Wind Tunnel.

The experiment was conducted in the 0.61 m x 0.61 m (2 ft x 2 ft) test section of the Trisonic Gasdynamic Facility (TGF) located at Wright-Patterson AFB, Ohio. The TGF is a closed circuit, variable density, continuous flow wind tunnel capable of operating at subsonic, transonic, and supersonic velocities [Clark, 1982]. The tunnel schematic diagram is shown in Fig. 3.1. Freestream supersonic velocities are obtained with fixed area ratio nozzles that result in Mach numbers of 1.5 and 1.9. The total temperature during the test was kept near $311°K$ with a water cooled heat exchanger located upstream of the tunnel stagnation section. Stagnation pressures of 23,940 and 47,880 N/m^2 (500 and 1000 psf) were used at each Mach number. At Mach 1.5 these stagnation pressures corresponded to Reynolds numbers per meter of 0.30 and 0.64 million respectively. At Mach 1.9 the corresponding Reynolds numbers per meter were 0.27 and 0.55 million.

3.2 Experimental Models.

Two generic model configurations were tested: 1) a fixed flat plate positioned near a moving wedge shaped store as shown in Fig. 3.2, and 2) a fixed ogive positioned near a moving wedge shaped store (Fig. 3.3). Each configuration was limited to a cross-sectional area of 3% of the test section area to avoid a choked condition in the Mach 1.5 test section. In all configurations, the fixed models were mounted on a central stationary sting and instrumented to measure dynamic surface pressures. The separating store, one of three different angled wedges, was connected to a two-way air cylinder located in a housing assembly mounted to the tunnel floor.

A dynamic separation was initiated by the motion of a store either towards (closure) or away (separation) from the central sting mounted model. Separation

distances between the store and the center sting-mounted model were measured with a linear variable differential transformer (LVDT). Pressure and separation distance data for a single separation event were collected simultaneously in order that surface pressure and the store position could be correlated.

3.2.1 Plate. The pressure instrumented plate, shown in Fig. 3.4, was center-sting-mounted at a zero degree AOA with the pressure-sensing side facing the wedge-store. The plate, of surface area 3.35 m^2, included a 12.7-cm-diameter instrumentation disk free to rotate 180 degrees in the plane of the plate. Both the plate and instrumentation disk were made of 4130 annealed steel and milled smooth as an assembled unit. On the opposite side of the plate-sensing side an aluminum instrumentation cover protected the transducers wires and tubing.

Sixteen dynamic pressure transducers, (5 psi differential transducer manufactured by Kulite Semiconductor Products Inc., XCW-062-5D, with more details in Section 3.4.2) were mounted flush to the surface along the disk radius and spaced 0.33 centimeters between the centers of the transducer sensing screens. The transducers orientation, ϕ, with the freestream was varied from 0 to 180 degrees in 15° increments, and held fixed by a pin inserted into the prenotched internal edge of the instrumentation disk. The relative positions of the transducers are diagrammed in Fig. 3.5 for $\phi = 0, 30, 60, 90, 135,$ and 180 degrees, and the transducer positions are tabulated in Table 3.1 for $\phi = 0°$. At $\phi = 0°$ the radial aligned transducers are positioned parallel to the freestream from the disk center upstream towards the plate leading edge. The radial position label in Table 3.1 refers to the distance from the center transducer normalized by the distance to the outer most transducer, 4.93 cm, and X_{LE} refers to the distance from the plate leading edge normalized by the plate length, 20.32 cm.

3.2.2 Fixed Ogive. The ogive was also instrumented with dynamic pressure transducers (XCW-062-5D) and mounted on the center sting as an alternative con-

Table 3.1. Transducer positions on the stationary plate for $\phi = 0°$.

Radial Position	Distance from Center (cm)	X_{LE}
0.000	0.000	0.44
0.067	0.330	0.42
0.134	0.660	0.41
0.200	0.988	0.39
0.268	1.321	0.37
0.334	1.649	0.36
0.401	1.979	0.34
0.468	2.309	0.32
0.534	2.634	0.31
0.601	2.964	0.29
0.667	3.289	0.28
0.735	3.625	0.26
0.801	3.950	0.24
0.867	4.277	0.23
0.933	4.603	0.21
1.000	4.933	0.20

figuration to the plate. The body geometry is a tangent ogive forebody with a continuous cylindrical aft body, Fig. 3.6, and is geometrically similar to the model used by Cottrell and Lijewski of the Armament Directorate, Wright Laboratory [Cottrell and Lijewski, 1988]. The cylindrical aft body is the same diameter as the center sting and constructed of 4130 annealed steel.

Twelve pressure transducers were mounted flush with the surface along the axial length of the ogive, Fig. 3.6. Transducer positions are summarized in Table 3.2, where X is the axial distance from the nose measured in centimeters, and X/YE is the axial distance normalized by the radius (YE = 1.91 cm) of the cylindrical portion of the ogive model. The transducers were spaced 0.51 cm between center-lines beginning at 3.368 centimeters from the nose tip as measured along the ogive axis. The pressure transducers provide coverage across the surface transition region with six transducer on the ogive nose, $X/YE < 3.333$, and six transducers on the cylindrical aft body.

Table 3.2. Transducer positions on the stationary ogive.

Transducer	X (cm)	X/YE
1	3.368	1.768
2	3.876	2.035
3	4.397	2.308
4	4.900	2.572
5	5.410	2.840
6	5.913	3.104
7	6.421	3.370
8	6.932	3.638
9	7.435	3.903
10	7.940	4.168
11	8.446	4.433
12	8.954	4.700

The ogive could be rotated about the longitudinal axis from $\psi = 0$ (transducers nearest the store) to $\psi = 180$ degrees (transducers farthest from the store) in increments of 15 degrees. As with the plate, the transducer positions were held fixed and repeatable with a setting pin placed in predrilled notches.

3.2.3 <u>Separating Stores.</u> All stores were interchangeable and mounted to the actuator housing unit positioned below either the center-sting-mounted plate, Fig. 3.2, or ogive, Fig. 3.3. The position of the wedge-store leading edge with respect to the leading edge of the plate was such as to capture the initial shock wave induced by the wedge-store within the pressure transducer coverage area for all store separation distances. In the plate and store configuration, the wedge-store was centered beneath the plate with the leading edge 3.56 centimeters downstream of the leading edge of the plate. For the ogive and store configuration, the leading edge of the store and the nose of the ogive had the same streamwise position.

The stores were constructed of aluminum with identical attachment points for the air cylinder, the LVDT, and two guide posts. All wedges had the same dimensional block shape (20.96 cm x 6.35 cm x 1.27 cm) to insure identical full closure (near-touch) steady-state separation distances between the wedge-store shoulder and

the pressure instrumented model and to avoid model collisions during the dynamic closure events. However, each wedge-store differed in the wedge angle nearest the pressure sensing model. Three wedge angles were chosen to insure 1) a well-behaved initial induced shock wave and reflection shock at the pressure sensing model surface (3.53 degrees); 2) a reflection shock near the limit of becoming a Mach reflection (6.10 degrees); and 3) a detached shock wave at the vertex of the wedge (12.32 degrees), all based on two-dimensional oblique shock wave theory and a freestream velocity of Mach 1.5. The lower wedge angle (wedge face away from the pressure sensing model) was arbitrary. The double sided wedges are identified by the upper wedge angle such as the 3.53 degree wedge-store shown in Fig. 3.7 and the 6.10 degree wedge-store shown in Fig. 3.8. Finally, the 12.32 degree wedge-store is a simple one sided wedge, Fig. 3.9.

3.3 Actuator Housing Unit.

The actuator housing unit shown in Fig. 3.10 encloses a dual action air cylinder (Bimba model 5 cm stroke, 2.7 cm bore, with a cushioned retraction stroke), the LVDT, associated electrical and pneumatic lines, linear bearings, and cavities for the guide posts. The guide posts moved freely through linear bearings during a dynamic separation event and maintained a constant geometric angle of attack for the moving store. (Design and fabrication parallelism tolerances for the air cylinder, linear bearings, and guide posts resulted in a successful deployment even for the asymmetric 12.32 degree wedge-store, i.e., no binding.) The base of the unit was mounted to the tunnel floor downstream of the test section nozzle block where the electrical and air lines penetrated the tunnel outer wall. The housing unit was cantilevered 26.9 centimeters upstream of the nozzle block end to position the stores beneath the pressure-instrumented model and within the test section viewing window.

Design constraints included the 3% blockage restriction and the material strength requirement to withstand a tunnel start-up scenario of a normal shock on one side of the housing unit and a freestream condition on the opposite side.

3.4   Instrumentation

3.4.1   Linear Variable Differential Transformer.   The store separation positions were obtained using a Tran-Tek LVDT (model 0217-0000) and an oscillator / demodulator (model 1000-0012). (The oscillator converts DC input to AC, exciting the primary winding of the differential transformer. The demodulator converts the output to DC voltage.) The LVDT has a linear range of $\pm$ 2.54 cm and was calibrated to measure a continuous total stroke of 5.1 cm. This type of LVDT utilizes a variable pitch secondary winding which eliminates flat spots or steps as found in discrete segmented windings. The non-linearity was less than 0.25% of full scale.

The LVDT was statically calibrated as installed in the wind tunnel. The calibration data was within a standard deviation of 0.019 cm about the linear calibration equation, and the position resolution was 0.007 cm.

Since the LVDT was used dynamically it was important to examine the frequency response of the system. According to the manufacture the frequency response of the combined LVDT and oscillator / demodulator system is a minimum of 490 Hz. To insure that there were no phase lags within the expected range of operation a verification was made by attaching the LVDT and an accelerometer to a sinusoidal shaker unit. With the generic displacement of the shaker defined by $A \sin \omega t$ it follows that the acceleration is $-A\omega^2 \sin \omega t$. With the LVDT and the accelerometer opposite each other on the shaker bar, their frequency and phase was assessed using a Tektronic 2430A oscilloscope. No phase lag was discernible between the accelerometer and the LVDT within the frequency limit of the shaker unit, 150 Hz, which is greater than the expected frequency (20 Hz) of the store separation event (assuming that the motion of the wedge-store toward or away from the stationary model

corresponds to half a period). The typical time-histories of a wedge-store moving towards and away from a stationary model are shown in Fig. 3.11.

3.4.2 <u>Pressure Transducers.</u> All surface pressure measurements were made with XCW-062-5D dynamic pressure transducers manufactured by Kulite Semiconductor Products Inc. The $3.45x10^4 N/m^2$ (5 psi) differential transducer has a four-arm Wheatstone bridge bonded to a 0.071-cm-diameter sensory diaphragm which is protected by the manufacture's standard B screen. The transducers are thermally compensated with an operating range of 300°K to 355°K. The thermal sensitivity is $\pm 2\%/311°K$. The natural frequency as quoted by the manufacture is 150 KHz. The reference side of the transducers were connected to a manifold located at the tip of the center sting next to the base of the model. The manifold was connected to the tunnel static port lines with a 0.64 cm inner diameter tube.

Calibration of the transducers was done statically in the tunnel. The output signals from each transducer were amplified at gains of 100 and 200, depending on tunnel total pressure, with a D.C.-ground coupling. The typical sensitivity of these transducers is 0.003 $mv/N/m^2$ resulting in resolutions of 38.6 N/m^2 and 19.3 N/m^2 respectively for each gain. Dynamic calibration was determined unnecessary after considering observations made in Raman's [Raman, 1974.] shock tube tests where dynamic calibrations were only a few percent lower than those obtained statically.

3.4.3 <u>Data Acquisition.</u> The data acquisition system consisted of a Nicolet System 500 data acquisition unit, a 386 personal computer, and amplifiers. The Nicolet unit employs five multi-channel digitizers, each with four differential input channels and four independent analog-to-digital converters (ADC). The ADC is capable of digitizing input signals for each channel at a maximum rate of 1 megasample per second (MSPS) with 12 bits of resolution. Simultaneous data collection across all channels is possible since each channel has an individual trigger control.

IV. Experimental and Numerical Methods

4.1 Static Separation Events.

A thousand samples were collected with an acquisition rate of 50 KHz for four steady-state separation positions. Absolute separation distances between the wedge-store shoulder and the pressure sensing plate surface (or ogive shoulder) are listed in Table 4.1 in centimeters and as normalized by the store width (Y/D with D = 6.35 cm). These separation distances were arbitrarily chosen to gain steady-state locations within the near touch phase of separation, but were limited to two collar-block model changes due to the available tunnel time. The wedge-store extreme closure and separation positions were attained with the air cylinder piston respectively fully extended or retracted. Intermediate separation distances were accomplished with collar blocks of 2.5 and 3.8 cm placed between the wedge-store and the actuator housing unit (Fig. 4.1). The setting of an intermediate separation position involved passing the air cylinder rod through a collar block and attaching it to the store. The air cylinder was then retracted onto the collar block and held secure with facility air pressure.

Table 4.1. Static separation distances.

Separation Position	Wedge-store	
	cm	Y/D
Full Separation	5.65	0.89
1.0 in. Block	3.25	0.51
1.5 in. Block	1.97	0.31
Full Closure	0.53	0.08

4.2 Dynamic Separation Events.

A dynamic separation event was defined as the time-dependent motion of the store in the vicinity of the pressure sensing model. The vertical motion of the store

away from the stationary model, increasing the distance between the store and model, was called separation. Separation began with the air cylinder rod fully extended and the store placed near the model ($Y/D = 0.08$). When the valve was activated the air cylinder rod retracted, separating the store from the stationary model. A typical separation event involved moving the store a distance of 4.24 cm away from the stationary model within 26 ms at an average speed of 1.6 m/sec.

A closure event referred to the vertical motion of the store towards the stationary model. The closure began with the air cylinder rod in the fully retracted position and the store at its maximum distance from the stationary model ($Y/D = 0.89$). When the valve was activated, the air cylinder rod extended, thrusting the store towards the pressure instrumented model. A distance of 4.88 cm was covered in 27 ms at an average speed of 1.8 m/sec. (In general, the separation goal for free-fall type stores is to accelerate the store through a minimum distance of 7.6 cm and impart to the store a maximum velocity consistent with the structural capabilities of the aircraft and store. Typical separation velocities vary linearly from 6.1 m/sec for a 227 kg class store to 4.3 m/sec for a 907 kg class store [MIL-HDBK-244].)

Data was collected simultaneously for all the transducers (pressure and position) using the LVDT signal as a trigger to begin data acquisition. This procedure allowed post-test analysis and comparisons of different time-dependent events with respect to either time or store separation position. Initially, input signals were digitized at rates of 25, 50, and 100 KHz with checks at 200 KHz, but after reviewing a series of configuration results and considering the observed two-dimensional ramp-induced shock oscillations of 20 KHz-30 KHz at Mach 3 performed by Dolling and Murphy [Dolling and Murphy, 1983], the 50 KHz was chosen as the standard acquisition rate and was considered an appropriate rate for capturing transient effects of the wedge induced shock wave.

4.3 Data Reduction Process.

Local surface pressures were normalized by the calculated freestream static pressure ($P = P_w/P_\infty$). The original tunnel design places the static pressure ports upstream of the tunnel test section, due to structural interference and interchangeability of test sections, such that $M_{static\ port} < M_{test\ section}$. Since the Mach number in the test section is fixed by the area ratio of the nozzle test section and throat, increasing the tunnel total pressure changes only the static pressure. A tunnel calibration was performed to obtain the Mach number at the model. This calibrated Mach number along with the measured total pressure of the tunnel acquired during each store separation experiment were used to calculate the freestream static pressure at the model tunnel station. Presentation of the pressure data normalized by the calculated static pressure eliminates the confusion that would occur if the test section freestream pressure was normalized by the measured tunnel static pressure and resulted in a value less than 1.0.

The separation position is an absolute measurement from the plate sensing surface, or the cylindrical portion of the ogive, to the shoulder of the separating store normalized by the store width (D = 6.35 cm). The store width is an appropriate normalizing parameter because the shock initiated by the store is directly affected by the flow expansion around the wedge edge. (However, since all the wedge-stores had the same width, no parametric study was performed.)

The store position file acquired from the LVDT (time, position) was combined with surface pressure files (time, pressure) to produce files containing surface pressures relative to store position. Since all data was collected simultaneously it was possible to read in the data and write out the matched position and pressure data to a common file.

4.3.1 Steady-State Data Reduction. The sample statistics were determined for all surface pressure observations made at steady-state store separation positions

using the subroutines developed in Numerical Recipes [Press, et al., 1989]. The statistical values calculated were the mean, the variance, and the standard deviation. The mean of the samples $x_1, ..., x_N$,

$$\bar{x} = \frac{1}{N} \sum_{j=1}^{N} x_j \qquad (4.1)$$

simply represent the average pressure at a static store separation position. The variability of the surface pressure sample population about the mean is the variance,

$$\sigma^2 = \frac{1}{N-1} \sum_{j=1}^{N} (x_j - \bar{x})^2 \qquad (4.2)$$

and the standard deviation is the square root of the variance.

$$\sigma = \sqrt{\sigma^2} \qquad (4.3)$$

The uncertainty in the measurements, or the standard error, is denoted $\sigma_{\bar{x}}$ [Taylor, 1982]:

$$\sigma_{\bar{x}} = \frac{\sigma}{\sqrt{N}} \qquad (4.4)$$

Thus, the final result may be stated as

$$x = \bar{x} \pm \sigma_{\bar{x}} \qquad (4.5)$$

4.3.2 Dynamic Separation Data Reduction. Each dynamic separation run was repeated a minimum of five times, i.e., five closures or five separations. Thus, for a single tunnel and model configuration each surface pressure transducer on the stationary model has five data files associated with it, and each data file contained surface pressures with respect to the store separation positions (Y/D). The pressure at any Y/D was obtained from the simple average of pressures at non-dimensional positions Y/D = ±0.0005 about the Y/D of interest. The ensemble mean pressure

$(\bar{x})$ of N separation events containing the store separation positions Y/D is

$$\bar{x}(Y/D) = \frac{1}{N} \sum_{j=1}^{N} x_j(Y/D) \tag{4.6}$$

4.3.2.1 <u>Induced Wedge Angle Calculation.</u> In this subsection the method of determining the wedge-store velocity from the displacement data, as measured with the LVDT, is explained. As discussed in Section 2.1.1, for a given wedge-store position the time-dependency of a separation event is accounted for with the addition of α_u, Equation 2.2, into the steady-state flow calculations. In particular, α_u was used in the prediction of the time-dependent shock-wave angle, shock-wave impingement location, and pressure rise across the shock-wave front.

At each time-dependent separation position, $Y(t_1)$, the average wedge-store velocity was calculated with the difference quotient

$$v(t_1) = \frac{Y(t_o + h) - Y(t_o)}{h} \tag{4.7}$$

where $t_1 = t_o + \frac{h}{2}$. The digital implementation of Equation 4.7 was used to determine the average wedge-store velocity at every third data point over a range (h) of 18 data points. Thus, for an average wedge-store velocity of 1.8 m/sec and an acquisition rate of 50KHz, the wedge-store velocity calculations were performed for separation positions at approximate intervals of 0.010 cm, which is slightly larger than the LVDT resolution of 0.007 cm. For the same store velocity and acquisition rate the range, h, was equivalent to 0.4 milliseconds.

4.3.3 <u>Shock Wave Impingement.</u>

4.3.3.1 <u>Prediction with Plate Configuration.</u> Experimentally, the greatest difference in α_e occurs between the time-dependent separation and closure motions of the wedge-store. The time-dependent surface pressure and wedge-store dis-

placement data for the wedge-store moving towards the plate, closure, was arbitrarily chosen as the data set to use as a comparison. The data set associated with the wedge-store moving away from the plate, separation, was compared with the closure data set, and the separation data set was perturbed (adjusted to account for a small change in α_e) to predict the closure data set. The difference between the closure and the perturbed separation data set (closure prediction) will aid the identification of unsteady effects associated with the tangent separation of the wedge-store and plate.

Prediction of the shock wave impingement location on the plate surface during the wedge-store closure motion was determined by perturbing the separation data set such that the closure prediction and closure data sets had the same effective wedge angle (α_e). The determination of α_e (Equation 2.3) for each time-dependent event depended only on α_u (Equation 2.2) since ε remained fixed, and comparisons made with the same wedge-store. The wedge-store velocity required for α_u calculations was determined with Equation 4.7. After determining α_e for each time-dependent event, the shock wave angle (β) was calculated with Equation 2.4. The shock wave impingement location on the plate surface (X_{sh}) varies with the wedge-store position and was determined assuming a straight shock wave (verified with schlieren photographs in the Results chapter) attached to the wedge vertex at a given separation position (Y).

$$X_{sh} = Y/tan(\beta) \qquad (4.8)$$

Since the pressure history was available only at fixed surface locations, it was convenient to predict the particular wedge-store separation position needed for the attached shock wave to impinge at the location X. Setting X for the separation and closure events equal for the corresponding Y_s position during separation, a closure position, Y_c, can be calculated using the linear result, $X = Y * m + b$ (where m

and b are the slope and Y-axis intercept respectively of the $X - Y$ plot), resulting in

$$Y_c = \frac{Y_s m_s + b_s - b_c}{m_c} \qquad (4.9)$$

The subscripts "s" and "c" indicate separation and closure events respectively. Value of closure distance from Equation 4.9 will be compared with experimental closure event results. Discrepancy between predicted and experimental time-dependent results are henceforth defined as the transient effects.

Prediction of the pressure rise across the shock wave attached to a moving wedge-store vertex also began with the effective wedge angle, α_e (Equation 2.3), calculation which was used to determine the shock wave angle, β (Equation 2.4). With the calculated shock wave angle, the normal component of the freestream Mach number to the shock wave is given by

$$M_{1n} = M_1 \sin \beta \qquad (4.10)$$

The pressure rise across a shock wave was determined with the known shock wave relationship [Kuethe and Chow]

$$\frac{P_2}{P_1} = \frac{2\gamma}{\gamma + 1} M_1^2 - \frac{\gamma - 1}{\gamma + 1} \qquad (4.11)$$

where the subscripts 1 and 2 refer to the areas upstream and downstream of the shock wave respectively.

The prediction of the plate surface-pressure associated with the wedge-store closure motion was made by adding to the experimental separation surface-pressure the difference between the calculated pressure rise across the shock waves (Equation 4.11) of the separation and closure events. The experimental surface pressure (P_w) was normalized by the freestream static pressure, $P = P_w / P_\infty$. (There were small total pressure variations in the wind tunnel during configuration changes between

the separation and closure events.) The calculated pressure difference across the attached shock wave between separation (s) and closure (c) events is defined by

$$\Delta \frac{P_2}{P_1} = \frac{P_{2c}}{P_{1c}} - \frac{P_{2s}}{P_{1s}} \qquad (4.12)$$

Given that upstream of the incident shock wave the Mach number is the same for separation and closure, the normalized upstream pressure must also be equivalent, $P_{1c} = P_{1s} = P_1$. Therefore, the pressure downstream of the attached shock wave for a closure event may be predicted (P_{2p}) from the separation data (P_{2s}) and the calculated pressure difference between separation and closure events (Equation 4.12)

$$P_{2p} = P_1 \Delta \frac{P_2}{P_1} + P_{2s} \qquad (4.13)$$

The flow at the surface of the stationary model must pass through the oblique shock wave impingement (incident and reflection shock). Furthermore, the incident shock wave is affected by the three-dimensional flow induced by the finite wedge-store width. Therefore, there is some uncertainty as to what the total surface pressure change will be after the passage of the impinging shock wave. Despite experimental and numerical surface pressures do not conform to two-dimensional analysis, the attached shock wave remains nearly planar as discussed in the Results chapter, particularly for the close proximity of the wedge-store and plate ($Y/D \leq 0.89$). Thus, discrepancies between predicted and experimental results of the shock wave location will be the primary indicator for identifying the transient effects, and the comparison of predicted and experimental surface pressure values will be used for reference purposes to evaluate the potential magnitude of the transient pressures.

4.3.3.2 Predictions with Ogive Configuration. A true planar shock wave is not possible with the finite width wedge-store and ogive configuration for several reasons. First, the edge effects associated with the finite width wedge-store will in-

duce the attached shock wave to curve. Second, it can be shown by the methods Yin et al. [Yin and Aihara, 1990] outlined that downstream of the oblique-conical shock interaction the oblique shock wave angle continuously changes along the intersection line. Finally, downstream of the oblique-conical intersection the oblique shock wave will also curve under the influence of the conical flow field.

However, approximating the shock wave impingement location on the ogive surface using a straight two-dimensional shock wave in the wedge-store and ogive configuration symmetry plane, before and after the oblique-conical shock wave intersection, was assumed reasonable as long as the ogive and wedge were close together. The wedge-store edge effects on the oblique shock wave were minimized along the configuration symmetry plane, and the separation distance between the ogive and the oblique-conical shock wave intersection line was less than approximately half the wedge-store width, which reduced the conical flow effects upon the oblique shock wave.

The oblique shock wave angle was calculated with the two-dimensional wedge flow theory based on the total effective wedge angle as explained in the preceding section. The stationary, ogive induced shock wave angle was determined from the schlieren photographs of steady-state separation events. The conical shock wave angles at the oblique-conical shock wave intersection for time-dependent separation distances were found from an interpolation of four schlieren results for steady-state events.

4.4   Numerical Approach.

Numerical results were obtained for a steady-state plate and wedge-store configuration by the integration of the three-dimensional, time-dependent Euler equations using a finite-volume, multi-stage, time stepping algorithm. This code, the three-dimensional Euler/Navier-Stokes aerodynamic method (TEAM), was developed un-

der contract for Wright Laboratory, Wright-Patterson AFB [Raj, et al., 1987]. Details concerning the TEAM code are presented in Appendix A.

A numerical simulation was performed for the 6.1° wedge-store and plate with a separation distance between the two bodies of $Y/D = 0.51$. The computational domain took advantage of the flow field symmetry about the X-Y plane intersecting to the center-line of the plate and wedge-store surfaces. This computational domain represented the physical dimensions of 38.1 cm axial ($0 \leq X \leq 1.88$ normalized by plate length) by 22.2 cm in the lateral direction ($0 \leq Z \leq 1.09$ normalized by plate width), Fig. 4.2. The plate was treated as an infinite solid boundary at the maximum Y position of the computational domain. The minimum Y boundary of the computational domain was composed of a solid boundary for $0 \leq Z \leq 0.16$ (wedge-store surface) and a X-Z symmetry flow plane for $0.16 < Z \leq 1.09$. As in the wind tunnel set-up, the leading edge of the wedge-store was positioned 3.6 cm ($X_{LE} = 0.18$) downstream of the plate leading edge. The remaining boundary conditions were as follows: X minimum plane contained the freestream conditions, the X maximum and Z maximum were identified as far field boundaries, and the Z minimum was set as a X-Y flow symmetry plane.

The grid generation for the wedge-store and plate configuration was accomplished with a geometric spacing in the X and Z directions that resulted in finer grid spacing near the wedge-store leading and spanwise edge. Uniform spacing was maintained for the Y constant planes between the two bodies. The final grid density was 99 X 50 X 54 (X, Y, Z). Grid effects were reduced by doubling the grid density until the variation in results about the attached shock wave were insignificant. The difference between the final and last half grid resulted in a change in peak surface pressure across the impinging shock wave on the plate of only 3%. The numerical simulations were accomplished with the recommended input parameter values [Raj, et al., 1989], (i.e., stability criteria, dissipation, residual smoothing, and enthalpy damping) based on the grid configuration and the freestream conditions of

the flow. The ratio of the actual time-step used to the value estimated using the Courant-Friedrichs-Lewy stability criterion was set at the recommended value of 4 (CFL = 4).

V. Results

The experimental results, numerical solutions, and applied prediction methods presented in this chapter are organized according to model configuration as shown in Table 5.1. A majority of the results and discussion focus on the pressure-instrumented plate and the 6.1° wedge-store at a freestream Mach number of 1.52, and the pressure-instrumented ogive and the 6.1° wedge-store at a Mach number of 1.9. Changes in the wedge-store configuration or Mach number for a given pressure-instrumented model illustrate how experimental and prediction surface pressures are affected by the strength of the shock waves.

5.1   Plate with 6.1 Degree Wedge-Store at Mach 1.52.

5.1.1   <u>Bow Shock-Wave.</u> Upstream of the plate, a bow wave forms due to the proximity of the transducer cover to the plate leading edge (plate configuration shown in Fig. 3.2) and the plate leading edge angle of 33.7°. Therefore, a discussion of the bow wave characteristics and effects on the experimental data and prediction results is presented prior to the results as outlined in Table 5.1.

The bow wave shown in Fig. 5.1 was upstream of the plate and the shock wave pattern induced by the 6.1° wedge-store at the steady-state separation position of $Y/D = 0.89$ and a freestream Mach number of 1.52. (The horizontal lines midway between the wedge-store and plate are oil streaks on the tunnel window.) Though the plate was at a zero degree angle of attack, a shock wave was induced by the plate. However, this shock wave had little effect on the plate surface pressures and was possibly induced by the corner of the plate as the normalized surface pressures upstream of the wedge-induced incident-shock impingement was approximately 1.00.

The expected influence on the flow passing through the bow wave is a reduction in the downstream Mach number and a flow deflection towards the wedge-store.

Table 5.1. Cross reference of test configuration and section number. Transducer settings designated by ALL include $0°, 30°, 60°, 90°, 135°$, and $180°$.

Stationary Model	Wedge Store	Mach Number	Transducer Setting	Results Steady-State	CFD Prediction	Section Number
Plate	6.1°	1.52	ALL	Y/D = 0.89	-	5.1.2
				Y/D = 0.51	X	5.1.3
				Y/D = 0.31	-	5.1.4
				Y/D = 0.08	-	5.1.4
				Time Dependent	Closure Prediction	
Plate	6.1°	1.52	0°	X		5.1.5.1
			0°	X	X	5.1.6
	3.53°	1.52	0°	X	X	5.2
	6.1°	1.52	30°	X	X	5.3
			60°	X	X	5.4
			90°	X	X	5.5
			135°	X	X	5.5
			180°	X	X	5.5
	6.1°	1.9	180°	X	X	5.6.1
	12.3°	1.9	180°	X	X	5.6.2
Ogive	6.1°	1.9	0°	X	X	5.7.1
			30°	X	X	5.7.2
			60°	X	X	5.7.3
			90°	X	X	5.7.4
			135°	X	X	5.7.4
			180°	X	X	5.7.4
	12.3°	1.9	ALL	X	-	Appendix B
	6.1°	1.52	ALL	X	-	Appendix B
	12.3°	1.52	ALL	X	-	Appendix B

Thus, the measured shock-wave angle induced by the 6.1° wedge and a Mach number of 1.52 should be greater than the predicted two-dimensional, oblique shock-wave angle of 48.6°. As seen in Fig. 5.1, the initial shock wave is detached from wedge-store leading edge. Near the plate, the initial shock-wave angle is approximately 52 degrees as measured in the schlieren photograph (Fig. 5.1).

A multitude of Mach number and flow deflection combinations downstream of the bow shock may induce a shock wave angle of 52° based on two-dimensional assumptions. As seen in Fig. 5.2, the two-dimensional, oblique shock-wave angle (β) and wedge deflection angle (α_e) relationship is given for various Mach numbers. The combinations of Mach number and flow defection necessary to induce a 52°, two-dimensional, shock-wave angle downstream of the bow wave may be bounded by a wedge angle of 8.3° and a Mach number of 1.52 (a flow deflection without a change in Mach number), and a wedge angle of 6.1° and a Mach number of 1.45 (a reduction in Mach number without a flow deflection). In a similar manner, a multitude of Mach number and flow deflection combinations may result in a detached initial shock wave. For instance, if the flow across the bow wave was reduced to a Mach number of 1.41 and deflected 3.1° towards the wedge-store, a detached shock wave would form off the wedge-store leading edge. The two-dimensional, oblique shock wave angle and deflection angle relationship for the Mach number of 1.41 is also shown in Fig. 5.2.

A two-dimensional estimation of the flow parameters downstream of the bow wave, however, are well outside the combined Mach number and flow deflection boundaries needed to induce a shock wave angle of 52°. For example, the plate-induced bow wave angle near the wedge-store is approximately 56° as measured in Fig. 5.1. The two-dimensional, predicted Mach number is 1.13, and the flow deflection downstream of the plate bow wave (assuming a freestream Mach number of 1.52) is 10.2° towards the wedge-store. The minimum shock wave angle possible is the Mach wave angle, $\arcsin(1/M) = 62.2°$ for M = 1.13, which is greater than the shock wave angle found near the plate, 52°. The contradiction between the

measured wedge-store induced shock-wave angle and the estimated flow parameters downstream of the bow wave, and the fact that the plate does not span the test section leads to the conclusion that the plate bow wave has a three-dimensional characteristic.

Since the flow is complicated by the bow wave an exact analytical prediction of the wedge induced shock-wave angle is not possible, but changes in the shock-wave angle due to small changes in α_e are predictable for the following reasons:

1. The plate surface pressure upstream of the initial impinging shock wave induced by the wedge-store was nearly equal to the calculated freestream static pressure ($P_w/P_\infty \approx 1.0$) suggesting only a small change in Mach number.

2. As seen in Fig. 5.2, the shock wave angle and deflection angle relationship is approximately linear with a constant rate of change ($\Delta\beta/\Delta\alpha_e$) for small changes in the deflection angle at a constant Mach number, and thus, the objective of using a known time-dependent event to predict a new time-dependent event (i.e., a new α_e) using steady-state assumptions remains possible for small changes in α_e.

5.1.2 <u>Steady-State Y/D = 0.89.</u> The steady-state, surface pressures for the plate (Mach 1.52) are presented to illustrate the global, three-dimensional characteristics of the flowfield about the plate and wedge-store. With the pressure transducers set at $\phi = 0°$ (transducers positioned along the plate centerline and upstream of the instrumentation-disc center) and the 6.1° wedge-store at the full separation position (Y/D=0.89), only the initial shock wave emanating from the wedge vertex impinges within the pressure transducer coverage as identified by the lone normalized pressure peak ($P = P_w/P_\infty$) near $X_{LE} = 0.40$ shown in Fig. 5.3. (X_{LE} is the streamwise distance from the plate leading edge normalized by the plate length, 20.3 centimeters.) This measured shock-induced pressure peak value of 1.49 occurring near $X_{LE} = 0.40$ is 22% lower than the two-dimensional predicted pressure rise occurring across a

shock wave impingement induced by a 6.1° wedge in a supersonic flow of Mach 1.52. For example, a supersonic flow of Mach 1.52 encountering a 6.1° wedge results in an accompanying shock wave angle of 48.6 degrees and a normalized pressure rise across the initial shock of 1.35. At the plate surface the flow must also cross the impinging shock wave reflected from the plate surface and needed to turn the flow parallel to the body. The predicted normalized pressure rise across both the initial and reflection shock (i.e., shock wave impingement) is 1.91. The low shock-induced pressure peak measured on the plate surface (1.49) was the first experimental indication of a three-dimensional flow downstream of the initial shock wave attached to the wedge-store. (A numerical confirmation is presented in Section 5.1.3.) Upstream of the shock wave influence the surface pressure standard error, $\sigma_{\bar{x}}$, was 0.0001, and in the region of shock wave influence $\sigma_{\bar{x}} = 0.0003$.

A surface pressure contour plot from transducer settings of $\phi = 0$, 30, 60, 90, 135, and 180 degrees and the 6.1° wedge positioned at Y/D = 0.89 is shown in Fig. 5.4. The small circles superimposed on the plot identify the transducer positions. The pressure peak between $X_{LE} = 0.36$ and 0.46 indicates that only the initial shock wave from the wedge-store leading edge was impinging within the entire transducer footprint. Downstream of the pressure peak location at $X_{LE} = 0.40$, the surface pressure decreased in the X-direction and reached nearly a freestream condition by $X_{LE} = 0.65$. The flow expansion needed for the pressure decrease was not related to the geometry change between the two bodies since the pressure reduction started at $X_{LE} = 0.40$, well upstream of the wedge shoulder at $X_{LE} = 0.65$. Therefore, the flow must be expanding in the Z-direction away from the plate centerline. In the next section (5.1.3) a three-dimensional, numerical, Euler solution reveals that the low shock-induced pressure peak and the downstream pressure trough was the result of the three-dimensional flow field occurring about the wedge-store.

5.1.3 <u>Steady-State Y/D = 0.51.</u> The steady-state flow characteristics are presented in this section for the wedge-store positioned at Y/D = 0.51. Experimental

pressure results for the separation distance of Y/D = 0.51 are similar to the results for the wedge-store at Y/D = 0.89 and indicate that the initial shock wave was essentially unaffected by the change in separation distance. The three-dimensional, inviscid, computational simulation made for this plate and wedge-store separation distance (to be shown later) confirm the three-dimensional characteristics of the flowfield downstream of the initial shock wave, and the pressure troughs induced on the wedge-store surface counter a nose-down pitching moment.

In Fig. 5.3, the experimental surface pressures for the store separation distance of Y/D = 0.51 and transducer position $\phi = 0°$ reveal that only the initial shock wave attached to the wedge-store impinges within the region covered by the transducers at $\phi = 0°$. Except for the new upstream location of the pressure peak on the plate surface, as compared to the previous case of Y/D=0.89, no significant change occurred in the pressure profile. The peak pressure for Y/D = 0.51 is 1.50 at $X_{LE} = 0.34$. The upstream pressure influence is first seen $X_{LE} = 0.30$, an upstream influence distance from the peak location of $\Delta X_{LE} = 0.04$. A pressure rise upstream of a shock wave impingement is common for strong shock wave boundary layer interactions [Lees and Reeves, 1964]. Pressure rises upstream of a strong shock wave interaction by propagating through the subsonic boundary layer associated with the shock-induced separation bubble. The similar upstream pressure influences ($\Delta X_{LE} = 0.04$) for separation distances of Y/D = 0.89 and 0.51 further support the idea that the change in the separation distance had little influence on the shock wave strength indicating that the Mach number and deflection angle are about the same for the two separation distances. Finally, the initial shock wave angle for the wedge-store position of Y/D = 0.89 (Fig. 5.1) and Y/D = 0.51 (Fig. 5.5) is approximately the same, 52°, as measured in the schlieren photographs.

The plate contour surface pressure for Y/D = 0.51, shown in Fig. 5.6, reveals that the flow downstream of the initial shock-induced pressure peak ($X_{LE} = 0.34$) was expanded to near freestream conditions ($P \approx 1.0$ near $X_{LE} = 0.45$). The

expanded flow created a low pressure trough ($0.38 \leq X_{LE} \leq 0.55$) between the impingement of the initial and reflection shock waves on the plate surface. The pressure rise, downstream of the pressure trough, as recorded with the transducers set at $\phi = 135°$ and $180°$, was due to the impingement of the reflection shock wave coming from the surface of the wedge-store (P = 1.56 at $X_{LE} = 0.59$). The high pressure area associated with the transducers farthest from the center between $\phi = 90°$ and $135°$ ($Z \geq 0.125, 0.44 \leq X_{LE} \leq 0.55$) was due to the data smoothing method used to create the contour plots. Based on the computational simulation discussed next, an estimated but more likely representation of the pressure regions is shown in Fig. 5.7. The regions labeled 1 and 3 respectively represent the low pressure area upstream of the initial shock wave and the pressure trough that exists between the two impinging shock waves. The areas labeled 2 and 4 identify the high pressure regions induced by the initial and reflection shock waves.

The computational simulation modeled the steady-state experimental configuration of the 6.1° wedge-store and plate with a separation of Y/D=0.51, but eliminated the plate-induced bow shock by defining the Y-maximum boundary as an infinite plate (solid surface). This configuration modeling simplified the numerical simulation and provided another method of evaluating the significance of the bow shock in the experimental set up. The freestream numerical inputs were identical to the tunnel conditions: Mach number = 1.52, total pressure = 47,880 N/m^2 (1000 psf), and total temperature = $311°K$. The numerical surface pressure solution along the plate centerline was similar to the experimental result for $\phi = 0°$ as shown in Fig. 5.8. The difference in the experimental and numerical peak pressure locations, X_{LE} of 0.34 and 0.37 respectively, was small. The magnitude of the numerical, peak surface pressure was 4.6% greater than the experimental result. A summary of peak pressures due to the initial shock wave impingement on the plate surface is given in Table 5.2.

Table 5.2. Comparison of the peak normalized surface pressures, Y/D=0.51.

Variable	2D	3D Numerical	Experimental
P_w/P_∞	1.91	1.57	1.50

The numerical surface pressure solution for the plate is shown in Fig. 5.9. The X-axis identifies the centerline of the plate and indicates the distance downstream of the plate leading edge. The radial lines centered at $X_{LE} = 0.44$ represent the pressure transducer coverage used during the experimental phase of the test. The Z-axis identifies the spanwise distance (normalized by the plate width, 20.3 cm) from the symmetry plane located along the plate centerline. As in the experimental configuration, the orthogonal projection of the wedge-store into the plate (X-Z plane) places the leading edge of the store at $X_{LE} = 0.18$ and the spanwise edge at Z = 0.16.

All of the essential characteristics of the experimental plate surface pressures were matched by the numerical simulation except for location of the pressure peaks and troughs, which occur farther downstream in the numerical simulation (Fig. 5.8). The pressure trough in Fig. 5.9, reached a minimum pressure of 1.16 near $X_{LE} = 0.58$. Downstream of the trough the surface pressure increased as the flow encountered the reflection shock wave returning from the surface of the wedge-store. The numerical reflective shock-induced pressure peak at $X_{LE} = 0.66$ was approximately 1.43 as compared to 1.56 at $X_{LE} = 0.59$ in Fig. 5.6.

A discussion of the developing flow field about a wedge-store exposed to an instantaneous supersonic flow (M = 0.0 for $t < 0$) will assist the explanation of the expansion flow. The sketch in Fig. 5.10 illustrates the flow field in the X-Z plane about the wedge-store half-span as viewed from the plate. As the flow moves downstream from the freestream area A to area B the pressure increases across the initial shock wave attached to the wedge-store vertex. Beyond the spanwise edge of the wedge ($Z > 0.16$) there is no body present to deflect the flow; therefore,

initially (t = 0) there is no shock wave nor the associated pressure jump. The high pressure flow in area B expands into area C in an attempt to maintain a continuity in pressure. This expanded flow in area C has a different velocity vector than in the freestream area A. As the freestream in area A encounters the flow in area C with a different velocity vector, a shock wave develops due to the freestream flow deflection. The steady-state flow field is quickly established resulting in the following key characteristics: a variable strength shock wave exists between areas A-B and A-C, an expansion wave exists between areas B and C, and the pressure relationship becomes $P_B > P_C > P_A$.

The wedge numerical surface pressures ($Z \leq 0.16$) and lateral flow field pressures are shown in Fig. 5.11. Just downstream of the wedge vertex ($X_{LE} = 0.18$, $Z \leq 0.16$), the pressure rises to the two-dimensional predicted value (P = 1.35 as discussed in Sec 5.1.2) as it crosses the initial shock wave. As the flow continues downstream, the surface pressure reveals a pronounced three-dimensional expansion from $X_{LE} = 0.21$ near the edge of the wedge ($Z = 0.16$) to $X_{LE} = 0.44$ along the wedge-store centerline ($Z = 0.0$). This low pressure near the nose of the store may provide the mechanism to produce a pitch-up moment. A store pitch-up moment is an undesirable separation characteristic that often leads to a store-to-pylon collision [Arnold and Epstein, 1986].

The surface pressure results from the steady-state numerical and experimental investigations support three conclusions concerning the flow field about the plate and the wedge-store. First the bow shock upstream of the plate has only a small influence on the shock wave initiated by the wedge as the measured shock-induced pressure peak on the plate surface (with bow shock) was within 4.6% of the three-dimensional numerical Euler (bow shock absent) solution. Second, the three-dimensional flow expansion between the separating bodies significantly reduces the shock-induced pressure peak on the plate surface compared to a two-dimensional prediction. Third, the three-dimensional flow expansion downstream of a shock wave can create a pres-

sure trough region on either body surface not seen in a two-dimensional shock wave analysis.

5.1.4 <u>Steady-State Y/D = 0.31 and Y/D = 0.08.</u> At the next closure position, Y/D = 0.31, the surface pressure profile of the plate (Fig. 5.3) has multiple pressure peaks indicating the existence of a shock wave reflection pattern between the two bodies for $X_{LE} \leq 0.44$ ($\phi = 0°$). As shown in Fig. 5.3, the initial peak pressure has moved upstream to $X_{LE} = 0.30$ but only reaches a maximum pressure of 1.34. The pressure profile downstream of the initial peak has a small dip in pressure to P = 1.27 between $X_{LE} = 0.30$ and 0.36. It is unclear why the pressure induced by the initial impinging shock wave is lower than that for Y/D = 0.51 (where P = 1.50). Although the initial and reflection shock waves impinge closer together on the plate surface at the reduced separation distance, as shown in the schlieren photograph (Fig. 5.12), the initial shock wave does not appear significantly different from the shock wave associated with the previous separation position of Y/D = 0.51 as seen in Fig. 5.5. Downstream of $X_{LE} = 0.36$ (Fig. 5.3) a pressure trough develops between the impingement of the initial and reflection shock waves similar to those found at the greater separation distances.

The final steady-state separation distance was at the full closure position, Y/D = 0.08. At this near tangent position, the schlieren photograph in Fig. 5.13 shows that the initial shock wave resembles a Mach reflection at the plate surface, and no shock wave reflection pattern was observed between the two bodies downstream of the initial shock wave. Furthermore, all surface pressure transducers were downstream, or in the region, of the shock wave influence as shown in Fig. 5.3, and the pressure results were also absent of any shock wave reflection pattern characteristics (i.e., no pressure peaks and troughs). The steady-state surface pressures for the separation distances of Y/D = 0.31 and 0.51 will be further discussed and shown in the time-dependent results.

5.1.5　Dynamic Observations.　The induced angle ($\alpha_u = \arctan(v/U_\infty)$) caused by the wedge-store motion is shown in Fig. 5.14 for both the closure and separation events. The separation event began near Y/D=0.09 with $\alpha_u = -0.0017$ radian. The separating wedge-store obtained a near constant speed for $0.32 \leq Y/D \leq 0.70$ with an average $\alpha_u = -0.0045$ radians. The wedge-store begins to slow near Y/D = 0.70 as the driving piston meets the cushioned end of the air cylinder. During the closure motion an $\alpha_u = 0.0037$ radians was attained by Y/D=0.75, and an average $\alpha_u = 0.0047$ radians was maintained for decreasing separation distances of $0.65 \geq Y/D \geq 0.10$. The sudden change in α_u at Y/D=0.08 occurred as the air cylinder piston hit the mechanical stop at the end of the stroke. The maximum $\Delta\alpha_u$ between the separation and closure events was approximately 0.01 radians near Y/D = 0.5.

Dynamic data ($P = P_w/P_\infty$) are presented for selected pressure transducer locations and plotted against the separation distance (Y/D). The pressure transducer positions on the plate are identified by the polar coordinates (R, ϕ) as discussed in Section 3.2.1, where R is the distance between the transducer of interest and the center transducer normalized by the total distance covered by the 16 pressure transducers (4.93 cm). Since the data acquisition of the dynamic events was initiated with the movement of the wedge-store, all dynamic data occur within the two extreme steady-state separation positions of Y/D = 0.08 and Y/D = 0.89.

5.1.5.1　Transducers Set at $\phi = 0°$.　The dynamic surface pressure results along the plate centerline are discussed beginning with the most upstream pressure transducer, R=1.00. The surface pressure shown in Fig. 5.15 reveals that the pressure transducer at R=1.00 was upstream of the initial shock wave for $Y/D \geq 0.10$. For $Y/D < 0.10$, there was a small increase in pressure due to the upstream pressure influence of the initial impinging shock wave.

At R = 0.73 (Fig. 5.16), the initial shock wave induced pressure trace of the closure event lags the pressure trace of the separation event for $Y/D \leq 0.25$. The term "lag" simply means that the pressure profile characteristics of the closure event, such as a peak or trough, occur at a greater separation distance (Y/D) than for the separation event. The pressure magnitude and Y/D differences between the two time-dependent results follow the expected trend induced by the changes in the effective wedge angle (α_e). As discussed in Section 2.1.1, an increase in the steady-state wedge angle also produces an increase in the shock wave angle for a constant Mach number. Since the closure event has a larger effective wedge angle, the wedge-store in the closure event must be at a greater Y/D position than in the separation event for the shock impingement to occur at the same location on the plate (X_{LE}).

The first indication of the developing pressure trough also occurred at R = 0.73 as identified by the inflection on the closure event pressure trace at Y/D=0.16 (Fig. 5.16). Due to a smaller shock wave angle for the separation event, the transducer at R = 0.73 does not see the pressure trough downstream of the initial shock as discussed in Fig. 5.9. The next downstream position, R = 0.67 (a change in distance of 0.335 cm), supports this conjecture since both the closure and separation events have a distinct pressure peak and trough (Fig. 5.17).

The combination of two local peaks and troughs for each dynamic event at R=0.53 (Fig. 5.18) indicates the development of a shock wave reflection pattern between the two bodies. With the wedge-store at the fully separated steady-state position (Y/D = 0.89), the initial shock wave impinges downstream of R=0.53 (thus P = 1.0). As the closure pressure profile is traced for decreasing Y/D, the initial shock wave produces a local pressure peak at Y/D = 0.37 with P = 1.43. As the initial shock wave moves further upstream due to the closing motion of the wedge-store, the effect of the spanwise expansion flow causes a pressure trough at Y/D = 0.28. With further reductions in the separation distance the pressure rises again due to the influence of the reflection shock off the wedge-store surface. The reflection

shock creates a second peak at $Y/D = 0.25$. The pressure trough at $Y/D = 0.20$ supports the identification of the second peak as the passage of the reflection shock wave. This last pressure trough results from the flow expansion downstream of the reflection shock wave and occurs before the final pressure rise as the wedge-store approaches the near-touch position.

Surface pressures from the transducers located farther downstream, such as R $= 0.47$ and 0.40 shown respectively in Fig.s 5.19 and 5.20, reveal similar pressure profile characteristics as found at R $= 0.53$, Fig. 5.18. Each local pressure peak and trough identifies the passage of a shock wave over a pressure transducer. The pressure peak induced by the initial shock wave, near $Y/D = 0.5$ in Figs. 5.19 and 5.20, widens with respect to Y/D as the initial and reflection shock waves impinge farther apart on the plate surface.

The steady-state results compare favorably with the time-dependent, separation results independent of the transducer position, separation position, and the pressure profile characteristics. For example, at steady-state separation distances of $Y/D = 0.31$ and 0.51 (Figs. 5.18, 5.19, and 5.20) the steady-state pressures best match the time-dependent, separation pressure profiles at the initial pressure trough and the rise in pressure due to the impingement of the initial shock wave. This general agreement between steady-state and time-dependent, separation pressures may be due to the weaker shock wave induced by the slower moving wedge-store. In the near touch region, the separating wedge-store is just starting to move and has a slower speed than the closing wedge-store which is at its maximum speed. Thus, in the near touch region the effective wedge angle of the steady-state and separation events are nearly the same, and the induced surface pressures are expected to be similar. At greater Y/D positions, such as $Y/D = 0.31$ and 0.51, the wedge-store has nearly the same speed during the separation and closure events. Again, however, the steady-state results are closer to the separation rather than the closure results, perhaps because of the weaker shock wave associated with the separation event.

The standard error (Equation 4.4) for the time-dependent surface pressure is calculated with five samples (N = 5), i.e., five separation or five closure events. As an example, the surface pressure standard error, $\sigma_{\bar{x}}$, for the transducer at R = 0.47 is shown for the separation event in Fig. 5.21 and for closure in Fig. 5.22. In these figures the left axis is the normalized surface pressure, P, with a minor grid spacing of 0.04, and the right axis is the pressure standard error, $\sigma_{\bar{x}}$, with a maximum axis value of 0.04. A majority of the standard error for the separation event (Fig. 5.21) is less than 0.004, whereas the transducer resolution is 0.003. In Fig. 5.22, the standard error increases a little, $\sigma_{\bar{x}} \approx 0.008$, where the induced upstream pressure influence begins ($0.60 \leq Y/D \leq 0.65$), and a large magnitude spike ($\sigma_{\bar{x}} = 0.032$) is found near $Y/D = 0.20$ corresponding to the final pressure rise. Therefore, the actual pressures for the separation and closure events are as shown in the figures and discussed in the text plus or minus the above uncertainty.

At reduced separation distances, the flow between the bodies and downstream of the coalescing shock waves (schlieren photograph in Fig. 5.13) is dominated by mutual aerodynamic interference. An example is shown in the time-dependent pressure histories for R = 0.07, Fig. 5.23. For $Y/D \leq 0.17$, the pressure profiles are nearly constant at 1.67 and 1.76 respectively for the separation and closure events. These pressure plateaus are similiar to values predicted from two-dimensional piston theory as discussed in the following section.

5.1.6 <u>Closure Prediction Results for $\phi = 0°$.</u> In this section an effective wedge angle correction is made to the separation event to predict the time-dependent closure event. The following will discuss agreement between predicted and measured characteristic peaks and troughs of the closure event. As will be shown, the pressure influence of the initial impinging shock wave is successfully predicted for variations in α_e up to 0.5 degree – a value equivalent to the experimental limitation.

R = 0.74 was the first upstream pressure transducer position on the plate surface with a measurable difference between the time-dependent separation and closure events (Fig. 5.16), and thus it was also the first location at which the α_e correction method was applied. The initial shock wave induced pressure rise, $Y/D \leq$ 0.25 (Fig. 5.24), was well predicted up to a separation distance of $Y/D = 0.17$. At this point, the prediction results deviate from the measured values since the separation event (the database used to make the prediction) did not have an inflection in the pressure trace.

Recall the first upstream position on the plate surface to indicate the passage of the initial shock wave for both the separation and closure events occurred at R = 0.67. In Fig. 5.17, the shock wave passage during the closure event is identified by a pressure peak at $Y/D = 0.20$ and a low pressure trough at $Y/D = 0.16$. In Fig. 5.25, comparison of the predicted and measured closure pressure profiles show that the initial shock-induced pressure rise, $0.35 \geq Y/D \geq 0.23$, is well predicted. There was a discrepancy at $Y/D = 0.23$ where the separation profile had a pressure inflection absent from the closure event. The predicted pressure peak is within a 0.5% of the measured closure event, but the peak position was under predicted by a $\Delta Y/D = 0.01$. As in earlier results, an excellent match occurred for the near-touch increase in pressure, $Y/D \leq 0.15$. The closure event final pressure rise ($Y/D \leq 0.15$ in Fig. 5.25) occurs absent a reflection shock wave pattern. As the schlieren photographs of the wedge-store at $Y/D = 0.31$ (Fig. 5.12) and $Y/D = 0.08$ (Fig. 5.13) illustrate, incident and reflection shock waves coalesce to a single shock wave as the distance between the wedge-store and the plate decrease. Despite this, as further examples will show, the region of final pressure rise was well predicted for all centerline positions regardless of configuration or Mach number.

Further downstream on the plate at R = 0.47 the influence of both the initial and reflection shock waves was observed in the separation and closure events. The predicted, initial shock-wave-induced pressure profile for the closure event at

R = 0.47 (Fig. 5.26) was made for $0.70 \geq Y/D \geq 0.31$. The prediction of the closure event seems to also predict the reflection shock wave induced pressure rise for $0.30 \geq Y/D \geq 0.27$, but this is fortuitous as will be shown later for other downstream transducer positions.

Pressure transducer positions from R = 0.27 to R = 0.0 remain downstream of the initial shock wave induced pressure peak for the entire wedge-store range of motion. At each of these transducer positions there was a good prediction match for the downstream side of the initial peak pressure and the pressure trough. A representative example at R=0.07 is shown in Fig. 5.27, where for $Y/D \geq 0.45$ the initial shock wave was upstream of the pressure transducer.

The start of the final pressure rise was also predicted for all transducer positions (R). At R = 0.07, Fig. 5.27, the final pressure rise match occurred for decreasing separation distances beginning at Y/D = 0.35. However, whenever a pressure plateau existed at the near-touch position, $Y/D \leq 0.20$, the experimental closure event was always under-predicted in pressure. It appears that the plate surface pressure for near-touch positions was influenced more by a piston effect due to the motion of the wedge-store than by shock-wave motion.

In the near-touch phase of separation there are indications that the motion of the wedge-store has a major influence on the plate surface pressure. The surface pressure on the plate, downstream of the shock wave impingement location, was significantly higher for $Y/D \leq 0.20$ during a closure event than for the separation event. Although the effective wedge angle corrections did predict the start of the final pressure rise, the prediction method did not account for the near-touch pressure differences between the separation and closure events. Furthermore, though the surface pressures recorded during the near-touch phase of the wedge-store motion were similar to the responses found in a two-dimensional piston action [Heaslet and Lomax, 1949], the experimental pressure difference for the time-

dependent events exceeded the pressure difference predicted by the piston theory. An example will illustrate the point.

From piston theory, the plate surface pressure induced by the closure motion of the near-by wedge-store may be found with the following equation developed in Section 2.1.3:

$$P' - P'_2 = \rho'_2 a'_2 v' \tag{5.1}$$

where the prime variables denote dimensional quantities, v is the perturbed velocity of the flow into the plate surface, and the subscript 2 refers to the local static conditions. Since only a single shock wave exists between the wedge-store and plate at $Y/D = 0.08$, the local static conditions are assumed equivalent to a flow downstream of a normal shock wave with an upstream Mach 1.52. This assumption leads to the highest change in pressure due to the piston effect of the moving wedge-store. With the wedge-store closure velocity (1.80 m/sec) equivalent to the flow velocity into the plate surface, the change in the plate surface pressure as normalized by the freestream static pressure (P_∞) is

$$\Delta P = \frac{P' - P'_2}{P_\infty} = \frac{\rho'_2 a'_2 v'}{P_\infty} = 0.020 \tag{5.2}$$

Similarly, the change in pressure induced by the wedge-store moving away from the plate is $\Delta P = -0.008$. The reduced magnitude of the piston effect is due to the lower initial velocity of the wedge-store after initiation of separation ($v = -0.76$ m/sec). The measured pressure difference between the separation and closure events for R = 0.07 (Fig. 5.23) during the near-touch phase ($Y/D \leq 0.17$) was $\Delta P = 0.09$, approximately three times the piston theory prediction of $\Delta P = 0.028$.

In summary, the two-dimensional effective wedge angle correction method successfully predicts the closure surface pressure along the plate centerline with α_e varying as much as 0.5 degree between the separation and closure events. This indicates that a two-dimensional approach is adequate for predicting centerline shock

impingement location even within a rotational three-dimensional flow field. Additionally, pressure due to the initial shock wave attached to the moving wedge-store can be predicted by steady-state methods, including, the pressure rise during the near touch phase of the store closure motion (excluding final pressure plateau) as the shock-reflection pattern coalesces to a single shock wave.

5.2   3.53° Wedge-Store, Mach = 1.52.

The 3.53° wedge-store replaced the 6.1° wedge-store with similar relative position for the plate leading edge, $X_{LE} = 0.18$. With the transducers set at $\phi = 0°$, the same radial positions presented for the 6.1° wedge-store configuration (R = 0.73, 0.67, 0.47, and 0.07) are discussed in this section. Overall, the pressure profiles are similar for the two wedge-store configurations. The initial shock wave impinged farther downstream on the plate surface for the 3.5° wedge-store since the shock wave angle was smaller, and correspondingly, the magnitudes of the shock-induced surface pressures were also smaller due to the weaker shock wave. What will be shown is that in general, when the initial and reflection shock waves impinge farther apart on the plate, $Y/D \geq 0.40$, the prediction method matched the centerline pressure profile of the closure event in magnitude and separation position. As the separation distance was reduced, $Y/D \leq 0.35$, the prediction method began to over predict the magnitude of the initial shock-induced peak pressure, but continued to predict the closure event separation distance (Y/D). Finally, as with the 6.1° wedge-store configuration, the final pressure rise during the closure motion was always well predicted regardless of the transducer radial position.

The initial shock wave passage induced a pressure peak for R = 0.73 near Y/D = 0.27 (Fig. 5.28) and for R = 0.67 (Fig. 5.29) near Y/D = 0.32 during the time-dependent closure events. The closure prediction matched the measured separation distance of the initial shock induced pressure rise ($0.27 \leq Y/D \leq 0.32$) for R = 0.73 and R = 0.67 ($0.32 \leq Y/D \leq 0.38$) but over predicted the magnitude

of the pressure peaks. Separation distance and magnitude predictions were good, however, for both the radial positions during the final pressure rise, $Y/D \leq 0.21$. Further downstream at R = 0.47, the initial shock wave induced a pressure peak near Y/D = 0.50 as shown in Fig. 5.30. The initial shock wave induced pressure prediction matched the closure pressure profile for $0.36 \leq Y/D \leq 0.60$.

Finally, at the radial position R = 0.07, the pressure transducer remained downstream of the initial shock wave for the entire time-dependent separation event (Fig. 5.31). The prediction results matched the closure event expansion region immediately downstream of the initial shock-induced pressure peak, $Y/D \geq 0.50$, and as before (6.1° wedge), the final pressure rise was predicted for $Y/D \leq 0.38$.

The above results have shown that in the symmetry plane ($\phi = 0$) it is possible to predict the surface pressure on a stationary body induced by the initial shock wave attached to a near-by moving store. The prediction method included the steady-state assumption that a time-dependent wedge flow can be simulated in a steady-state reference frame by including the appropriate induced wedge angle, α_u, in the total effective wedge angle. In this manner, the separation event provided a database for predicting a closure event that differed in α_e and in direction of motion. The effective wedge angle corrections predicted the location of the initial shock wave independent of the wedge-store configuration and the separation distance between the two bodies although the predicted pressure magnitudes improved as the initial shock wave became more isolated from the shock reflection pattern (i.e., greater separation distances). The beginning of the final pressure rises were also predicted as the wedge-store approached the plate and the reflection shock pattern coalesced to a single shock wave.

5.3 Dynamic and Closure Prediction Results, $\phi = 30°$.

The time-dependent separation, closure, and closure prediction results are discussed together for the transducer setting of $\phi = 30°$. The pressure profiles for

these transducer positions were similar in nature to those along the plate centerline, $\phi = 0°$, including the steady-state results favoring the results of the time-dependent, separation event. In addition, the two-dimensional prediction method based on the effective wedge angle (α_e) continued to approximate the pressure magnitude of the closure event. However, lateral flow induced at the pressure transducers positioned near the wedge edge (Z = 0.16) reduced the magnitude of the pressure peaks and pressure differences associated with varying α_e. Finally, the separation distance predictions for the initial pressure peaks are less accurate due to the curvature of the initial shock wave.

The furthest upstream transducer position to sense a shock wave passage was at R = 0.93 $(X_{LE} = 0.24, Z = 0.11)$. In Fig. 5.32, the upstream influence of the initial shock wave at R = 0.93 occurs for a wedge-store position of Y/D = 0.29 for the closure event and Y/D = 0.25 for the separation event. The location of the shock-induced pressure peaks indicate the closure event (Y/D = 0.19) lagging the separation event (Y/D = 0.16). The difference in the separation distances (Y/D) are due to the greater shock wave angle for the closure event. Noting the magnitude of the initial pressure peaks are nearly equivalent, $P \approx 1.28$, and that the pressure peaks were induced while the wedge-store was close to the plate $(Y/D \leq 0.19)$, it is apparent that the flow expansion about wedge-store edge reduced the shock induced pressure influence. Two-dimensional corrections thus over-predicted the pressure peak magnitude of the closure event with P = 1.30 (Fig. 5.32) and under-predicted the initial pressure peak location at Y/D = 0.18.

The passage of the initial shock wave at R = 0.80 in Fig. 5.33 $(X_{LE} = 0.27, Z = 0.10)$ occurred during both the separation (Y/D = 0.26) and closure (Y/D = 0.30) events. With R = 0.80 nearer the plate centerline, as compared to R = 0.93, there is a strengthening of the two-dimensional effects evidenced by the increase in magnitude of the peak pressure and the pressure difference between the time-dependent events induced by the initial shock passage. The prediction of the initial shock wave-

induced pressure peak for the closure event, shown in Fig. 5.33, was over-predicted for the pressure magnitude ($\Delta P \approx 0.02$) and again under-predicted for the separation position.

For the transducer positions of $0.67 \geq R \geq 0.40$, the initial shock wave passage occurred at greater separation distances allowing the induced pressure peaks to become more developed and isolated from the reflection shock wave impingement as shown in the closure profiles at Y/D = 0.45 for R = 0.67 (Fig. 5.34) and Y/D = 0.52 for R = 0.60 (Fig. 5.35). At R = 0.67 (Fig. 5.34), the edge effects diminished (the initial shock-induced pressure peak of the closure event increased to P = 1.45 as compared to P = 1.28 at R = 0.93).

Comparisons of the prediction and closure events are shown for R = 0.67, 0.60, and 0.40 in Figs. 5.34, 5.35, and 5.36 respectively. The prediction method approximated well the pressure magnitudes for transducers nearer to the plate centerline (maximum Z = 0.08 for R = 0.67). However, the wedge-store separation distance continued to be under predicted apparently due to the spanwise curvature of the initial shock wave.

As R was reduced further, the pressure transducers remained downstream of the initial shock wave-induced pressure peak for the entire range of motion. A representative transducer location is R = 0.13 shown in Fig. 5.37. The downstream side of the initial pressure peak is shown for $Y/D \geq 0.45$, and the pressure peaks near Y/D = 0.37 were due to the reflection shock wave impingement. No predictions were made at these radial locations since the prediction method was intended only for the initial shock wave.

5.4 Dynamic and Prediction Results, $\phi = 60°$.

The dynamic results discussed in this section will focus on the initial shock wave and the surface pressure characteristics found during the near-touch phase of separation. Overall, the streamwise pressure transducer coverage (X_{LE}) for $\phi = 60°$

was only half the streamwise coverage for transducers along the plate centerline, $\phi = 0°$. Only pressure transducer positions $R < 0.47$ were downstream of the initial shock-induced pressure peak for the entire separation event, and pressure transducers, $R \geq 0.80$, were outside the edge of the wedge-store ($Z \geq 0.16$). Steady-state results continue to closely match the time-dependent, separation events. This general agreement leads to the conclusion that time-dependent motion of the wedge-store does not significantly affect the shock wave strengths developing between the two bodies.

At R = 1.00 ($X_{LE} = 0.32$, Z = 0.21), the initial shock wave induced pressure peaks, Y/D = 0.35 (Fig. 5.38), for the separation and closure events were similar. Pressure differences due the induced wedge angle did not occur at this pressure transducer because of its location outside the orthogonal projected area of the wedge-store. However, the shock wave impingement location was affected by the motion of the wedge-store as shown by the differences in the upstream pressure influence for the separation and closure events about $0.35 \leq Y/D \leq 0.50$. As the separation distance was reduced ($Y/D \leq 0.17$), the separation event began to lag the closure event, a reversal of that found for pressure transducer locations closer to the plate centerline. Finally, the pressure difference between separation and closure during the near-touch phase of separation, $Y/D \leq 0.13$, was also insignificant indicating a reduction in the piston effect.

Closer to the edge of the wedge-store, at R = 0.80 ($X_{LE} = 0.34$, Z = 0.17), the initial shock-induced pressure peaks for separation and closure were influenced by difference in α_e as shown in Fig. 5.39. The upstream pressure influence for the closure event occurred at a greater Y/D position than for the separation event and had a larger pressure peak magnitude. During the final pressure rise ($Y/D \leq 0.24$) the separation event lagged the closure event until a peak pressure was attained at Y/D = 0.15. The flow expansion near the wedge edge reduced the surface pressure

as the separation distance decreased, unlike the typical pressure plateau found at the locations near the plate centerline.

The two-dimensional α_e correction method (Fig. 5.39) matched the initial induced pressure peak and the upstream pressure influence of the closure event at the separation distances of $0.58 \leq Y/D \leq 0.70$. Since the separation event lagged the closure event for $Y/D \leq 0.24$, the correction method over-predicted the final pressure rise.

The above results indicate that plate pressures are sensitive to the proximity of transducers to the wedge-store edge. When the wedge-store is close to the plate ($Y/D < 0.20$) the edge effects dominate. The edge effects diminish rapidly, however, as the wedge-store moves farther away from the plate. This reduction in the edge effects is shown in Fig. 5.39 for R = 0.80 (Z = 0.17) at $\phi = 60°$, where pressure change due to the effective wedge angle occurred for separation distances greater than half the wedge-store width ($Y/D > 0.5$). Thus, the pressure difference for separation and closure induced by the initial shock wave is reduced both because of location near the wedge edge (Z = 0.16) and to the store separation distance (Y/D).

The next inward pressure transducer position (R = 0.73), shown in Fig. 5.40, was within the projected wedge-store area (X_{LE} = 0.35, Z = 0.15). The initial pressure peak was similar to the pressure profile of R = 0.80. The closure event had a greater peak pressure and lagged the separation event for $Y/D > 0.60$. During the near-touch phase of the wedge-store separation, $Y/D \leq 0.15$, the closure event also induced a slightly higher pressure, but the difference was small ($\Delta P \approx 0.02$) because of the wedge-store edge effects. The two-dimensional closure prediction (Fig. 5.40) was good for the initial shock-induced pressure peak, at Y/D = 0.63, but with a slight over-prediction in separation position, $\Delta Y/D \approx 0.01$.

The position R = 0.40 (X_{LE} = 0.39, Z = 0.09) was downstream of the initial shock-induced pressure peak for the entire separation event as shown in Fig. 5.41. The expansion flow behind the initial shock wave was essentially the same for both

dynamic events for separation distances of $0.40 \leq Y/D \leq 0.80$. During the near-touch phase, the piston effect was apparent and the closure event pressures exceeded those of the separation event with a $\Delta P = 0.05$.

5.5   Dynamic Results, $\phi = 90°, 135°$, and $180°$.

With the wedge-store at any position all pressure transducers were downstream of the initial shock induced pressure peak for the transducer settings of $\phi = 90°, 135°$, and $180°$. No shock-induced pressure predictions were made for these transducer positions since again the correction in α_e was intended only for the initial shock wave. Instead, the following discussion of the time-dependent events will focus on the near-touch phase of separation and the wedge-store edge effects. Steady-state results continue to match the major pressure profile characteristics of the time-dependent events, and as stated previously, the steady-state results tend favor the separation pressures.

The dynamic closure induced surface pressures for radial positions of R = 0.07, 0.60, and 1.0 are shown in Fig. 5.42 for $\phi = 90°$. The radial transducer position R = 0.60 (Z = 0.15) was within the projected edge of the wedge-store (Z = 0.16), while the R = 1.00 (Z = 0.24) transducer was positioned the farthest outside the projected area of the wedge-store. The pressure magnitudes just downstream of the initial shock induced peak, $Y/D > 0.40$, increase as R increases and correspond to a reduction of the expansion flow strength downstream of the initial shock wave. An inverse correlation exists for the near-touch phase of separation and the flow expansion downstream of the initial shock wave. Essentially, the greater the pressure in the near-touch phase of separation ($Y/D \leq 0.15$), the lower the pressure downstream of the initial shock wave. This correlation is not a time-dependent phenomenon, nor new, as the same conclusion can be drawn from Belk's study [Belk, et al., 1985] where a higher shock-induced pressure corresponds to a lower induced expansion pressure for both steady-state and time-dependent cases (Fig. 1.4a). However, the

implication of the correlation concerning high pressures and strong expansion flows is that aircraft and store integration effort should strive to reduce the high near-touch pressures and strong shock waves to moderate the flow expansion. By avoiding the high near-touch pressure (e.g. with boundary layer control, and store design considerations), the associated strength reduction in the expansion flow would retard the flow-induced pitch-up mechanism encouraged by the low pressure region near the nose of the store.

The pressure profile characteristics for R $= 0.07$ (Fig. 5.43) at $\phi = 135°$ ($X_{LE} = 0.45, Z = 0.01$) were similar to the R $= 0.07$ position at $\phi = 90°$ (Fig. 5.42). The pressure was highest ($P \approx 1.75$) during the near-touch phase, $Y/D < 0.18$, and the flow expansion downstream of the initial shock wave, $Y/D = 0.46$, reduced the pressure to near the freestream static. Again, the pressure difference ($\Delta P \approx 0.12$) between the closure and separation events during the near-touch phase exceeded the piston theory corrections. (From theory $\Delta P = 0.020$ as discussed in Section 5.1.6).

Downstream at R$=0.60$, $\phi = 135°$ ($X_{LE} = 0.54, Z = 0.10$) in Fig. 5.44, only a small region of the initial shock-induced flow expansion, $Y/D > 0.60$, was observable due to this farther downstream position of the transducer. As the wedge-store moved toward the plate the passage of another reflection shock wave induced a local peak pressure at $Y/D = 0.43$ and a small pressure trough at $Y/D = 0.36$. Finally, as the store moved to the near-touch position the piston influence was extended to $Y/D = 0.30$. The magnitude of the pressure plateau and the pressure difference ($\Delta P \approx 0.04$) in the region of $Y/D < 0.2$, however, was reduced during the near-touch phase as compared with the previous cases (e.g., at R $= 0.07$ in Fig. 5.43) due to the flow expansion near the wedge-store edge.

Further downstream at R $= 0.93$ and $\phi = 135$ ($X_{LE} = 0.60, Z = 0.16$), the near-touch pressure ($Y/D < 0.30$) decreased with decreased Y/D (Fig. 5.45) in contrast with the characteristic pressure plateau at the more inboard and upstream pressure transducer positions. Since the transducer was close to the wedge edge, not

only was the near-touch pressure reduced, but the pressures for the time-dependent events were similar. Thus, the piston effects near the wedge-store edge were diffused by the edge-induced expansion flow.

For transducer settings at $\phi = 180°$, Figs. 5.46 and 5.47, the pressure transducers were near the wedge-store shoulder ($X_{LE} = 0.65$). The transducer position R = 0.87, at $\phi = 180°$ in Fig. 5.46, was located opposite the wedge-store shoulder at $X_{LE} = 0.65$, and as expected, the expansion of the flow at the wedge-store shoulder induced a decrease in pressure for $Y/D < 0.30$. Figure 5.47 shows the results for R = 0.80 and illustrates the effect of shoulder-induced expansion flow, as the pressure dropped over an upstream distance of $\Delta X_{LE} = 0.02$ (compare results in Fig.s 5.46 and 5.47) for the store separation position of $Y/D = 0.08$.

5.6   6.1° and 12.3° Wedge-Stores at Mach 1.9.

For the results described below, the pressure transducers were set at $\phi = 180°$ and the wedge-store leading edge placed 6.35 cm ($X_{LE} = 0.31$) downstream of the leading edge of the plate, a location which placed the initial shock wave within the pressure sensing region of the plate. (For the Mach number of 1.9, the transducer setting of $\phi = 0°$ placed the transducer upstream of the initial shock wave. Therefore, there is no need for analysis at $\phi = 0°$ and only $\phi = 180°$ results will be presented.) The shock wave boundary layer interaction on the plate surface induced a large time unsteadiness in pressure and even the ensemble average did not remove the unsteadiness for Mach 1.9 results, unlike the previous Mach 1.52 results. As will be seen the two-dimensional prediction method was again good for the pressure influence induced by the initial shock wave impingement, but not as good for the final pressure rise as they were for Mach 1.52. The following discussion of the 6.1° and 12.3° wedge-store results is for selected transducer positions that best highlight the influence of the initial shock wave.

5.6.1 6.1° Wedge-Store. At the radial position of R = 0.73 ($X_{LE} = 0.62, Z = 0.0$), the rise in pressure for $0.45 \leq Y/D \leq 0.89$ (Fig. 5.48) was due to the initial attached shock wave emanating from the vertex of the 6.1° wedge. The two-dimensional method predicted the closure event well only from the start of the upstream influence through the expansion region downstream of the initial shock-induced pressure peak ($0.34 \leq Y/D \leq 0.80$).

For the further downstream transducer position R = 0.87, $X_{LE} = 0.65$ in Fig. 5.49, the prediction method again matched the region of initial shock wave-induced pressure rise and downstream expansion of the closure event, $0.75 \geq Y/D \geq 0.55$. However, for the final pressure rise, $Y/D \leq 0.20$, predictions were poor.

5.6.2 12.3° Wedge-Store. Since the 12.3° wedge-store induced a larger shock wave angle than the 6.1° wedge, the start of the pressure rise due to the initial shock wave occurred further upstream at $X_{LE} = 0.55$. The shock wave boundary-layer interaction induced an pressure fluctuations as shown in Fig. 5.50 for $Y/D \leq 0.70$, but despite this the prediction method matched well the initial shock-induced pressure rise as shown in Fig. 5.51 for $Y/D \leq 0.75$. For the surface pressure associated with the initial shock wave ($0.85 \leq Y/D \leq 0.35$), similar good prediction results were found at $X_{LE} = 0.60$ as shown in Fig. 5.52.

5.7 Isolated Ogive and Mach = 1.9.

The steady-state experimental surface pressure results for the isolated ogive exposed to a Mach 1.9 freestream condition compared well with a method of characteristics solution for an axisymmetric body [Zucrow and Hoffman, 1976] as shown in Fig. 5.53. In this figure the ogive axial length (X) is normalized by the cylindrical radius of the aft portion of the model (YE = 1.91 cm), and the surface pressure is normalized by the freestream static pressure ($P = P_w/P_\infty$). The kink in the curve at X/YE = 3.37 was due to flow expansion in the region where the ogive forebody

transitions into the cylindrical aft body of the model. The small differences in predicted values at X/YE = 2.04, 2.84, and 3.10 may be due to surface irregularities involving the transducer installation, but as seen later posed no problems in comparing time-dependent events for fixed X/YE positions. (The pressure transducers were placed so that the sensing surface of the pressure transducer was flush with the curved surface, but the flat transducer sensing surface may have induced a small surface discontinuity in the high curvature area on the ogive nose; however, careful installation of the pressure transducers ensured that the sensing surface was either flush or below the ogive surface.)

Schlieren photographs of the steady-state positions Y/D = 0.89, 0.31, 0.21, and 0.08 are shown respectively in Figs. 5.54, 5.55, 5.56, and 5.57. At the fully separated position, Y/D = 0.89, the initial shock wave initiated by the wedge-store impinges near the most downstream transducer position X/YE=4.70 (Fig. 5.54). When the separation distance decreases to Y/D=0.31 (Fig. 5.55), the wedge-induced shock wave and the conical shock reflecting off the wedge surface impinge within the transducer coverage area. At the full closure position, Y/D=0.08 (Fig. 5.57), the initial and conical reflection shock waves impinge on the ogive forebody surface $(X/YE \leq 3.37)$.

5.7.1 6.1° wedge-store and ψ = 0°. For this angle, the pressure transducers were adjacent to the wedge-store. Three transducer positions will be discussed in order to illustrate the different shock wave interactions occurring on the surface of the ogive: two positions are representative of the ogive forebody with the remaining position representative of the cylindrical aft body. The steady-state, time-dependent, and closure prediction results are shown together for the remaining ogive and wedge-store configurations. The steady-state results again match the major characteristics of the time-dependent pressure profiles, and as it was for the plate, the steady-state results tend to be closer to the separation than the closure results.

The surface pressure for the forebody position X/YE = 2.57 is shown in Fig. 5.58. The upstream influence due to the initial shock wave impingement began at Y/D = 0.51 for the closure event, and the initial shock-induced pressure peak for the closure and separation events were at Y/D = 0.36 and at Y/D = 0.33 respectively. The pressure profile characteristics, including the pressure trough at $0.20 \leq Y/D \leq 0.30$, were similar to the pressure profiles found with the plate and wedge-store configurations. As with the earlier plate investigation the pressure trough about Y/D = 0.25 was due to the three-dimensional expansion of the flow downstream of the initial impinging shock wave as discussed in Section 5.1.3.

The usual two-dimensional prediction method accounting for α_u continued to predict well the initial shock wave influence of the closure event as shown in Fig. 5.58 as seen for the upstream influence area (Y/D = 0.50) through the initial peak pressure at Y/D = 0.36. As with the plate and wedge-store configuration, the prediction method only approximates the reflection shock-induced pressure profile, $0.15 \leq Y/D \leq 0.24$.

Downstream on the ogive nose at X/YE = 3.10 in Fig. 5.59, the initial shock wave-induced pressure peak at Y/D = 0.49 occurred for a greater separation distance than at X/YE = 2.57 (which had a peak pressure at Y/D = 0.36). The prediction method matched the upstream influence region of the closure event starting at Y/D = 0.62 and the magnitude of initial shock-induced peak pressure, but it under-predicted the separation position for $0.55 \geq Y/D \geq 0.49$. The correction method again approximated the reflection shock-induced pressure profile from Y/D = 0.30 to 0.25 and matched the final pressure rise for $0.22 \geq Y/D \geq 0.18$. A pressure plateau occurred during the near-touch phase, $Y/D \leq 0.16$, in both the separation and closure events, but the pressure difference ($\Delta P = 0.03$) between the time-dependent events was not as large as for the centerline of the plate configuration. The three-dimensional surface of the ogive reduced the piston action effect as

seen on the fixed plate, and for this case, the α_e prediction method over-predicted the pressure magnitude of the closure pressure plateau.

The most upstream pressure transducer on the cylindrical aft body is at X/YE = 3.64, and the pressure profile for that transducer is shown in Fig. 5.60. The initial shock-induced pressure peak for the closure event occurred at a separation distance of Y/D=0.62, and the pressure was lower (compared with X/YE = 3.10 in Fig. 5.59) due to flow expansion across the surface transition from the ogive nose to the cylindrical aft body. The pressure induced by the reflection shock wave was also lower and only induced a pressure inflection (at Y/D = 0.32) on the closure pressure trace as compared to the typical local pressure peak found on the ogive nose (e.g., Y/D = 0.18 in Fig. 5.58). The final pressure plateau was also significantly reduced in pressure ($\Delta P \approx 0.3$) as compared to the forebody position X/YE = 3.10 (Fig. 5.59), but the plateau pressure region was extended to a separation distance of Y/D = 0.25 during the closure event.

The prediction method based on α_e failed to match the initial shock-induced upstream pressure rise and the peak pressure of the closure event for $0.68 \geq Y/D \geq 0.61$ (Fig. 5.60). This weakness of the prediction does not appear to be a primary function of the flow expansion about the ogive model surface curvature since the upstream transducer positions on the ogive nose also showed trends of under predicting the influence of the initial shock wave. The weakness in the prediction method resides in the assumption that the initial oblique shock wave remains straight after it intersects the near conical shaped shock wave induced by the ogive nose. When the ogive and the wedge-store are close together the distance from the oblique-conical shock interaction to the ogive surface was small; therefore, the straight shock wave assumption was reasonable within the conical flow. Indeed, at X/YE = 2.57 (Fig. 5.58), the initial peak pressure occurred at a separation distance of Y/D = 0.36, and the prediction was good. Whereas for an increased wedge-store separation location, the oblique shock wave must pass through a greater distance downstream of the conical

shock before impinging on the ogive surface. As the oblique shock wave propagates from the conical shock intersection to the ogive surface it will encounter continuously changing flow velocities associated with the conical flow that will induce small changes to the oblique shock wave angle. At X/YE = 3.64 the initial peak pressure occurred at nearly twice the separation distance as at X/YE = 2.57 with Y/D = 0.62 (Fig. 5.60); thus, the prediction of the closure event continued to degrade with the increase in the separation distance.

5.7.2 $\underline{\psi = 30°}$. The flow deflection across a shock wave impinging on the ogive surface at $\psi = 30°$ is smaller than a deflection at $\psi = 0°$ due to the transducer orientation to the shock wave. Calculating the flow deflection and conditions through a three-dimensional shock wave interaction may be accomplished by the method outlined in Section 2.2. As an example, consider the simple configuration of a two-dimensional oblique shock wave intersecting a cylindrical body, Fig. 2.8. The intersection of the shock wave and body surface results in an intersection line, L. If P is a point on the intersection line, then a unit tangential vector ($\vec{l}$) to the line L at P is defined by the normalized cross product of the unit normal vectors for the oblique shock wave and cylindrical body. Therefore, the initial flow field configuration may be defined by the following vectorial relationships:

$$\vec{V_1} = (V_1, 0, 0) \tag{5.3}$$

$$\vec{n_w} = (\sin\beta, -\cos\beta, 0) \tag{5.4}$$

$$\vec{n_c} = (0, -\cos\psi, \sin\psi) \tag{5.5}$$

where $\vec{n_w}$ is the unit normal vector to the oblique shock wave, $\vec{n_c}$ is a unit outward normal vector to the cylinder surface, and $\vec{V_1}$ is the velocity vector upstream of the shock wave.

With the transducers set at $\psi = 0°$, $\vec{V_1}$, $\vec{n_w}$, $\vec{n_c}$, and the velocity vector downstream of the shock wave, $\vec{V_2}$, are all planar. Thus, in the vicinity of P the flow

pattern is a two-dimensional shock reflection. By setting a solid boundary condition on the cylinder surface (i.e., flow remains parallel to the surface downstream of the reflected shock), we can use the Rankine-Hugoniot twice and obtain the flow parameters in each region. If we simplify the experimental 6.1° wedge-store at Mach 1.9 scenario by ignoring the conical shock wave, then the flow deflection on the cylindrical portion of the ogive model would be given by

$$\delta_2 = \delta_3 = 6.1°$$ (5.6)

The resulting pressure rise across this reflection shock is $P_3/P_1 = 1.87$.

However, when the transducers are set at $\psi = 30°$, $\vec{n_c}$ is no longer planar with the velocity vectors upstream and downstream of the shock wave. In order to make a two-dimensional shock wave analysis, the velocity vectors may be decomposed along the intersection line in the direction of $\vec{l}$. By choosing to decompose the freestream velocity vector into a vector tangent to $\vec{l}$ at P,

$$V_l \vec{l} = (\vec{V_1} \cdot \vec{l}) \vec{l}$$ (5.7)

we can determine the upstream velocity vector that is co-planar with $\vec{n_c}$.

$$\vec{V_{1r}} = \vec{V_1} - V_l \vec{l}$$ (5.8)

The magnitude of the velocity vector normal to the shock wave at P is

$$V_{1n} = \vec{V_{1r}} \cdot \vec{n_w}$$ (5.9)

The velocity downstream of the shock wave may be determined by using the results developed in Section 2.2 where

$$\vec{V_2} = \vec{V_1} - \frac{2}{\gamma + 1}\left(1 - \frac{a^2}{V_{1n}^2}\right)V_{1n}\vec{n_w} \qquad (5.10)$$

To determine the flow deflection necessary to maintain a parallel surface flow downstream of the reflection shock the angle of $\vec{V_2}$ directed towards the surface at P must be found.

$$\delta = \arccos\frac{\vec{V_2}\cdot\vec{n_c}}{\left|\vec{V_2}\right|\left|\vec{nc}\right|} - \frac{\pi}{2} \qquad (5.11)$$

The reflection shock needs to turn the flow 5.28° to satisfy the parallel flow at the surface. Whereas, the flow was deflected 6.1° twice for $\psi = 0$, at $\psi = 30$ the flow was deflected 6.1° through the initial shock, but only turned 5.28° through a reflection shock. The pressure rise across the shock impingement at $\psi = 30$ is $P_3/P_1 = 1.80$. The ratio of the calculated pressure found at $\psi = 30$ to the pressure at $\psi = 0$ is 0.96. This ratio holds as an estimate to the experimental results even though the conical shock wave was ignored, and the oblique two-dimensional assumptions made. The ratio of the initial shock-induced pressure peaks for the separation events at X/YE = 3.64 as measured from Figs. 5.60 ($\psi = 0$) and 5.61 ($\psi = 30$) is 0.94.

The pressure profiles and prediction results for a transducer located on the cylindrical portion of the model at $\psi = 30$, X/YE = 3.64, are shown in Fig. 5.61. The initial shock wave induced pressure peak magnitude for the closure event was 1.26 at Y/D = 0.53, and it was predicted from the upstream influence region till just past the pressure peak, $0.57 \geq Y/D \geq 0.48$. As the wedge-store was positioned closer to the ogive, there was a surface pressure decrease due to the flow expansion downstream of the initial shock wave. Decreasing the separation distance further reveals that the passage of the reflection shock wave was not discernable since the second local pressure peak was absent during the final pressure rise, $Y/D \leq 0.35$. Finally, a pressure plateau developed during the near-touch phase of separation,

$Y/D < 0.17$, but the pressure difference between the separation and closure events was insignificant. The piston influence of the moving wedge-store degraded as the transducers were rotated away from the configuration symmetry plane, $\psi = 0°$ (e.g., compare the piston influence shown in Fig. 5.60).

The surface pressures for the most downstream transducer position, X/YE = 4.70, is shown in Fig. 5.62. The apparent discrepancy between the steady-state pressure for Y/D = 0.89 and the time-dependent pressures is due to the appearance of the initial shock wave for a small change in the wedge-store position. (As will be shown later the transducer continued to respond correctly for ogive rotations of $\psi = 135°$ and 180°.) The initial pressure peak occurred at a greater separation distance (Y/D = 0.75). Indications of the reflection shock wave remain absent during the final pressure rise $0.50 \geq Y/D \geq 0.34$, as it was for the upstream transducer position at X/YE = 3.64. At reduced separation distances the surface pressure decreased and showed no significant difference in the pressure magnitude or the separation distance (Y/D) between the separation and closure events.

5.7.3 $\underline{\psi = 60°}$. The reduction in magnitude of the shock-induced pressure peaks continued as the transducer rotational positions increased to $\psi = 60°$. In Fig. 5.63, the passage of the initial shock wave ($0.15 \leq Y/D \leq 0.31$) on the ogive nose at X/YE = 2.31, produced only a small pressure difference between the time-dependent events and a peak pressure of 1.40. The primary factor that contributed to the small pressure magnitude and pressure difference between the time dependent events was the angle between the ogive surface normal vector and the downstream unit normal vector of the oblique shock wave. Furthermore, by following the same analytical approach as in the previous section it can be shown that the flow deflection through the shock wave reflecting off the ogive nose is nearly half of the flow deflection angle found on the cylindrical aft body.

To simplify the analysis, assume an oblique shock wave impinged on the forebody at X/YE = 2.31 ($\psi = 60°$). In addition, assume the oblique shock wave angle was $\beta_w = 37.31°$, which results from a freestream Mach = 1.9 and a wedge angle of 6.1°. The velocity vector tangent to the forebody at X/YE = 2.31 and upstream of the oblique shock wave was $\vec{V_{1s}} = 473 \cdot (0.94, -0.17, 0.29)$ m/sec as determined by the method of characteristics. Downstream of the oblique shock wave, the deflection angle for $\vec{V_2}$ was 2.31° into the ogive surface. Therefore, the reflection shock wave must deflect the flow away from the surface by the same absolute angle to ensure the velocity vector remains tangent to the ogive surface downstream of the shock wave impingement

The transducer at X/YE = 3.64 was the first downstream transducer positioned on the cylindrical aft body. Based on the methods of characteristics, the normalized surface velocity at X/YE = 3.64 increased beyond the freestream value due to the surface transition from ogive forebody, $\vec{V_{1s}} = (1.06, 0, 0)$. After passing through the oblique shock wave the normalized velocity vector becomes $\vec{V_2} = (1.03, 0.15, 0)$, and a reflection shock deflection of 4.13° is required to maintain tangent surface flow, almost twice the reflection shock deflection at X/YE = 2.31, 2.31°. Therefore, at X/YE = 3.64 a larger initial shock-induced pressure difference is expected than at X/YE = 2.31 between the time-dependent events. As shown in Fig. 5.64 the pressure difference between the time-dependent events is realized for $0.43 \geq Y/D \geq 0.35$.

The surface pressure results for a position further downstream on the cylindrical portion of the ogive, X/YE = 4.43, are shown in Fig. 5.65. The passage of the initial shock wave during the closure event was indicated by the local pressure peak about $0.60 \geq Y/D \geq 0.45$, and the maximum pressure peak ($Y/D \approx 0.55$) was predicted in both magnitude and separation position. As the separation distance decreased, $Y/D \leq 0.45$, the surface pressure began to increase, but the pressure profile did not give any indication of a reflection shock passage. During the near-touch

phase of separation, $Y/D \leq 0.22$, the pressure decreased due to a flow expansion about the wedge edge.

The two-dimensional prediction method worked well despite its simplified assumption that the oblique shock wave remains straight downstream of the oblique-conical shock wave intersection. At $\psi = 0°$ where the velocity vectors remain coplanar before and after the oblique shock wave the prediction method matched the initial shock-induced pressure peak at $Y/D \leq 0.45$. Although the predicted shock position degraded with increases in separation distances due to the shock wave curvature, the pressure magnitude corrections remained appropriate. As the ogive was rotated to $\psi = 30°$ and $60°$ the predicted pressure magnitudes were too large as the difference in the flow deflection through the shock wave reflection off the ogive nose was less than the flow deflection difference at the oblique-conical shock wave intersection. Downstream on the cylindrical aft body where flow deflection across the shock wave impingement was on the order of the deflection found at the oblique-conical shock wave intersection, the prediction method again approximated the influence of the initial shock wave in position and pressure magnitude.

5.7.4 $\underline{\psi = 90°, 135°, \text{ and } 180°}$. With the transducers set at $\psi = 90°$, there was no significant difference in surface pressure between the two time-dependent events, and the two-dimensional prediction method was no longer applicable. For example, on the ogive nose at X/YE = 2.57, the time-dependent surface pressures are essentially identical following a smooth shock-induced pressure rise for $Y/D \leq 0.28$ (Fig. 5.66).

Downstream at the first position on the cylindrical aft body, X/YE = 3.64, the shock-induced pressure rise starts at a greater separation distance ($Y/D \leq 0.60$), but does not show any difference in pressure until the final pressure rise at Y/D = 0.20 (Fig. 5.67). A pressure plateau exits for $Y/D \leq 0.16$, and the piston effects remain small similar to the results of $\psi = 60°$.

A rotation of the ogive model to 135° and 180° places the transducers into the model shadow, i.e., the initial oblique shock wave cannot impinge directly on the transducers. For the transducer positions at X/YE = 2.57 for ψ = 135° and 180°, there were no difference in surface pressures associated with the different time-dependent events. The ogive nose was upstream of the initial shock wave induced pressure rise as represented in Figs. 5.68 and 5.69 for ψ = 135° and 180° respectively. At X/YE = 3.64, the initial shock wave does induce a small pressure rise as seen in Fig. 5.70 for ψ = 135° and Fig. 5.71 for ψ = 180°. The same characteristic results were also found at the most downstream position, X/YE = 4.70, as shown for ψ = 135° and ψ = 180° in Figs. 5.72 and 5.73, respectively.

5.8   Alternative Ogive and Wedge-Store Configurations.

The remaining ogive configurations tested were the 6.1° wedge-store at Mach 1.52, and the 12.3° wedge-store at Mach 1.52 and 1.90. However, predictions with the two-dimensional method were not possible on these configurations, since the oblique-conical shock interaction results in an irregular intersection for even the simplest case of ψ = 0°. It was thought initially that the stronger shock interactions would be more likely to produce the time-dependent lags in the shock wave development as originally identified by Belk [Belk, et al., 1985] during his numerical investigation. However, upon reviewing the raw data, no significant differences were found between the different dynamic events that would exceed the expected magnitude of the effective angle of attack corrections. A discussion of the raw data for these new configurations would not add any new insights since the pressure profiles are very similar to the results of the 6.1° wedge-store at Mach 1.90. However, the time-dependent data is unique and suited for providing a good base for CFD comparisons because of the clean flow (i.e., no bow shock); therefore all the ogive pressure results are given in Appendix B.

VI. Discussion of Results

The experimental results discussed in the previous chapter cover the change in configurations as outlined in the test matrix (Table 5.1): Mach number (1.52 and 1.90), wedge-stores (3.5°, 6.1°, and 12.3°), stationary models (plate and ogive), and transducer settings (ϕ, ψ). Assimilation of such a large data set is a formable task; therefore, this chapter will include a summary and discussion of the significant findings. The characteristics of the surface pressure results for different test configurations are addressed within three categories: steady-state experimental and numerical results, experimental time-dependent results, and time-dependent predictions. Each category includes significant trends and common surface pressure characteristics found in this investigation.

6.1 Steady-State Events.

The analysis of the steady-state experimental and numerical results identified three-dimensional flow characteristics downstream of the initial shock wave attached to the wedge-store vertex. Since the wedge-store was of a finite width, the flow expanded into the spanwise region off the edge of the wedge-store where the pressure was lower. Unlike planar shock waves that induce uniform flow deflections and an increase pressure, the three-dimensional flow downstream of the wedge-store initiated shock wave resulted in regions of nonuniform flow deflections, low shock-induced surface pressures, decreasing pressures, and curving shock waves.

For example, a two-dimensional flow of Mach 1.52 encountering a 6.1° wedge has a normalized pressure jump (P_2/P_∞) across the initial shock wave of 1.35. At the plate, where the wedge induced shock wave impinges, the flow must also cross the shock wave reflecting off the plate surface to maintain a flow parallel to the plate surface. Thus, the total predicted pressure ratio (P_3/P_∞) across a two-dimensional shock wave impingement on the plate surface is 1.91.

In Section 5.1.2, for the above configuration the experimental simulation used a finite width wedge-store of 6.1° at the separation position of Y/D = 0.89, and experienced a pressure peak of 1.49 near $X_{LE} = 0.40$ (Fig. 5.3), 22% lower than the two-dimensional predicted value. Similar experimental results were found with the wedge-store at the reduced separation position of Y/D = 0.51. A three-dimensional inviscid numerical (Euler) simulation of this configuration confirmed that the three-dimensional expansion region downstream of the initial shock wave was responsible for the experimental pressure magnitudes being lower than the two-dimensional analytical predictions.

The numerical surface pressure solution for the plate at the above test configuration (Y/D = 0.51) was shown in Fig. 5.9 of Section 5.1.3. The magnitude of the normalized pressure peak induced by the initial shock wave was slightly higher (1.57) than the experimental pressure peak (1.50), but still significantly less than the analytical two-dimensional predicted value (1.91). Overall the main characteristics of the plate surface pressure found in the experimental results were predicted by the three-dimensional Euler simulation.

The pressure troughs downstream of the shock waves were the most significant characteristic of the flow field between the wedge-store and stationary models. Contrary to the expectation of obtaining an increase in surface pressure while moving downstream through a shock wave reflection pattern as shown by the schlieren photograph in Fig. 5.5, the experimental surface pressure results (Fig. 5.6) reveal a flow expansion, to near freestream conditions at the plate centerline, between the impinging initial and reflection shock waves (P = 1.0 at $X_{LE} = 0.45$). The numerical surface pressure results for the plate (Fig. 5.9) also show a pressure trough near $X_{LE} = 0.59$ that extends in the streamwise and spanwise direction from the plate centerline to the intersection of the initial curving shock wave near $X_{LE} = 0.79$ and Z = 0.59. Of course, the three-dimensional flow expansion not only created a low

pressure region on the plate surface, but also created regions of low pressure in the flow field between the bodies and on the surface of the wedge-store.

Numerical results showed that there is a flow expansion downstream of the shock wave which reduced the wedge-store surface pressures to a freestream value, as seen in Fig. 5.11. (Immediately downstream of the wedge-store vertex ($X_{LE} = 0.18, Z \leq 0.16$), the surface pressure rises to the two-dimensional predicted value as it crosses the attached shock wave, P = 1.35. The decrease in pressure begins at $X_{LE} = 0.21$ near the edge of the wedge (Z = 0.16) and reaches a near freestream condition along the wedge-store centerline by $X_{LE} = 0.44$.) This region of low pressure near the vertex of the wedge-store may provide the mechanism to produce a pitch-up moment. As mentioned in Section 5.1.3, a store pitch-up moment is an undesirable separation characteristic that often leads to a store-to-pylon collision [Arnold and Epstein, 1986].

Numerical and experimental surface pressure results for steady-state wedge-store positions indicate that first, the three-dimensional expansion about the edge of the wedge-store will reduce the strength of the shock waves and decrease the surface pressure rise induced by a shock wave below that for a two-dimensional shock wave. Second, the three-dimensional flow expansion downstream of a shock wave can create a low pressure trough, near freestream static, on both the body surfaces between the initial and reflection shock waves. These regions of flow expansion between the separating bodies are an unfavorable condition for stores having pitch-up tendency and conformal shaped stores designed to reduce aerodynamic drag and radar signature. Finally, the three-dimensional flow expansion complicates the analysis of a wedge-store separating from a stationary body. Without prior knowledge of the flow field, a simplifying two-dimensional assumption overlooks the possibility of an expansion flow. Thus, an analysis of wedge-store separation using oblique, two-dimensional shock wave relationships prematurely predicts a Mach disk that results in higher pressures and omits the existence of a shock reflection pattern. Incorpo-

rating an artificial two-dimensional expansion (Prandtl-Myer flow) into the analysis is not any better since doing so allows the flow to become over-expanded compared to experimental or three-dimensional numerical results.

6.2 Time-Dependent Event: Plate and Moving Wedge.

Time-dependent events were defined by the direction of the wedge-store vertical motion. The motion of the wedge-store away from the stationary model was the called the separation event. A typical separation event included movement of the wedge-store 4.24 cm within 26 ms at an average speed of 1.6 m/sec and a maximum $\alpha_u = -0.0051$ radians for a freestream Mach number of 1.52. The closure event was defined by motion of the wedge-store towards the stationary model. A distance of 4.88 cm was covered in 27 ms at an average speed of 1.8 m/sec and reached a maximum $\alpha_u = 0.0057$ radians (M = 1.52).

Along the plate centerline ($\phi = 0$), the steady-state results compared favorably with the time-dependent results independent of the transducer position, the wedge-store separation distance, and the shock-induced pressure profile characteristic. For example, at separation distances of Y/D = 0.31 and 0.51 (Figs. 5.18 and 5.20) the steady-state pressures follow the trend of the time-dependent pressure profiles. Although there are small differences in pressure between the steady-state and the time-dependent events due to the magnitude of the effective wedge angle, there are no significant differences induced solely by the shock wave movement.

The differences between two time-dependent (separation and closure) pressure results are due to changes in the effective angle (α_e). As discussed in Section 2.1.1, an increase in the effective wedge angle ($\alpha_e = \alpha_u + \varepsilon$) at a constant Mach number produces an increase in the shock wave strength and wave angle (β). Since the closure event was associated with a larger shock wave angle, the shock-induced pressure magnitude was greater than in the separation event, and the wedge-store must be at a greater Y/D distance than in the separation event for an initial shock impingement

at the same location on the plate (X_{LE}), as shown previously in Fig. 2.4. Therefore, according to the normal store separation convention of the store moving away from an aircraft, the closure event lagged the separation event as seen by surface pressures at corresponding separation distances (Y/D) for example see Fig. 5.18.

Time-dependent motion of the wedge-store does not significantly affect the shock wave developing between the two bodies as successful predictions of the shock-induced surface pressures on the plate are made for closure events using steady-state assumptions. However, the plate surface pressures are dependent upon the velocity of the wedge-store particularly at the near-touch separation positions. For transducer positions that are well downstream of the shock wave patterns during the near touch phase ($Y/D \leq 0.20$), mutual aerodynamic interference dominates the surface pressure characteristics. For instance, the time-dependent pressure histories for R = 0.07, $\phi = 0°$ ($X_{LE} = 0.42$), shown in Fig. 5.23, indicate surface pressures during the closure event were greater than surface pressures of the separation event, with closure pressure profiles resembling those associated with a piston action [Heaslet and Lomax, 1949]; both pressure profiles experience a nearly constant pressure, 1.67 and 1.76 respectively, for the separation and closure events for $Y/D \leq 0.17$. The largest piston type pressure difference observed between the separation and closure events was $\Delta P \approx 0.12$ at the off axis position of R = 0.07, $\phi = 135°$ ($X_{LE} = 0.45$) for $Y/D \leq 0.20$ (Fig. 5.43) which exceeds the piston theory results of $\Delta P \approx 0.028$.

Off-axis pressure transducers on the plate surface near the region of the orthogonal projection of the wedge-store edge (Z = 0.16) revealed an increase flow expansion effect. For separation distances less than half a wedge width ($Y/D \leq 0.50$), the flow expanding downstream of the shock waves reduced the magnitude of the plate surface pressures associated with the shock-wave impingements and the near-touch piston action. In addition, the pressure differences, due to the changes in α_e, between the time-dependent separation and closure events were also reduced at plate locations

near the wedge edge orthogonal projection. Several examples are given below to emphasize these edge effects on the surface pressure.

For a transducer setting of $\phi = 30°$, the furthest upstream position to capture a shock wave passage was at R = 0.93 ($X_{LE} = 0.24$, Z = 0.11). In Fig. 5.32, the separation distances for shock-induced pressure peaks show the closure event (Y/D = 0.19) lagging the separation event (Y/D = 0.16). The closure event shock-induced pressure peak occurred at a greater separation distance due to the increase in α_e and the associated shock wave angle. Although the closure event induced a stronger shock wave than the separation event, the magnitude of the shock-induced pressure peaks were nearly equal ($P \approx 1.28$). The peak pressure were nearly the same because the flow expansion about the wedge-store edge reduced the pressure influence of the initial shock wave impingement and eliminated the pressure difference between the time-dependent separation and closure events.

Similar initial shock-wave-induced pressure characteristics were observed for pressure transducers outside the projected area of the wedge-store. In Fig. 5.38 for R = 1.00, $\phi = 60°$ ($X_{LE} = 0.32$, Z = 0.21), the difference in the peak pressures induced by the closure and separation events was insignificant as seen at about Y/D = 0.35. Again the closure event was associated with the stronger shock wave as evident by the greater upstream pressure influence ($0.35 \leq Y/D \leq 0.50$), but an increase in pressure was not realized for reasons explained in the previous paragraph.

At greater separation distances, however, the plate surface pressure was less influenced by the flow expansion about the wedge-store edge. In Fig. 5.39, for the pressure transducer positioned farther downstream ($X_{LE} = 0.34$, Z = 0.17) and closer to the projected wedge-store edge, Z = 0.16, the initial-shock-induced pressure peaks were influenced more by the change in α_e than the edge-induced flow expansion. The passage of the initial shock wave on the plate surface (closure event peak pressure at Y/D = 0.58) occurred at a greater separation distance than for the upstream pressure transducer locations. In this case, there was a difference in the shock-

induced pressure peaks ($\Delta P = 0.03$) between the separation and closure events, whereas in the preceding paragraphs the shock-induced pressure peaks were equal. Yet, as the separation distance decreased to the near-touch phase ($Y/D \leq 0.20$), the edge effects eliminate the pressure plateau and the pressure difference between the time-dependent separation and closure events (Fig. 5.39).

An expansion flow about the wedge-store edge reduces the pressures and eliminates the pressure plateaus at the outboard locations as seen in a comparison of outboard and inboard plate positions during the near-touch phase of separation. For example, compare outboard results in Fig. 5.39 ($X_{LE} = 0.34$, Z = 0.17) with inboard results along the plate centerline ($X_{LE} = 0.34$, Z = 0.0) in Fig. 5.20, for $Y/D < 0.20$ the pressure in Fig. 5.20 continues to increase in magnitude until the end of the closure event. Both the separation and closure events exceed P = 1.80 by Y/D = 0.10, and the closure event maintained the greatest pressure magnitude. At the outboard location (Fig. 5.39) however, the surface pressure peaks near P = 1.52 at Y/D = 0.15 were significantly less than at the plate centerline, and as the separation distance decreased the surface pressure also decreased, a result opposite of the inboard results.

The influence of the flow expansion about the wedge-store edge during the near-touch phase is seen in Fig. 5.42 for the transducers set at $\phi = 90°$. All transducers are at streamwise location, $X_{LE} = 0.44$, but differ on their distance from the plate centerline: R = 0.07 (Z = 0.02), R = 0.60 (Z = 0.15), and R = 1.00 (Z = 0.24). Progressing outward from the plate centerline, surface pressures decreased for $Y/D \leq 0.20$ due to the proximity of the wedge-store edge. Additionally, a correlation exists between the influence of the wedge edge expansion flow and the range of the surface pressure magnitudes downstream of the shock waves. Basically, the area of the plate influenced by the wedge edge expansion had a lower pressure magnitude for $Y/D \leq 0.20$ and a smaller pressure variation downstream of the shock waves ($Y/D \leq 0.40$). For example in Fig. 5.42, R = 1.00 had a maximum pressure

of 1.41 at Y/D = 0.10 and a minimum pressure of 1.15 at Y/D = 0.26 for a range in pressure of $\Delta P = 0.26$. Whereas, near the plate centerline, R = 0.07, the maximum pressure at Y/D = 0.10 was P = 1.74, and the minimum pressure was P = 1.02 at Y/D = 0.30 for a pressure range three times that of R = 1.00 ($\Delta P = 0.72$). In other words, the flow expansion at the outboard plate positions reduces the pressure peaks and pressure difference between the separation and closure events due to α_e, while the flow expansion inboard induces a larger pressure variation between the peak and trough within a single separation or closure event.

Expansion of the flow between the two bodies during the near-touch phase of separation had the most significant effect on the surface pressures and the greatest implications to the store separation event. The experimental results revealed that the greater the surface pressures, the stronger the flow expansion became. This characteristic of the expansion flow implies that the aircraft and store integration should strive to avoid high near-touch pressures in order to moderate the pressure variation at greater separation distances. Reducing the strength of the expansion flow would retard the unfavorable flow-induced pitch-up mechanism encouraged by the low pressure region between the bodies.

6.3 Time-Dependent Event: Ogive and Moving Wedge.

The ogive baseline test configuration consisted of the pressure instrumented ogive and the 6.1° wedge-store at the freestream Mach 1.9. The leading edge of the wedge-store was placed at the same streamwise position as the nose of the ogive to capture the passage of the initial shock wave within the region of the pressure transducer locations. The ogive configuration flow field characteristics differed from that of the plate configuration in several ways. First, the initial shock wave attached to the wedge-store intersected a conical shaped shock wave induced by the ogive prior to impinging on the ogive surface. Second, the magnitude of the shock wave-induced

pressure peaks and the piston action influence were reduced on the three-dimensional ogive surface as compared to the two-dimensional surface of the plate.

The pressure profile for the ogive transducer position of X/YE = 3.10, $\psi = 0°$ (Fig. 5.59), indicates similar spatial characteristics to those found along the plate centerline: shock wave induced pressure rise, flow expansions downstream of the shock waves, and piston type responses at the appropriate near-touch conditions. With respect to the closure event, the initial shock-wave-induced pressure peak occurred at Y/D = 0.49. The three-dimensional flow expansion downstream of the wedge-induced shock-wave resulted in a pressure reduction (trough) for separation distances of $0.31 \leq Y/D \leq 0.49$. The reflection of the conical shock wave from the wedge-store surface is indicated by the small pressure peak at Y/D = 0.25. Finally, a pressure plateau is apparent for $Y/D \leq 0.15$, but the pressure difference due to the piston action of the time-dependent separation and closure events is small, $\Delta P = 0.03$, compared to the pressure differences along the plate centerline, $\Delta P \approx 0.12$.

At locations rotated away from the wedge-store, $\psi > 0°$, the magnitude of the shock-induced pressure peaks were reduced due to the orientation the impinging shock wave. At $\psi = 0°$, a full deflection of the flow crossing the shock wave occurred such that flow tangency to the surface of the ogive was maintained. As ψ increases, only a component of the velocity vector downstream of the impinging shock wave is directed towards the ogive surface; therefore, the deflection angle through the reflection shock wave is also reduced as is the resulting pressure increase. The pressure reduction associated with increasing ψ was predicted using the analytical method from Yin [Yin and Aihara, 1990]. That simplified analysis ignored the conical shock wave induced by the ogive, and indicated the ratio of pressure for an impinging planar shock at $\psi = 30°$ to that of $\psi = 0°$ to be 0.96. Experimental results shown in Fig. 5.61 ($\psi = 30°$) and Fig. 5.60 ($\psi = 0°$) revealed a similar value of pressure ratio of 0.94 between the separation events at the transducer location of X/YE = 3.64.

There was no significant difference in surface pressure between the time-dependent separation and closure events for the transducers set at $\psi \geq 90°$. The shock-wave-induced pressure rise, shown in Fig. 5.66 for X/YE = 2.57 and $\psi = 90°$, was smooth and absent of any significant differences. Pressure profiles for the transducers further downstream on the cylindrical portion of the ogive model, where the pressure plateaus existed for $Y/D \leq 0.16$ (Fig. 5.67), were also absent of any differential piston effects. Thus, the pressure perturbations induced by the change in α_e did not propagate into ogive surface regions not impinged upon by the initial shock wave.

6.4   Prediction Results.

An absence of time-dependent effects associated with a shock-wave development was inferred from a comparison of experimental closure data with predictions based on steady-state assumptions. The initial shock-wave-induced surface pressure for the closure event was predicted from separation data that was perturbed so that the closure and perturbed separation events had the same α_e. As discussed in Section 2.1.1, the shock wave location was calculated based on the determined α_e as a function of the wedge-store separation distance and the two-dimensional shock wave relationships. Since the shape of initial shock wave attached to the wedge-store was assumed to be two-dimensional, at least within the plane of symmetry normal to the wedge-store surface, and the change in shock wave angle was approximately linear for small changes in the effective wedge angle, the prediction of the shock wave location was the primary indicator for identifying unsteady effects. Pressure predictions were used for reference purposes to indicate the strength of the unsteady effects.

6.4.1   Plate Configuration.   The pressure influence of the initial impinging shock wave was predicted for the closure event along the plate centerline ($\phi = 0°$). Examples of the prediction method are given for R = 0.47 ($X_{LE} = 0.32$) with the 6.1° (Fig. 5.26) and the 3.5° (Fig. 5.30) wedge-store configurations. In Figs. 5.26 and 5.30, the closure event pressures from the upstream influence position of $Y/D \approx 0.60$

through the pressure peaks at Y/D = 0.45 for the 6.1° wedge-store (Fig. 5.26) and at Y/D = 0.50 for the 3.5° wedge-store (Fig. 5.30), show a good agreement of the prediction method with the closure data. Since only steady-state assumptions were used to predict the closure event, the match between prediction and closure leads to the conclusion that no significant time-dependent shock-wave-induced pressures are associated with the movement of the wedge-store.

Whereas the predicted shock wave position was correct, the pressure magnitude predictions were based only on the freestream flow crossing an assumed two-dimensional shock wave (i.e., ignored the reflection shock at the stationary model surface) and the pressure magnitude match may have been coincidental. Examples of apparent pressure magnitude predictions matching the closure data for $\phi = 0°$ were shown for the configurations of the 3.5° (Fig. 5.26) and the 6.1° (Fig. 5.30) wedge-stores at Mach 1.52, and the 6.1° (Fig. 5.48) and 12.3° (Fig. 5.51) wedge-stores at Mach 1.9.

The unsteady effects associated with the initial shock wave at transducer positions located off the plate centerline ($\phi = 30°$ and 60°) were more difficult to assess due to the influence of the flow expansion that occurred about the wedge-store edge. However, when the shock wave passing occurred at separation distances greater than a half a wedge width (i.e., the initial shock-induced pressure peak was found at $Y/D > 0.50$) the prediction method matched the magnitude of the closure event pressure profile. Examples are given for R = 0.60, $\phi = 30$ in Fig. 5.35 and R = 0.80, $\phi = 60°$ in Fig. 5.39. Although the results of the prediction method could not assess the possibility of off-centerline shock wave unsteadiness, the experimental results did show that any potential shock-induced unsteadiness would be small.

In the near-touch phase, however, the unsteady effects cannot be ruled out. As seen in Fig. 5.43, the region of plate surface pressures free of direct shock wave influences were significantly higher for the closure event than for the separation event. The largest pressure difference found during the near-touch phase (R = 0.07

for $\phi = 135°$ shown in Fig. 5.43) was $\Delta P \approx 0.12$, and it was approximately four times greater than the piston theory correction. Though the surface pressures were similar to the responses found in a two-dimensional piston action [Heaslet and Lomax, 1949], the experimental closure pressure exceeded the predicted pressure magnitude of the piston theory due to several factors. First, the flowfield about the wedge-store and plate during the near-touch phase of separation is a complicated three-dimensional flow, but predicted surface pressures were based on a simplified two-dimensional analytical theory. Second, the boundary-layer on the plate increases downstream of the coalescing shock waves during the near-touch phase of separation. This thick boundary-layer is not accounted for in Newtonian assumptions, and additionally, the boundary-layer may allow an upstream pressure propagation.

6.4.2 Ogive Configuration. Again the closure event was predicted using steady-state assumptions to assess the potential of an unsteady shock wave development during a time-dependent separation of near tangent bodies. In the ogive and wedge-store separation event an oblique-conical shock-wave interaction is the potential source of unsteadiness that is being assessed. The effective angle correction for the initial attached shock wave in the wedge-store and ogive configuration was only made along the symmetry plane from the wedge vertex to the oblique-conical shock wave intersection. Downstream of the oblique-conical shock wave intersection, the refracted oblique shock wave was assumed to propagate along a straight path to the ogive surface. Where the wedge-store and ogive were close together ($Y/D < 0.60$), the distance from the oblique-conical intersection was small, and the straight shock wave assumption was reasonable within the conical flow. A closure event prediction is shown for X/YE = 2.57 with $\psi = 0°$ (Fig. 5.58), where the initial shock-induced pressure peak occurred at Y/D = 0.36. However, the two-dimensional planar shock-wave assumption within the conical flow becomes unreliable at greater separation distances as the oblique shock wave begins to curve. For example, the initial shock-

induced pressure peak in the closure event was under-predicted as seen in Fig. 5.60 near Y/D = 0.62 for the ogive surface location of X/YE = 3.64.

Further around the ogive ($\psi > 0°$) a reduction in the magnitude of the shock-induced pressure rise was noted, especially on the nose ($X/YE \leq 3.33$) as seen in Fig 5.63. At forward transducer positions, the α_e prediction method was inappropriate as there was little difference between the time-dependent events (e.g., X/YE = 2.31 at $\psi = 60°$). However, downstream on the cylindrical portion of the model where the flow deflection across the shock impingement was similar in magnitude to the flow deflection at the oblique-conical shock interaction, the prediction method approximated the initial shock-induced pressure influence.

At $\psi \geq 90°$ the transducers were in the model shadow such that the initial shock wave could not directly impinge on the pressure transducers. The shock-induced pressure rise at these transducer locations was small and absent of α_u effects. Since the pressure differences between the time-dependent separation and closure events were insignificant, no predictions were made for $\psi \geq 90°$.

VII. Conclusions

Numerical simulations of the supersonic separation of tangent bodies, accomplished by Belk [Belk, et al., 1985] and Meakin [Meakin, 1990], revealed that the time-dependent solutions of shock wave influences are reduced in magnitude (pressure and aerodynamic coefficients) and lagged in phase (location of shock wave) compared with the equivalent steady-state solutions. Before this investigation, there was no consensus on why these transient lags occurred or if the transient lags physically existed. Therefore, the objective of this investigation was to determine experimentally the significance of transient effects associated with the time-dependent separation of tangent bodies at supersonic conditions, and to address the validity of using steady-state assumptions to predict perturbed time-dependent separation events.

7.1 Transient Effects Associated with the Initial Shock Wave.

The evaluation of transient effects and the use of steady-state assumptions was made by comparing the shock-wave-induced pressure profiles of the steady-state, time-dependent, and prediction results of wedge-store separation events. The uncorrected surface pressure versus separation distance showed that the steady-state surface pressure of the stationary model compared favorably with the surface pressures induced during the time-dependent separations. The small differences between the pressure profiles follow the expected trend in shock-wave-induced magnitude and separation position due to the known differences in the effective wedge angle (α_e). Furthermore, the agreement between the steady-state and time-dependent events for the major characteristics of the pressure profile points to the conclusion that the time-dependent motion of the wedge-store does not significantly affect the shock waves developing between the two bodies.

Since it was not possible to experimentally achieve time-dependent separation events having equivalent effective angles of attack while at the same time having different induced angles of attack (as in Belk's numerical study), the transient effects had to be determined indirectly using steady-state assumptions to perturb a selected time-dependent database to predict a second time-dependent event that differed in α_e and direction of the wedge-store motion. This prediction method matched the time-dependent closure event along the plate centerline ($\phi = 0°$). Predictions were also favorable within the configuration symmetry plane on the stationary ogive surface ($\psi = 0°$) for separation distances less than 60% of the wedge width. The result of the prediction method matching the closure event indicates that within the configuration symmetry plane the steady-state assumptions are valid, and that there are no significant unsteady effects associated with the initial shock wave attached to a moving store.

Surface pressure predictions for locations off the plate centerline ($\phi \neq 0°$) were more difficult to accomplish due to the curving initial attached shock wave and the limitations of the two-dimensional prediction method. However, as the distance from the configuration symmetry plane increased, the pressure differences due to the changes in the effective wedge angle (α_e) decreased; therefore, any unsteady effects that may exist outside the configuration symmetry plane are small.

Several conclusions may be drawn concerning the shock-wave induced by a moving wedge-store:

1. Steady-state assumptions are valid for time-dependent shock wave predictions.

2. There are no significant unsteady effects associated with a moving initial shock wave.

3. Off-axis prediction deficiencies are attributed to the limitations of the two-dimensional assumptions.

7.2 Time-Dependent Piston Effects.

In the near-touch phase of separation where body interference dominates the flow (separation distances less than 20% of the store width) and in the region free of the shock wave influence, there are indications that the time-dependent effects are significant. The surface pressures on the plate and ogive were greater during the closure event than for the separation event, and the pressure characteristics were similar to the responses found in a piston action [Heaslet and Lomax, 1949]. However, the experimental pressure differences between the two time-dependent events exceeded the magnitude of the piston theory predictions. The discrepancy between experimental and theory is due, in part, to the theory assumptions not accounting for a thick boundary-layer. This boundary-layer contradicts the Newtonian assumptions and provides a mechanism for an upstream pressure propagation.

7.3 Implication of Results to Store Separation Predictions.

Finding no significant unsteady pressure effects associated with the initial shock wave gives preliminary support for the quasi-steady wind tunnel methods currently used in store separation predictions. The captive trajectory support (CTS) and the grid survey wind tunnel techniques, which position the store at a steady-state attitude that includes an estimated induced angle, will simulate the appropriate time-dependent flow field with respect to a secondary stationary model. Thus, there are no additional concerns about the unsteady development of the shock waves between the bodies with separation distances greater than 20% of the store width for the steady-state experimental and semi-empirical prediction methods. However, unsteady surface pressure cannot be ruled out for separation distances less than 20% of the store width.

The piston pressure characteristic found on the stationary models is also assumed to influence the moving wedge-store, but currently there are no time-dependent store surface pressures available for confirmation. Since the initial conditions of the

store separation event can make the difference between a store and aircraft collision or clearance, as discussed by Wood [Wood, 1988], the dynamic effects of unsteady pressures, such as store pitch-up, occurring during the near-touch phase of separation remain a concern.

The unsteady piston effects are exacerbated when semi-two-dimensional bodies are separated from the tangent position, such as was simulated by the plate and wedge-store configuration. Thus, aircraft configured with conformal or tangent carriages combined with angular shaped stores (flat surface adjacent to aircraft) will be more susceptible to the unsteady piston effects. These desired aircraft and store configurations that are designed to reduce drag and radar signature are inherently more difficult to separate, and therefore, trajectory predictions become more complicated. The unsteady piston effect during a time-dependent store separation event will differ from the measured steady-state wind tunnel results. Although the unsteady piston effect has been identified experimentally, future studies will be required to address how time-dependency information can be integrated into the initial conditions of appropriate store trajectory prediction methods.

The flow expansion downstream of the shock waves creates a low pressure region near the nose of the store that may provide the mechanism to produce a store pitch-up moment. Pressure trough characteristics are very likely to be found on flat-sided stores which are similar to the wedge-store in the present study. Furthermore, the strength of the expansion flow, which induces the low surface pressures, is related to the strength of the upstream shock wave and the magnitude of the near-touch pressure. Future integration of flat-sided stores with conformal or tangent mounting should strive to reduce the near-touch pressures so that the flow expansion about the store is moderated and the possibility of a store-to-pylon collision reduced.

7.4 Major Findings.

1. Steady-state assumptions are valid ($Y/D > 0.20$).

- Time-dependent separation events may be predicted from steady-state data.

- A time-dependent separation event may be predicted from another time-dependent event that differs only in α_e.

2. Time-dependent piston effects exist ($Y/D \leq 0.20$).

   - Pressure is dependent on the store motion.

3. Three-dimensional flow expansion is a significant factor for store separations in supersonic flow.

   - Regions of low pressure, equivalent to freestream static, exist on the bodies downstream of the shock waves.

7.5 Future Studies.

This investigation was the first experimental time-dependent store separation study accomplished that provided quantified results in the form of dynamic surface pressures. Since unsteady effects were identified during the near touch phase of separation the need to expand the research is justified. Particular research focus should be placed on the transient effects induced upon a store ejected from a tangent position.

Research on the transient effects may be accomplished using CFD to analyze the ogive and wedge-store results. If the results on the stationary ogive are appropriately matched using CFD, then the resulting transient effects found on the wedge-store would identify the significance of including time-dependency in the trajectory predictions. Of course, overcoming the technical challenges of measuring the transient induced effects directly on a moving store would also provide valuable insight into the dynamic contributions involved in a time-dependent separation event.

Bibliography

Anderson, et al., 1984.   Anderson, Dale A., John C. Tannehill, and Richard H. Pletcher. Computational Fluid Mechanics and Heat Transfer. Washington Hemisphere Pub. Corp.; New York: McGraw-Hill, 1984.

Anderson, 1990.   Anderson, J. D., Jr. Modern Compressible Flow with Historical Perspective. Second edition, McGraw-Hill Publishing Company, 1990. pg. 90 and 129-130.

Arabshahi and Whitfield, 1989. Arabshahi, Abdoliah and David L. Whitfield. "A Multiblock Approach to Solving the Three-Dimensional Unsteady Euler Equations about a Wing-Pylon-Store Configuration", *AIAA Paper 89-3401*, 1989.

Arnold and Epstein, 1986.   Arnold, R. J. and C. S. Epstein. "Store Separation Flight Testing", AGARD-AG-300-VOL. 5, April 1986. pg 2.

Batcho, et al., 1989.   Batcho, P. F., A. C. Ketchum, S. M. Bogdonoff, and E. M. Fernando. "Preliminary Study of the Interactions Caused By Crossing Shock Waves and A Turbulent Boundary Layer", 27th Aerospace Sciences Meeting, (AIAA-89-0359), 1-11, January 1989.

Belk, et al., 1985.   Belk, Dave M., J. Mark Janus and David L. Whitfield. "Three-Dimensional Unsteady Euler Equations Solutions on Dynamic Grids", *AIAA Paper 85-1704*, 1985.

Carman, et.al, 1980.   Carman, J. B. Jr., D. W. Hill Jr., and J. P. Christopher. Store Separation Testing Techniques at the Arnold Engineering Development Center, AEDC-TR-79-1 Volume 2. Arnold AFS, Tennessee: Arnold Engineering Development Center, 8-12, June 1980.

Carman, 1980.   Carman, J. B. Jr., Store Separation Testing Techniques at the Arnold Engineering Development Center, AEDC-TR-79-1 Volume 1 Arnold AFS, Tennessee: Arnold Engineering Development Center, August 1980.

Chapman, et al., 1958.   Chapman, D. R., D. M. Kuehn, and H. K. Larson. Investigation of Separation in Supersonic and Subsonic Streams with Emphasis on the Effect of the Transition, NACA Report 1356, 1958.

Clark, 1982.   Clark, Gary F., Trisonic Gasdynamic Facility User Manual. AFWAL-TM-82-176-FIMM, April 1982.

Cottrell and Lijewski, 1988.   Cottrell, Charles J. and Lawerence E. Lijewski. "Finned, Multibody Aerodynamic Interference at Transonic Mach Numbers," Journal of Aircraft, 25:9 827-834, September 1988.

Cottrell and Martinez, 1988.   Cottrell, Charles J. and Agusto Martinez. "Study of Multibody Aerodynamic Interference at Transonic Mach Numbers", AIAA Journal, 26:5, 553-560, May 1988.

Delery and Marvin, 1986.   Delery, J. and J. G. Marvin. "Shock-Wave Boundary Layer Interactions," AGARD-AG-280, Part I, section 3.5, 63-64, February 1986.

Dillenius and Nixon, 1988.   Dillenius, Marnix, F. E. and David Nixon. "Prediction Methods for Store Separation", NEAR Conference on Missile Aerodynamics, paper 9 p. 26, Oct. 31 - Nov. 2, 1988.

Dolling and Murphy, 1983.   Dolling, D. S. and M. T. Murphy. "Unsteadiness of the Separation Shock Wave Structure in a Supersonic Compression Ramp Flow Field," AIAA Journal, 21:12, 1628-1634, December 1983.

Dougherty, et al., 1985.   Dougherty, F. C., J. A. Benek, and J. L. Steger. On Applications of Chimera Grid Schemes to Store Separation, NASA TM 88193, October 1985.

Dougherty and Kuan, 1989.   Dougherty, F. C. and J-H Kuan. "Transonic Store Separation Using a Three- Dimensional Chimera Grid Scheme," AIAA 89-067, 27th Aerospace Science Meeting, January 9-12, 1989.

Dougherty and Kuan, 1990.   Dougherty, F. C. and J-H Kuan. "Computational Store Separation Simulation," Store Carriage, Integration and Release. April 4-6 1990, The Royal Aeronautical Society. 27.1-27.13.

Epstein, 1988.   Epstein, Charles S., "The Integration of Stroes on Modern Tactical Aircraft. Where We Have

	Been, And What We Should Do For the Future," NEAR Conference on Missile Aerodynamics. paper 12, p. 4-5, Oct. 31 - Nov. 2, 1988.
Erdos and Pallone.	Erdos, J. and A. Pallone. "Shock/Boundary Layer Interactions and Flow Separation," Heat Transfer and Fluid Mechanics Institute Procs., Stanford University Press.
Gadd, et al., 1954.	Gadd, G. E., D. W. Holder, and J. D. Regan. "An Experimental Investigation of the Interaction Between Shock Waves and Boundary Layers," Proceedings of the Royal Society of London. Series A, Vol. 226, 227-253, 1954.
Degrez, et al., 1987.	Degrez, G., C. H. Boccadoro, and J. F. Wendt. "The Interaction of an Oblique Shock Wave with a Laminar Boundary Layer Revisited. An Experimental and Numerical Study." Journal of Fluid Mechanics, vol. 177, 247-263, 1987.
Hakkinen, et al., 1959.	Hakkinen, R. J., I. Greber, L. Trilling, and S. S. Abarbanel. The Interaction of an Oblique Shock with a Laminar Boundary Layer. NASA MEMO 2-18-59W, March 1959.
Hayakwa and Squire, 1982.	Kayakwa, K. and L. C. Squire. "The Effect of the Upstream Boundary Layer State on the Shock Interaction at a Compression Corner," Journal of Fluid Mechanics, Vol. 122, 369-394, 1982.
Heaslet and Lomax, 1949.	Heaslet, M. A. and H. Lomax. Two-Dimensional Unsteady Lift Problems in Supersonic Flight, NACA Report 945, pg. 472, 1949.
Keen, 1990.	Keen, K. Scott. "New Approaches to Computational Aircraft/Store Weapons Integration", 28th Aerospace Sciences Meeting, 1-10 January 1990.
Keen, 1985.	Keen, K. Scott. Improved Techniques for the Computational Determinationof the Separation Trajectories of Stores from Aircraft, AEDC-TR-85-59. Arnold AFS, Tennessee: Arnold Engineering Development Center, November 1985. (Unclassified/Limited)

Kuehn, 1959.   Kuehn, D. M. Experimental Investigation of the Pressure Rise Required for Incipient Separation of Turbulent Boundary Layer in 2-D Supersonic Flow. NASA MEMO 1-21-59A, 1959.

Kuethe and Chow.   Kuethe, Arnold M. and Chuen-Yen Chow. Foundations of Aerodynamics: Bases of Aerodynamic Design, 3rd ed. (John Wiley & Sons, 1976), p. 233.

Lamb, 1932.   Lamb, Horace. Hydrodynaics. Cambridge University Press, 1932. 479-481.

Lees and Reeves, 1964.   Lees, L., and B. L. Reeves. "Supersonic Separated and Reattaching Laminar Flows: I. General Theory and Application to Adiabatic Boundary Layer / Shock Wave Interactions," AIAA Journal, Vol. 2, No. 11, 1907-1920, November 1964.

Lijewski, 1989.   Lijewski, Lawrence E. "Transonic Euler Solutions on Mutually Interfering Finned Bodies", 27th Aerospace Sciences Meeting. January, 1989.

Marconi, 1983.   Marconi, F. "Shock Reflection Transition in Three-Dimensional Steady Flow About Interfering Bodies", AIAA Journal, 21:5, 707-713, May 1983.

Meakin and Suhs, 1989.   Meakin, R. L. and N. E. Suhs. "Unsteady Aerodynamic Simulation of Multiple Bodies in Relative Motion," AIAA paper 89-1996-CP, 1989.

Meakin, 1990.   Meakin, R. L. "Transient Flow Field Responses about the Space Shuttle Vehicle during Ascent and SRB Separation," Store Carriage, Integration and Release. The Royal Aeronautical Society, 29.1-29.16, April 4-6 1990.

Mendenhall, 1988.   "Missile Aerodynamics Panel". Ed. Mendenhall, Michael R. NEAR Conference on Missile Aerodynamics. paper 15, p.2, Oct. 31 - Nov. 2, 1988.

Mendenhall, 1988.   "Store Separation Panel". Ed. Mendenhall, Michael R. NEAR Conference on Missile Aerodynamics. paper 16, p.3, Oct. 31 - Nov. 2, 1988.

Milling, 1981.   Milling, Robert W. An Experimental Study of Tollmien-Schlichting Wave Cancellation. Ph. D. Dissertation. Purdue University, 1981.

Pai, 1952.

Pai, S. I. "On the Flow Behind an Attached Curved Shock," Journal of the Aeronautical Sciences, 19, 734-742, November 1952.

Press, et al., 1989.

Press, William H., Brian P. Flannery, Saul A. Teukolsky and William T. Vettering. Numerical Recipes: The Art of Scientific Computing. 455-456, Cambridge University Press, 1989.

Raj, et al., 1987.

Raj, P., J. E. Brennan, J. M. Keen, K. K. Mani, C. R. Olling, J. S. Sikora, S. W. Singer. Three-Dimensional Euler Aerodynamic Method (TEAM). AFWAL-TR-87-3074, Vol. 1, July 1987.

Raj, et al., 1989.

Raj, P., J. S. Sikora, and C. R. Olling. Three-Dimensional Euler Aerodynamic Method (TEAM). AFWAL-TR-87-3074, Vol. 3, June 1989.

Raman, 1974..

Raman, K. R., A Study of Surface Pressure Fluctuations in Hypersonic Trubulent Boundary Layers. NASA CR-2386, Febuary 1974.

Roshko and Thomke, 1976.

Roshko, A. and G. J. Thomke. "Flare-Induced Interaction Lengths in Supersonic Turbulent Boundary Layers," AIAA Journal, Vol. 14, No. 7, 873-879, July 1976.

Schindel, 1975.

Schindel, L. H. Store Separation, AGARD-AG-202, 88-90, June 1975.

Sears, 1954.

General Theory of High Speed Aerodynamics. Ed. William Rees Sears. Princeton: Princeton University Press, 1954.

Settles, et al., 1976.

Settles, G. S., S. M. Bogdonoff, I. E. Vas. "Incipient Separation of a Supersonic Turbulent Boundary Layer at High Reynolds Number," AIAA Journal, Vol. 14, No. 1, 50-56, January 1976.

Spaid and Frishett, 1972.

Spaid, F. W. and J. C. Frishett. "Incipient Separation of a Supersonic Turbulent Boundary Layer, Including Effects of Heat Transfer," AIAA Journal, Vol. 10, No. 7, 915-922, July 1972

Taylor, 1982.

Taylor, John R. An Introduction to Error Analysis: The Study of Uncertainties in Physical Measurements. California: University Science Books, 1982, p.89.

Tran and Bogdonoff, 1987.

Tran, T. T. and S. M. Bogdonoff. "A Study of Unsteadiness of Shock Wave/Turbulent Boundary Layer Interactions from Fluctuating Wall Pressure Measurements", AIAA 25th Aerospace Sciences Meeting, 1-9, January 1987.

Tran, et al., 1985.

Tran, T. T., D. K. M. Tan and S. M. Bogdonoff. "Surface Pressure Fluctuations in a Three-Dimensional Shock Wave/Turbulent Boundary Layer Interaction at Various Shock Strengths", AIAA 18th Fluid Dynamics andPlasmadynamics and Lasers Conference. (AIAA-85-1562) 1-12, July 1985.

Wood, 1988.

Wood, M. E. "Application of Experimental Techniques to Store Release Problems", NEAR Conference on Missile Aerodynamics. paper 5, p. 33-35, Oct. 31 - Nov. 2, 1988.

Yin and Aihara, 1990.

Yin, X. Z. and Yasuhiko Aihara. "A Method for Calculating Three-Dimensional Shock Interaction (Part 1) Regular Case", Japan Society for Aeronautical and Space Sciences, 33:100, 55-65, August 1990.

Zucrow and Hoffman, 1976.

Zucrow, M. J. and J. D. Hoffman. Gas Dynamics, Volume I. New York: John Wiley & Sons, 1976.

MIL-HDBK-244.

Military Standardization Handbook, Guide to Aircraft/Stores Compatibility. 1 August, 1975. pg. 61.

Figure 1.1. Comparison of empty dispenser trajectory data for release at M = 0.45 [Wood, 1988].

Figure 1.2. Store and plate model geometry [Belk et al., 1985].
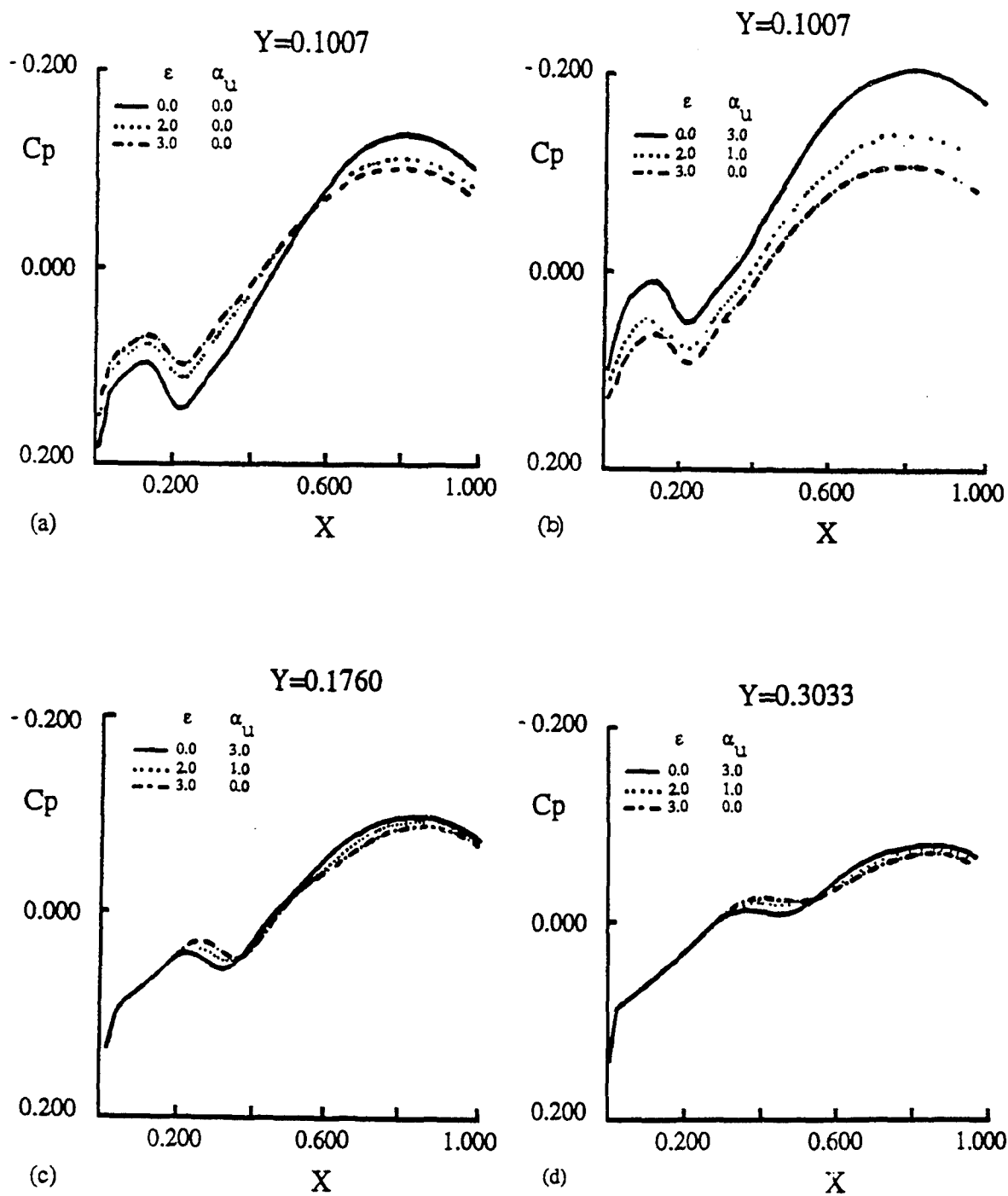
Figure 1.3. Store surface pressure coefficient [Belk et al., 1985].
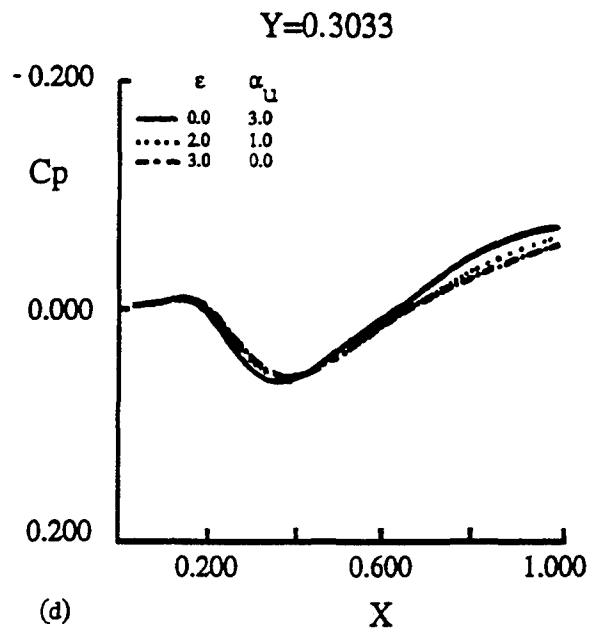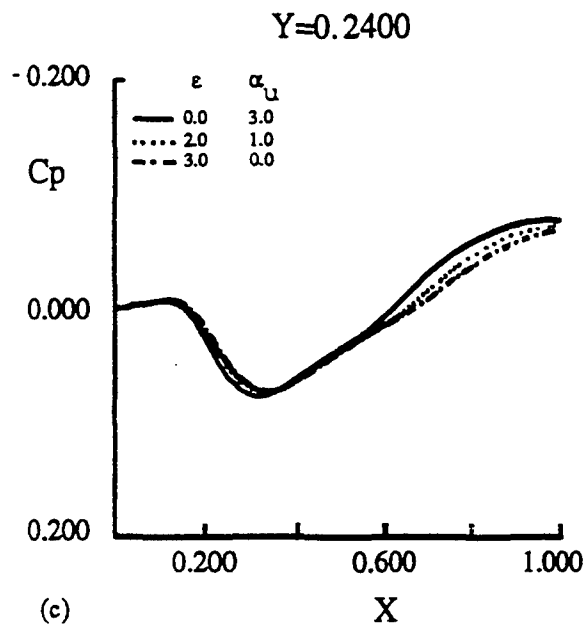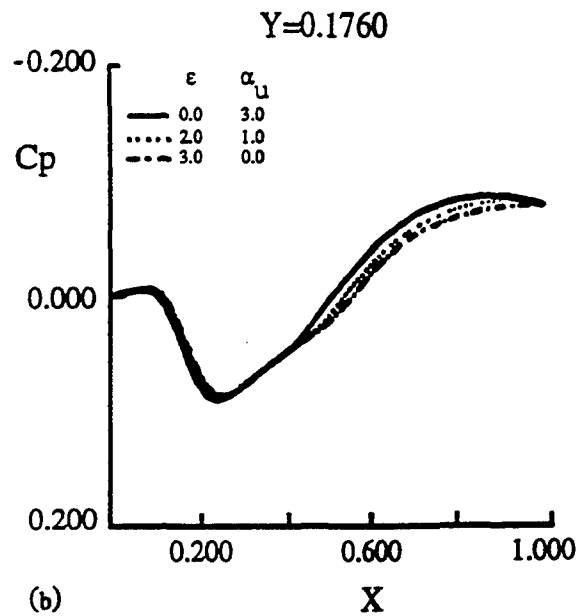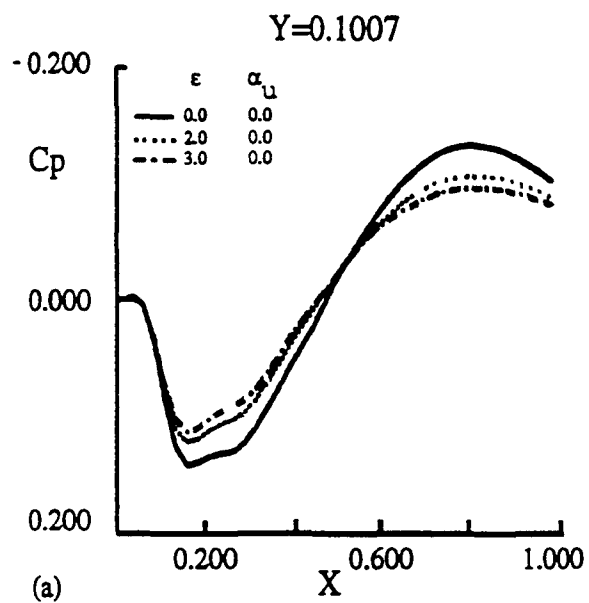
Figure 1.4. Plate surface pressure coefficient [Belk et al., 1985].
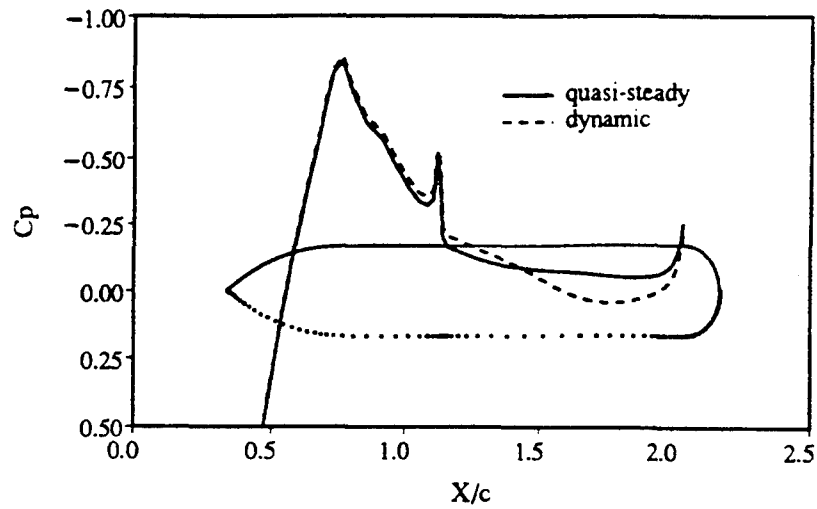
Figure 1.5. Surface pressure coefficient for the external tank at M = 1.023 [Meakin, 1990].

a)   b)
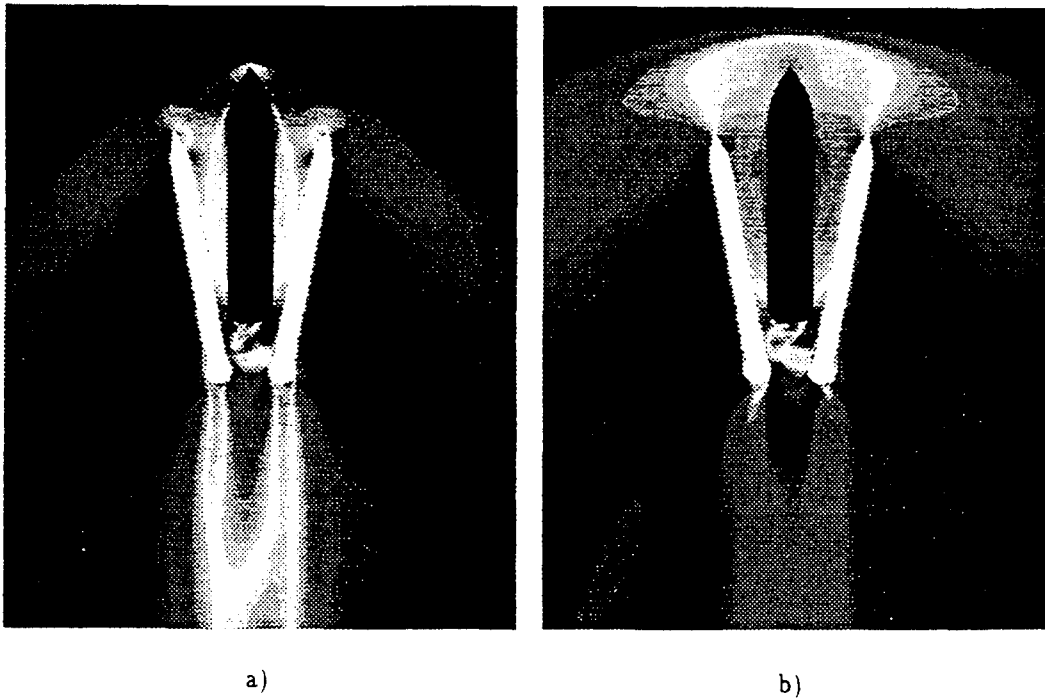
Figure 1.6. Comparison of Mach contours between a) dynamic and b) quasi-steady results. M=1.023 [Meakin, 1990].
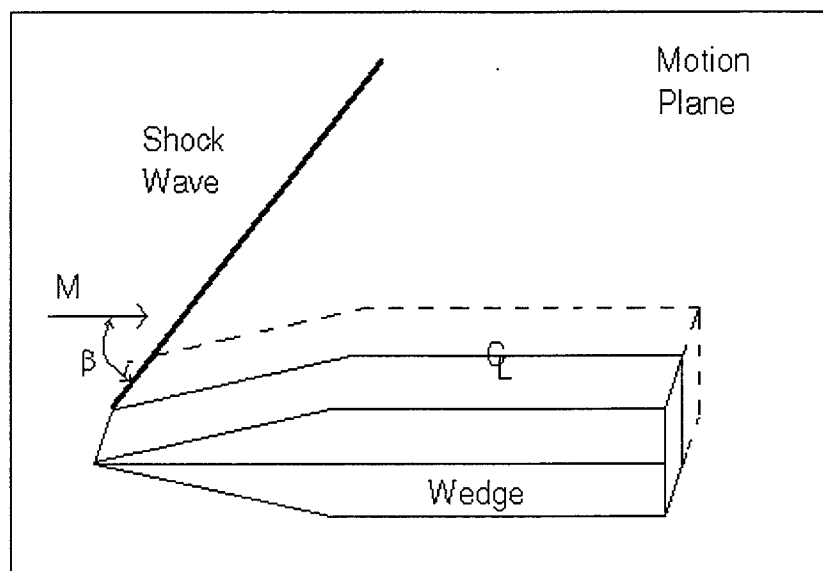
Figure 2.1.   A straight shock-wave assumed within the wedge-store plane of motion.
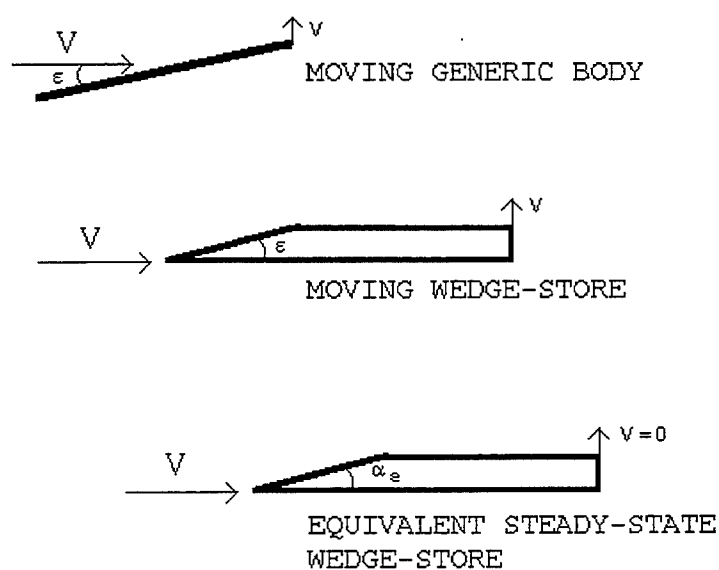
Figure 2.2. Transfer of the effective angle of attack to an effective wedge angle.
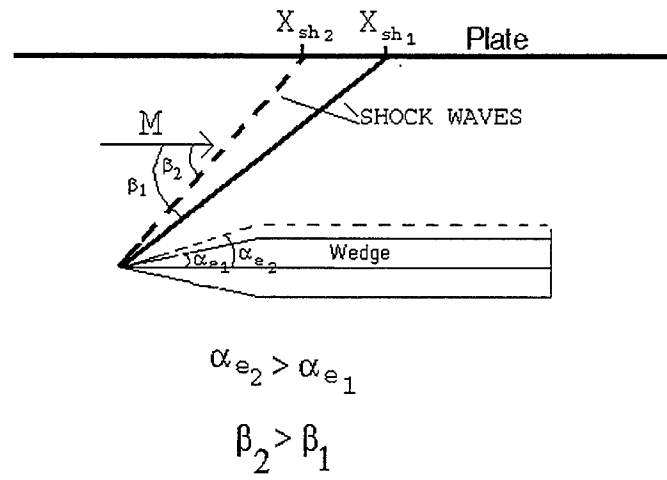
Figure 2.3. An increase in the shock wave angle moves the shock impingement location upstream on the plate for a fixed store position.
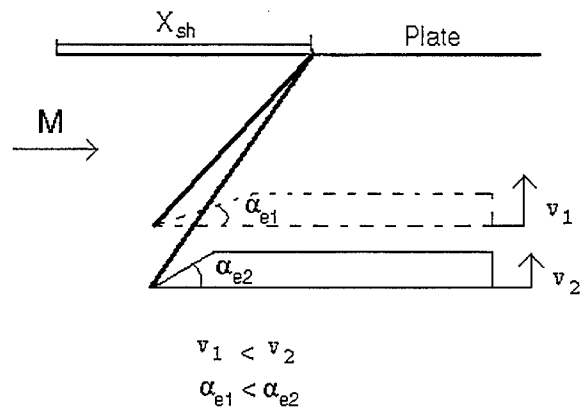
Figure 2.4. An increase in the shock wave angle requires a greater separation distance for a concurrent shock impingement location.

Figure 2.5. Oblique-conical shock-wave interaction.

Figure 2.6. Velocity vector decomposed into vectors parallel and normal to the oblique-conical shock intersection line, L.
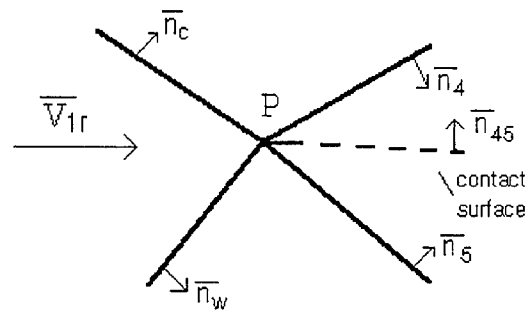
Figure 2.7. Two-dimensional shock wave schematic shown within plane D.
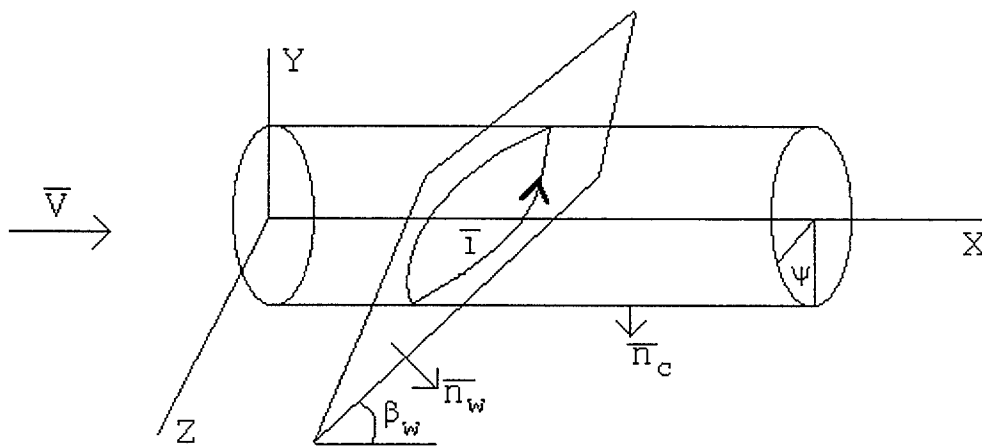
Figure 2.8. An oblique shock wave intersecting a cylindrical body.
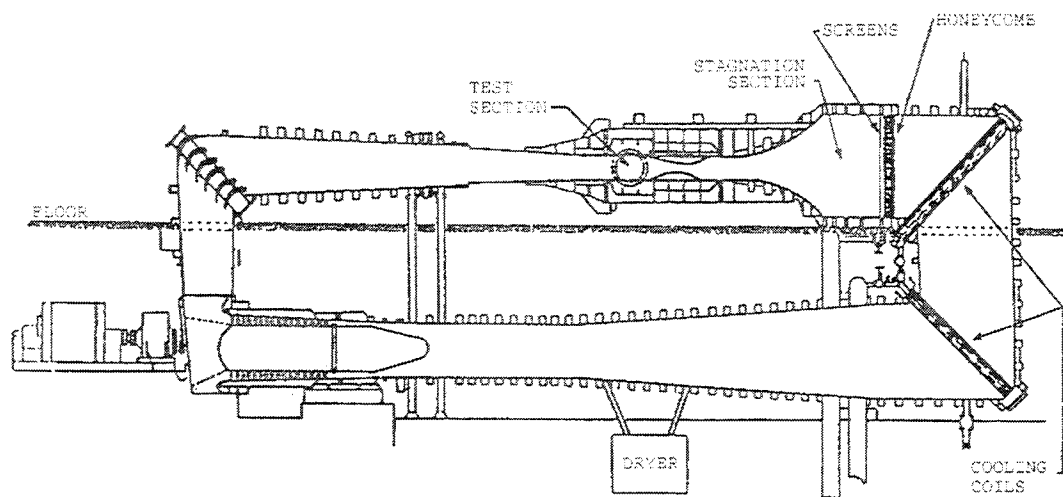
Figure 3.1. Trisonic Gasdynamic Facility 2 foot wind tunnel (ref [Clark, 1982]).
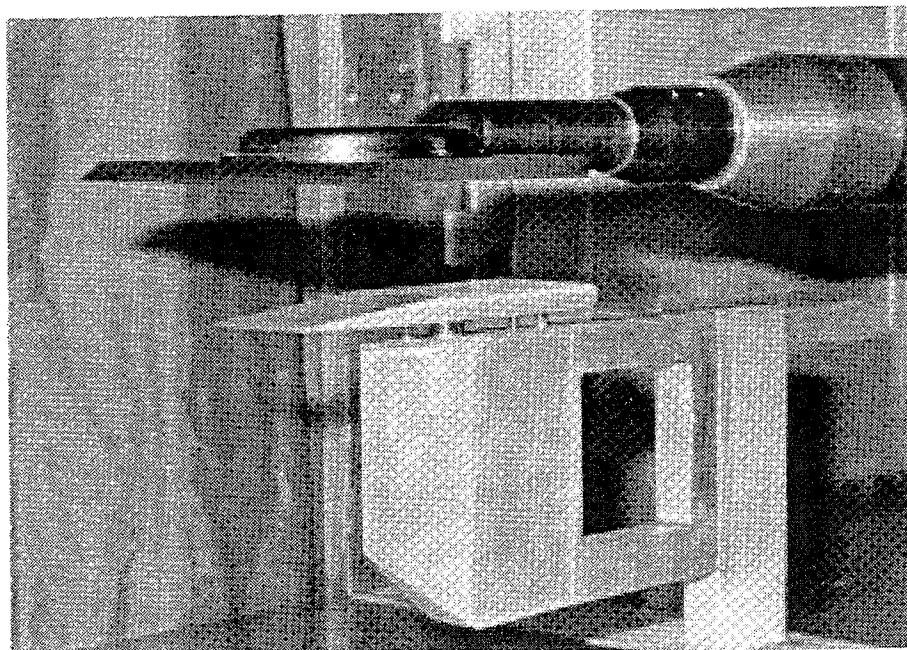
Figure 3.2. Plate and store configuration.
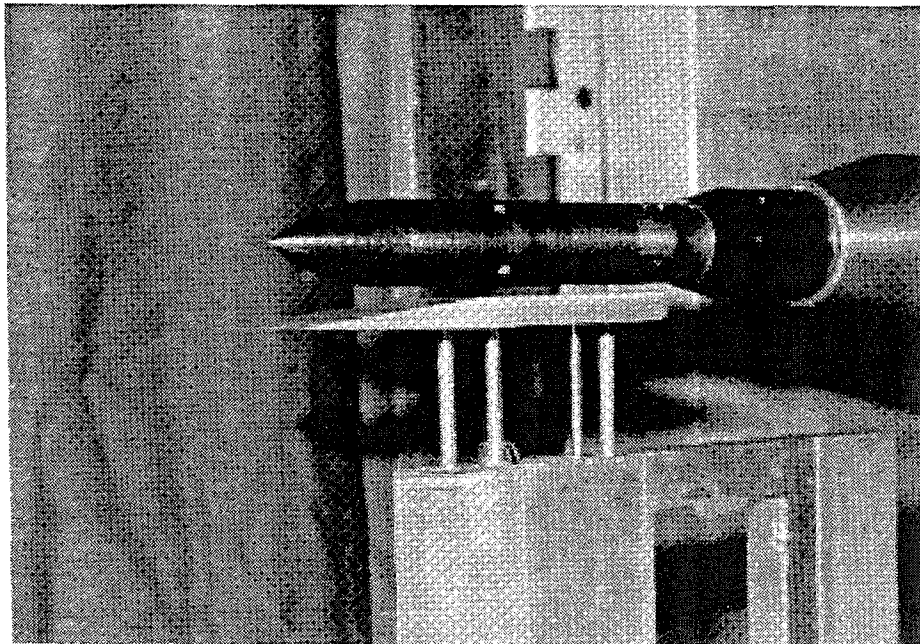
Figure 3.3. Ogive and store configuration.
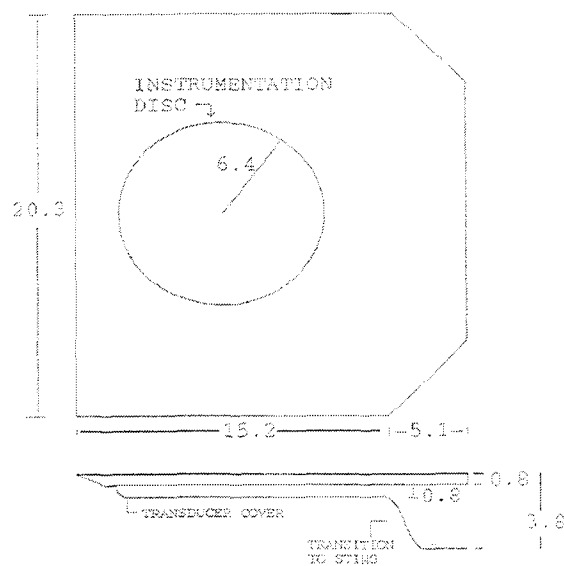
Figure 3.4. Plate model configuration (units in cm).
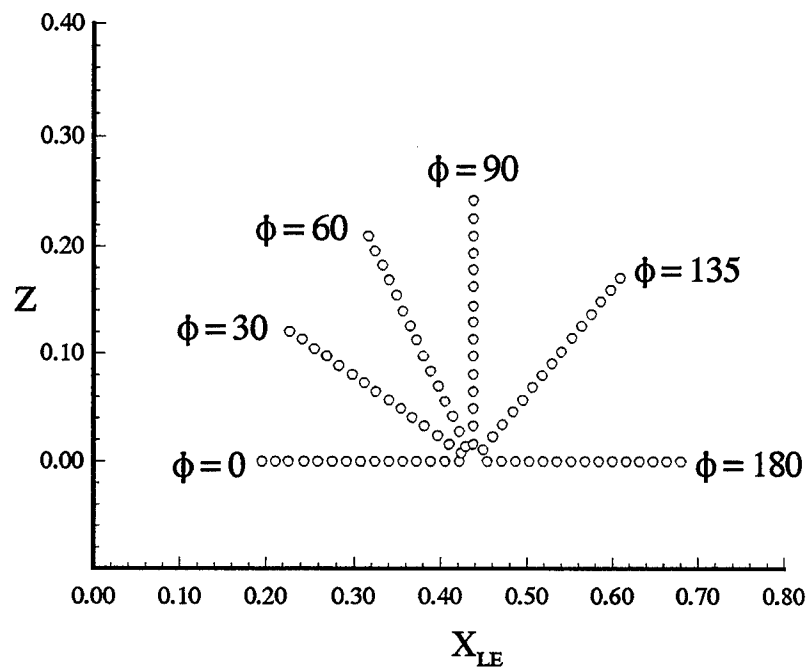
Figure 3.5. Transducer positions on the plate surface.
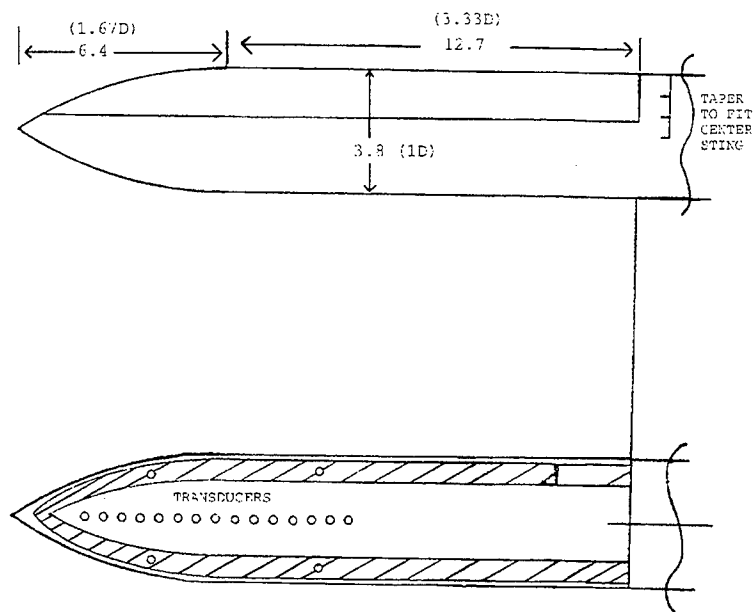
Figure 3.6. Ogive model configuration (units in cm).
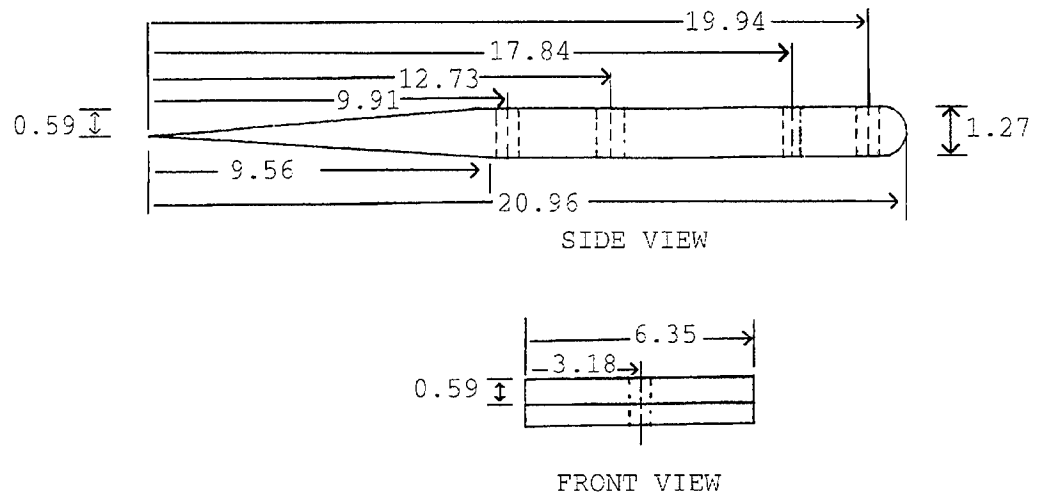
Figure 3.7. 3.53° wedge-store (units in cm).
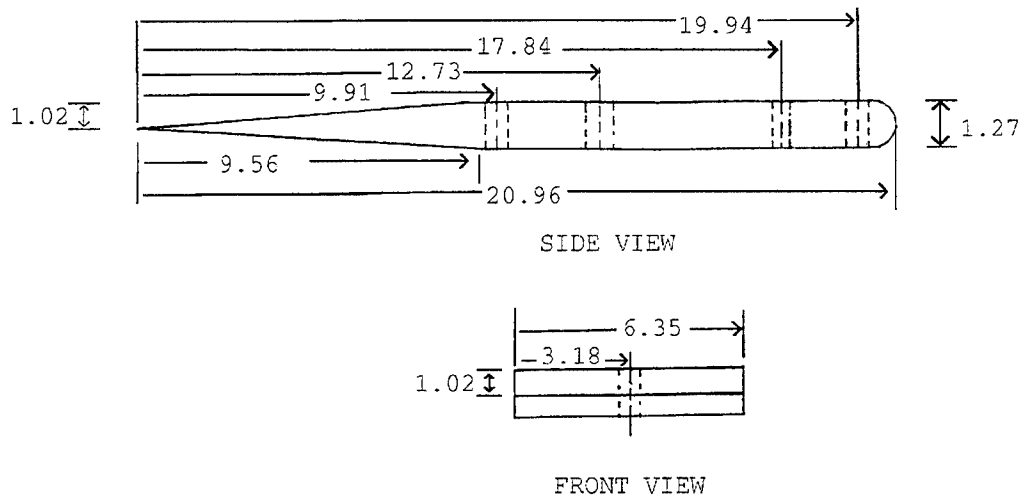
Figure 3.8. 6.10° wedge-store (units in cm).
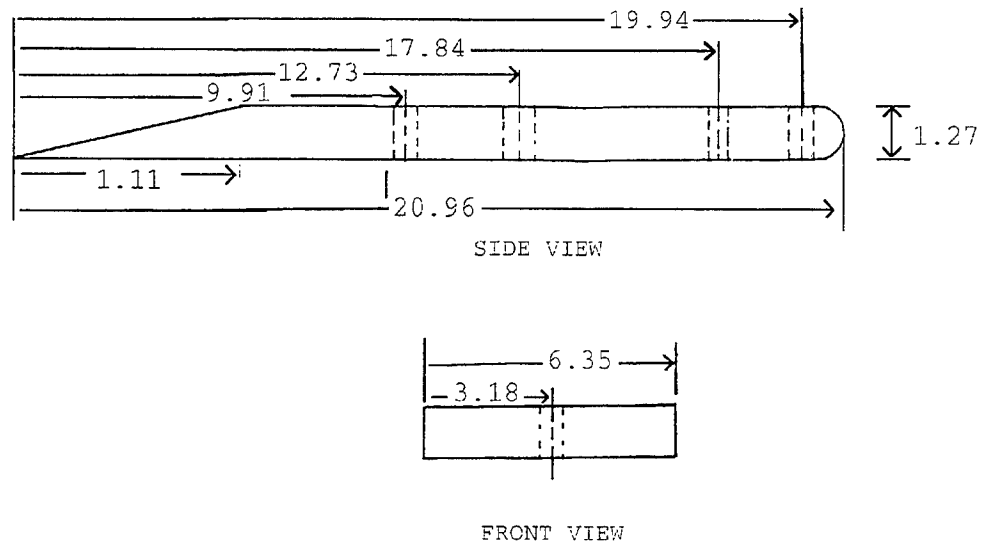
Figure 3.9. 12.32° wedge-store (units in cm).
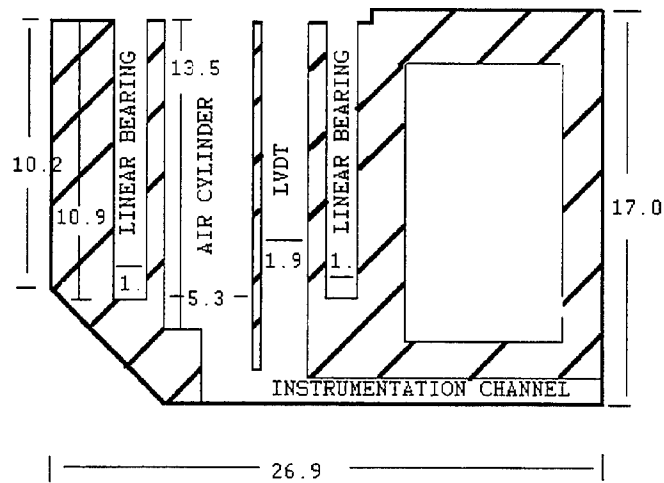
Figure 3.10. Actuator housing unit (units in cm).
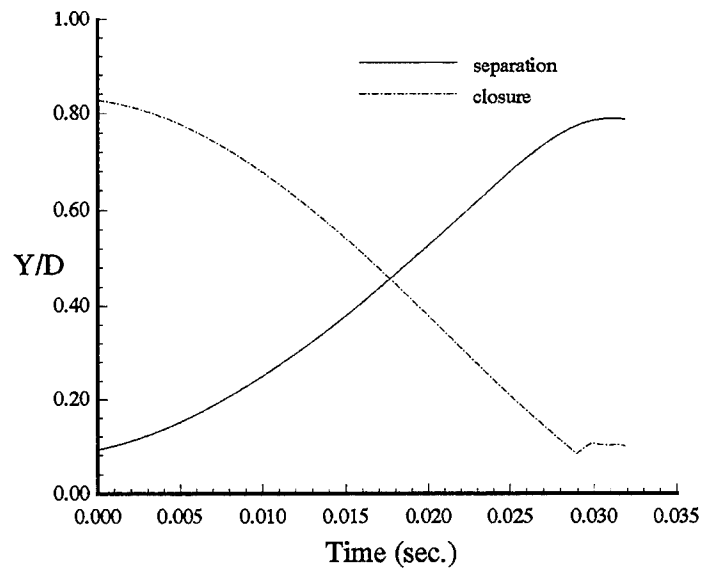
Figure 3.11. Time versus the wedge-store separation position for a time-dependent
separation and closure event.
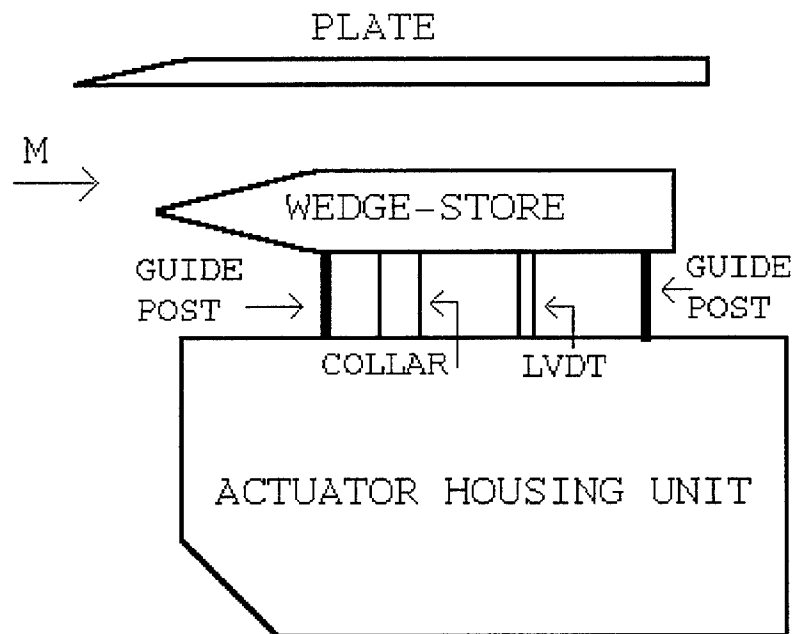
Figure 4.1. Steady-state separation distance held with collar block.
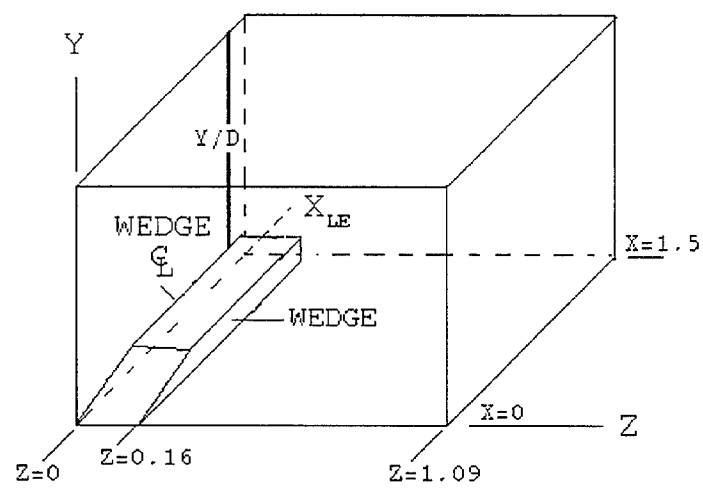
Figure 4.2. Computational domain for the plate and wedge-store configuration (Y/D = 0.51).
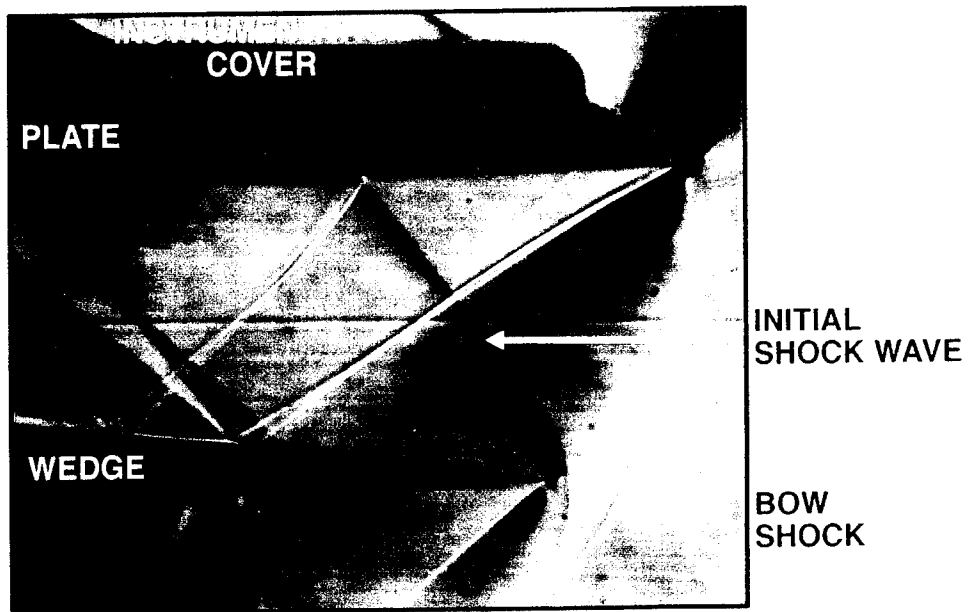
Figure 5.1. Schlieren photograph: M=1.52, 6.1° wedge, and Y/D = 0.89
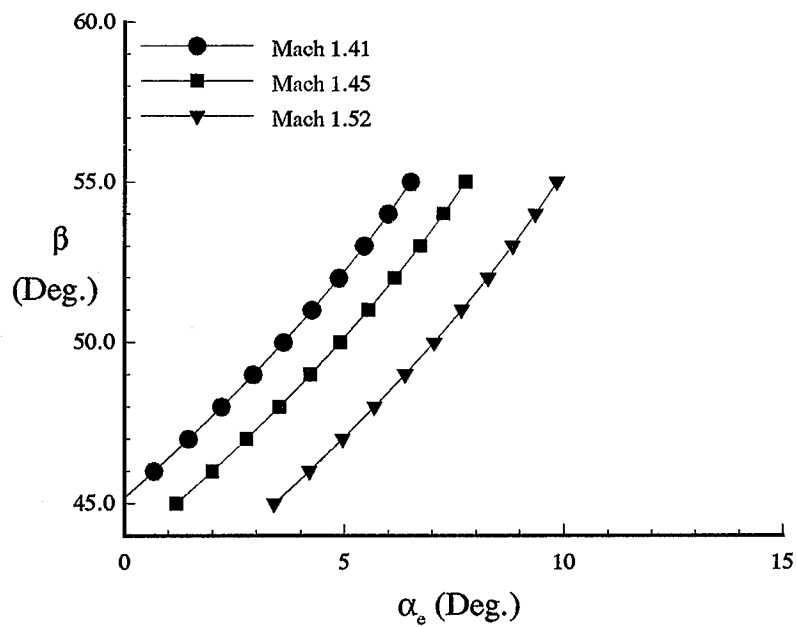
Figure 5.2.   The two-dimensional shock wave angle (β) and deflection angle (α_e) relationship.
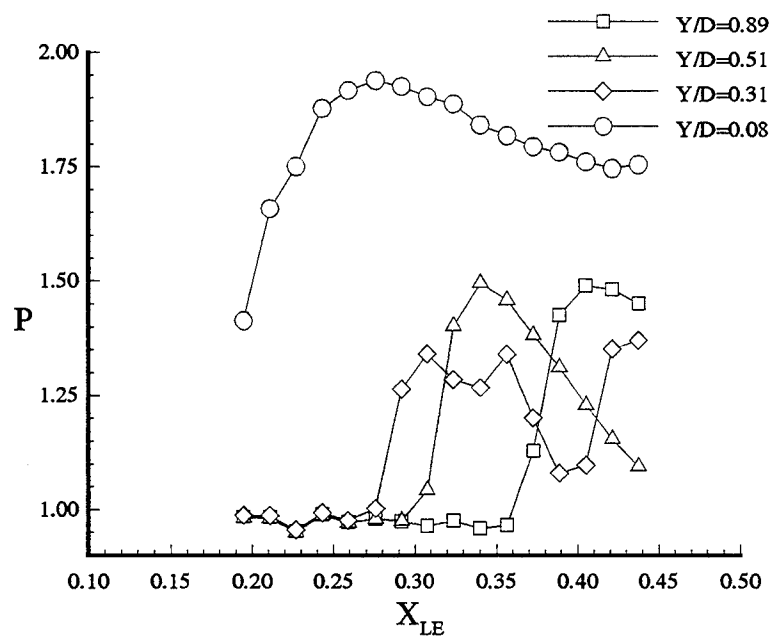
Figure 5.3. Plate normalized surface pressure: M=1.52, 6.1° wedge, and $\phi = 0$
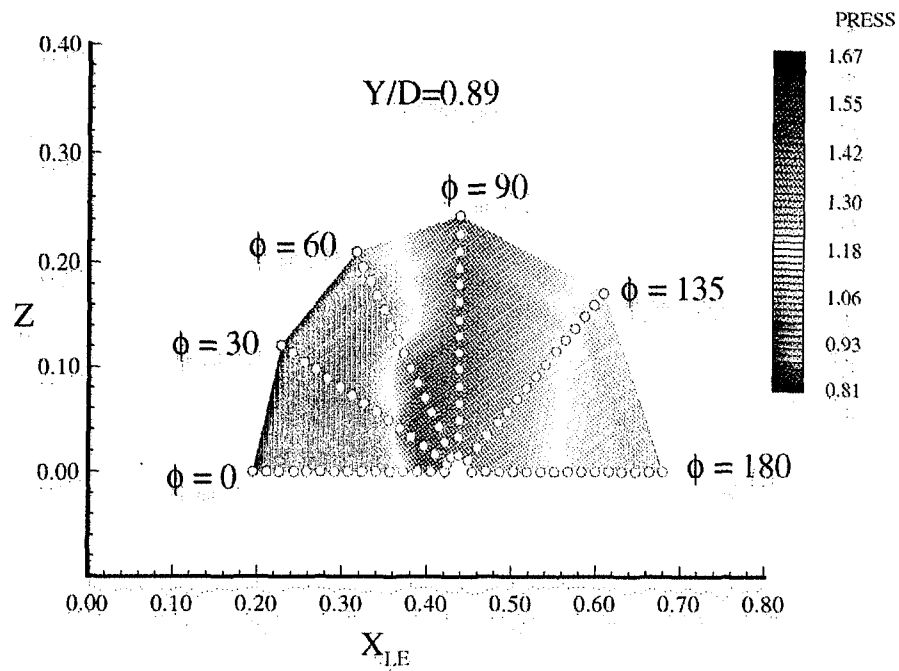
Figure 5.4. Plate experimental surface pressure plot for M=1.52, 6.1° wedge, and Y/D = 0.89
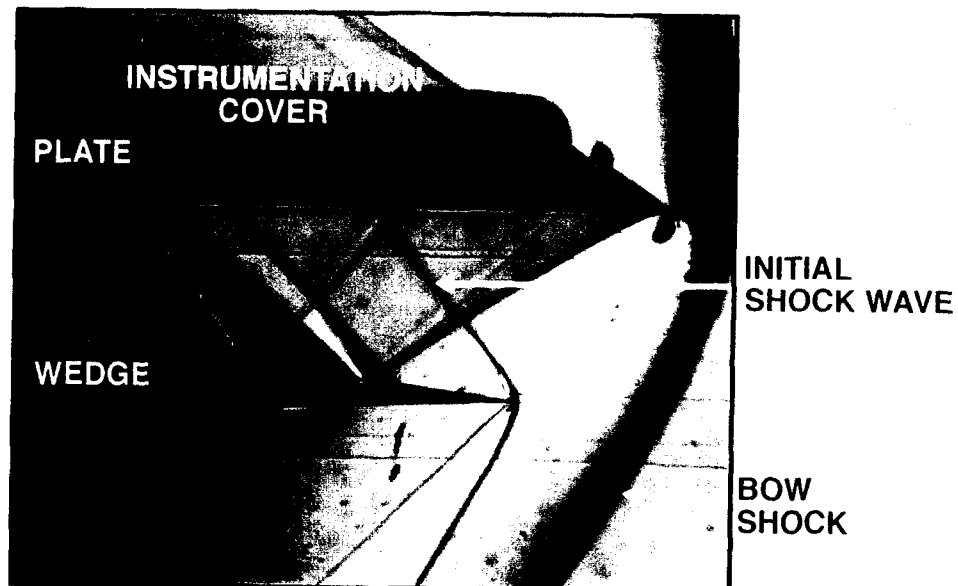
Figure 5.5. Schlieren photograph: M=1.52, 6.1° wedge, and Y/D = 0.51
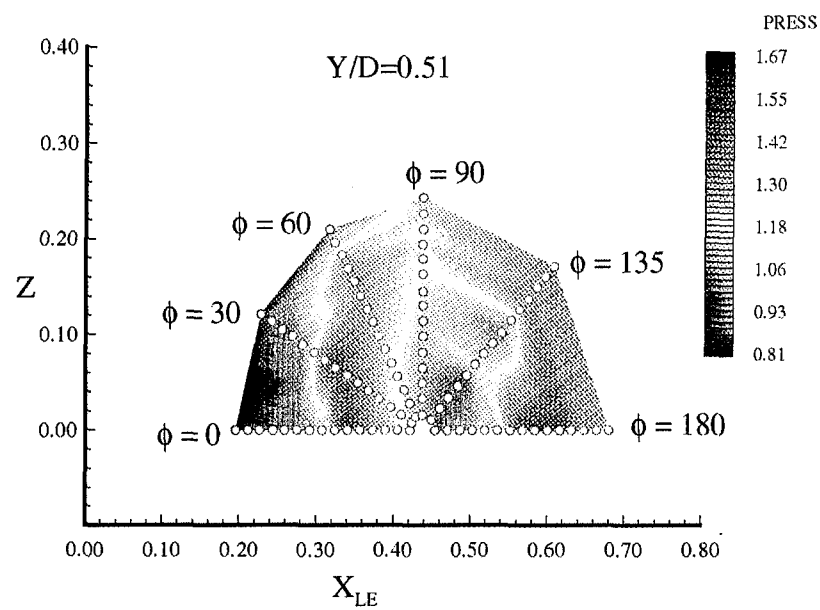
Figure 5.6. Plate experimental pressure contour: M=1.52, 6.1° wedge, Y/D=0.51
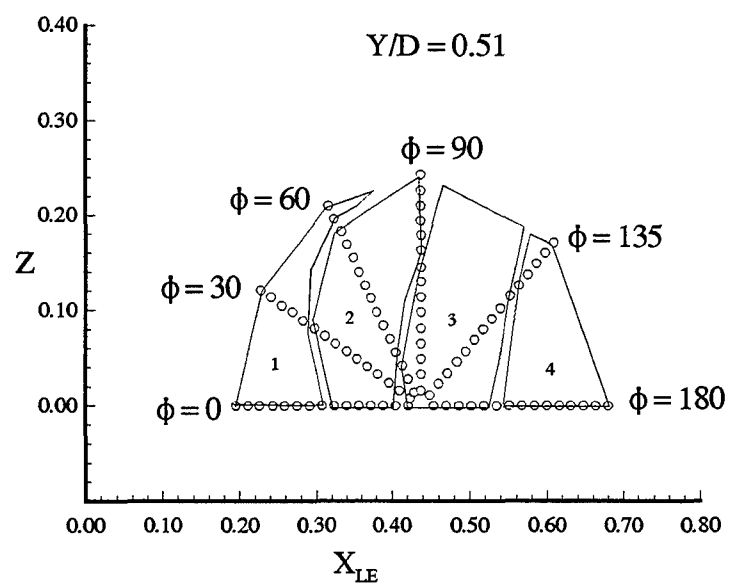
Figure 5.7. Plate experimental pressure sketch: M=1.52, 6.1° wedge, Y/D=0.51
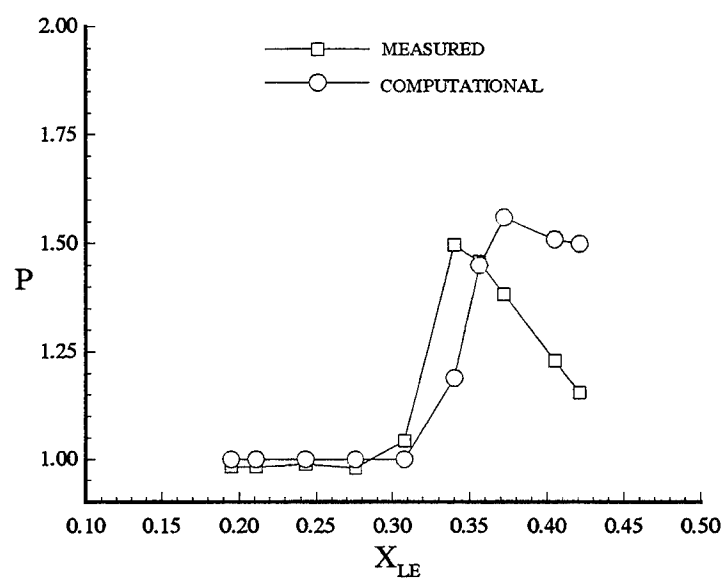
Figure 5.8. A numerical and experimental comparison of the plate surface pressure. (M=1.52, 6.1° wedge, Y/D = 0.51)
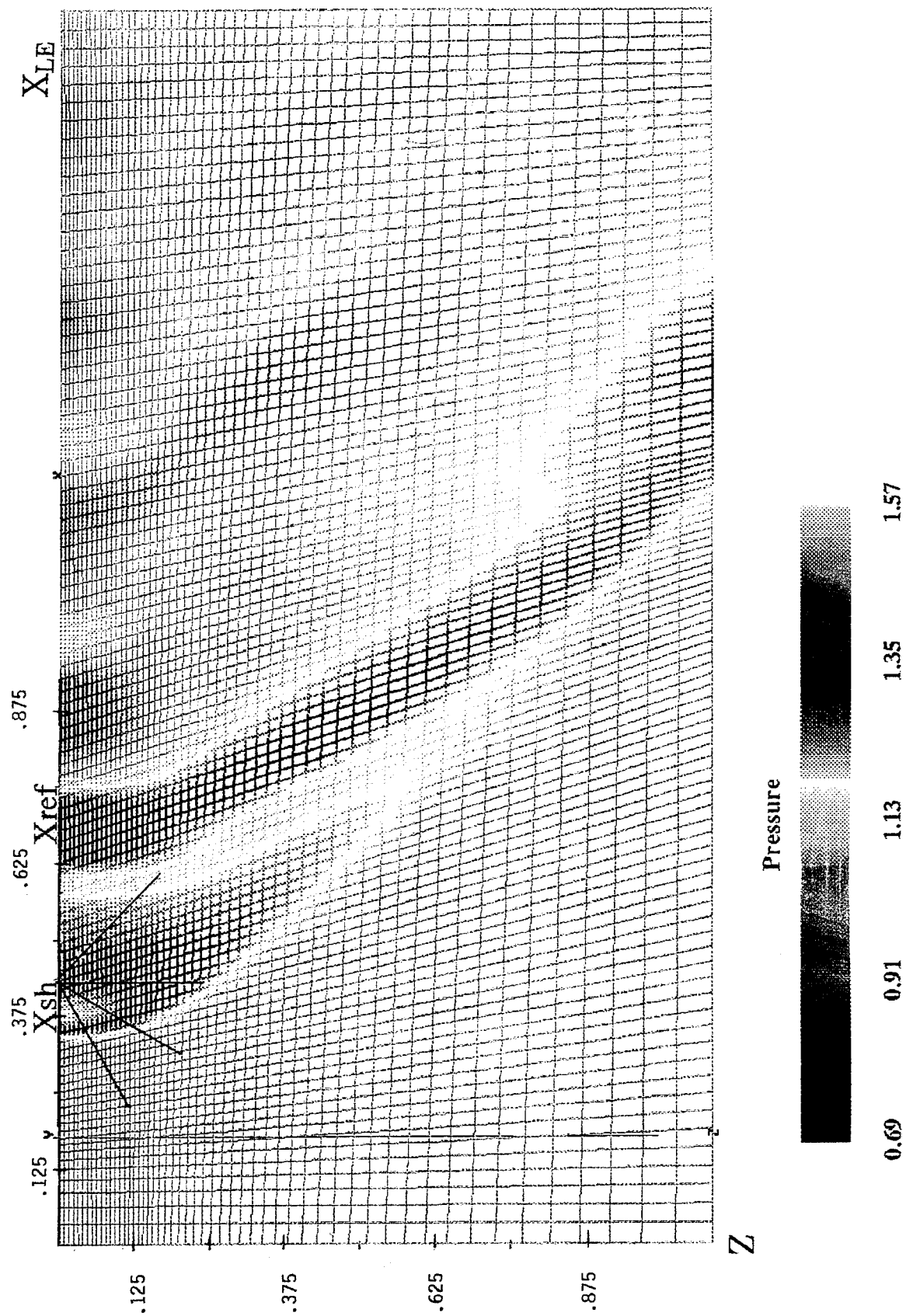
Figure 5.9. Plate numerical surface pressure: M=1.52, 6.1° wedge, Y/D = 0.51
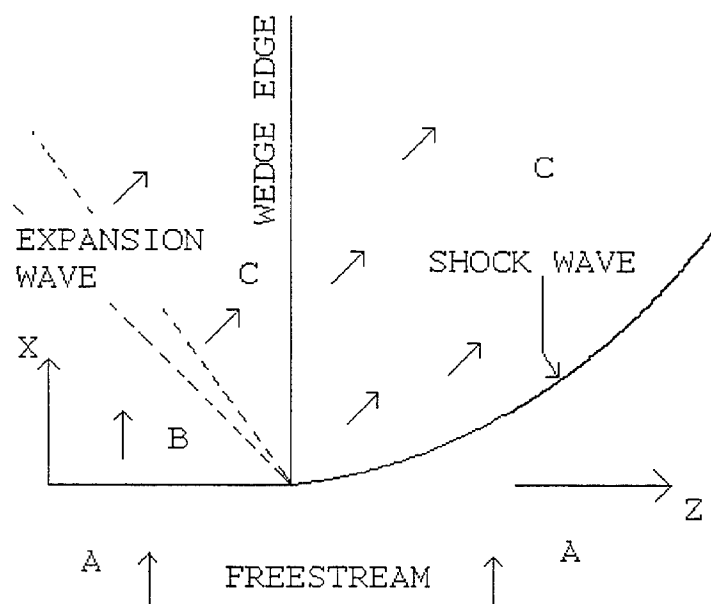
Figure 5.10.   Three dimensional illustration of the supersonic flow about the wedge store.
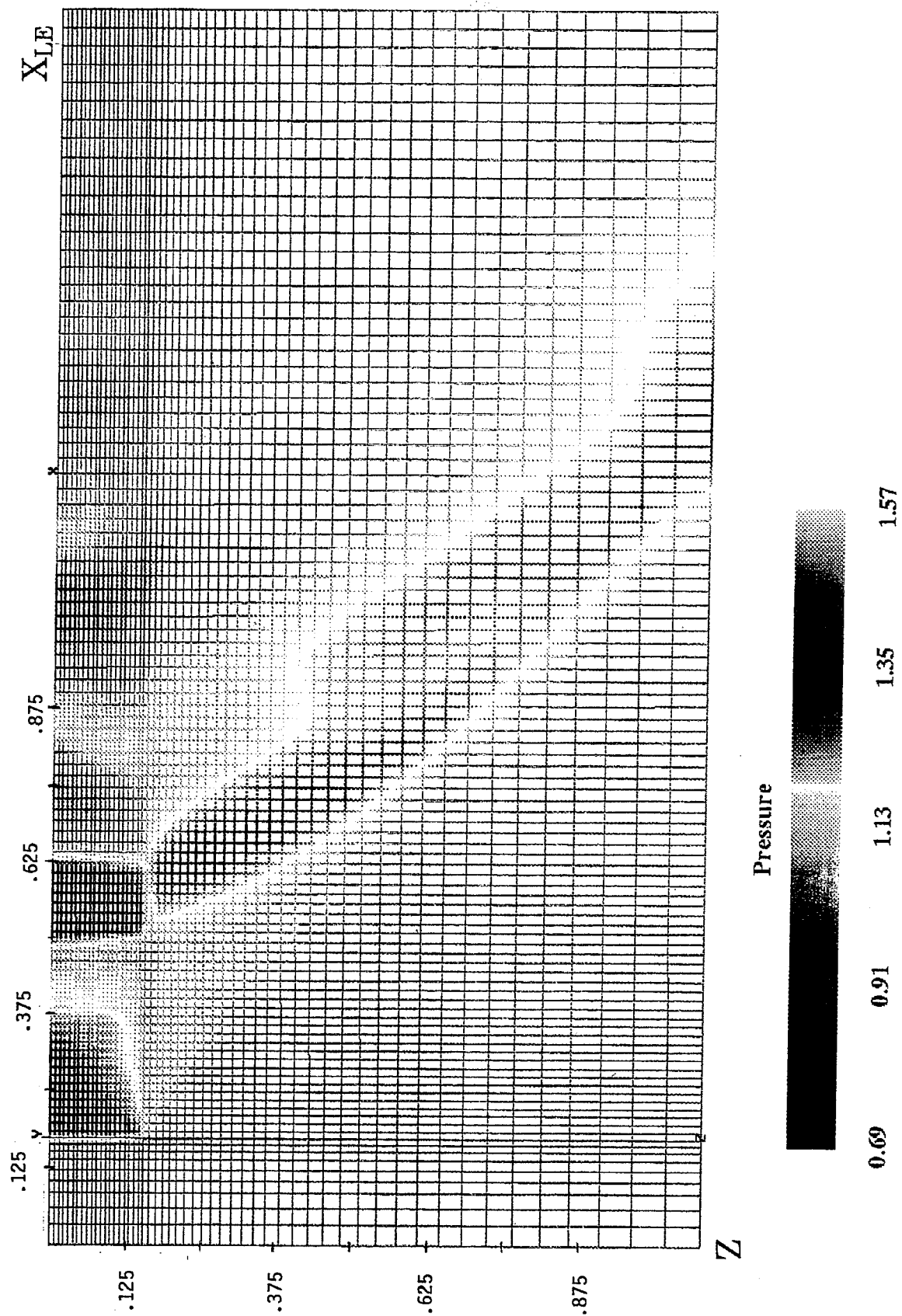
Figure 5.11. The 6.1° wedge numerical surface pressure, M=1.52.
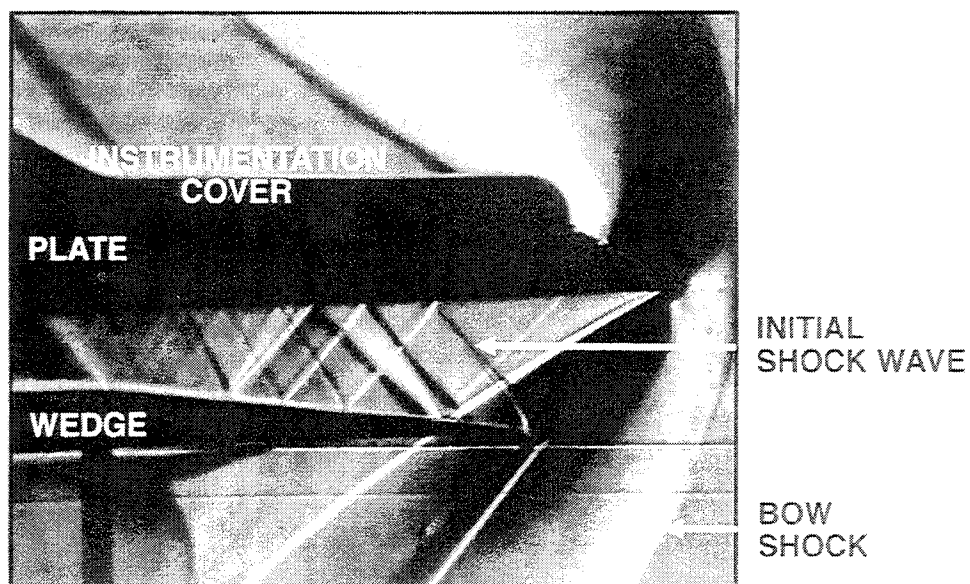
Figure 5.12. Schlieren photograph for 6.1° wedge at Y/D = 0.31, M=1.52.
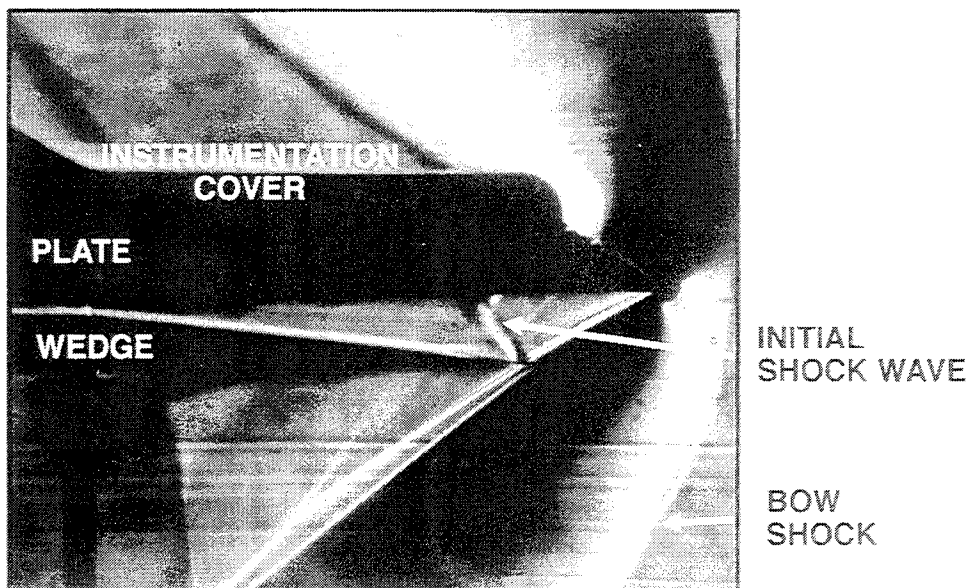
Figure 5.13. Schlieren photograph for 6.1° wedge at Y/D = 0.08, M=1.52.
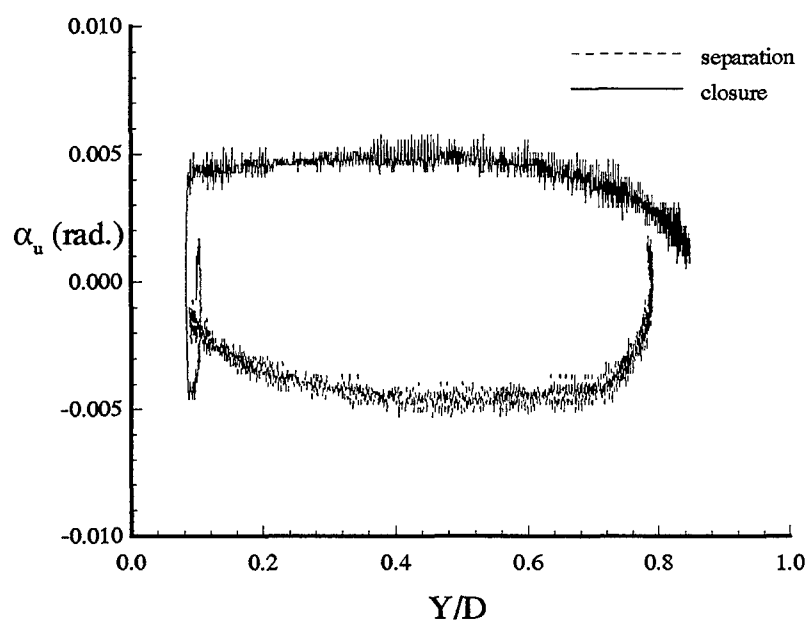
Figure 5.14. Induced angle of attack, α_u, for dynamic closure and separation events.
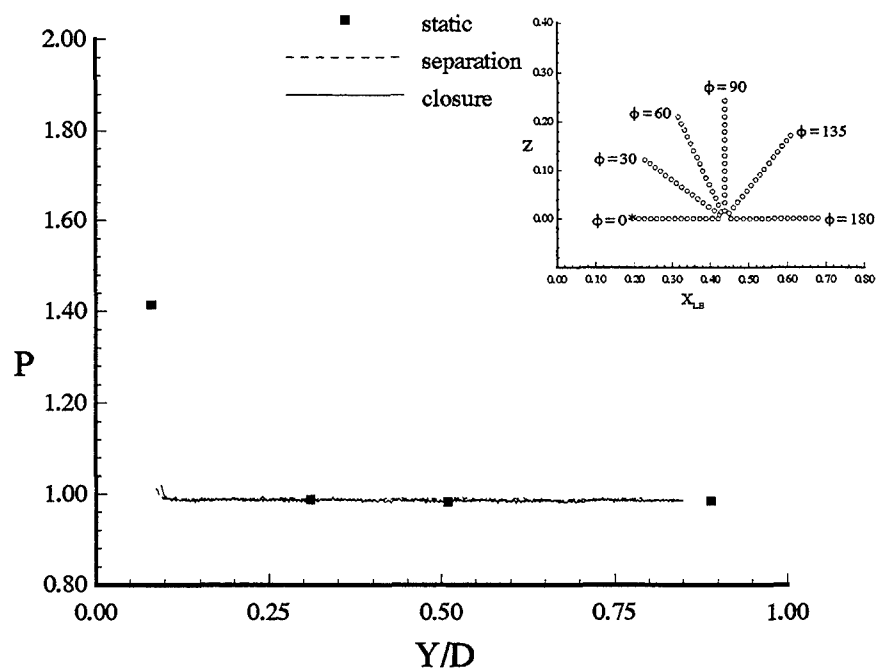
Figure 5.15.   Normalized plate surface pressure for dynamic motion with 6.1° wedge
and M=1.52 ($\phi = 0$, R=1.00).
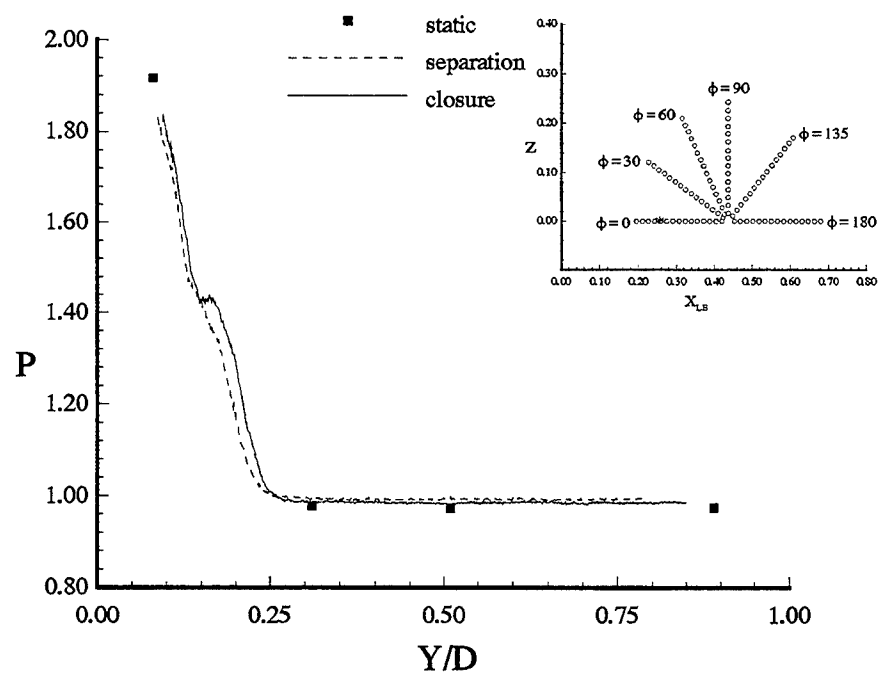
Figure 5.16. Normalized plate surface pressure for dynamic motion with 6.1° wedge and M=1.52 ($\phi = 0$, R=0.73).
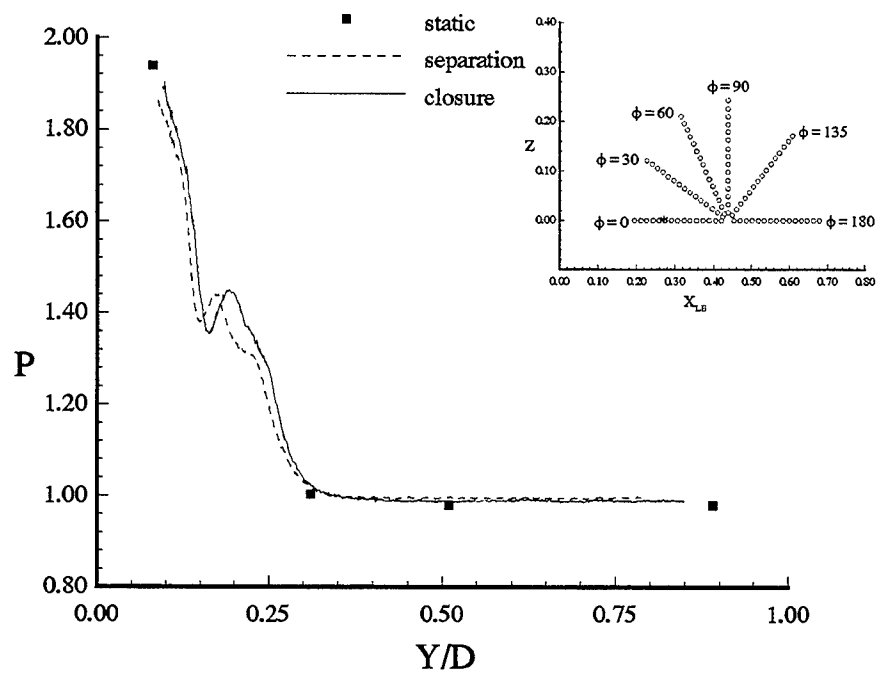
Figure 5.17. Normalized plate surface pressure for dynamic motion with 6.1° wedge and M=1.52 ($\phi = 0$, R=0.67).
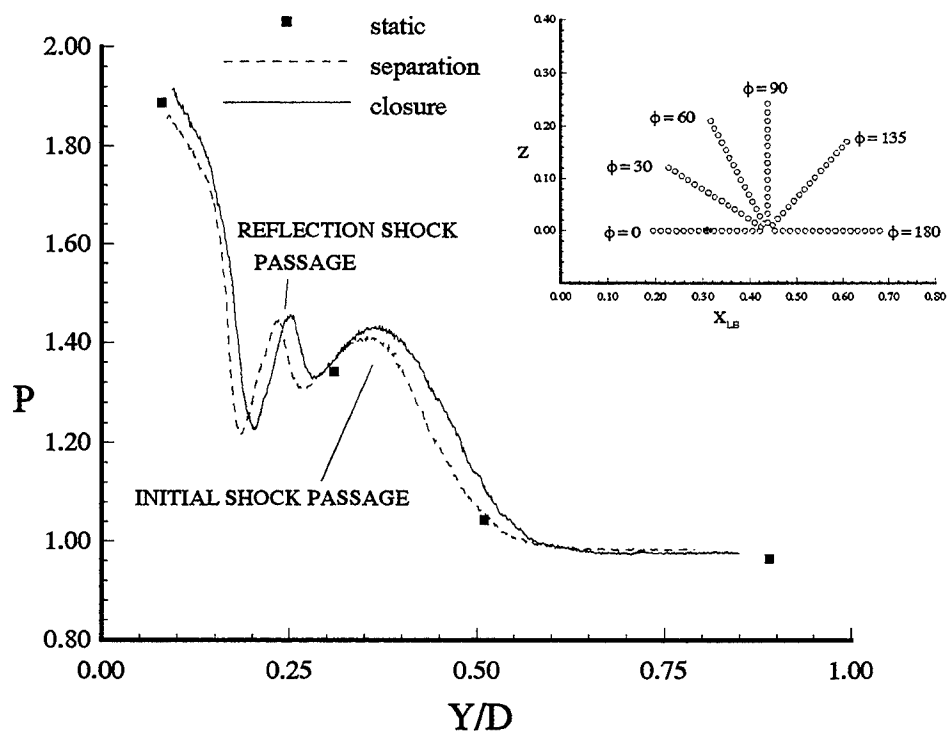
Figure 5.18. Normalized plate surface pressure for dynamic motion with 6.1° wedge
and M=1.52 ($\phi = 0$, R=0.53).
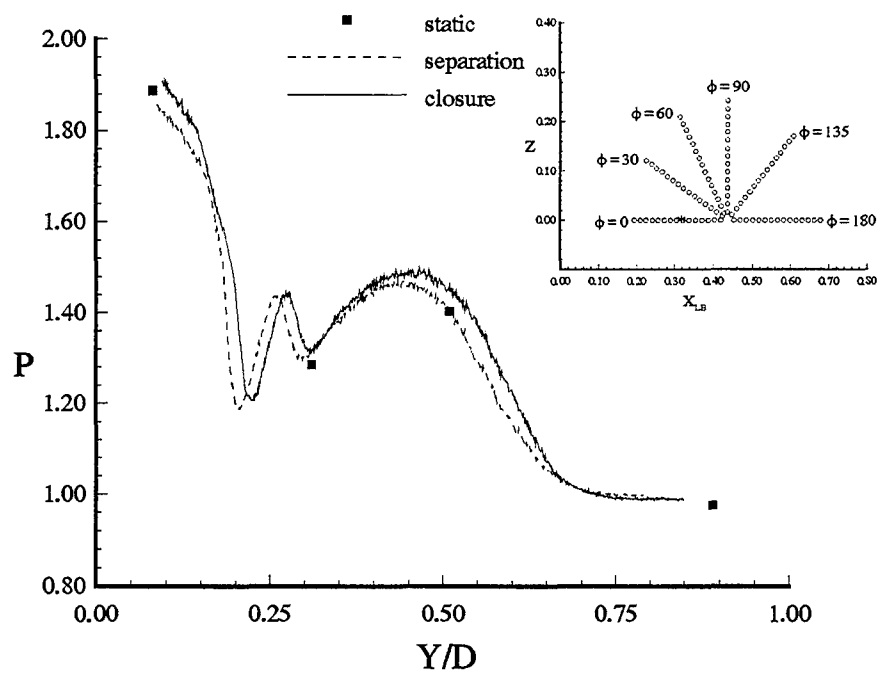
Figure 5.19. Normalized plate surface pressure for dynamic motion with 6.1° wedge and M=1.52 ($\phi = 0$, R=0.47).
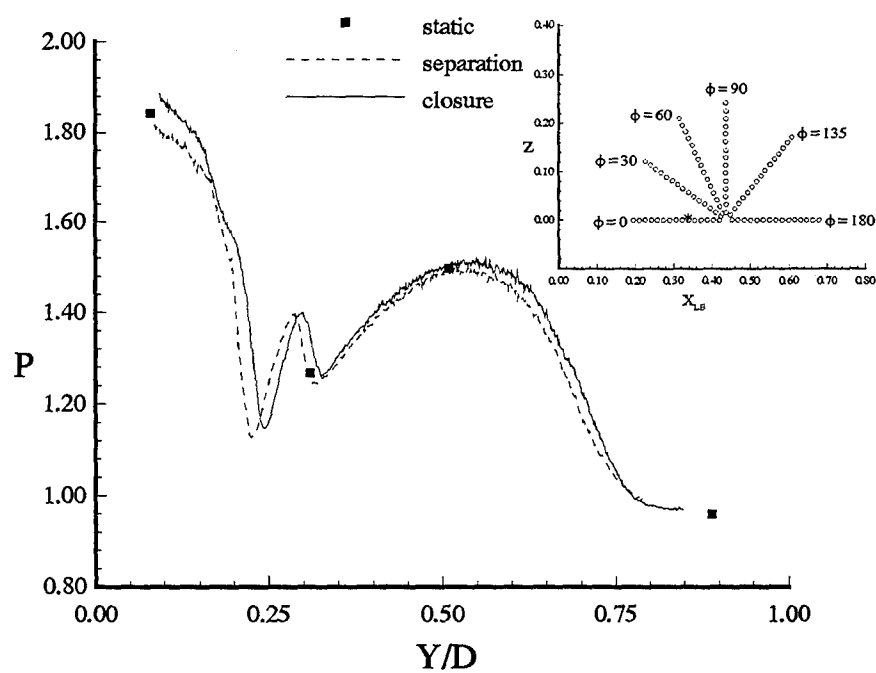
Figure 5.20.   Normalized plate surface pressure for dynamic motion with 6.1° wedge
                and M=1.52 ($\phi = 0$, R=0.40).
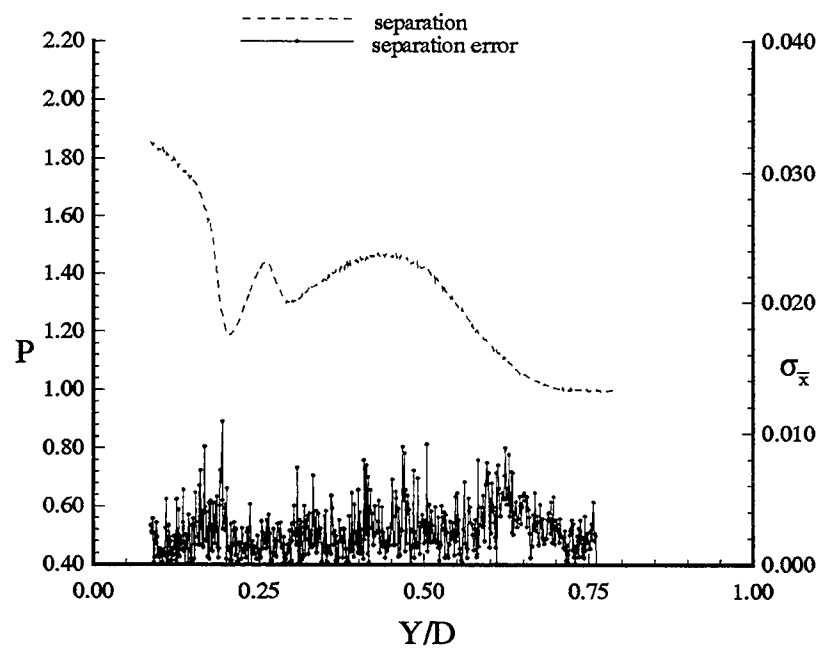
Figure 5.21. Normalized plate surface pressure and standard error for separation
with 6.1° wedge and M=1.52 ($\phi = 0$, R=0.47).
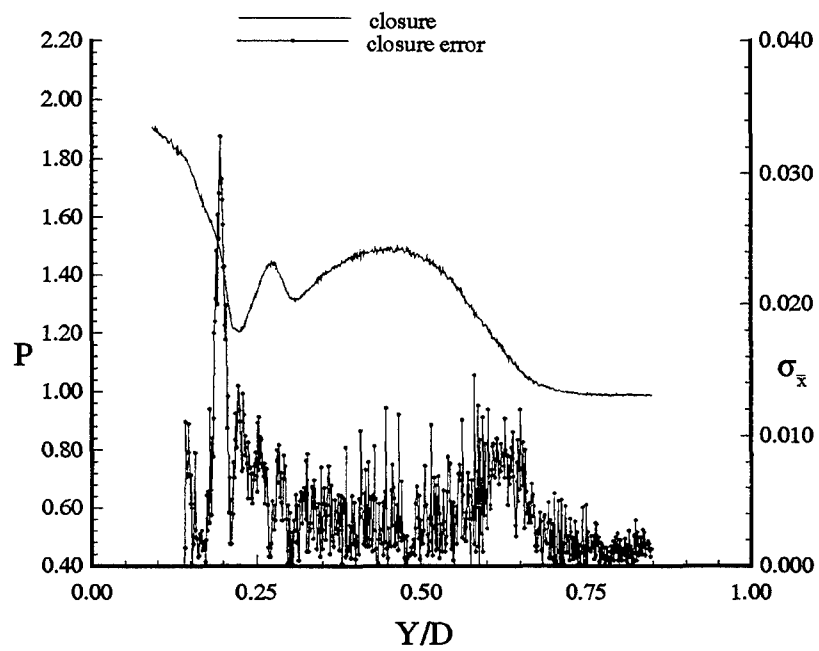
Figure 5.22. Normalized plate surface pressure and standard error for closure with 6.1° wedge and M=1.52 ($\phi = 0$, R=0.47).
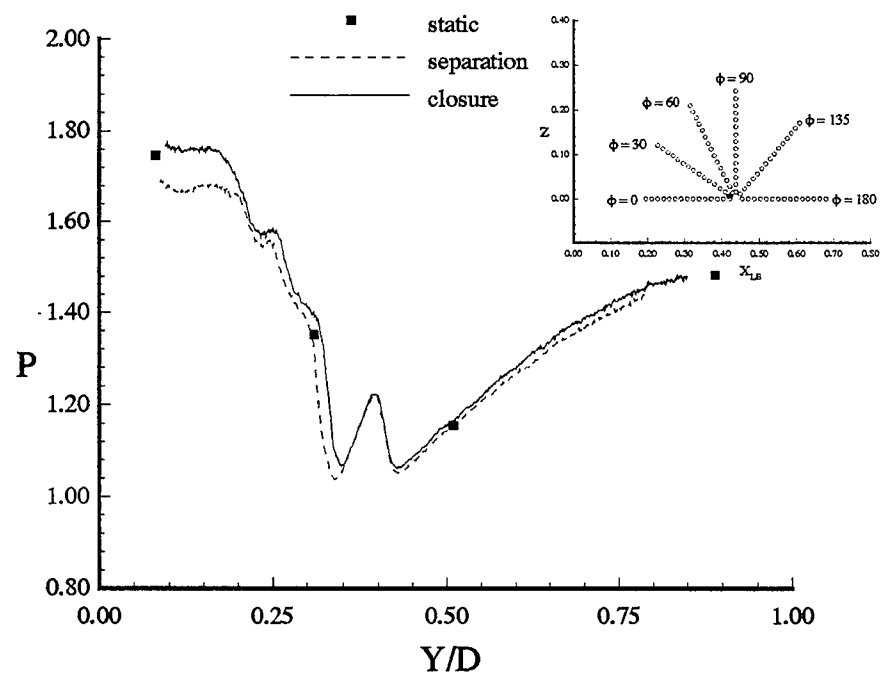
Figure 5.23. Normalized plate surface pressure for dynamic motion with 6.1° wedge and M=1.52 ($\phi = 0$, R=0.07).
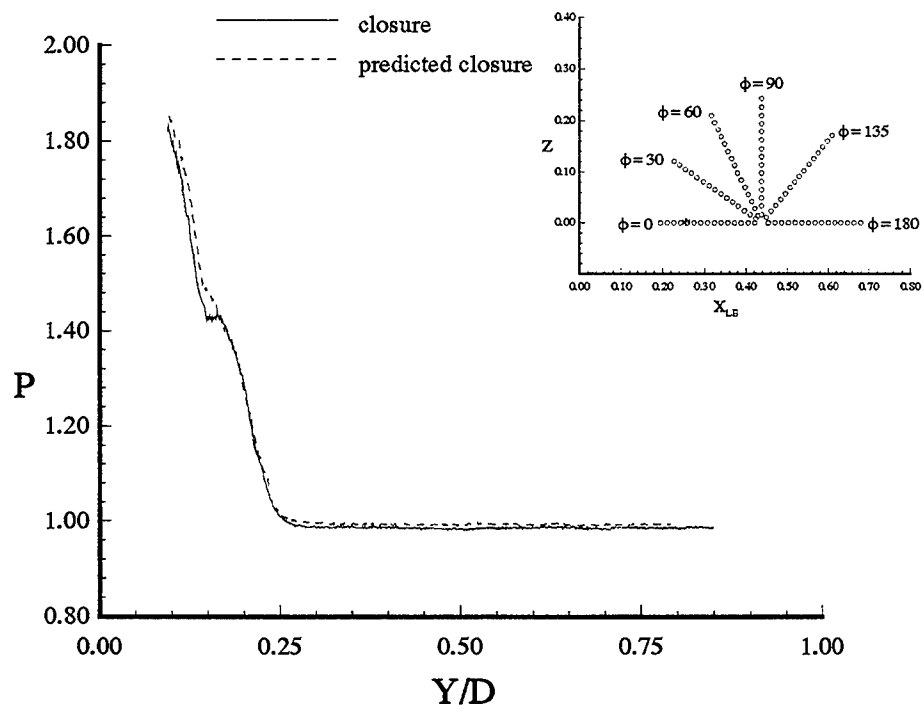
Figure 5.24.   Closure event prediction for the 6.1° wedge and M=1.52 (ϕ = 0, R = 0.74).
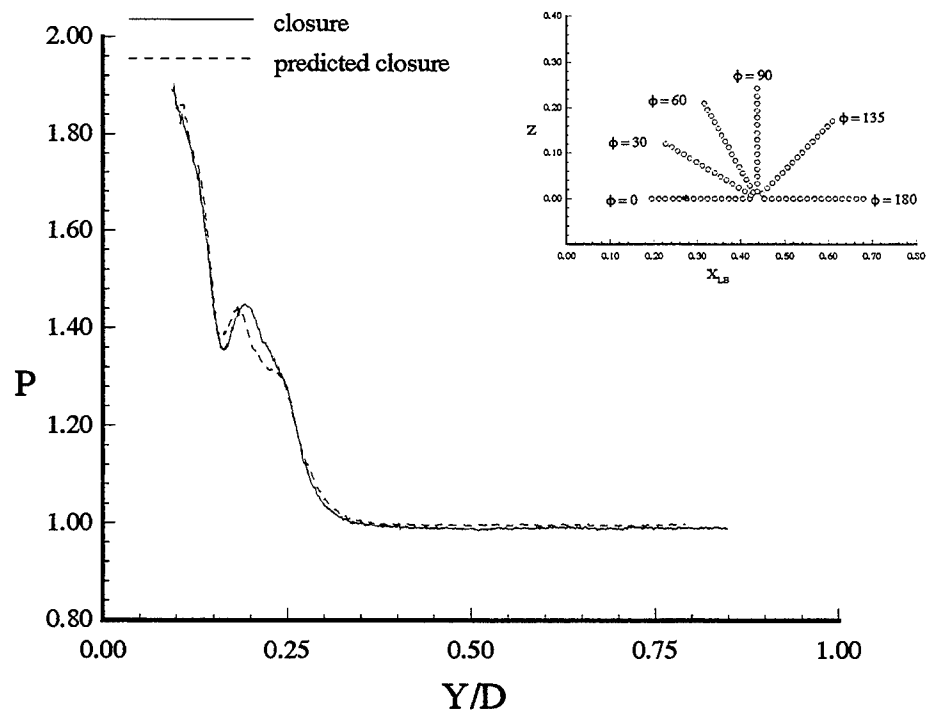
Figure 5.25. Closure event prediction for 6.1° wedge and M=1.52 (ϕ = 0, R = 0.67).
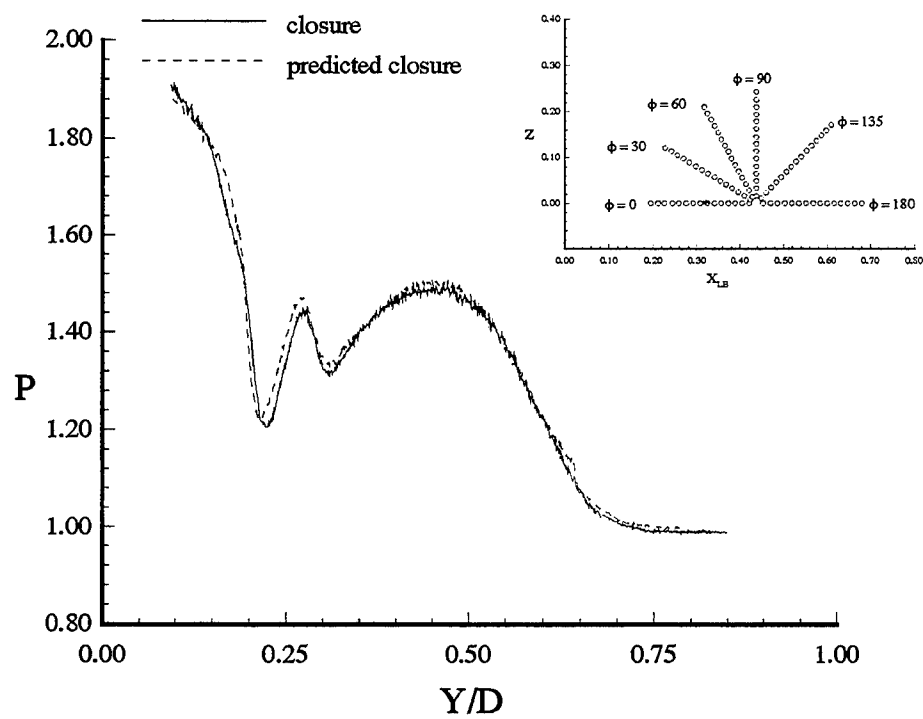
Figure 5.26. Closure event prediction for 6.1° wedge and M=1.52 (ϕ = 0, R = 0.47).
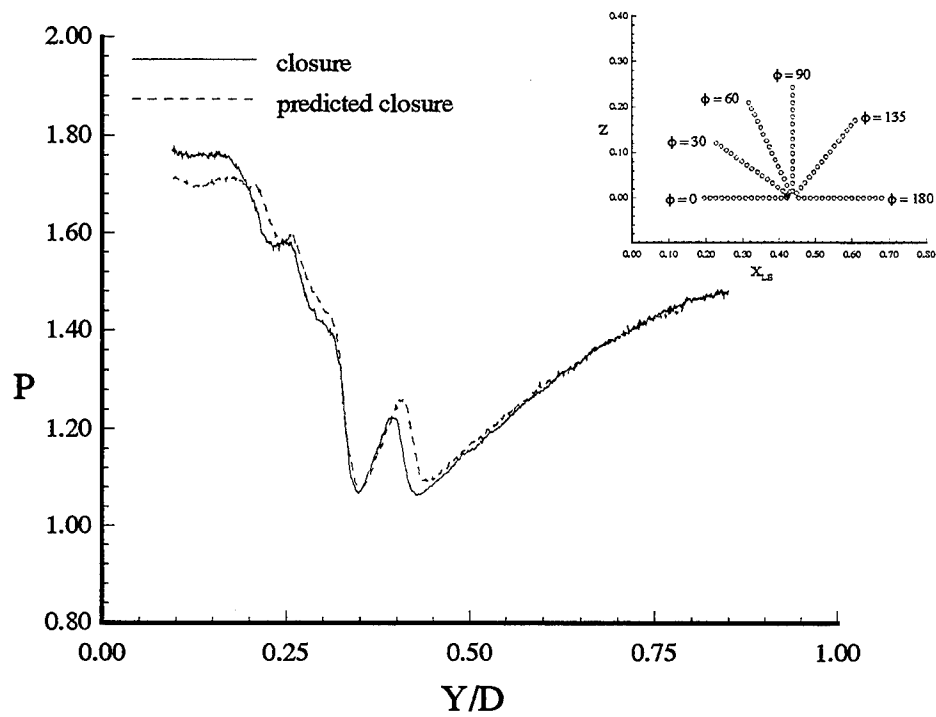
Figure 5.27.   Closure event prediction for 6.1° wedge and M=1.52 (ϕ = 0, R = 0.07).
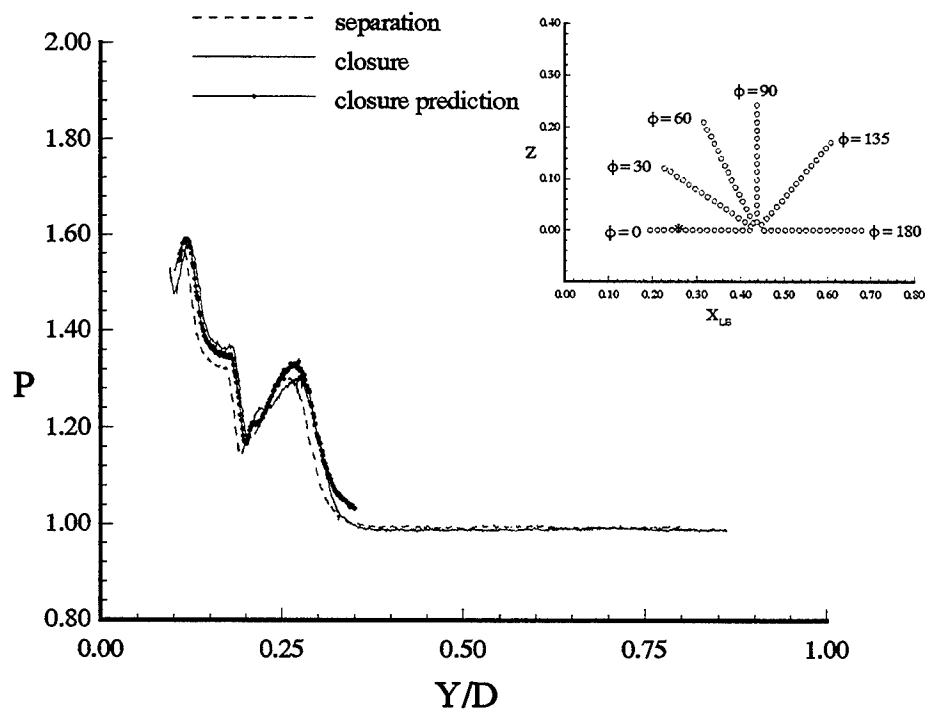
Figure 5.28.   Closure event prediction for 3.53° wedge and M=1.52 (ϕ = 0, R = 0.73).
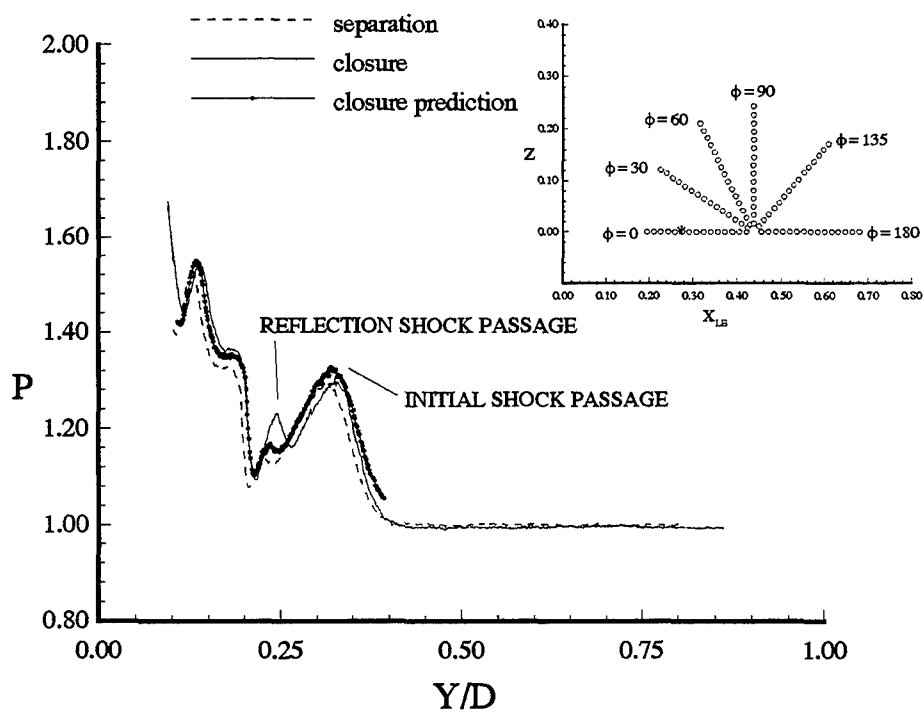
Figure 5.29.   Closure event prediction for 3.53° wedge and M=1.52 (ϕ = 0, R = 0.67).
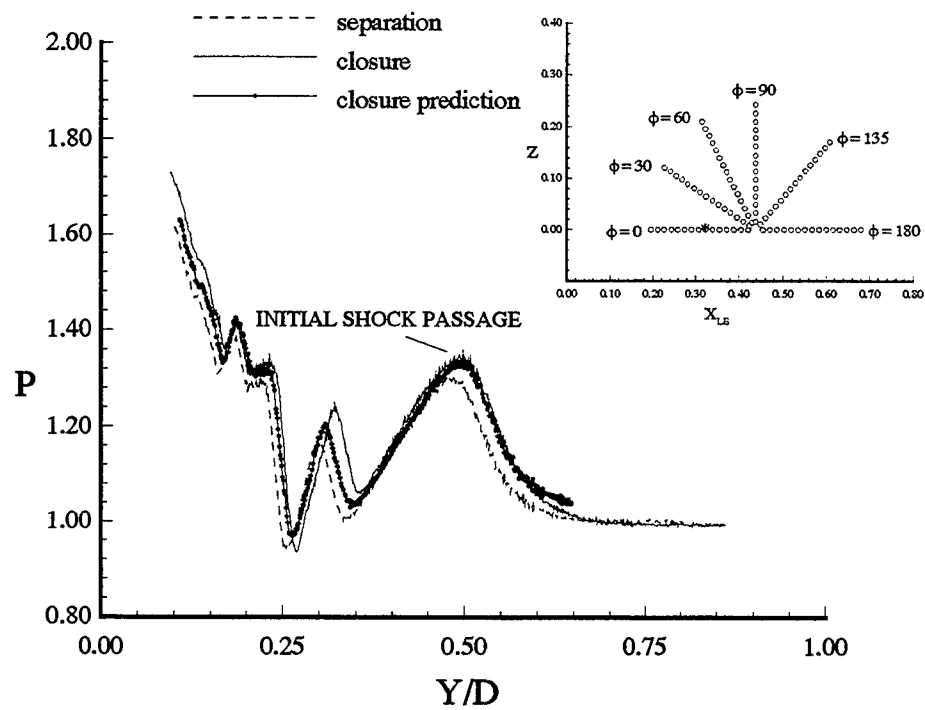
Figure 5.30. Closure event prediction for 3.53° wedge and M=1.52 (ϕ = 0, R = 0.47).
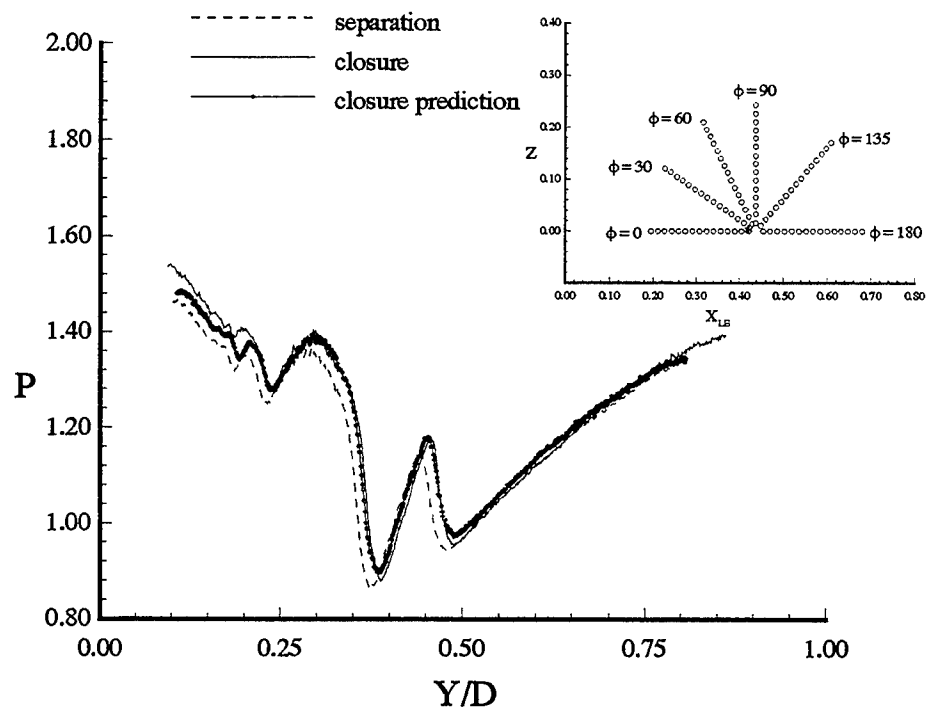
Figure 5.31. Closure event prediction for 3.53° wedge and M=1.52 (ϕ = 0, R = 0.07).
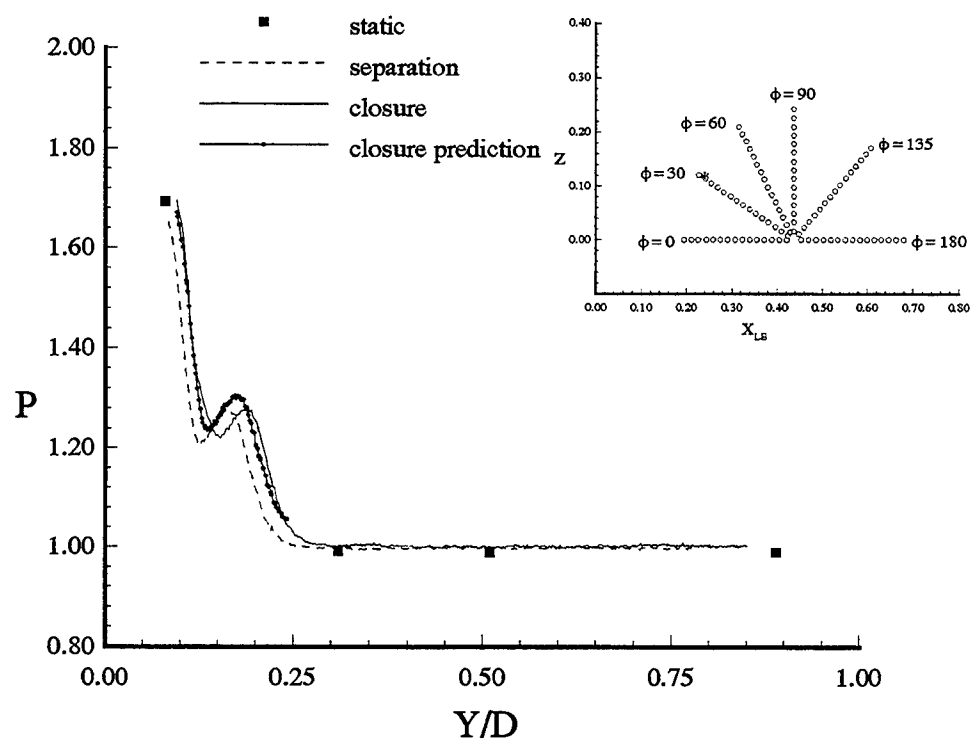
Figure 5.32. Separation events and closure prediction with the 6.1° wedge and M=1.52 (ϕ = 30, R = 0.93).
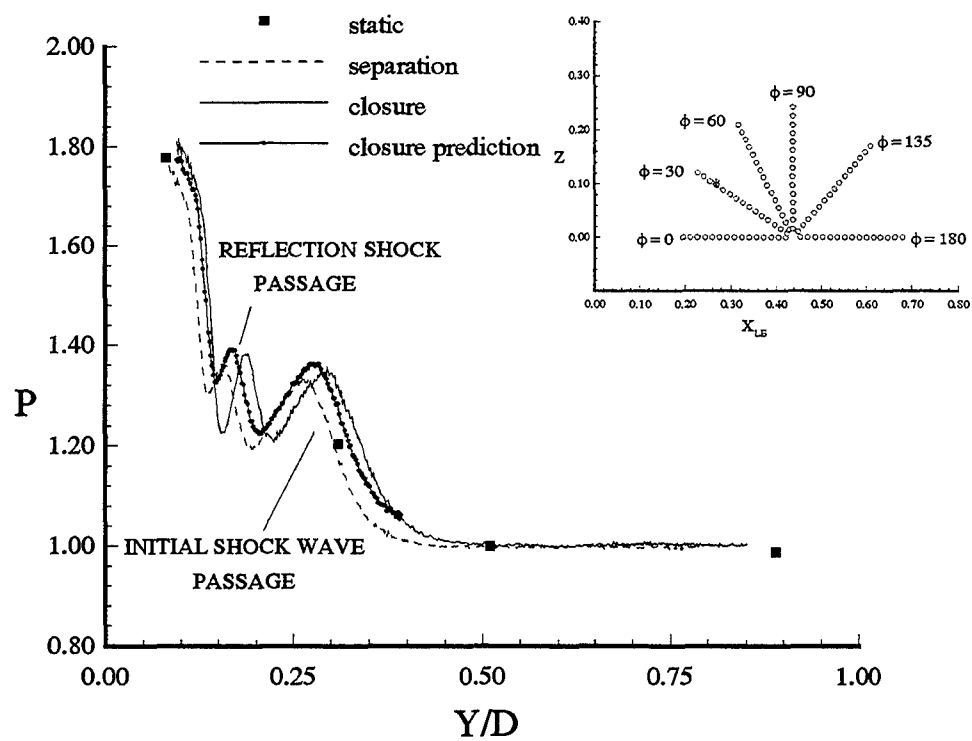
Figure 5.33. Separation events and closure prediction with the 6.1° wedge and M=1.52 (ϕ = 30, R = 0.80).
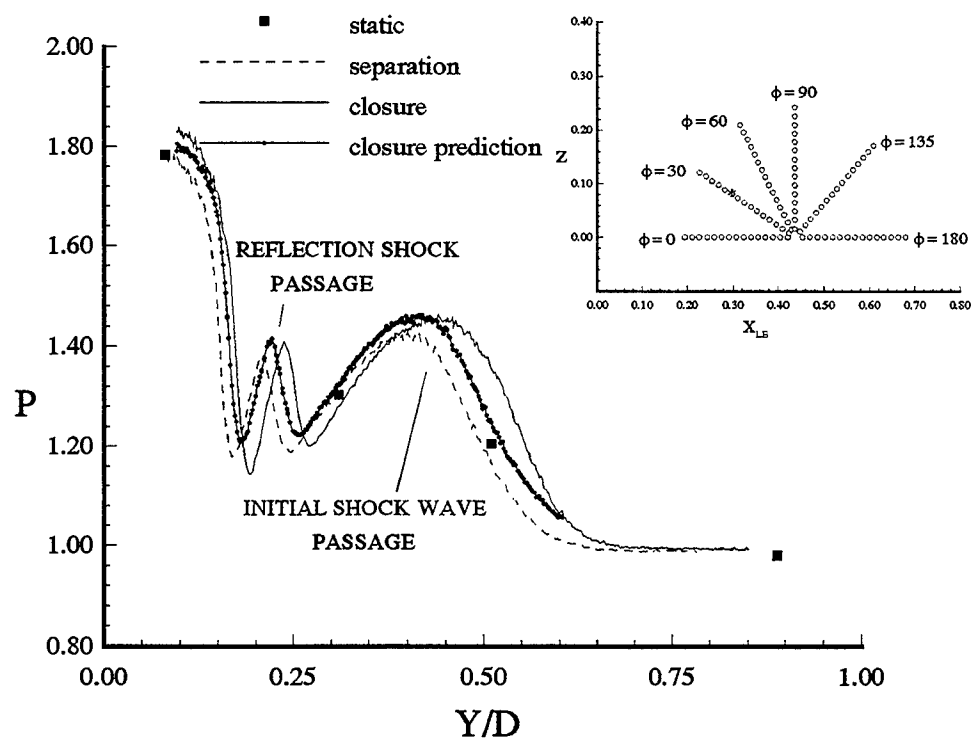
Figure 5.34.   Separation events and closure prediction with the 6.1° wedge and M=1.52 (ϕ = 30, R = 0.67).
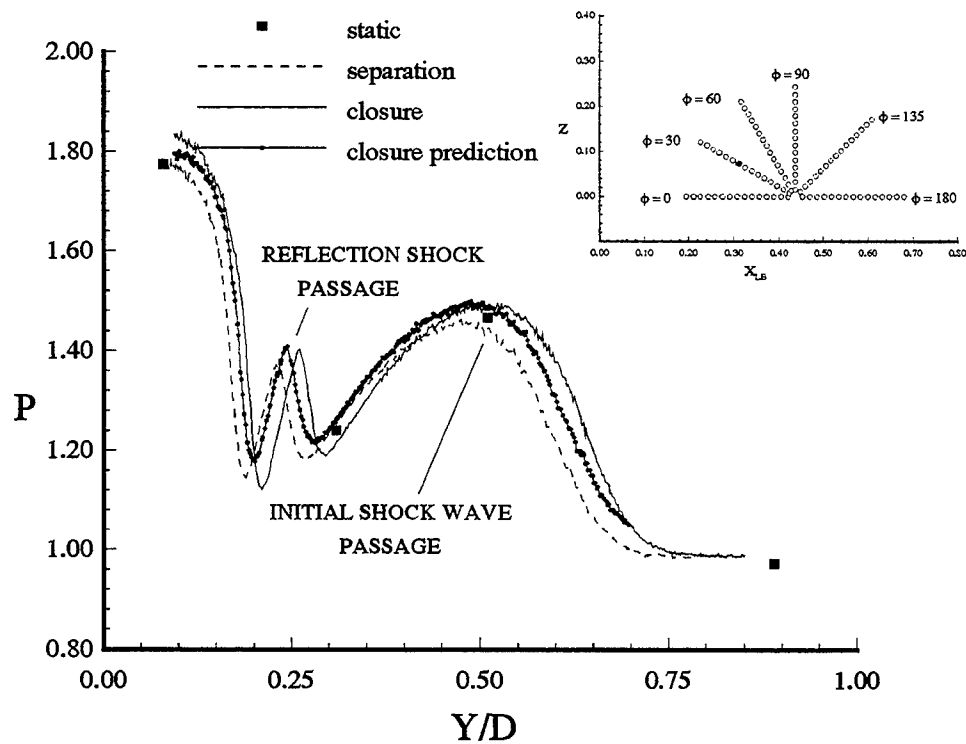
Figure 5.35.   Separation events and closure prediction with the 6.1° wedge and M=1.52 (ϕ = 30, R = 0.60).
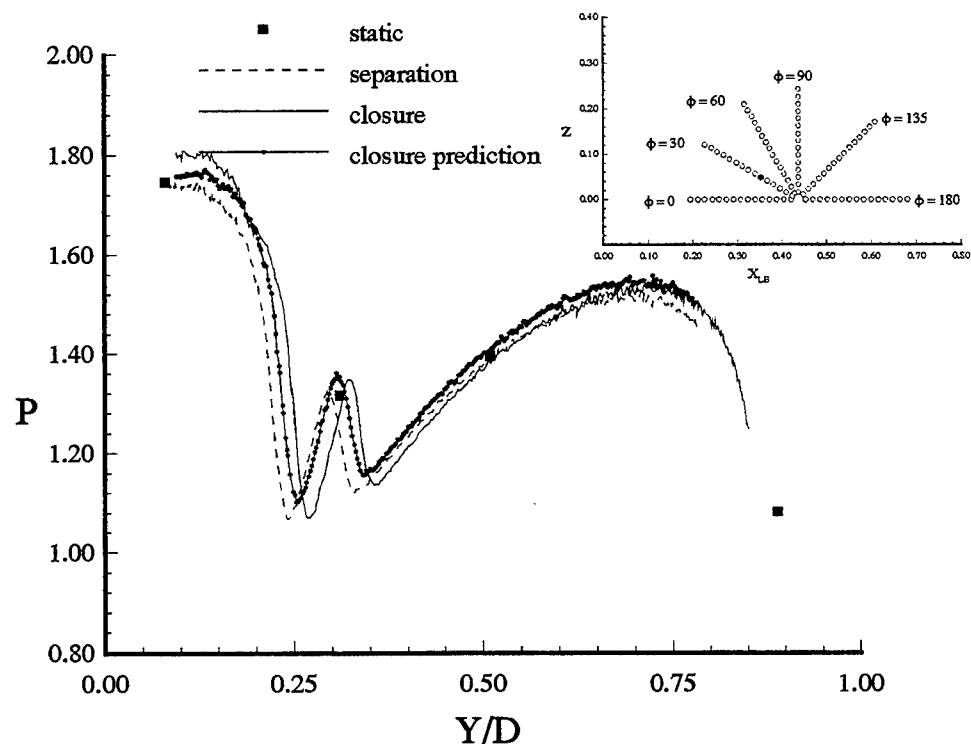
Figure 5.36. Separation events and closure prediction with the 6.1° wedge and M=1.52 ($\phi = 30$ at R = 0.40).
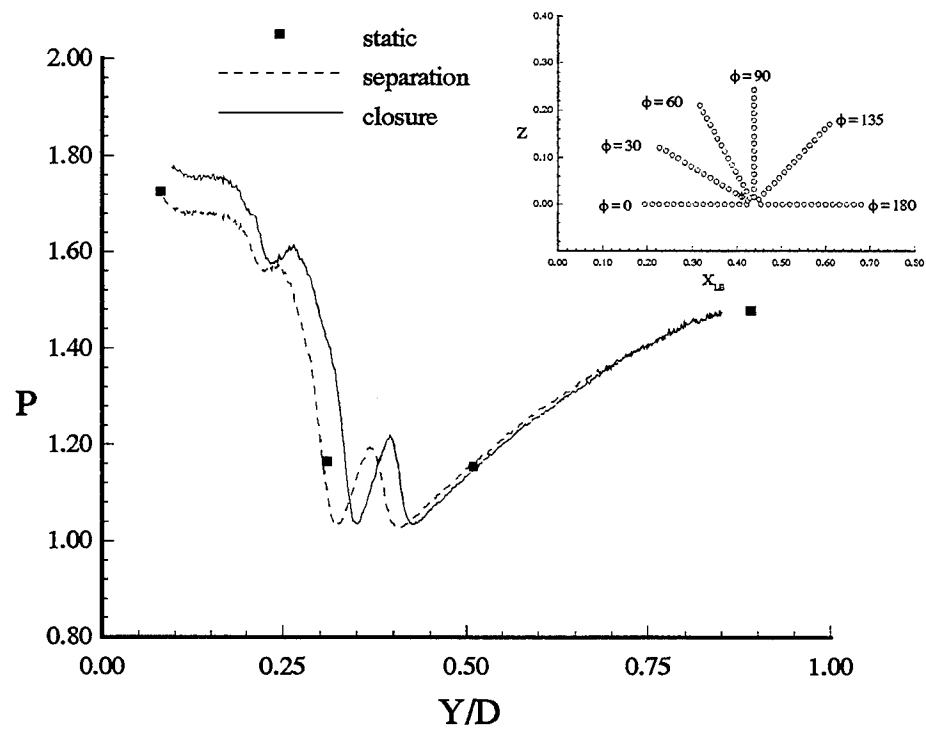
Figure 5.37. Separation events with the 6.1° wedge and M=1.52 ($\phi = 30$ at R = 0.13).
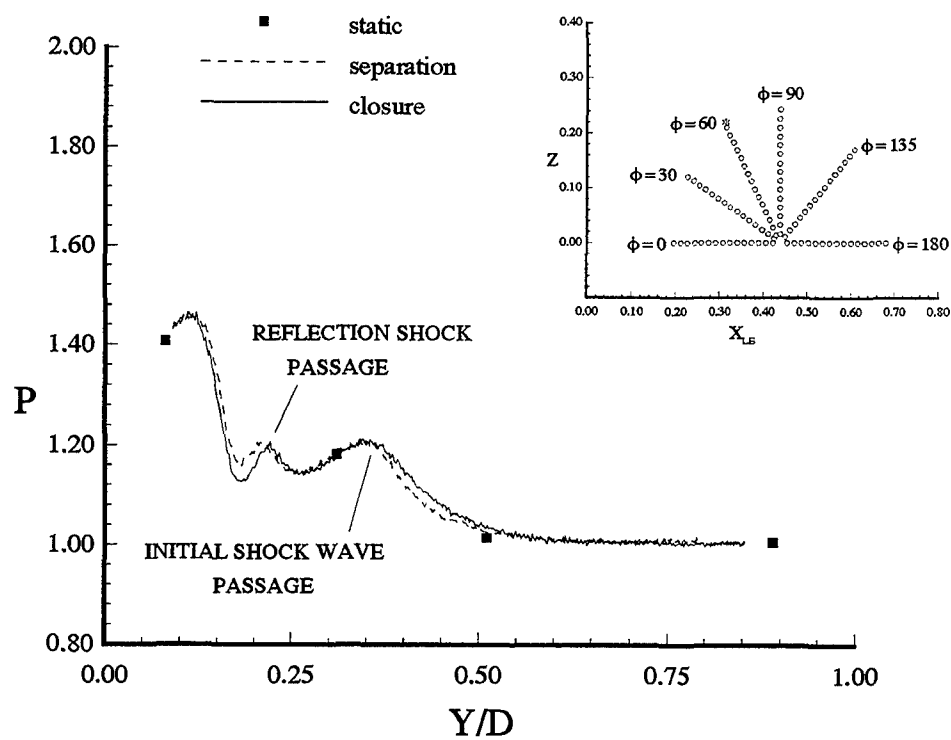
Figure 5.38. Separation events with the 6.1° wedge and M=1.52 (ϕ = 60, R = 1.00).
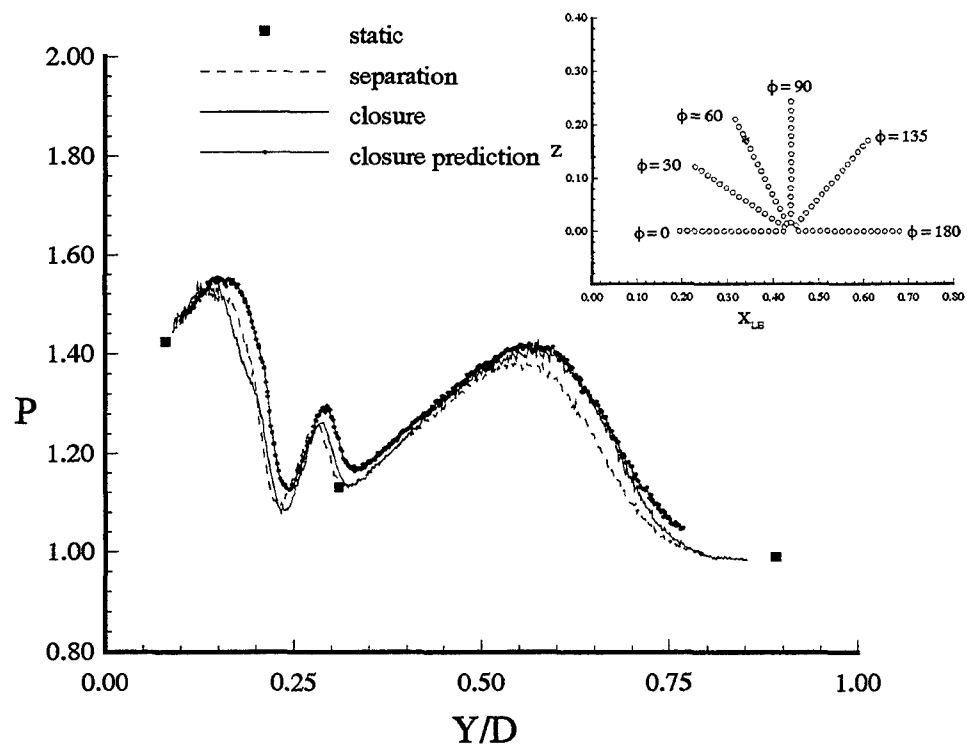
Figure 5.39. Separation events and closure prediction with the 6.1° wedge and M=1.52 (ϕ = 60, R = 0.80).
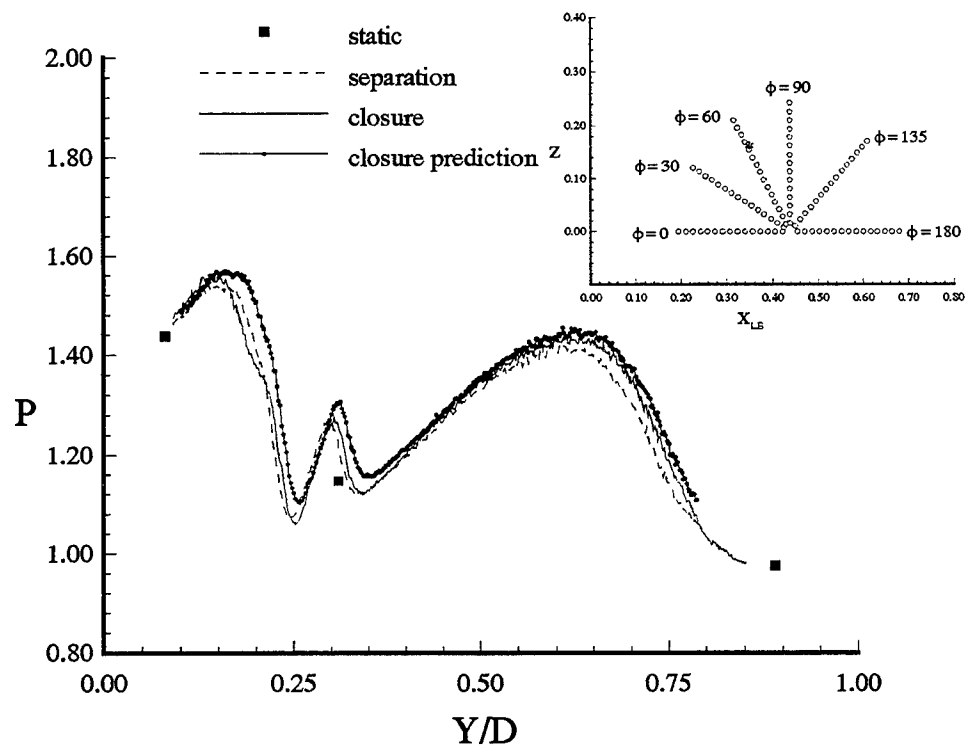
Figure 5.40. Separation events and closure prediction with the 6.1° wedge and M=1.52 (ϕ = 60, R = 0.73).
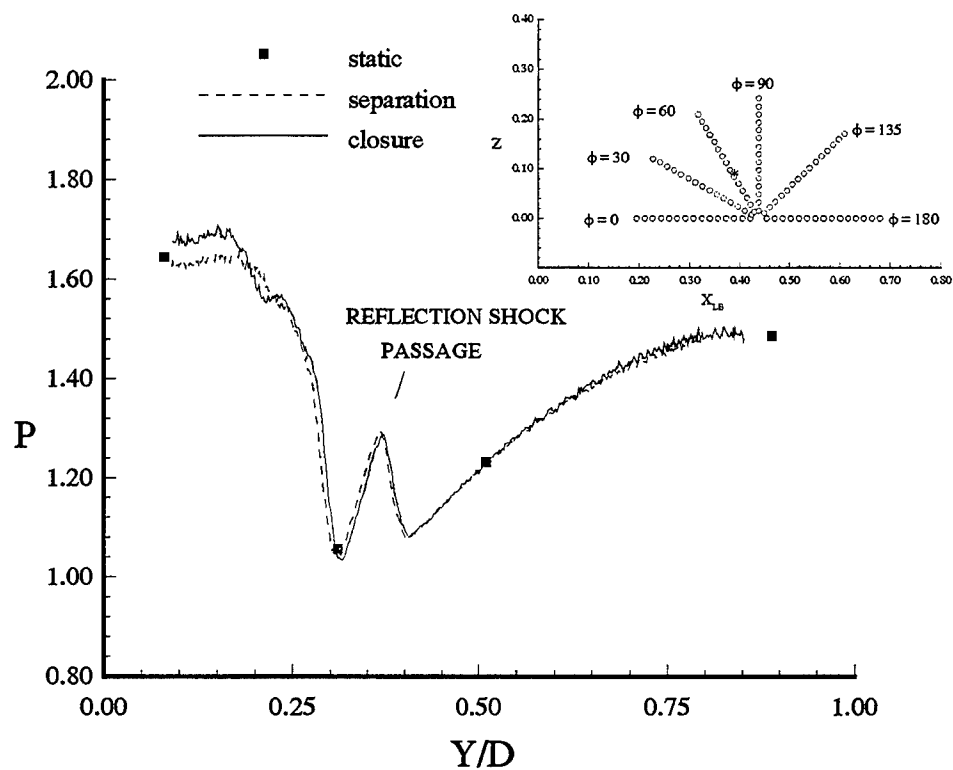
Figure 5.41. Separation events with the 6.1° wedge and M=1.52 (ϕ = 60, R = 0.40).
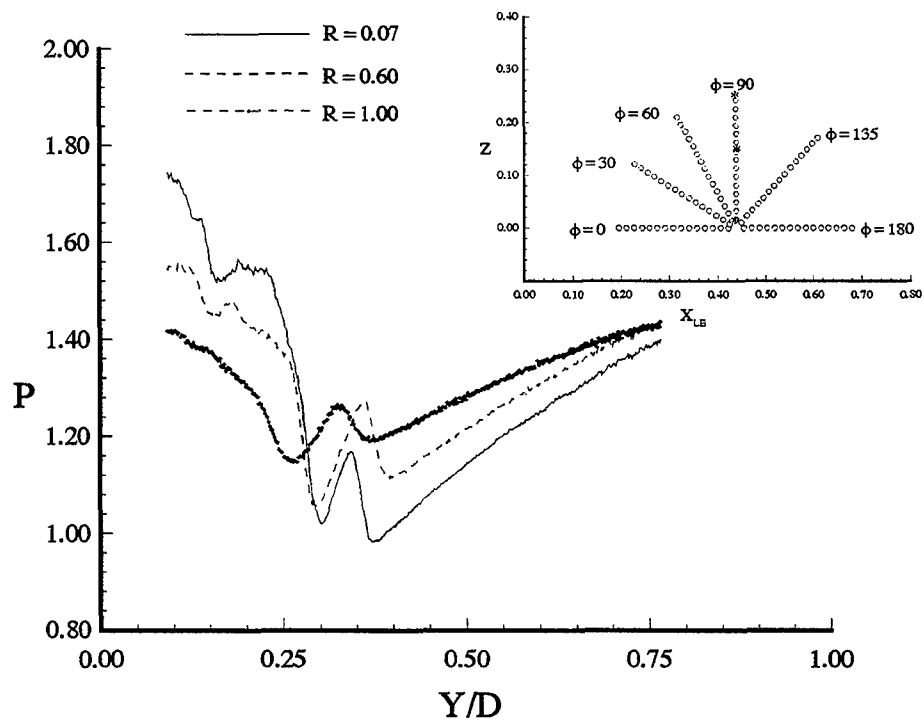
Figure 5.42. Dynamic closure with the 6.1° wedge and M=1.52 for R = 0.07, 0.60,and 1.00 ($\phi = 90°$)
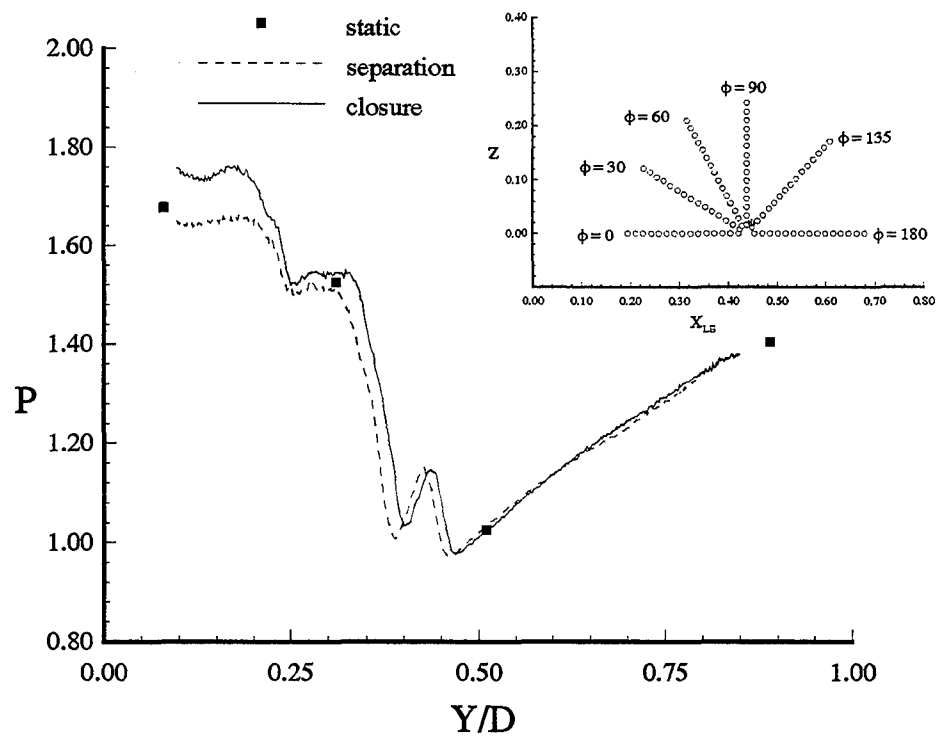
Figure 5.43. Separation events with the 6.1° wedge and M=1.52 (ϕ = 135, R = 0.07).
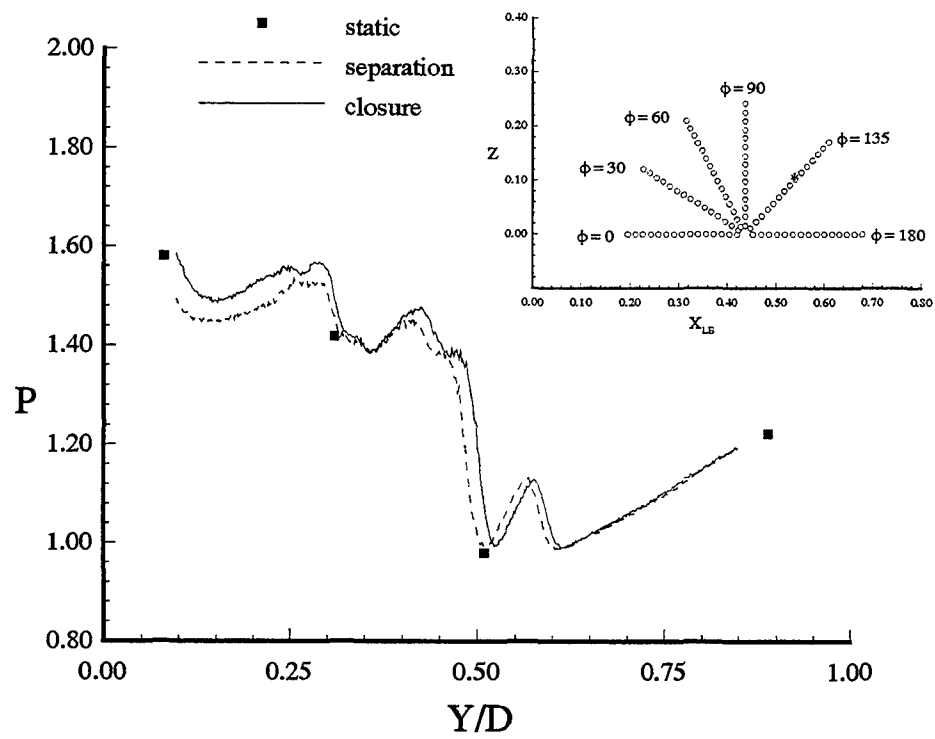
Figure 5.44. Separation events with the 6.1° wedge and M=1.52 (ϕ = 135, R = 0.60).
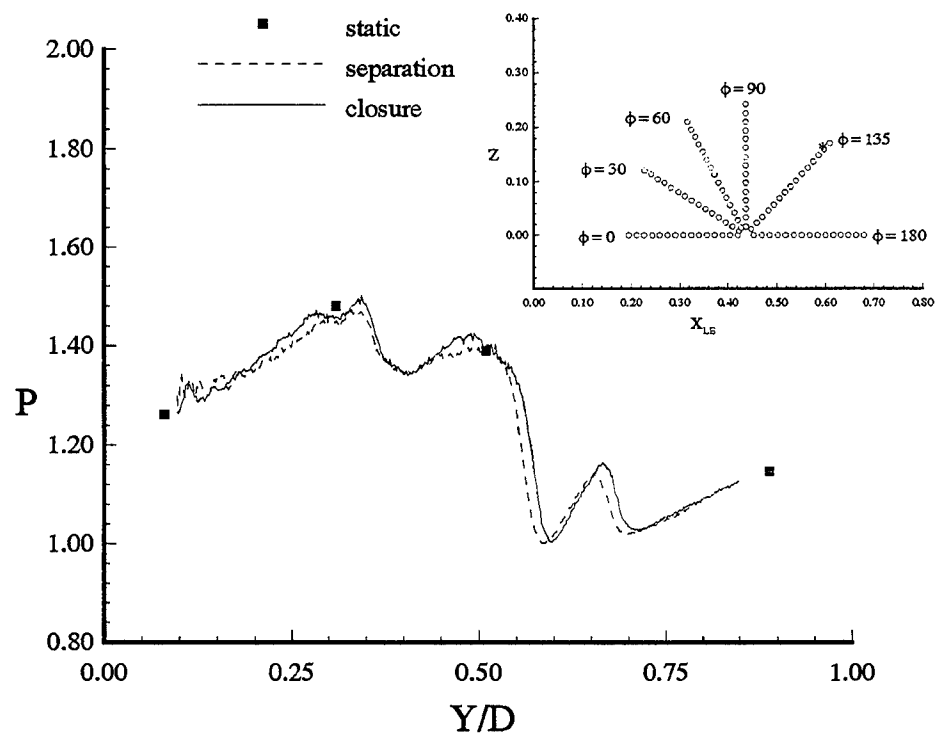
Figure 5.45. Separation events with the 6.1° wedge and M=1.52 (ϕ = 135, R = 0.93).
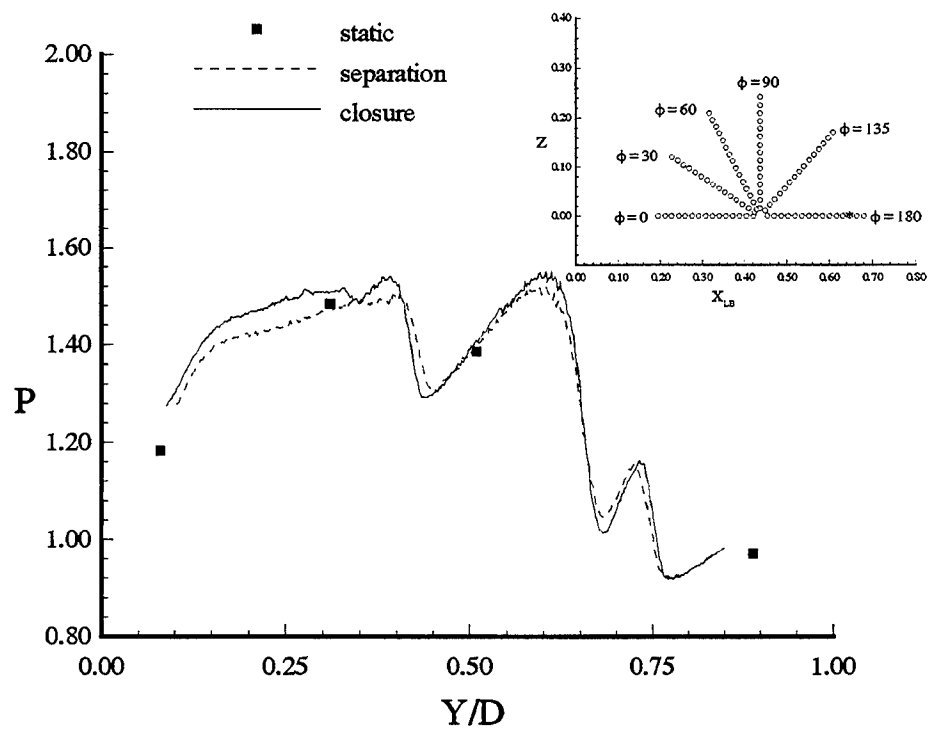
Figure 5.46. Separation events with the 6.1° wedge and M=1.52 (ϕ = 180, R = 0.87).
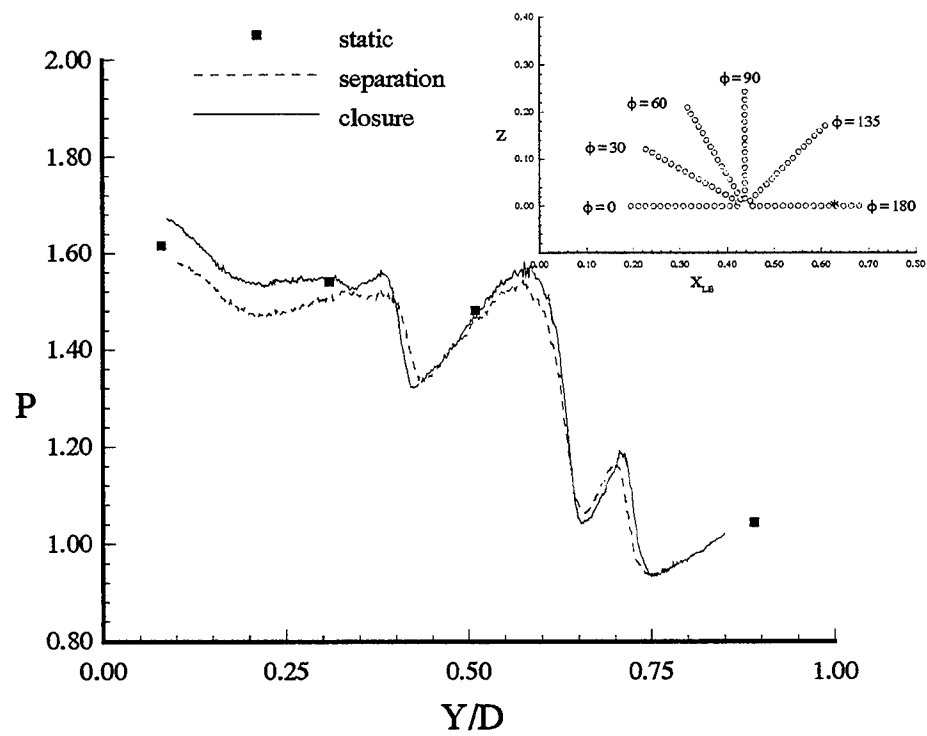
Figure 5.47. Separation events with the 6.1° wedge and M=1.52 (ϕ = 180, R = 0.80).
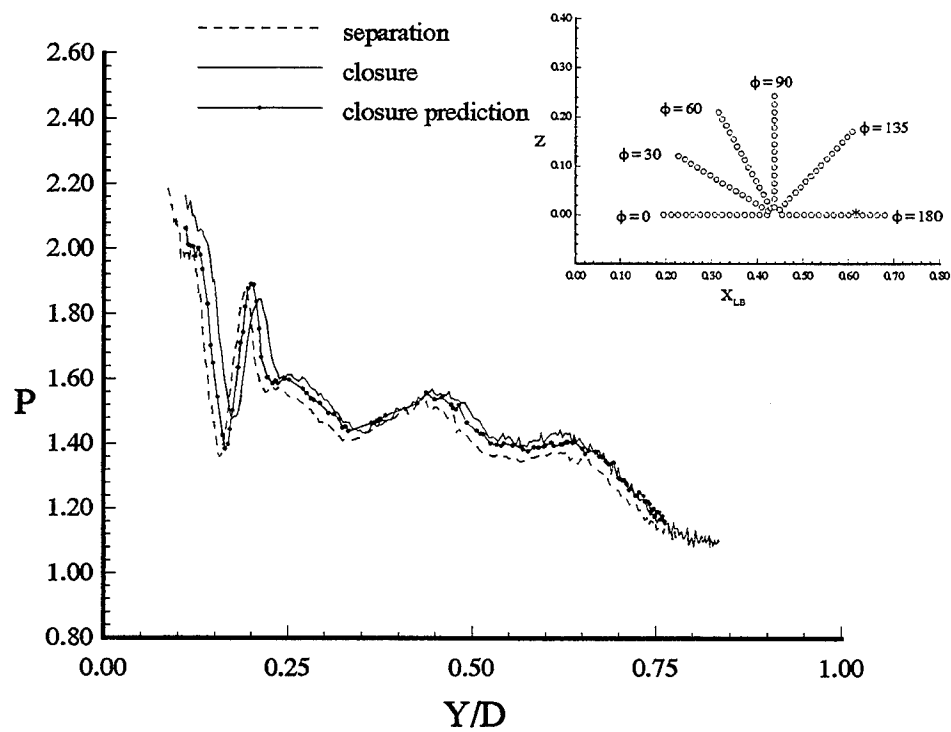
Figure 5.48. Separation events with the 6.1° wedge and M=1.9 (ϕ = 180, R = 0.73).
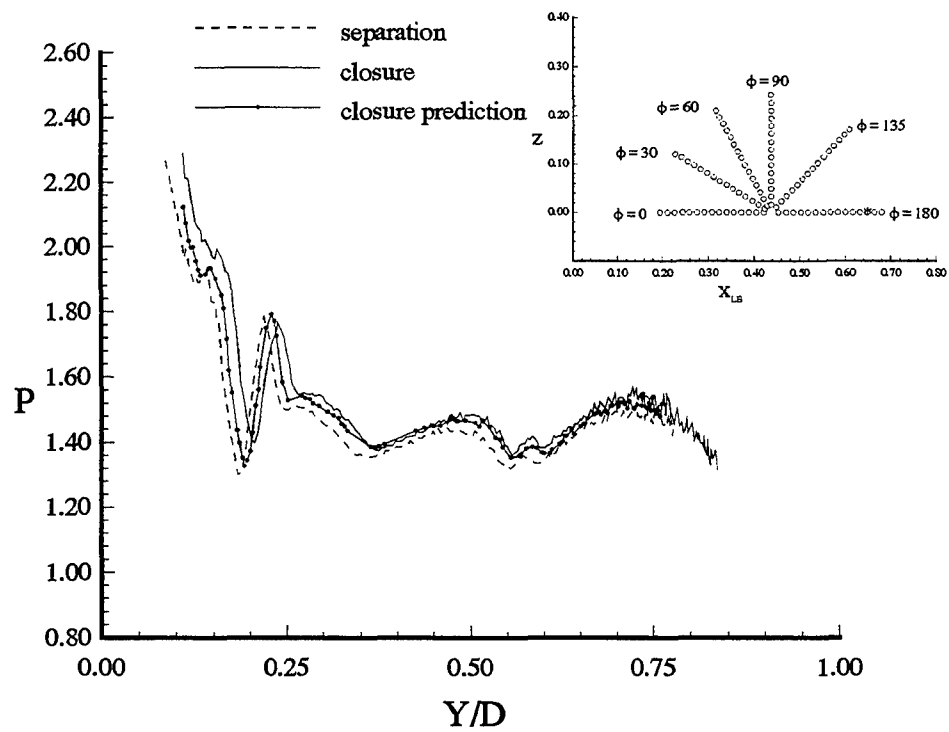
Figure 5.49. Separation events with the 6.1° wedge and M=1.9 (ϕ = 180, R = 0.87).
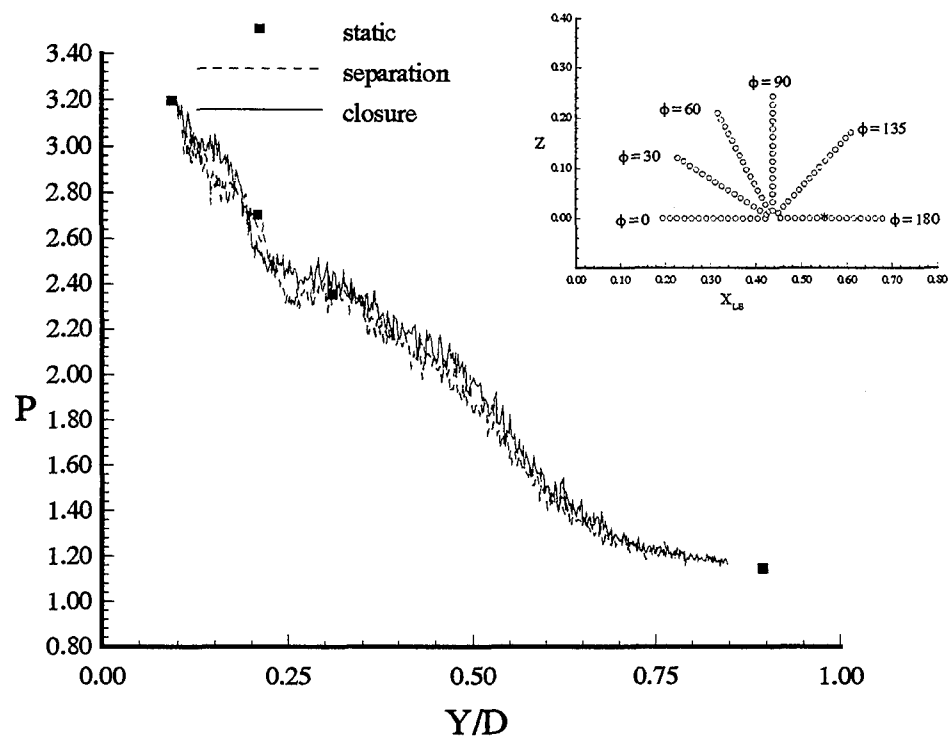
Figure 5.50. Separation with 12° wedge at M=1.9 (ϕ = 180, R = 0.47).
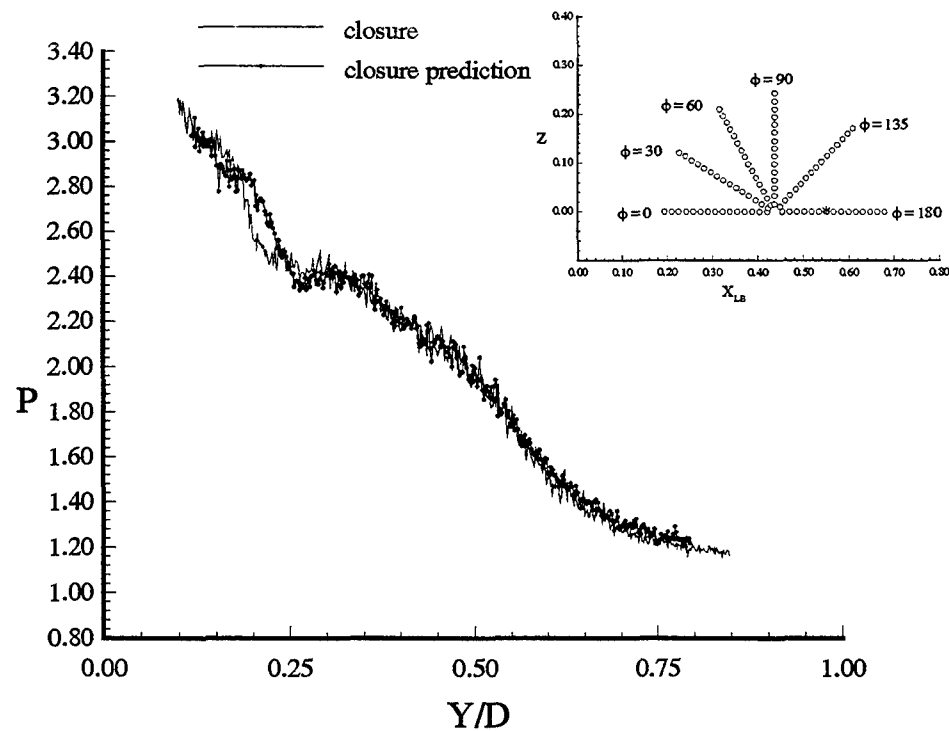
Figure 5.51. Closure prediction with 12° wedge at M=1.9 (ϕ = 180, R = 0.47).
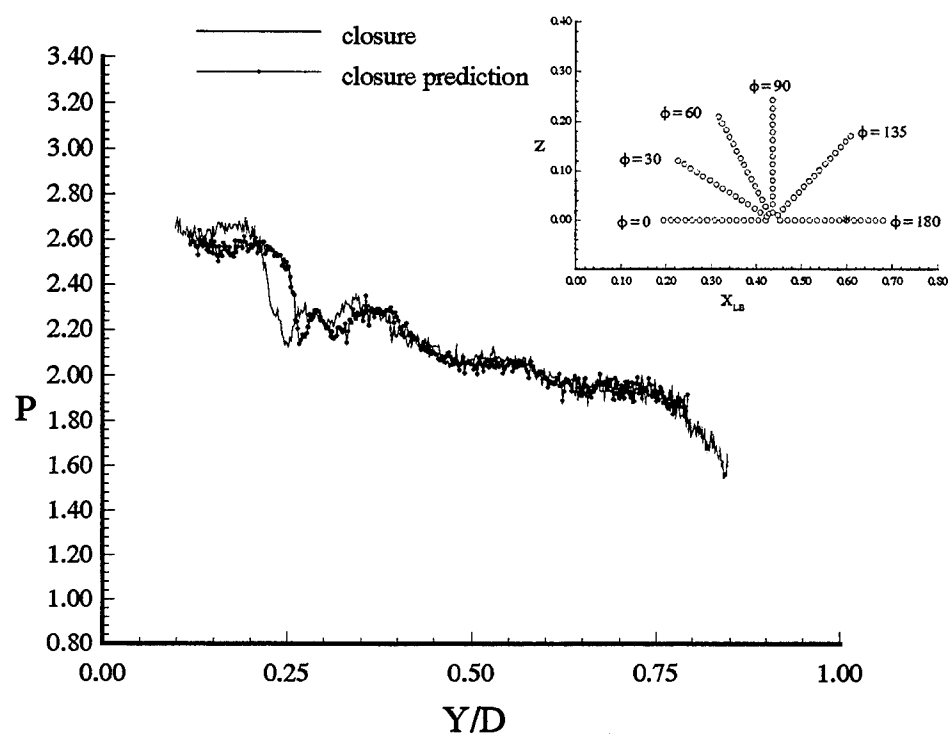
Figure 5.52. Closure prediction with 12° wedge at M=1.9 (ϕ = 180, R = 0.67).
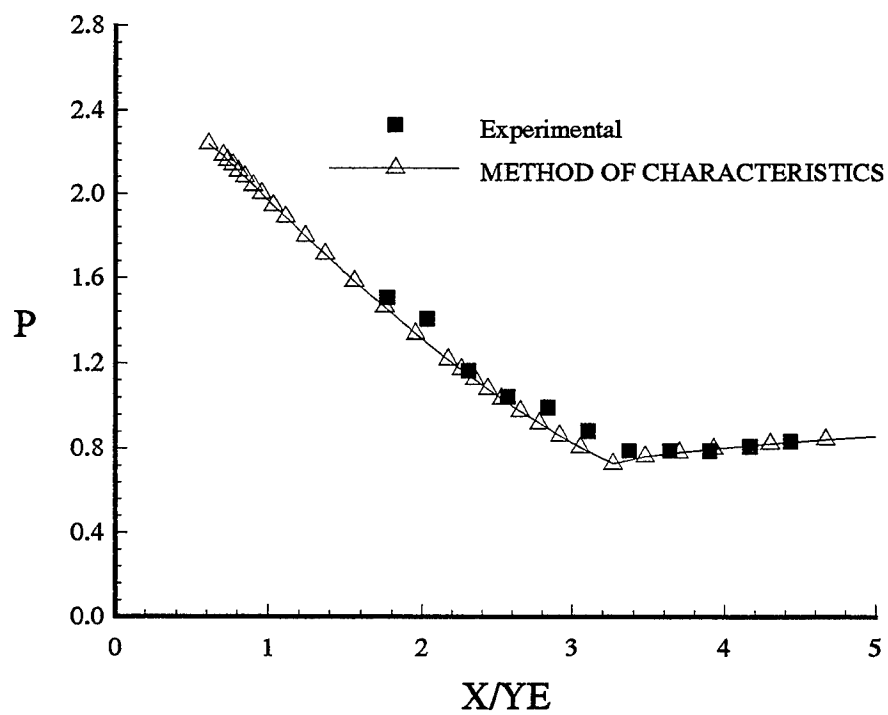
Figure 5.53. Isolated ogive surface pressure predicted by method of characteristics, M=1.9.
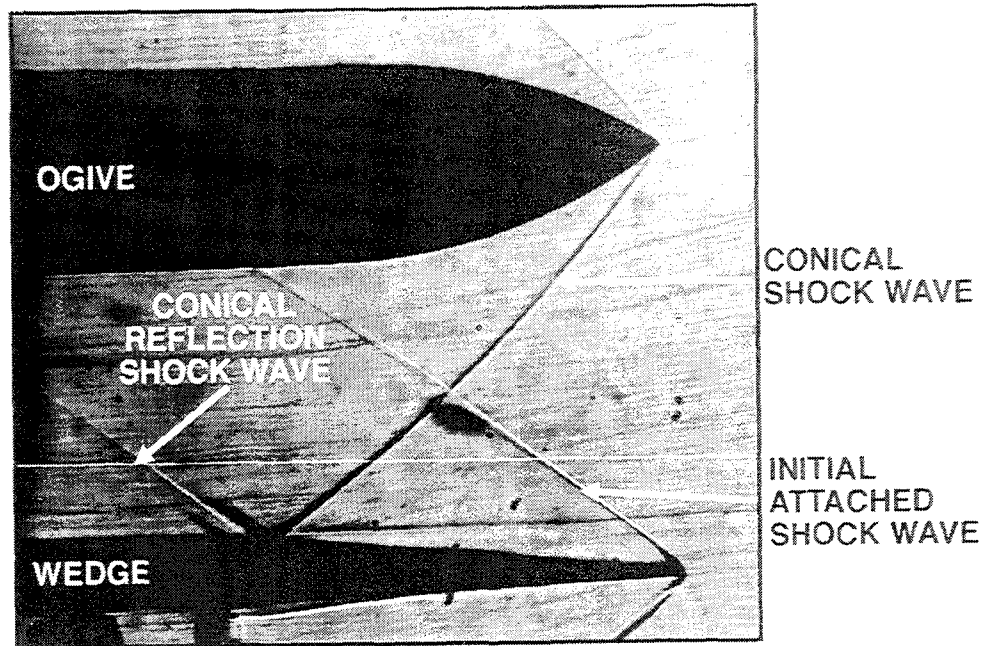
Figure 5.54. Schlieren photograph of ogive and 6.1° wedge at Y/D=0.89, M=1.9.
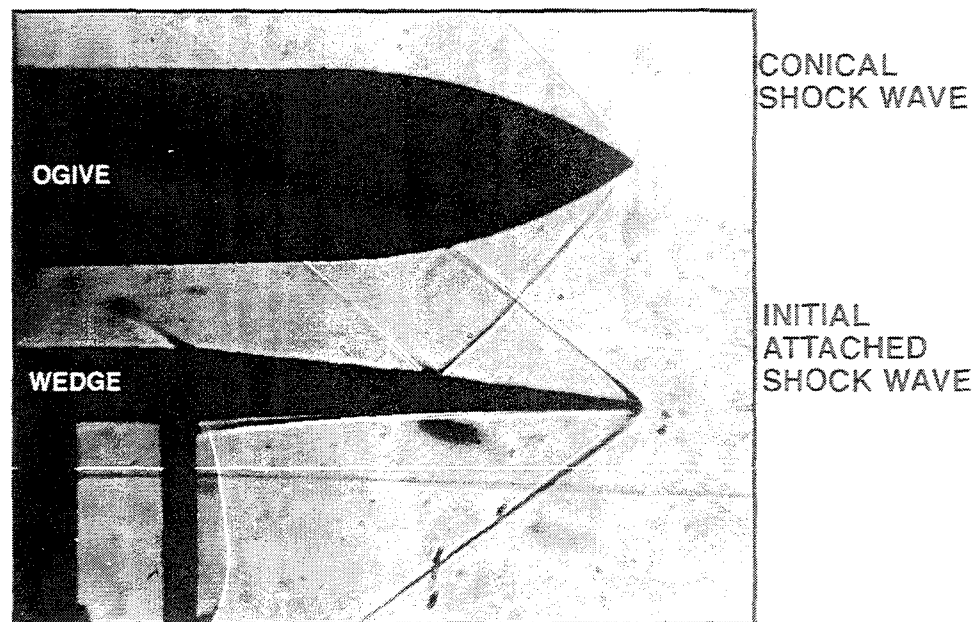
Figure 5.55. Schlieren photograph of ogive and 6.1° wedge at Y/D=0.31, M=1.9.
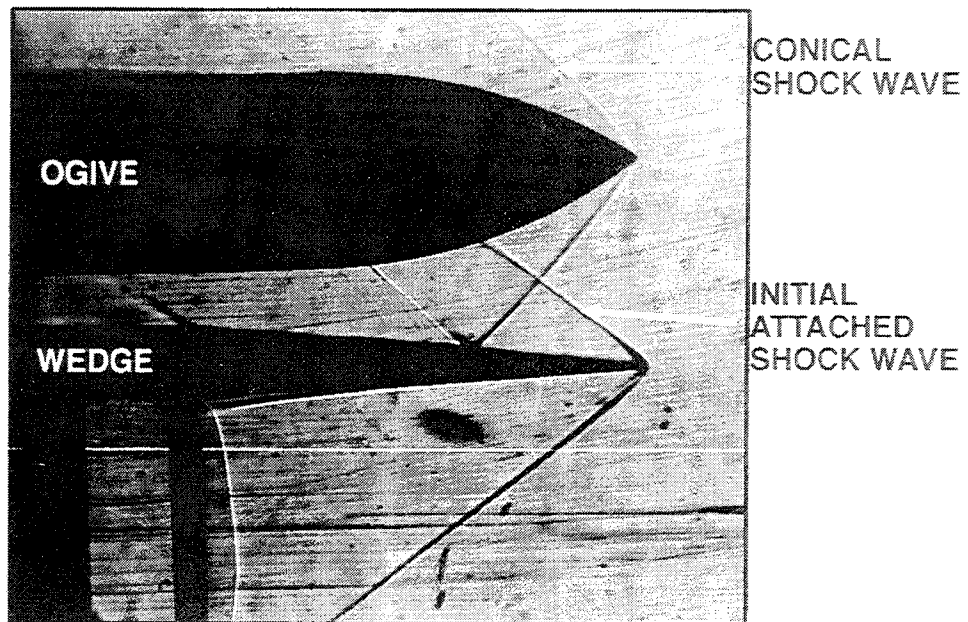
Figure 5.56. Schlieren photograph of ogive and 6.1° wedge at Y/D=0.21, M=1.9.
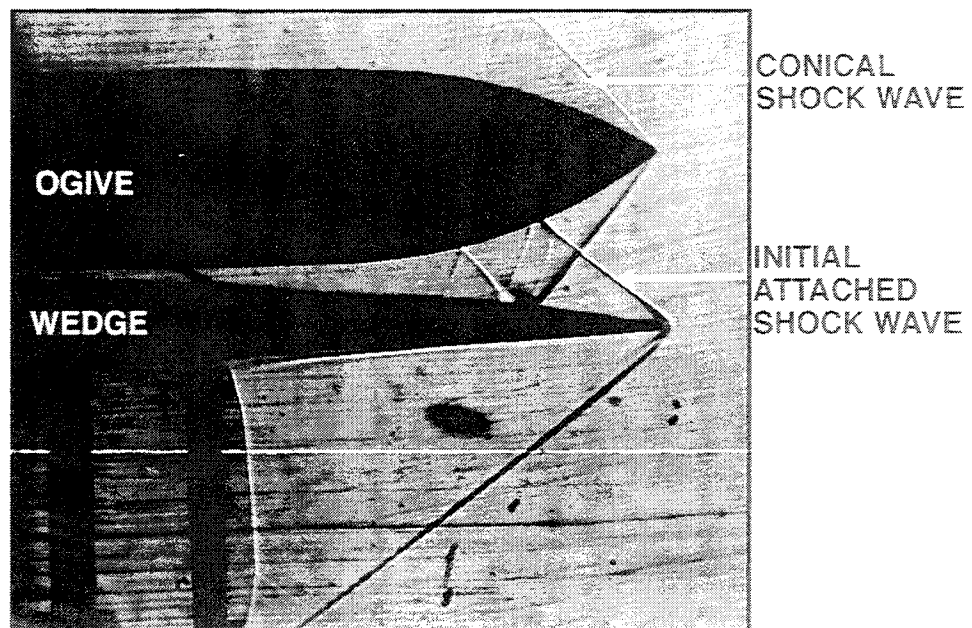
Figure 5.57. Schlieren photograph of ogive and 6.1° wedge at Y/D=0.08, M=1.9.
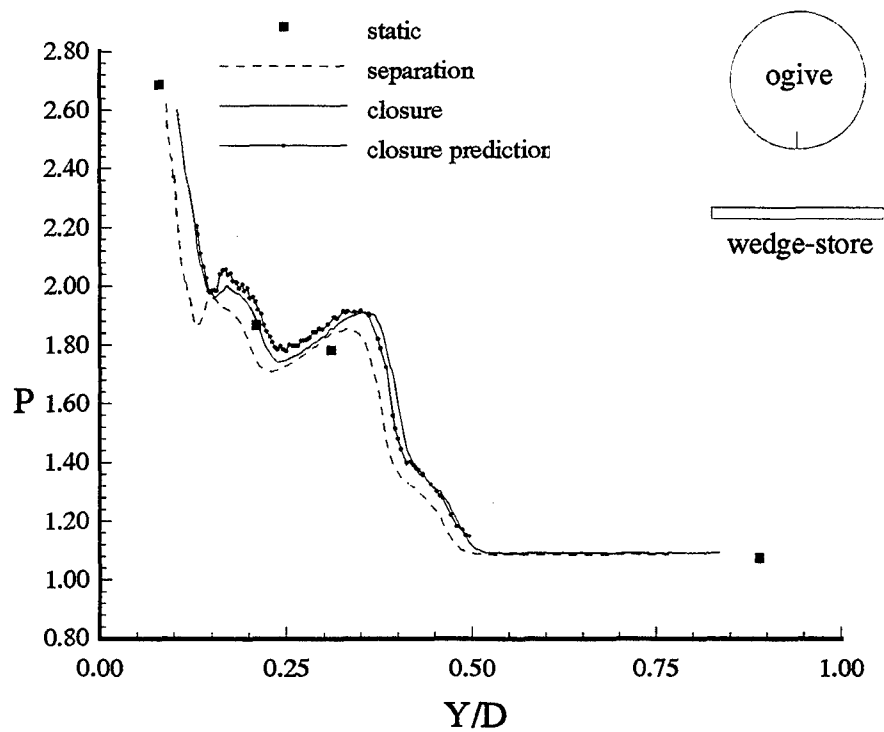
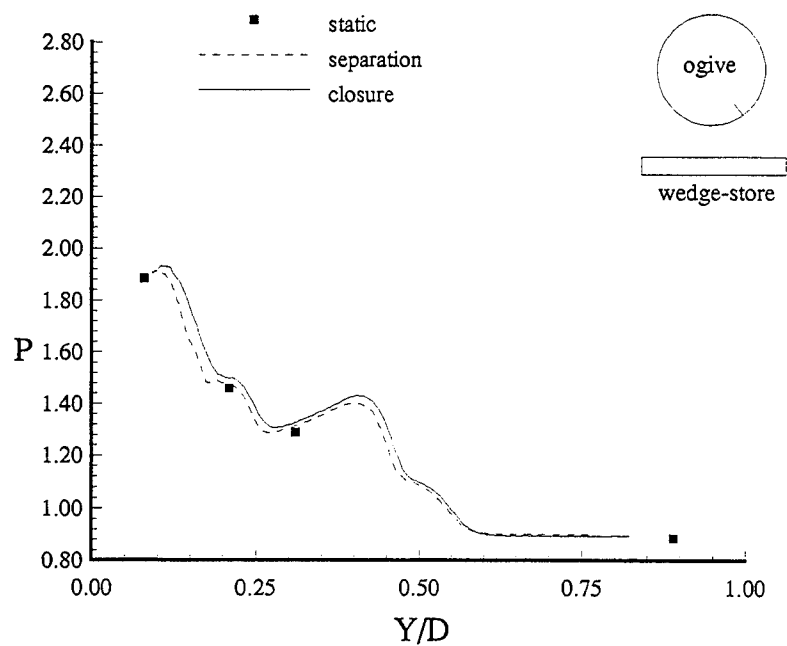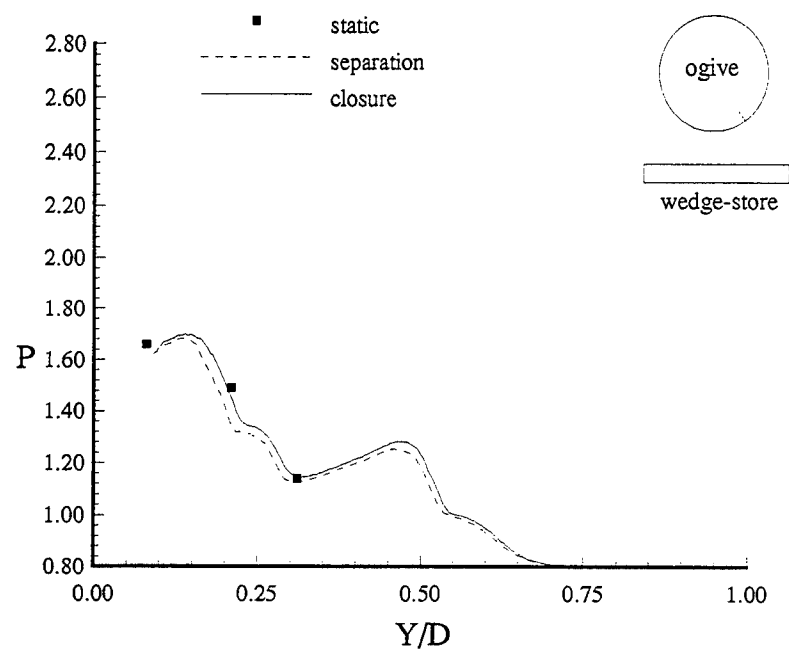Figure 5.58. Ogive surface pressure at X/YE=2.57 and $\psi = 0°$ (6.1° wedge-store, M = 1.9).
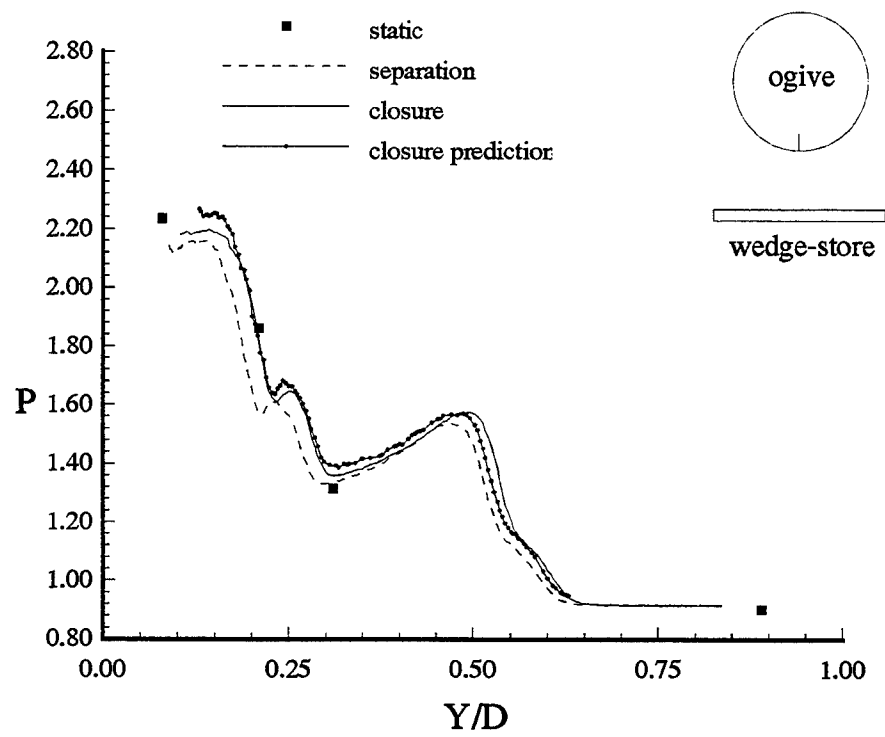
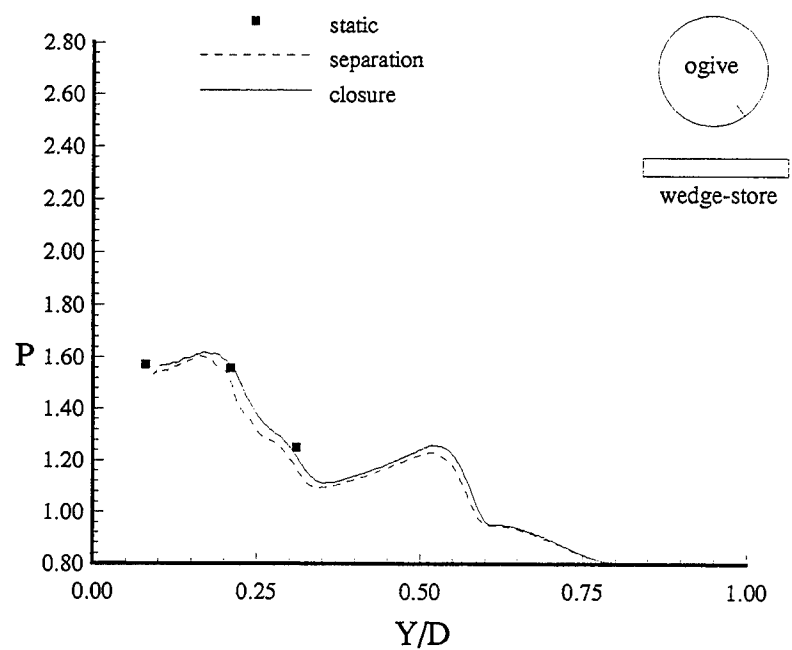Figure 5.59. Ogive surface pressure at X/YE=3.10 and $\psi = 0°$ (6.1° wedge-store, M = 1.9).
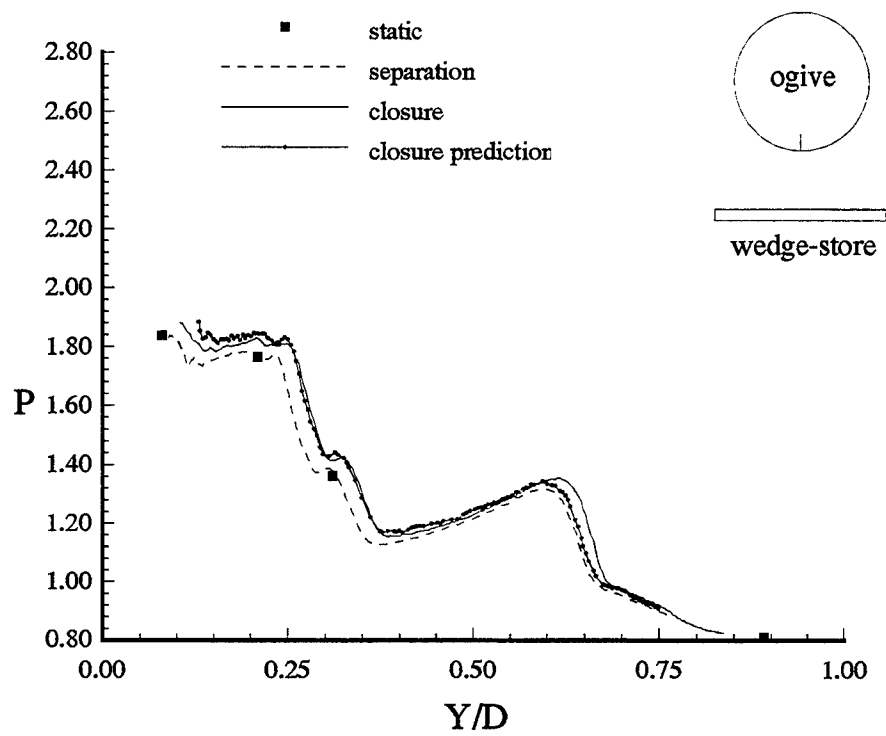
Figure 5.60.   Ogive surface pressure at X/YE=3.64 and $\psi = 0°$ (6.1° wedge-store, M = 1.9).
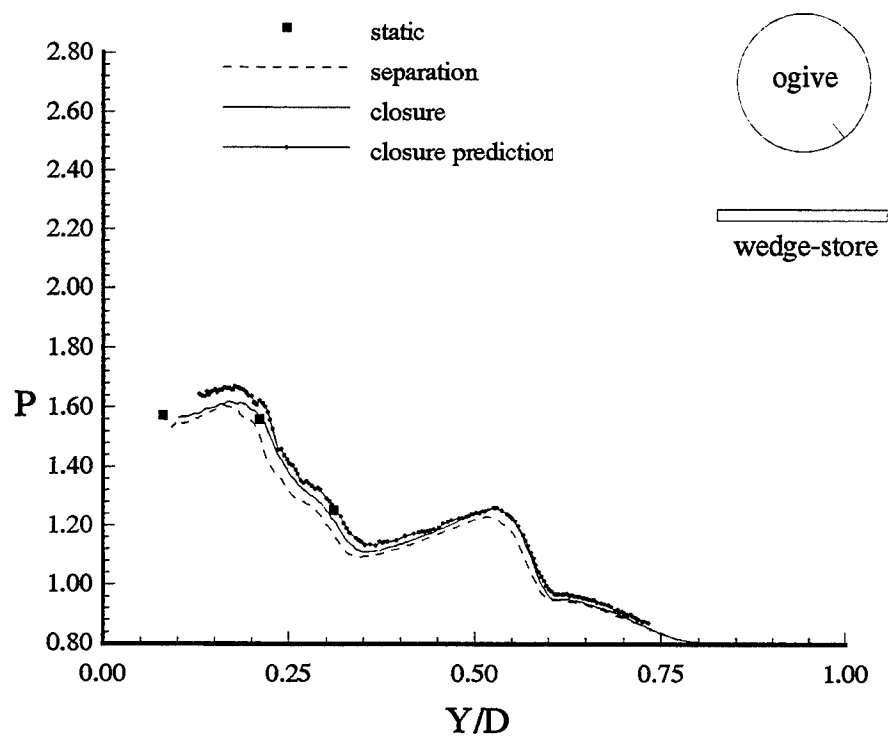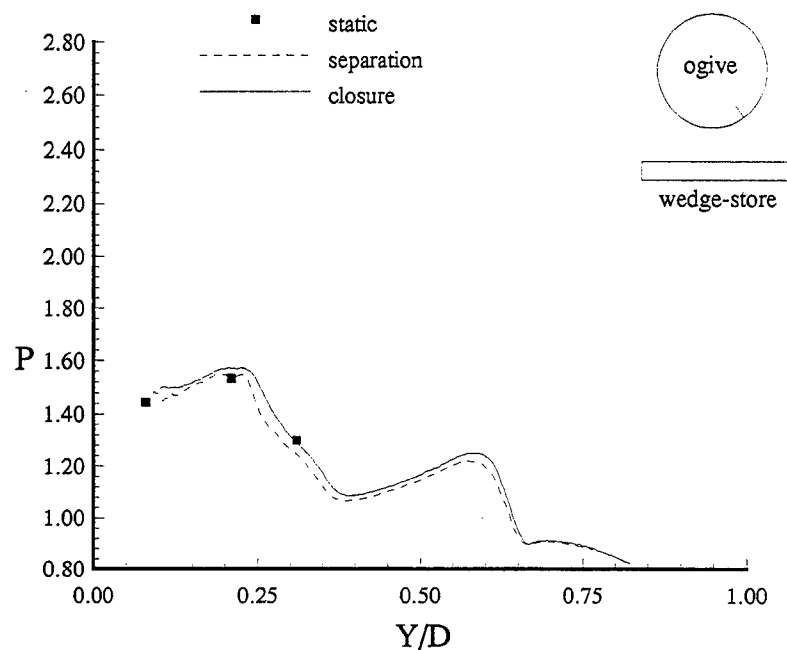
Figure 5.61. Ogive surface pressure at X/YE=3.64 and $\psi = 30°$ (6.1° wedge-store, M = 1.9).
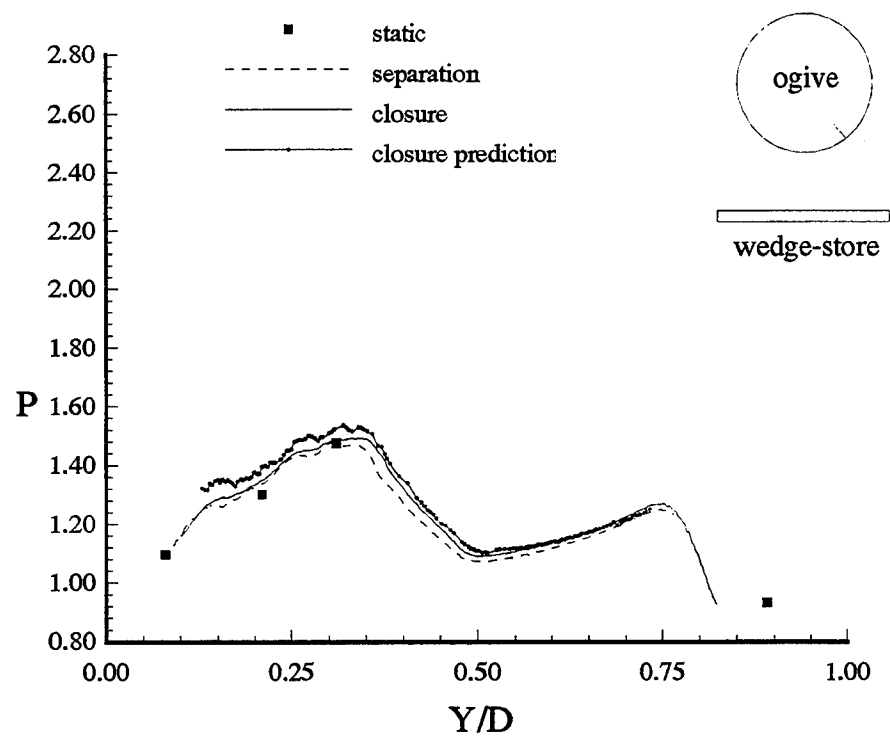
Figure 5.62. Ogive surface pressure at X/YE=4.70 and $\psi = 30°$ (6.1° wedge-store, M = 1.9).
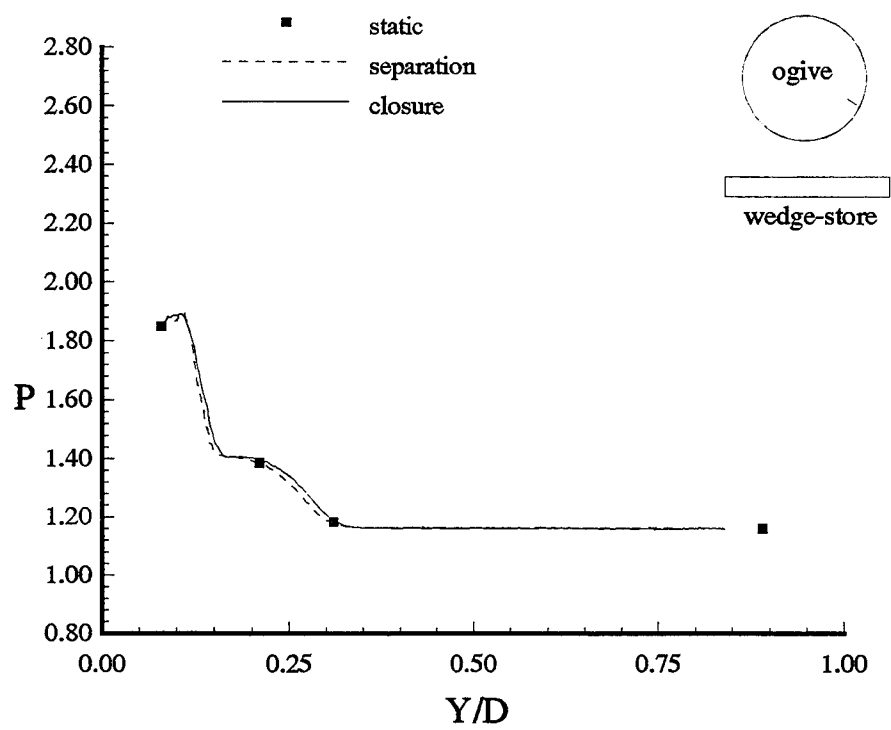
Figure 5.63. Ogive surface pressure at X/YE=2.31 and $\psi = 60°$ (6.1° wedge-store, M = 1.9).
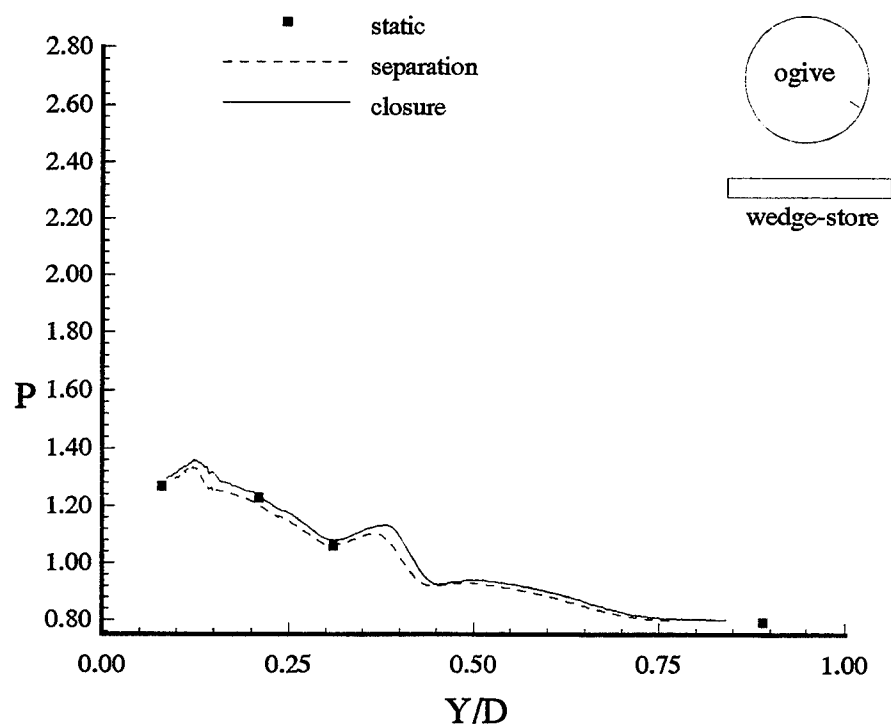
Figure 5.64.   Ogive surface pressure at X/YE=3.64 and $\psi = 60°$ (6.1° wedge-store, M = 1.9).
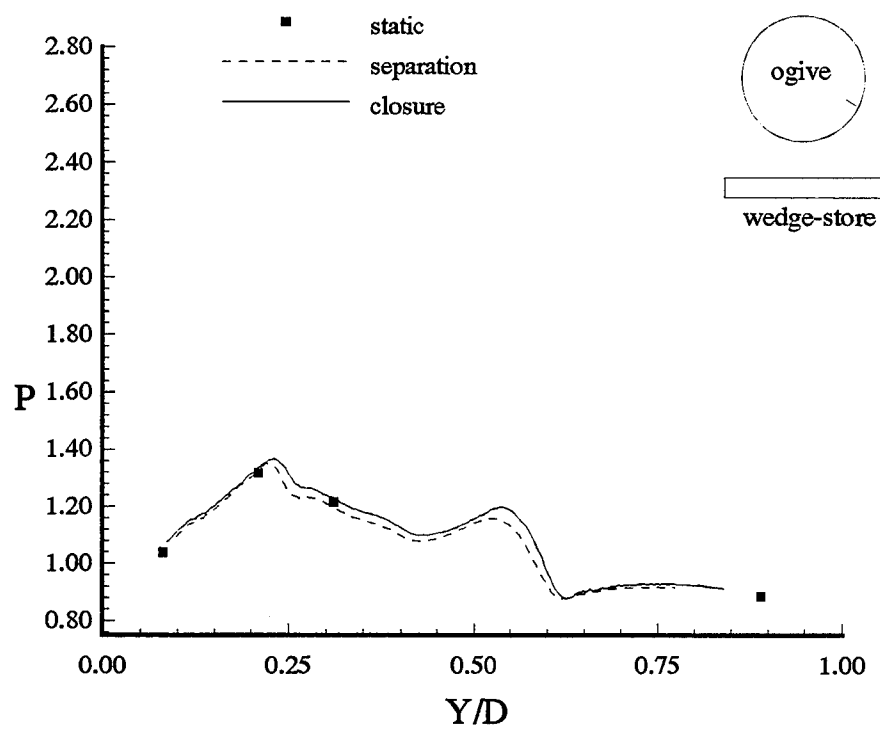
Figure 5.65. Ogive surface pressure at X/YE=4.43 and $\psi = 60°$ (6.1° wedge-store, M = 1.9).
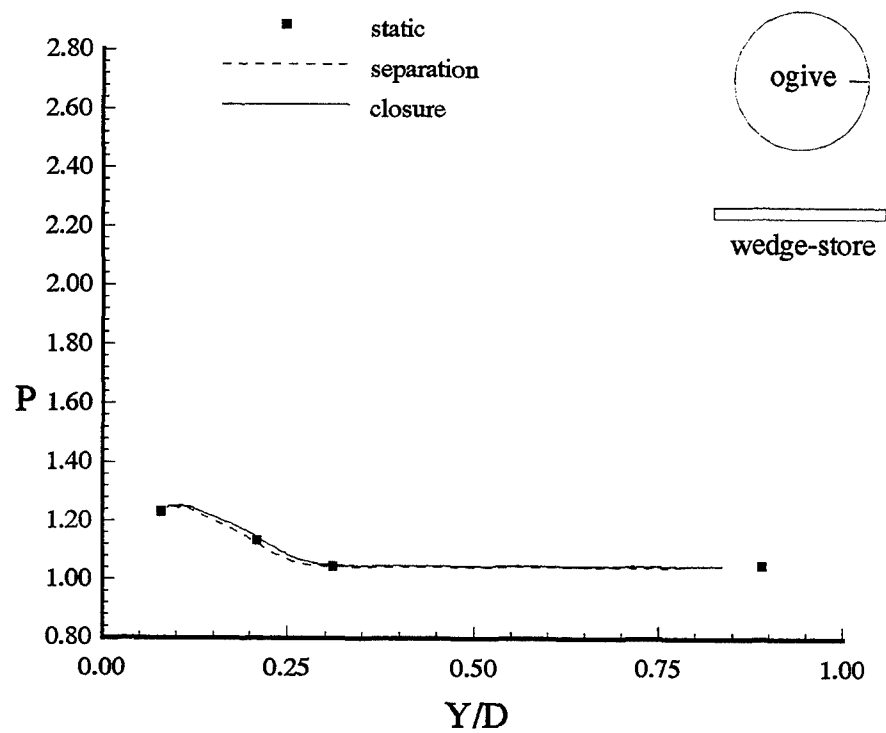
Figure 5.66. Ogive surface pressure at X/YE=2.57 and $\psi = 90°$ (6.1° wedge-store, M = 1.9).
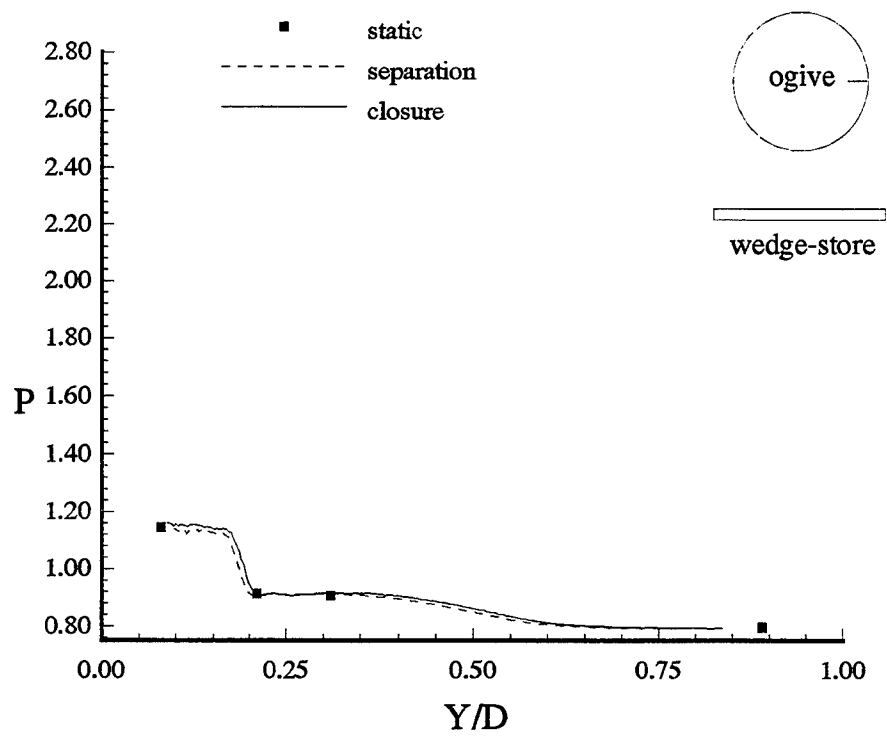
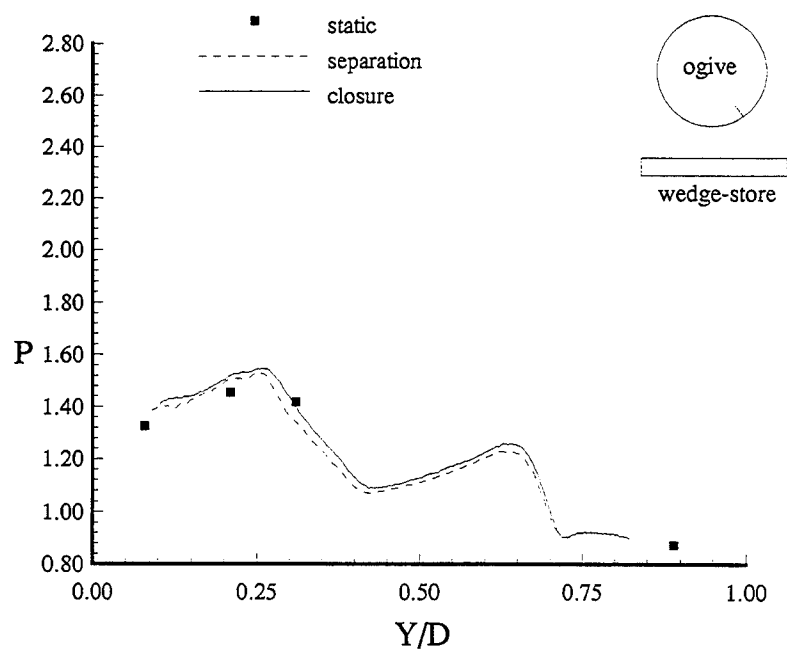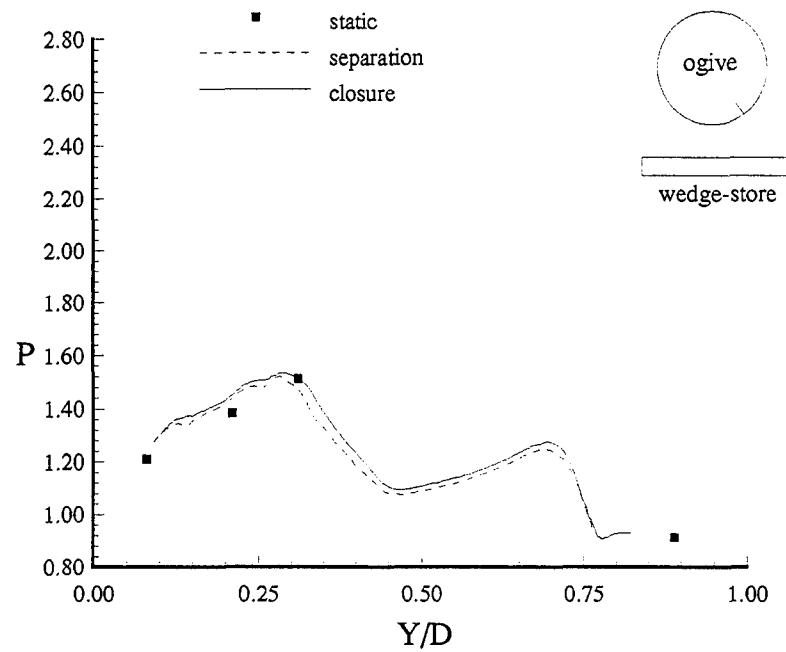Figure 5.67.   Ogive surface pressure at X/YE=3.64 and $\psi = 90°$ (6.1° wedge-store, M = 1.9).
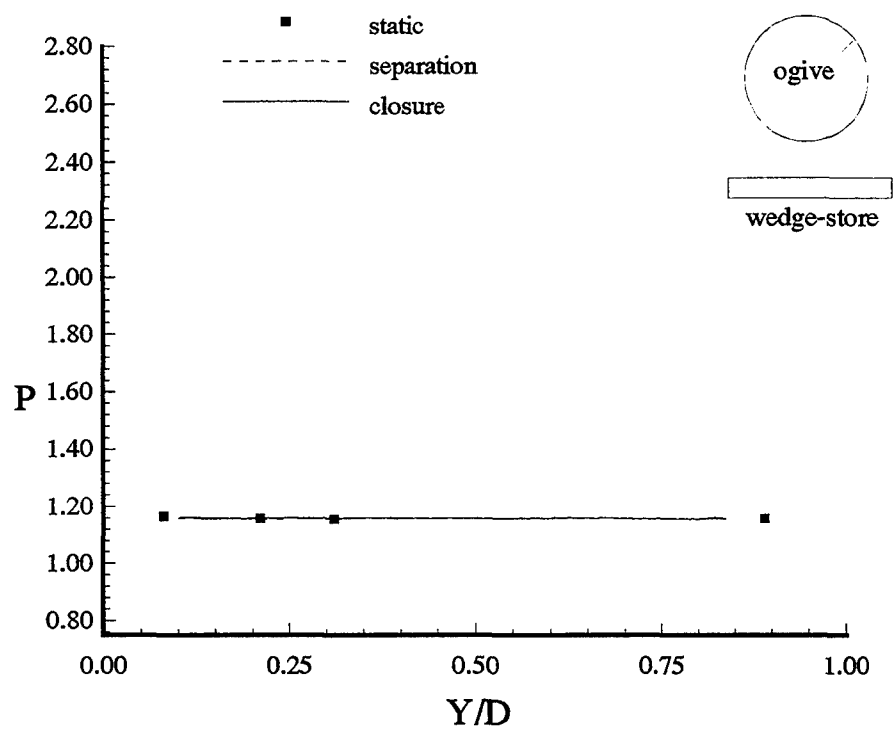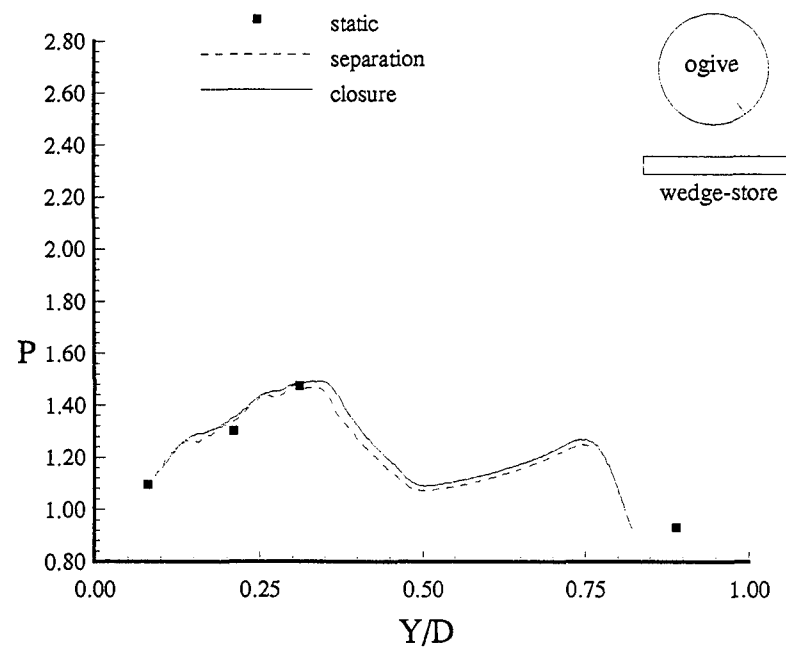
Figure 5.68. Ogive surface pressure at X/YE=2.57 and $\psi = 135°$ (6.1° wedge-store, M = 1.9).
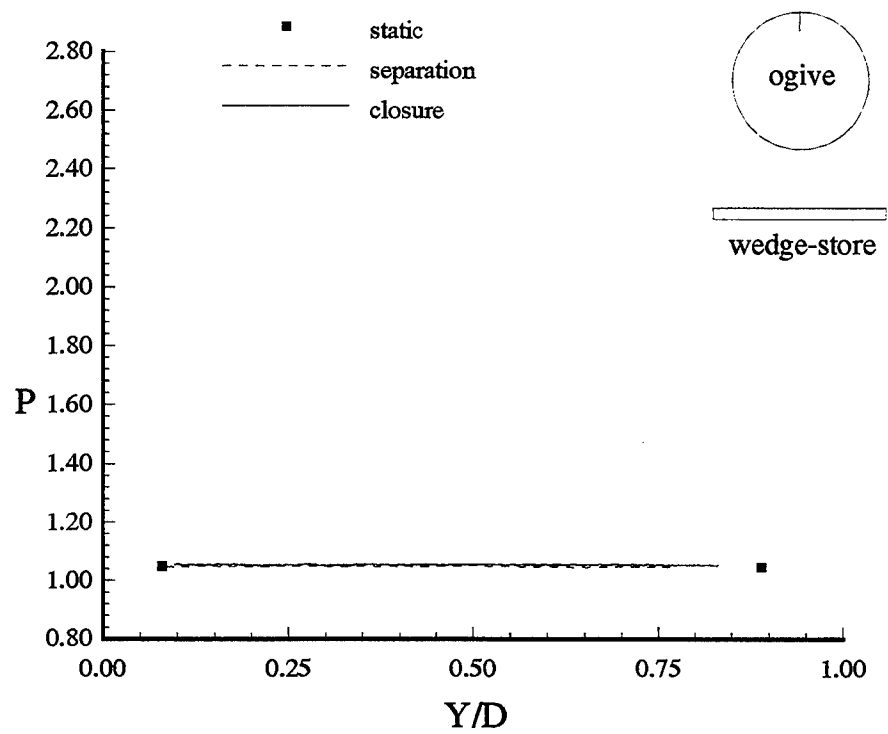
Figure 5.69. Ogive surface pressure at X/YE=2.57 and $\psi = 180°$ (6.1° wedge-store, M = 1.9).
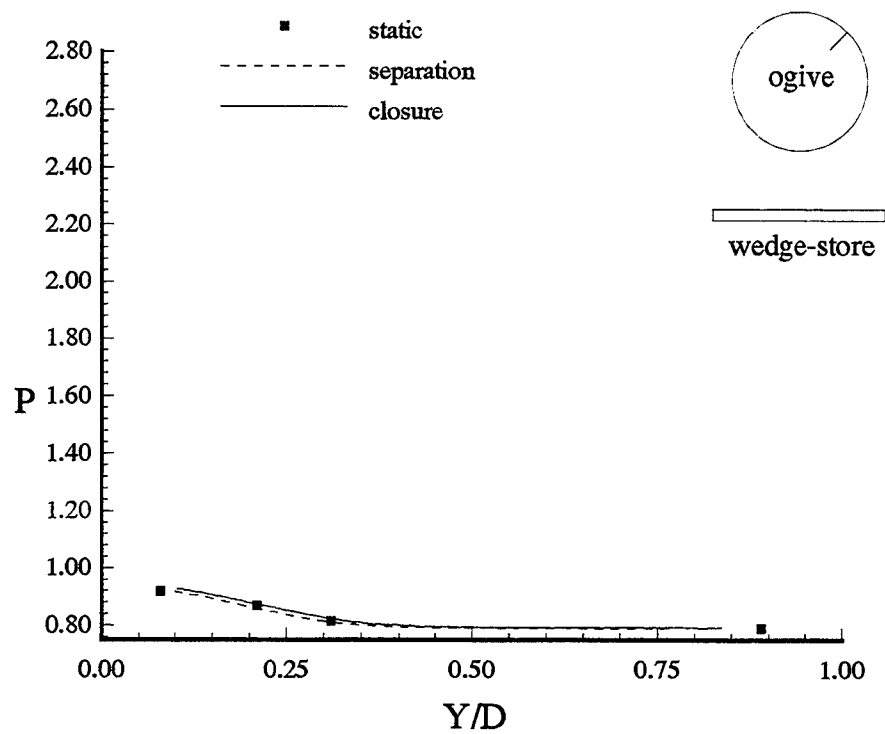
Figure 5.70.   Ogive surface pressure at X/YE=3.64 and $\psi = 135°$ (6.1° wedge-store, M = 1.9).
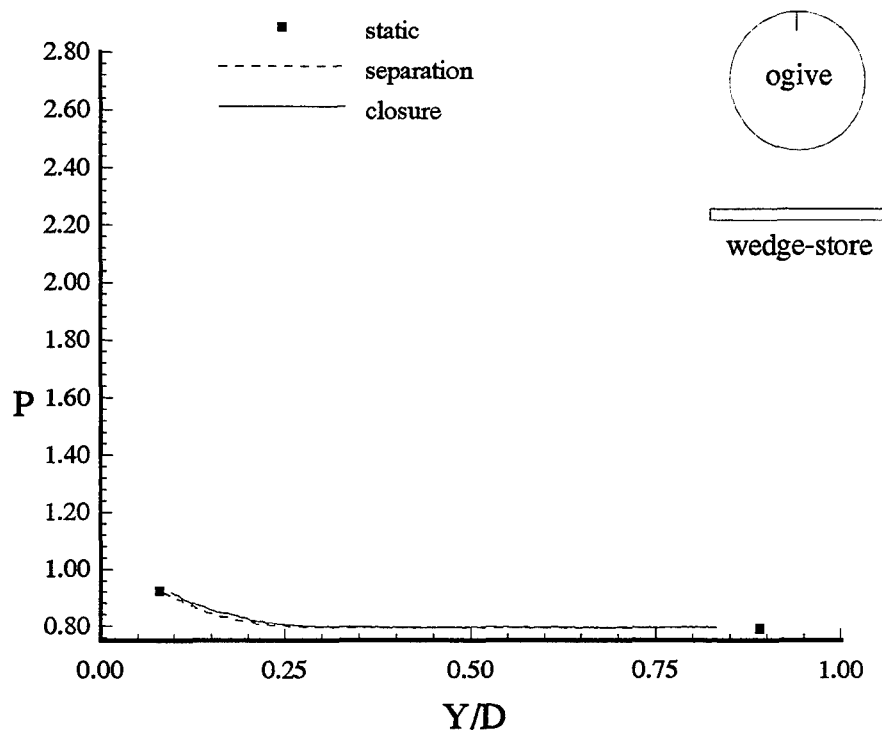
Figure 5.71. Ogive surface pressure at X/YE=3.64 and $\psi = 180°$ (6.1° wedge-store, M = 1.9).
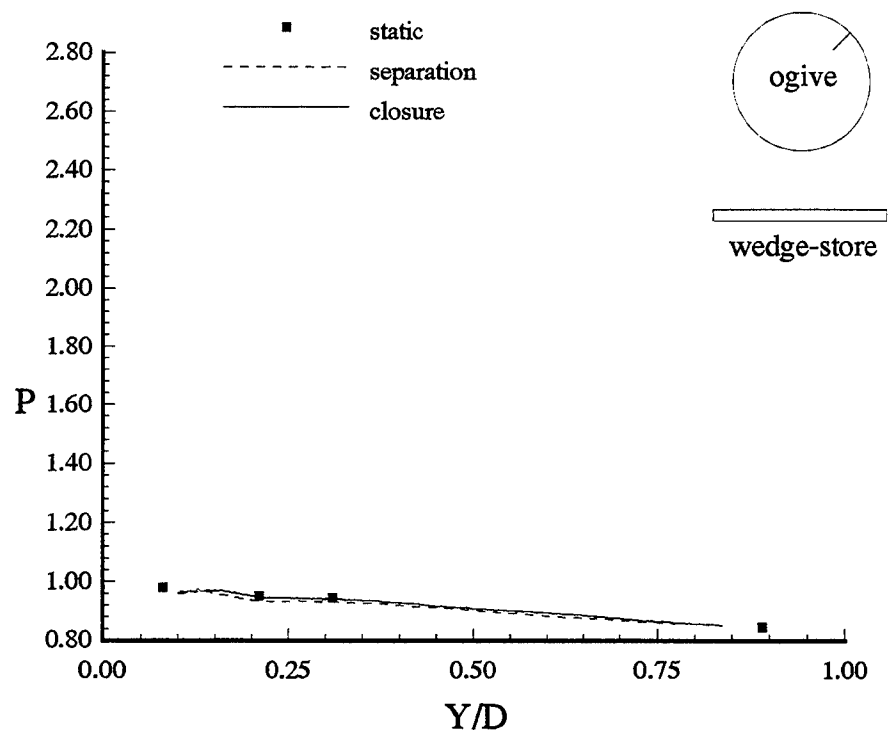
Figure 5.72. Ogive surface pressure at X/YE=4.70 and $\psi = 135°$ (6.1° wedge-store, M = 1.9).
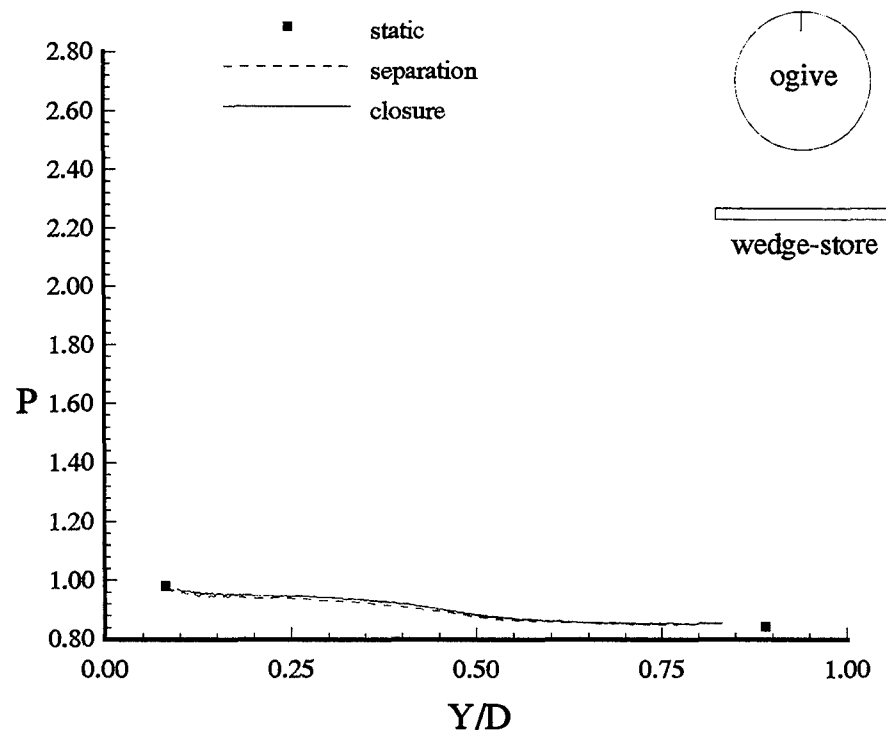
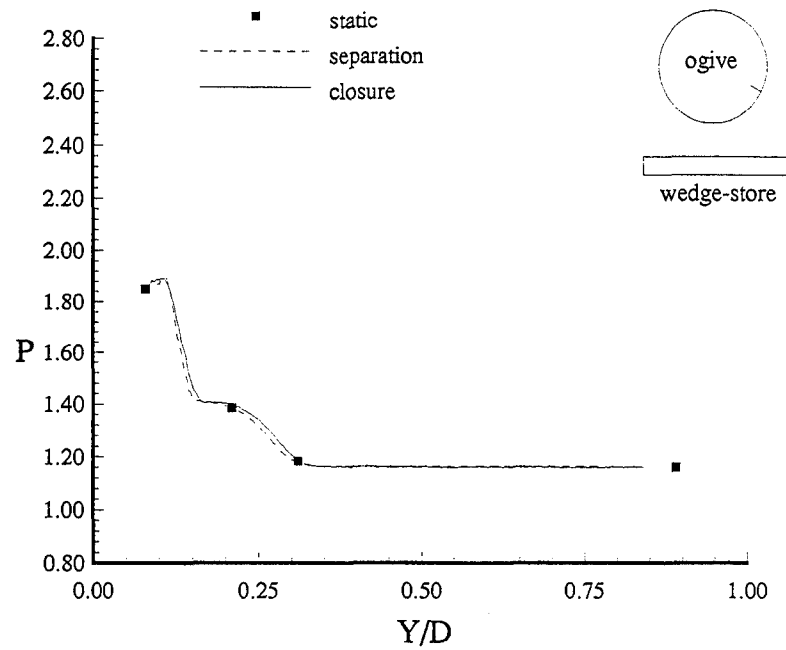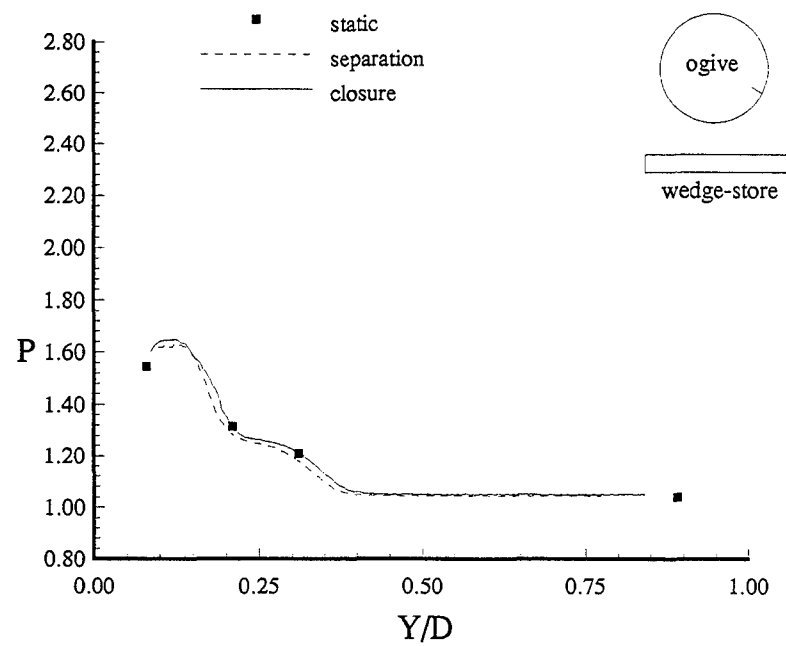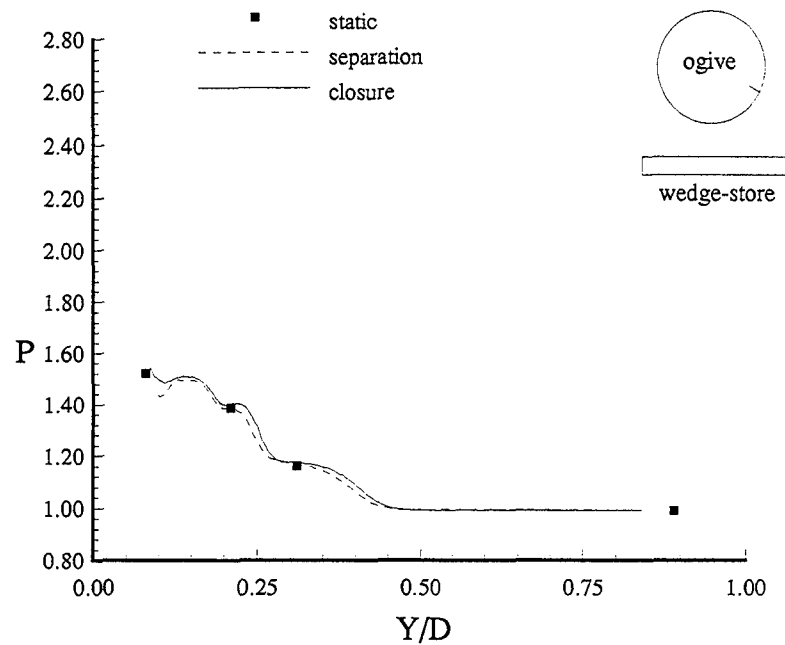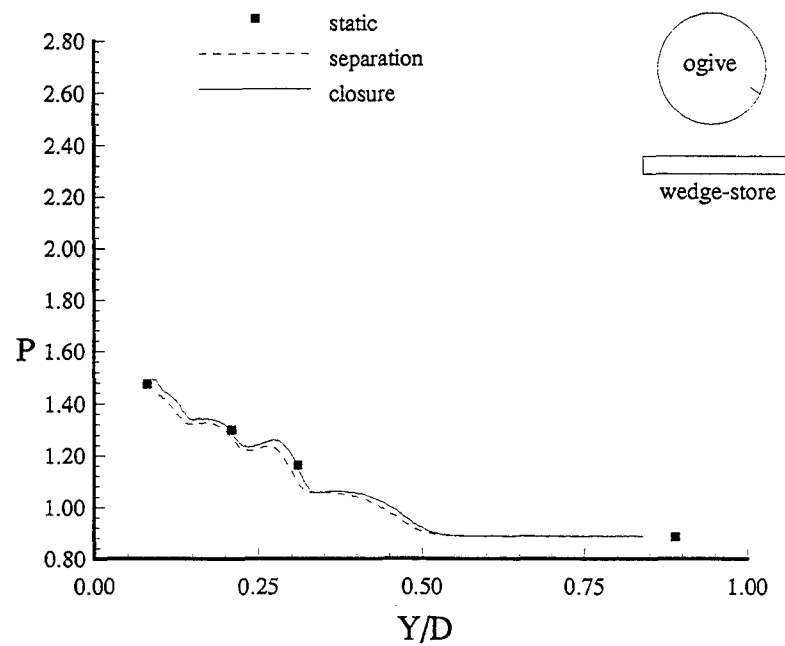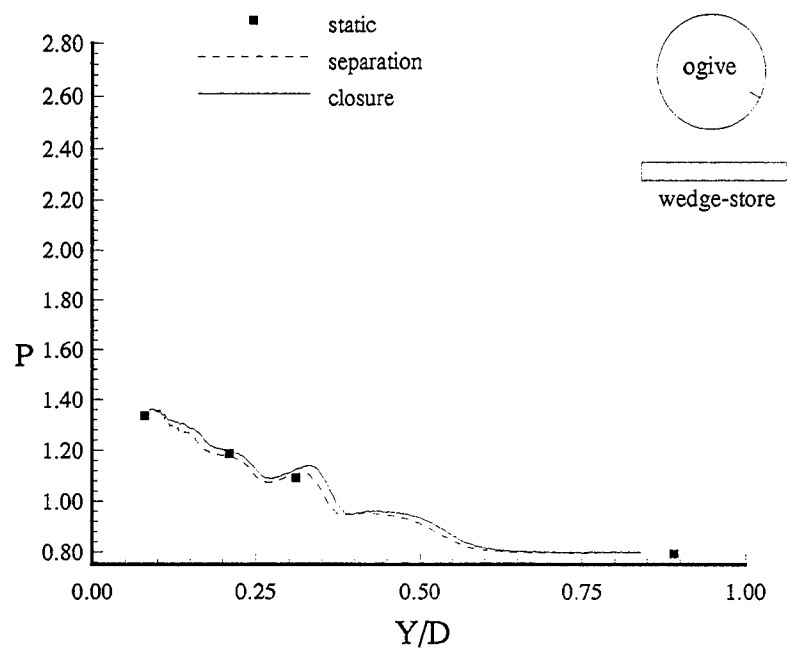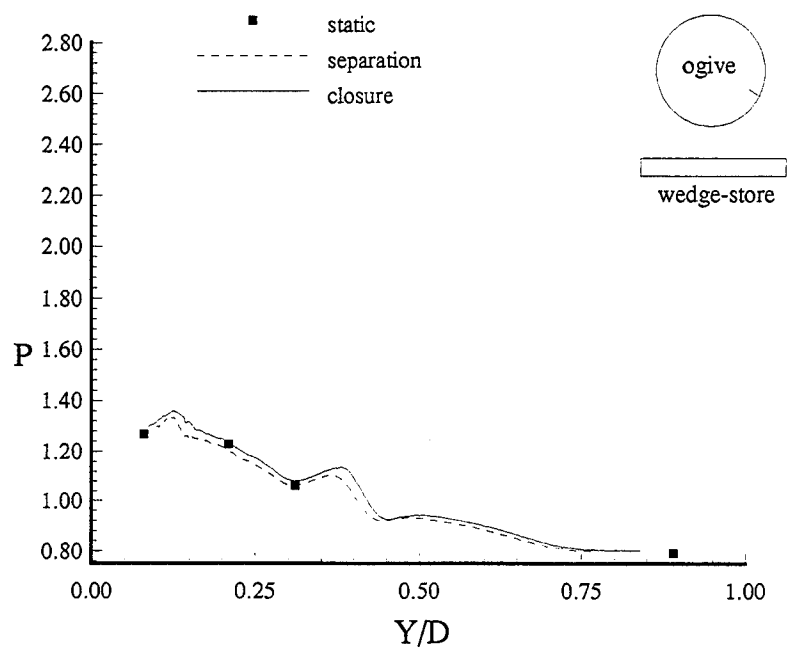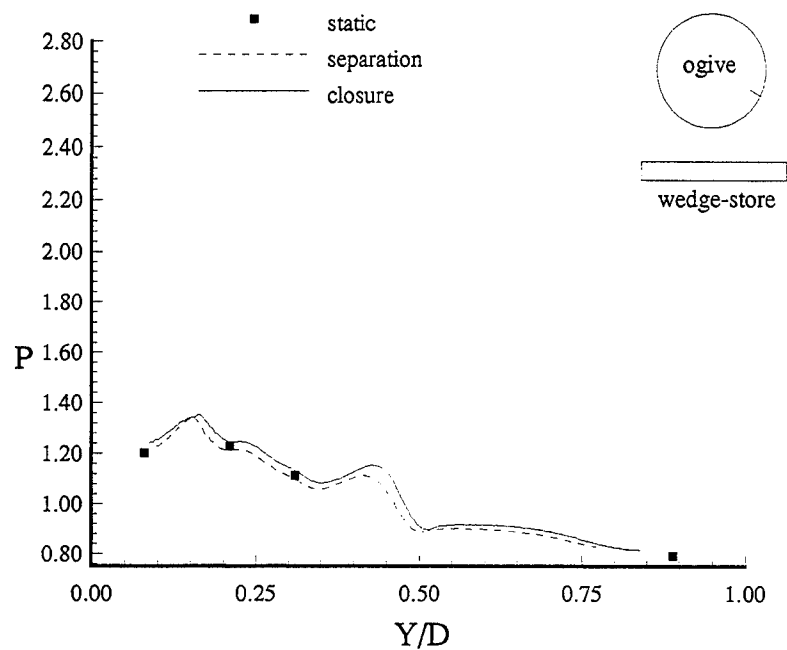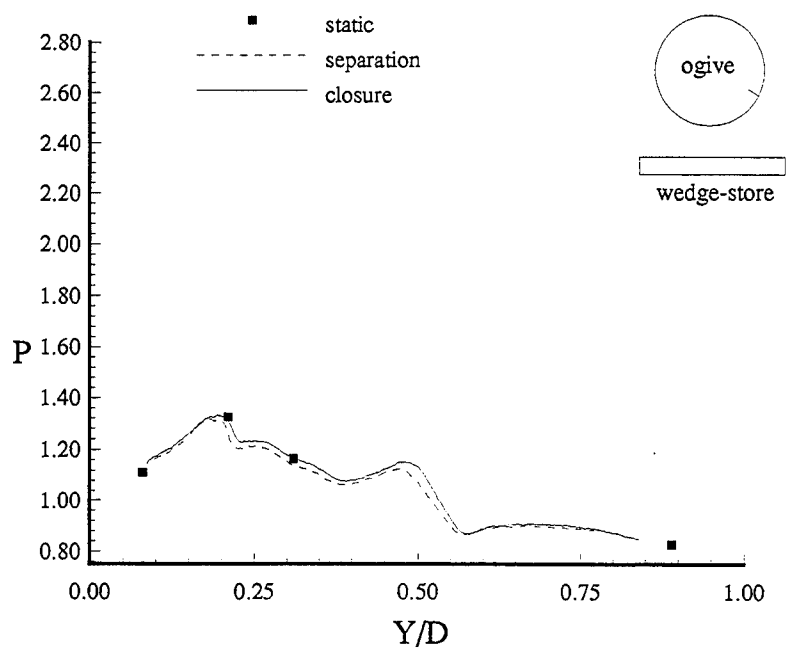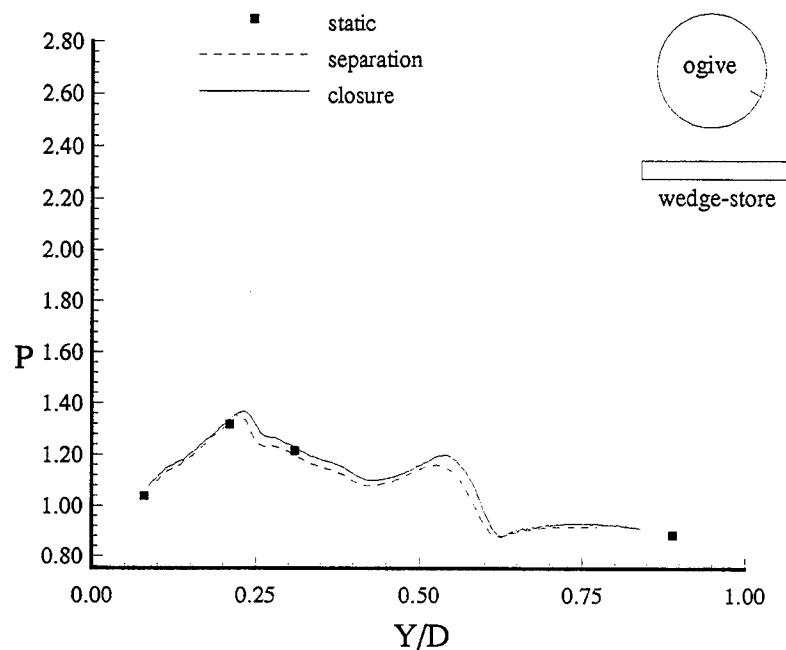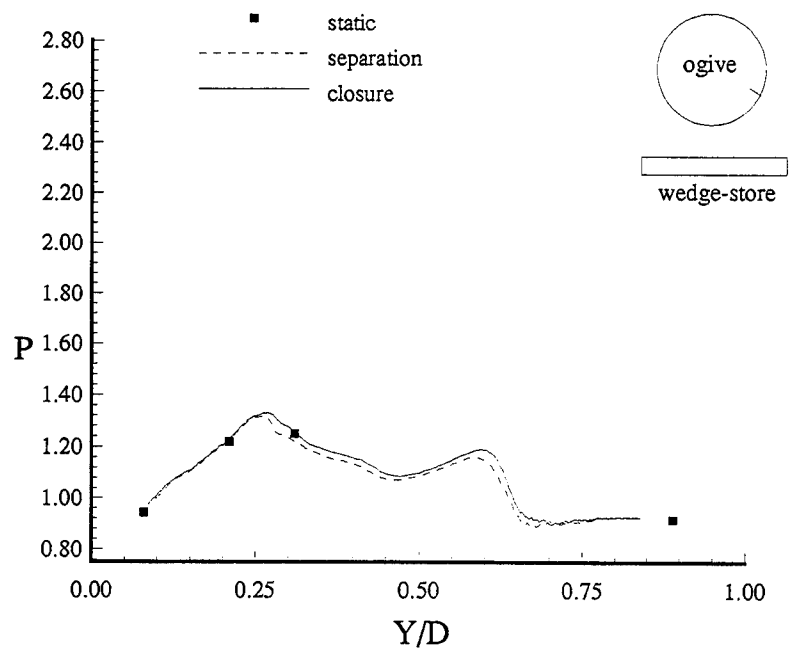Figure 5.73. Ogive surface pressure at X/YE=4.70 and $\psi = 180°$ (6.1° wedge-store, M = 1.9).

Appendix A. Computational Method

Computational analysis of the store separation events were accomplished on the Wright Laboratory Cray using the Three-Dimensional Euler Aerodynamic Method (TEAM) code [Raj, et al., 1987]. The TEAM code, developed for computational simulation of inviscid subsonic, transonic and supersonic configurations, consists of four major modules: the preprocessor, the grid generation, the flow solver, and the post-processor. Each module is briefly described below.

1. Preprocessor Module. The preprocessor module processes predefined geometry data to construct surface grids needed for the internal field grid generation. If surface grids are available from other sources or codes then preprocessor processing is not necessary, and computations may begin immediately in the grid generation module.

2. Grid Generation Module. The grid generation module generates the three dimensional field grids from the given surface grids. The computational domain is bounded by the prescribed outer boundary and the inner defined configuration surface.

3. Flow Solver Module. The flow solver module uses a finite-volume, multi-stage time stepping algorithm. A converged steady state solution is declared when the average residual (rms net mass flux) is reduced three to four orders of magnitude. This module produces on output for the entire grid and flow field: density, components of momentum, total energy, and static pressure.

4. Post-processor Module. Aerodynamic characteristics of the inner surface is determined with the fluid dynamic variables from the flow solver module, i.e. forces, moments, and surface pressure distributions. Furthermore, the extracted data from the flow solver module may be put into useable graphical format for contour plotting, vector fields, and X-Y plotting.

A.1 Governing Equations.

As stated above the TEAM code solves the time-dependent Euler equations. The unsteady integral form of the Euler equation for an arbitrary control volume Ω, bounded by the surface A is expressed as follows:

$$\frac{\partial}{\partial t} \int_\Omega Q d\Omega + \int_A \mathbf{F} \cdot \hat{n} d\mathbf{A} = \mathbf{0} \qquad (A.1)$$

where Q is the dependent vector

$$Q = \begin{bmatrix} \rho \\ \rho u_i \\ \rho E \end{bmatrix} \qquad (A.2)$$

and the flux vector is expressed as:

$$\cdot \; \mathbf{F} \cdot \hat{\mathbf{n}} = \begin{bmatrix} \rho \left(u_j n_j \right) \\ \rho u_i \left(u_j n_j \right) \\ \rho H \left(u_j n_j \right) \end{bmatrix} + \begin{bmatrix} 0 \\ p n_j \delta_{ij} \\ 0 \end{bmatrix} \qquad (A.3)$$

Where H is defined as the total enthalpy

$$H = E + p/\rho$$

and the static pressure is given by the equation of state

$$p = (\gamma - 1)\rho(E - \frac{1}{2}u_j u_j + H)$$

The standard notation used above corresponds to the Cartesian coordinates (X, Y, Z) with i or $j = 1, 2, 3$ respectively. Furthermore, the variables above are defined as follows: ρ is density, u_i is the Cartesian velocity components, E is total energy, n_i is the surface normal unit vector, and γ is the ratio of specific heats. The basic

A-2

assumptions made in using the governing equations were inviscid flow, no external forces, perfect gas with constant γ ($\gamma = 1.4$ for air), and adiabatic flow.

A.2 Spatial Discretization.

The TEAM algorithm ensures the steady state solution is independent of time by discretizing the spatial and time dependent terms separately. The spatial discretization is accomplished by subdividing the region about a configuration into hexahedral cells. Within each cell the dependent variables are located at the center, and the net flux is computed across the cell faces. Thus for any cell the semi-discrete governing equation is written as:

$$\frac{d}{dt}\left(\Omega_{I,J,K} Q_{I,J,K}\right) + F_{I,J,K} = 0 \qquad (A.4)$$

where Ω is now the cell volume and F is net convective flux for cell. The subscripts I, J, and K identifies the cell and the cell's center within the Cartesian coordinates; whereas, the faces for a particular cell may be found by adding or subtracting $\frac{1}{2}$ from the appropriate index.

The surface area of the cell faces, Fig. A.1, are determined with the cross products of two diagonal vectors:

$$A = \frac{1}{2}\left(\mathbf{r_{AC}} \times \mathbf{r_{BD}}\right)$$

The outward surface normal vector is positive. Cross products are also used to determine the cell volume. Each cell is divided into two and each of these partitions consists of three tetrahedrals as shown in Fig. A.2. Thus total cell volume may be found by:

$$\Omega = \frac{1}{6}\mathbf{r_{71}} \cdot \left[\left(\mathbf{r_{31}} \times \mathbf{r_{24}}\right) + \left(\mathbf{r_{61}} \times \mathbf{r_{52}}\right) + \left(\mathbf{r_{81}} \times \mathbf{r_{45}}\right)\right] \qquad (A.5)$$

The flux vector needs to be found at the cell face for the interfaces of the face between neighboring cells and the bordering computational zones. An alternative flux averaging procedure was incorporated into the TEAM code as shown:

$$\mathbf{F} \cdot \hat{\mathbf{n}} = \begin{bmatrix} (\rho u_j)\, n_j \\ (\rho u_i u_j + p\delta_{ij})\, n_j \\ (\rho u_j H)\, n_j \end{bmatrix} \tag{A.6}$$

Where the quantities in parentheses are the averaged values taken from two neighboring cell centers and denoted as the flux occurring at the cell face. This scheme is second-order accurate, and gives the appropriate jump results across a shock wave that is aligned with the cell face.

As stated the method developed needed to account for all cell faces. For the common face between cells in the same computational zone the average quantities found at the two cell centers were transferred to the common face surface. The flux at a zonal interface however, is obtained by averaging the quantities in the boundary and image cell. The TEAM code can handle several zonal interface to include grid density mismatch and maintaining conservation with loaded conditions within one zone. For the store separation study all the zonal interfaces had matching grids, and the variables were of the same order and accuracy in the image and boundary cells of neighboring zones.

A.3   Boundary Conditions.

The boundary conditions may be considered a class of zonal interfaces, and as such are handled in a somewhat similiar manner. In this case the boundary conditions are assigned to the dependent variable in the image cell such that averaging the fluxes in the image and boundary cell results in the value of the flux vector at the cell face. Boundary conditions at the far field, a solid interface, and a symmetry plane are discussed below.

A.3.1 <u>Far Field.</u> The far field boundary conditions are applied at the boundaries of the computational domain. It is important that these boundaries properly address the qualities of the flow entering and exiting the domain without reflecting outgoing waves back in. With supersonic flows, as was the case for this study, the far field boundary is specified to have their freestream values. Since all the characteristic directions leave the domain at an outflow boundary, the image cell values are defined equivalent to the boundary cell values (zero order extrapolation).

A.3.2 <u>Solid Boundary.</u> The flow cannot pass through a solid surface so a tangent, or no normal, flow condition is imposed. In a finite-volume formulation this conditions requires that all cell faces interfacing with the solid boundary have their convected flux set to zero. The only contribution to the momentum flux is the surface pressure.

A.3.3 <u>Symmetry Plane.</u> The reflection principle is used at the symmetry plane boundary. For example, a flow passing through a symmetry plane in the X-Z plane would have the Y component of momentum change signs. Whereas, all other variables in the image cell would have the same value as those in the boundary cell across the symmetry plane.

A.4 <u>Numerical Dissipation.</u>

The cell-centered finite-volume method for solving the Euler equations requires numerical dissipation to smooth out truncation errors, and provide artificial viscosity for realistic shock capturing [Anderson, et al., 1984]. The Euler equation, unlike the Navier-Stokes equation, has no implicit dissipative terms. Thus, artificial dissipation must be introduced to ensure that the entropy condition is maintained (second law of thermodynamics), and that short-wave motion is suppressed without effecting the global features of the flow. Furthermore, outgoing waves cannot be reflected from

boundaries back into the computational domain. To accomplish this TEAM has incorporated three dissipation methods.

A.4.1 <u>Standard and Modified Adaptive Dissipation.</u> The standard adaptive dissipation uses the formulation as proposed by Jameson et al [Jameson, et al.,1981]. The formulation is re-illustrated here for any interior cell face with a surface normal along the j-direction. The dissipative flux in the j-direction is:

$$d_{I,J+\frac{1}{2},K} = \varepsilon_2 e_{I,J+\frac{1}{2},K} - \varepsilon_4 \left(e_{I,J+\frac{3}{2},K} - 2e_{I,J+\frac{1}{2},K} + e_{I,J-\frac{1}{2},K} \right) \qquad (A.7)$$

where

$$e_{I,J+\frac{1}{2},K} = \alpha \left(Q_{I,J+1,K} - Q_{I,J,K} \right) \qquad (A.8)$$

$$\alpha = \frac{1}{2} \left(\Lambda_{I,J,K} + \Lambda_{I,J+1,K} \right) \qquad (A.9)$$

$$\Lambda_{I,J,K} = \lambda^I_{I,J,K} + \lambda^J_{I,J,K} + \lambda^K_{I,J,K} \qquad (A.10)$$

This dissipative flux is for the common cell face $(I, J + \frac{1}{2}, K)$ located between neighboring cells (I, J, K) and $(I, J + 1, K)$. Furthermore, λ denotes the spectral radius of the flux-Jacobian matrix with the superscript denoting the direction and the subscripts referring to the cell or cell-face. In the I direction for example:

$$\lambda^I = q^I + c \left(A_i \left|_{I,J,K} \; A_i \left|_{I,J,K} \right)^{\frac{1}{2}} \right. \right. \qquad (A.11)$$

where

$$q = u_i A_i \left|_{I,J,K} \right.$$

and

$$A_i \left|_{I,J,K} \right. = \frac{1}{2} \left(A_i \left|_{I+\frac{1}{2},J,K} \right. + A_i \left|_{I-\frac{1}{2},J,K} \right. \right)$$

Additionally, u_i denotes the Cartesian velocity component, A_i the surface area vector components with the summation notation of i=1,2,3 corresponding directly to X, Y, Z, and c represents the speed of sound.

The coefficients in equation A.7, ε_2 and ε_4, are chosen to be effective at capturing shock waves. The coefficients are defined by taking the normalized second difference of pressure:

$$\nu_{I,J,K} = \left| \frac{P_{I,J+1,K} - 2P_{I,J,K} + P_{I,J-1,K}}{P_{I,J+1,K} + 2P_{I,J,K} + P_{I,J-1,K}} \right| \tag{A.12}$$

and defining

$$\overline{\nu_{I,J+\frac{1}{2},K}} = max\left(\nu_{I,J+2,K}, \nu_{I,J+1,K}, \nu_{I,J-1,K}\right) \tag{A.13}$$

Then

$$\varepsilon_2 = K_o \overline{\nu_{I,J+\frac{1}{2},K}} \tag{A.14}$$

$$\varepsilon_4 = max\left(0, K_1 - \varepsilon_2\right) \tag{A.15}$$

Program input parameters, specified by the user, define K_o and K_1 which lead to the calculation of ε_2 and ε_4 respectively. K_o is the input variable VIS-2 used in equation A.14. ε_2 provides the needed dissipation found near shock waves and stagnation points. Input VIS-4 is divided by 64 to define K_1 and used in ε_4 which suppresses overshoots and oscillations.

The net dissipative flux in the different direction are: i-direction:

$$D_{I,J,K}^{I} = d_{I+\frac{1}{2},J,K} - d_{I-\frac{1}{2},J,K} \tag{A.16}$$

j-direction:

$$D_{I,J,K}^{J} = d_{I,J+\frac{1}{2},K} - d_{I,J-\frac{1}{2},K} \tag{A.17}$$

k-direction:

$$D^K_{I,J,K} = d_{I,J,K+\frac{1}{2}} - d_{I,J,K-\frac{1}{2}} \qquad \text{(A.18)}$$

The net dissipative flux for the entire cell is simply the sum:

$$D_{I,J,K} = D^I_{I,J,K} + D^J_{I,J,K} + D^K_{I,J,K} \qquad \text{(A.19)}$$

The modified adaptive dissipation scheme differs from the standard adaptive dissipation scheme only by the scaling of the first-difference terms. The scaling factor α used in equation A.8 is redefined as:

$$\alpha = \frac{1}{2} \left(\lambda^J_{I,J,K} + \lambda^J_{I,J+1,K} \right) \qquad \text{(A.20)}$$

Thus, the first difference are scaled by the corresponding eigen values. And ε_2 is further restricted as follows:

$$\varepsilon_2 = min \left(\frac{1}{2}, K_o \overline{\nu_{I,J+\frac{1}{2},K}} \right)$$

.

A.4.2 $\underline{\text{Flux-Limited Dissipation.}}$ In order to remove oscillations about the shock waves, TEAM incorporates an alternative formulation developed by Jameson [Jameson,1981]. This scheme for dissipation uses flux limitation which lead to a total variation diminishing (TVD) method if coefficients are correctly chosen. The dissipative flux term at a cell-face, in the j-direction, is defined as:

$$d_{I,J+\frac{1}{2},K} = B \left(e_{I,J+\frac{3}{2},K}, e_{I,J+\frac{1}{2},K} \right) - 2e_{I,J+\frac{1}{2},K} + B \left(e_{I,J+\frac{1}{2},K}, e_{I,J-\frac{1}{2},K} \right) \qquad \text{(A.21)}$$

where

$$e_{I,J+\frac{1}{2},K} = \alpha \left(Q_{I,J+1,K} - Q_{I,J,K} \right)$$

$$\alpha = \frac{\beta}{2}\left(\lambda_{I,J,K}^{J} + \lambda_{I,J+1,K}^{J}\right)$$

Here B is defined for two arguments as:

$$B(a,b) = (s(a) + s(b))min(|a|,|b|)$$

$$s(a) = \begin{array}{l} 1/2, a \geq 0 \\ -1/2, a < 0 \end{array}$$

And λ_J is the j-direction spectral radius of the flux-Jacobian matrix. Furthermore, β is defined as:

$$\beta = min\left(\frac{1}{2}, K_o + K_1\overline{\nu_{I,J+\frac{1}{2},K}}\right)$$

Where K_o and K_1 are calculated by VIS-2 and VIS-4 as explained in the adaptive dissipation scheme.

For all the dissipation methods, the cells near the boundaries must be handled differently. By the schemes described above calculations involving the boundary cells would attempt using cells that were not defined. There are four boundary schemes incorporated into the TEAM code. The boundary method chosen for this study was proposed by Rizzi and Eriksson [Rizzi and Eriksson, 1984]. In this method the first and third differences are set to zero at the boundary face ($J = \frac{3}{2}$)

$$d_{I,\frac{3}{2},K} = 0$$

While the opposite face ($J = \frac{5}{2}$) becomes:

$$d_{I,\frac{5}{2},K} = \varepsilon_2 e_{I,\frac{5}{2},K} - \varepsilon_4\left(e_{I,\frac{7}{2},K} - e_{I,\frac{5}{2},K}\right)$$

This scheme is globally conservative and ensures globally positive dissipation.
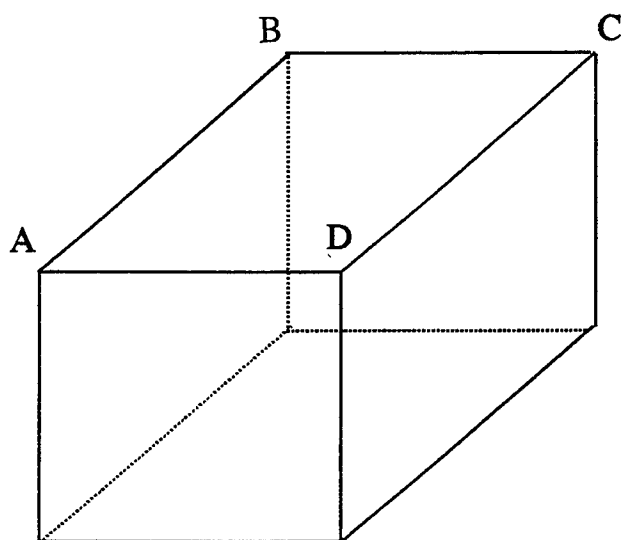
Figure A.1. Computational cell.
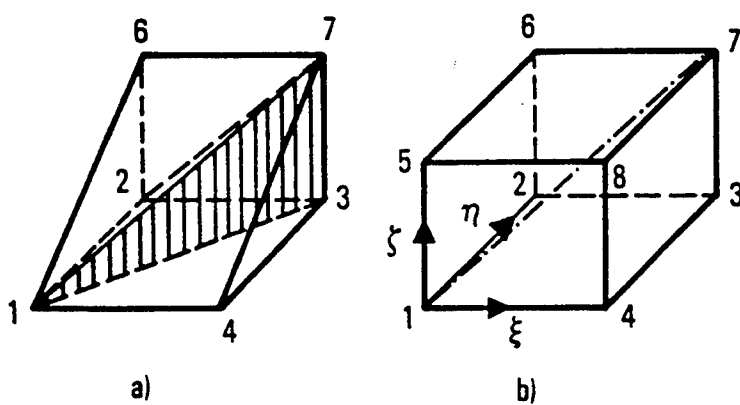
Figure A.2. Cell volume partitions.
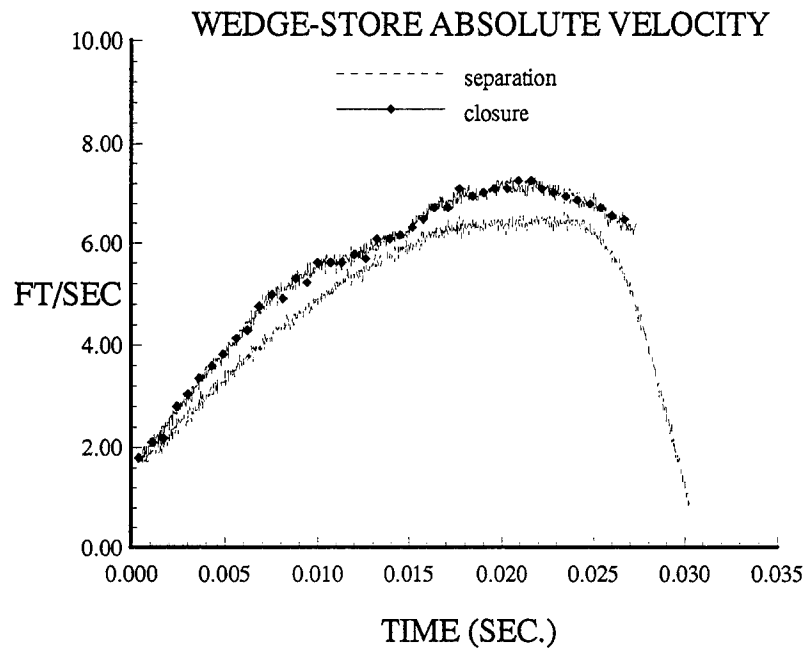
Figure B.1. The wedge-store absolute velocity with respect to time.
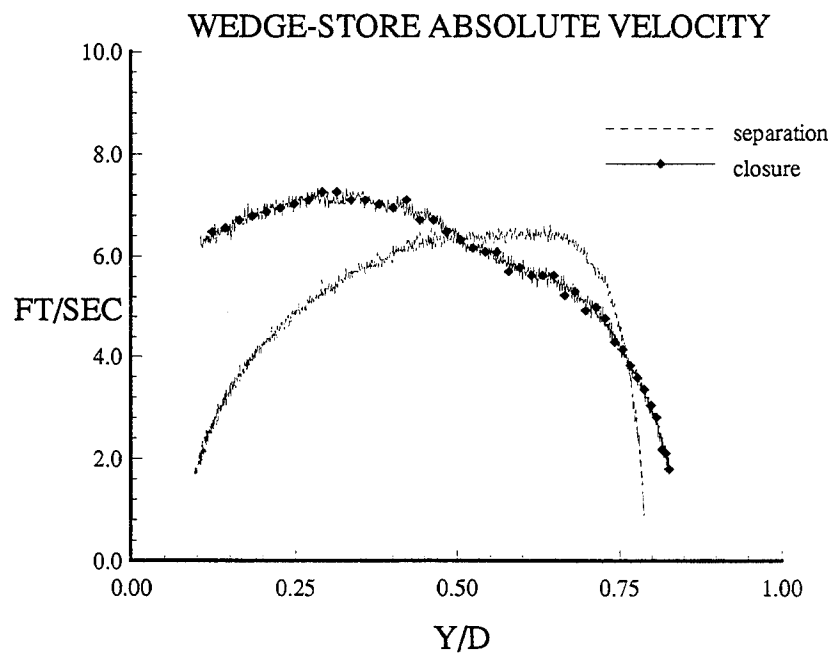
Figure B.2. The wedge-store absolute velocity with respect to position.
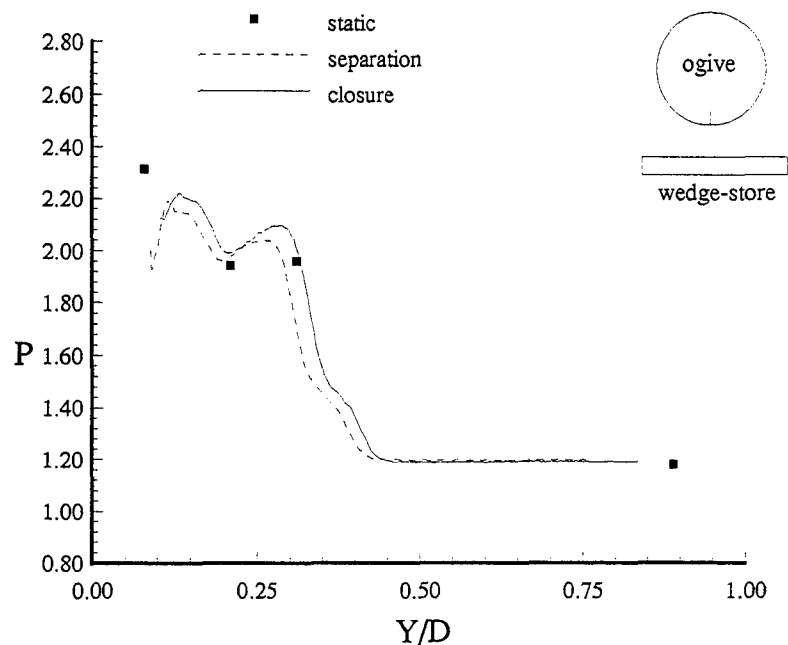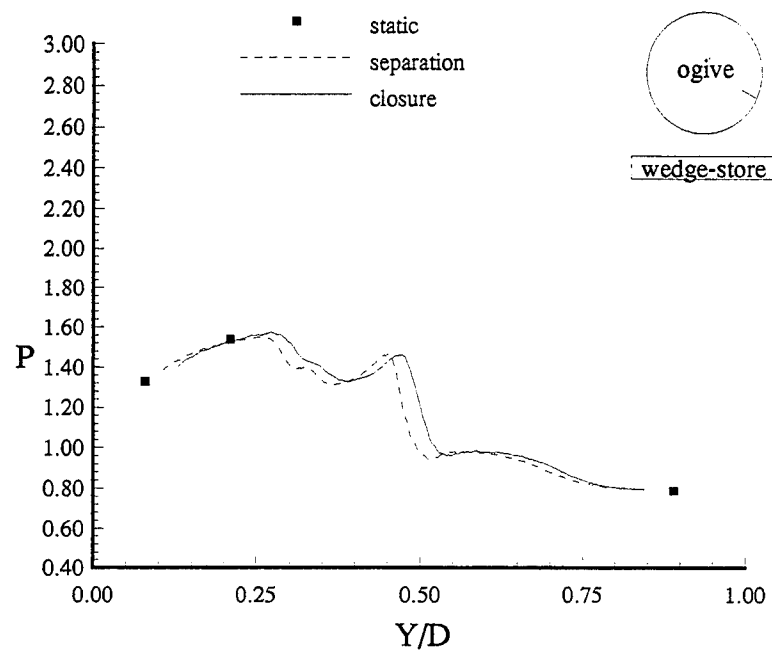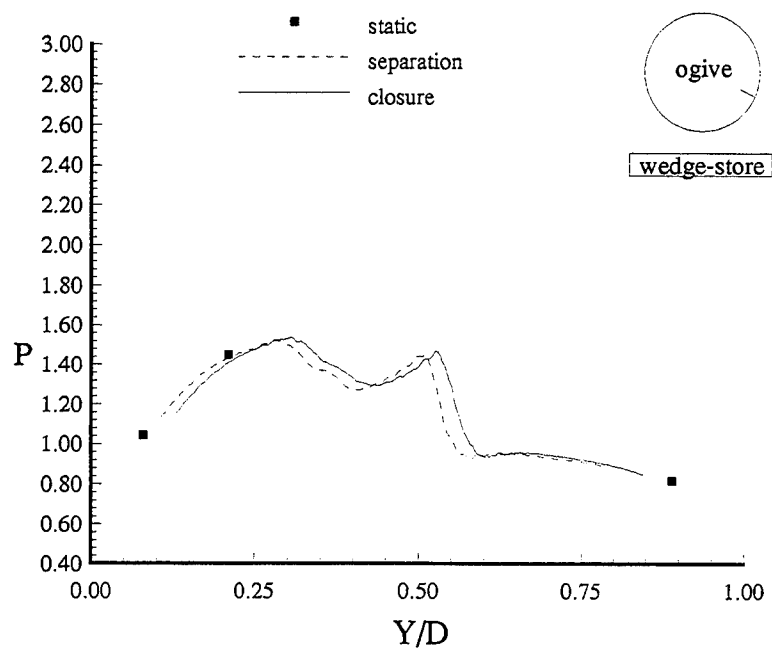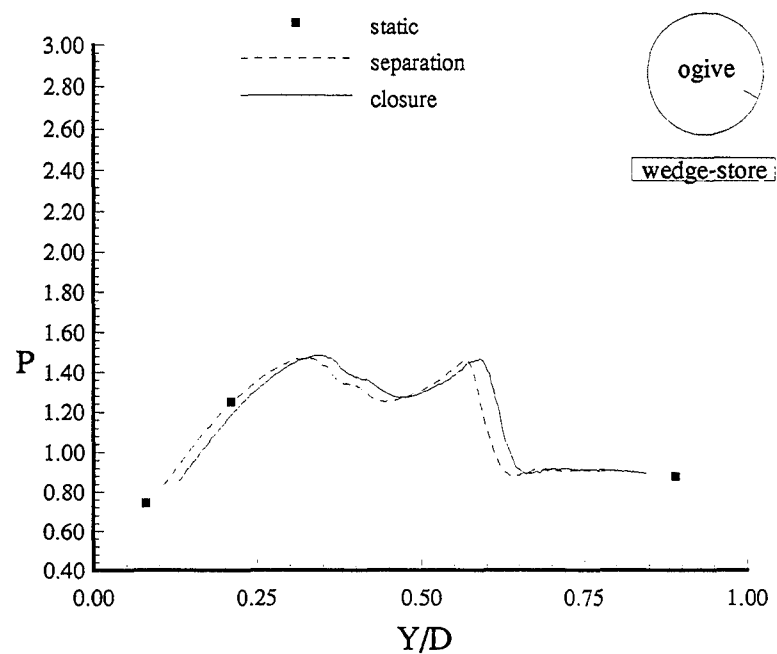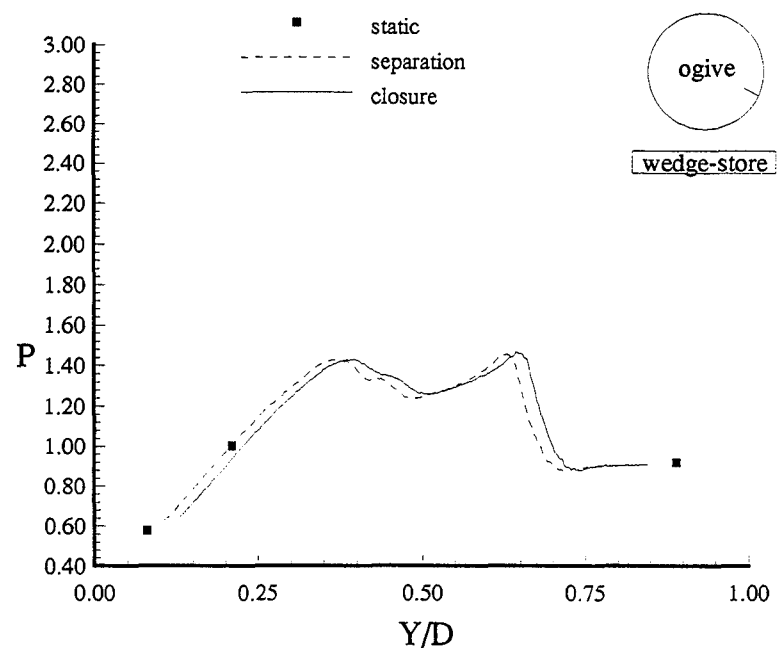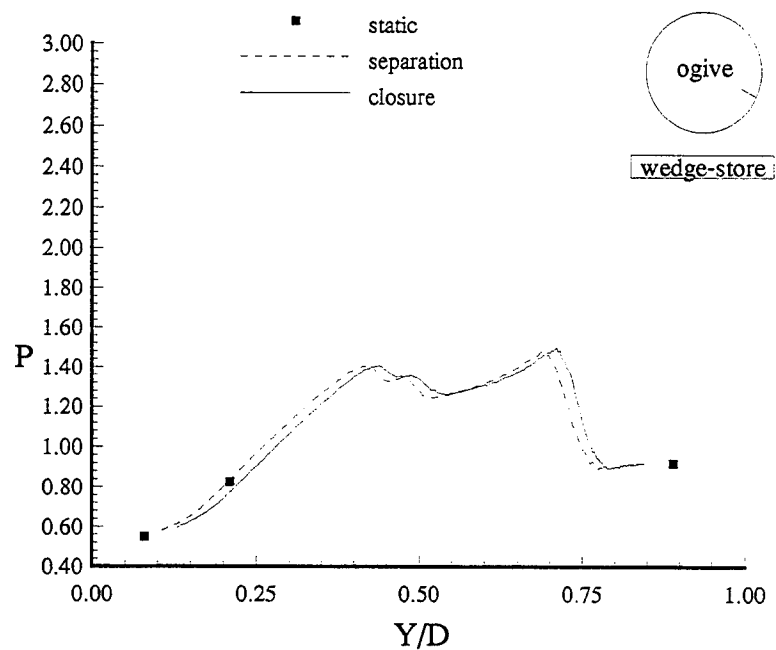
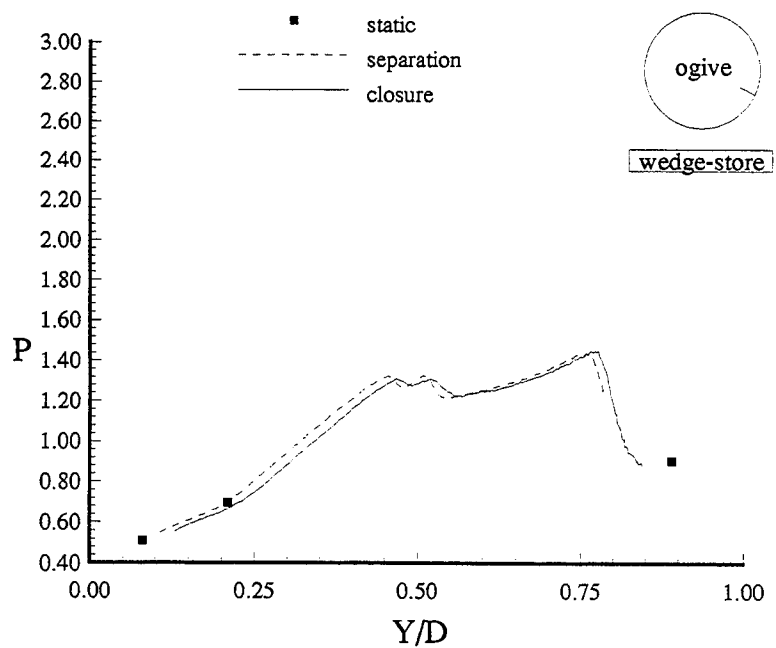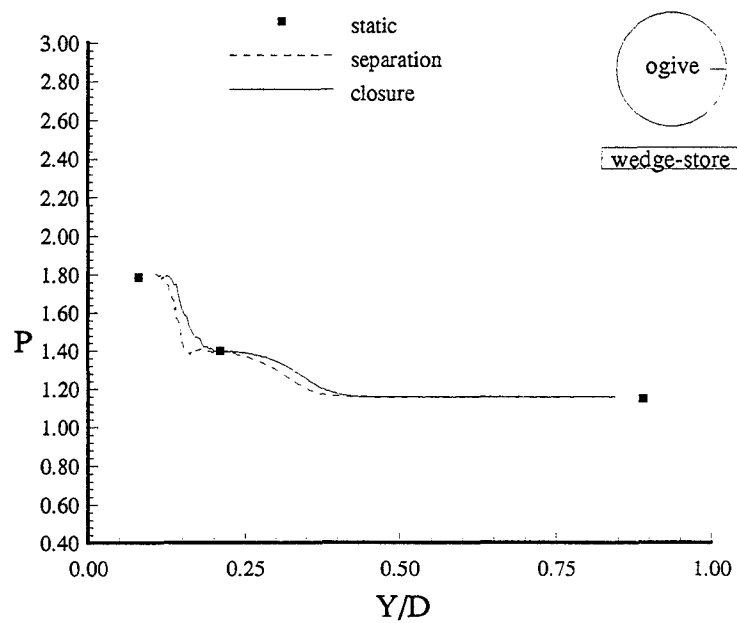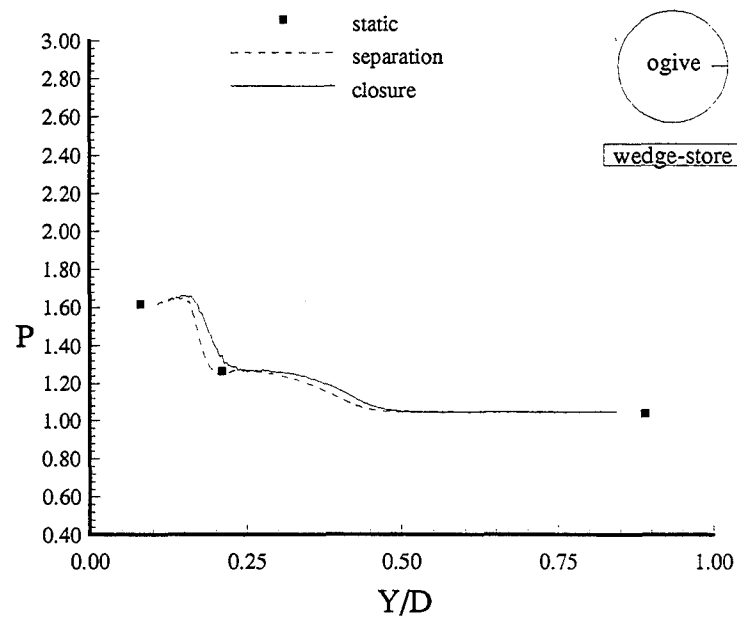Figure B.3. Ogive surface pressure at X/YE=2.31 and $\psi = 0°$ (6.1° wedge-store, M = 1.9).
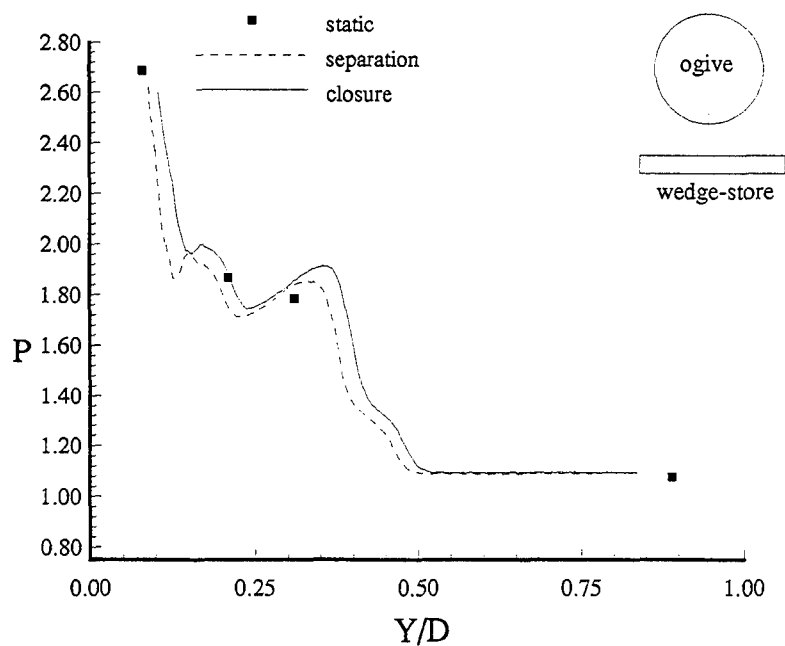
Figure B.4. Ogive surface pressure at X/YE=2.57 and $\psi = 0°$ (6.1° wedge-store, M = 1.9).
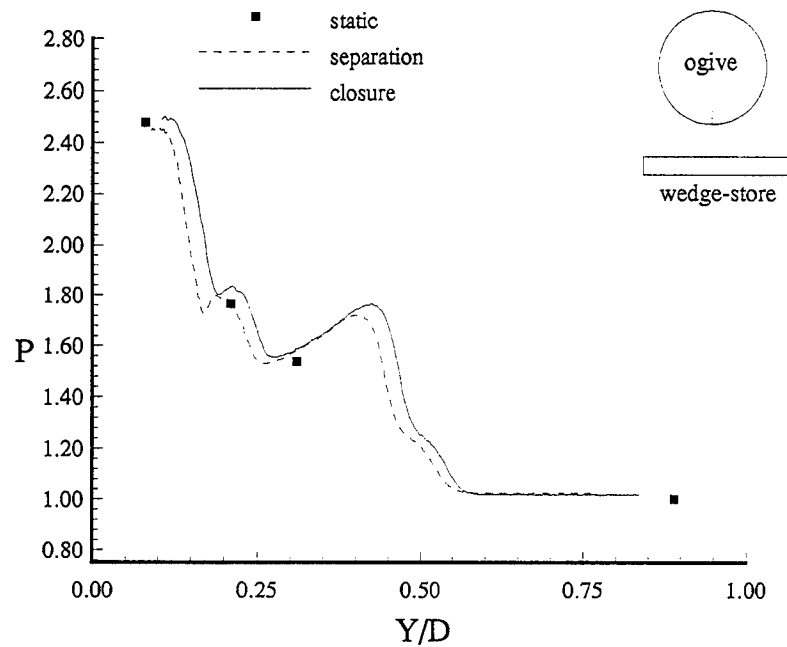
Figure B.5. Ogive surface pressure at X/YE=2.84 and $\psi = 0°$ (6.1° wedge-store, M = 1.9).
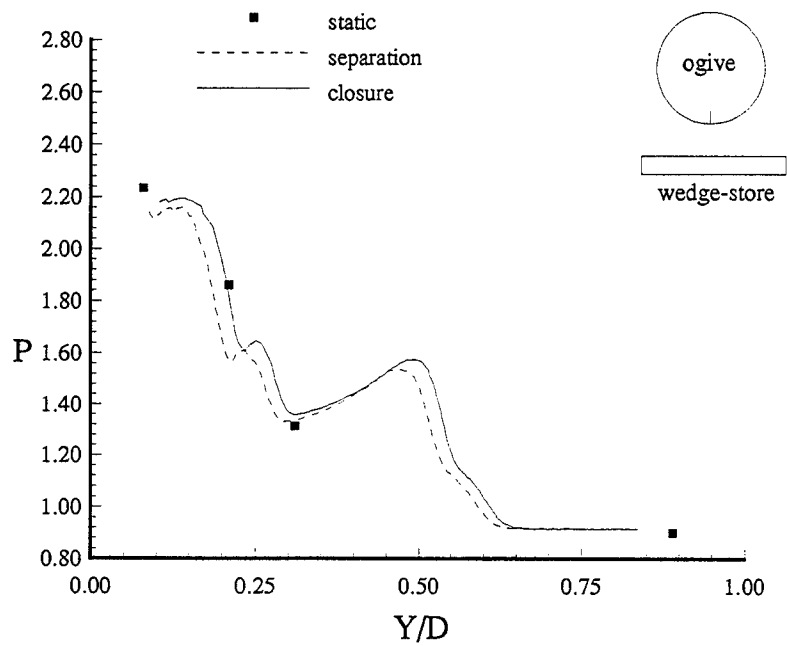
Figure B.6. Ogive surface pressure at X/YE=3.10 and $\psi = 0°$ (6.1° wedge-store, M = 1.9).
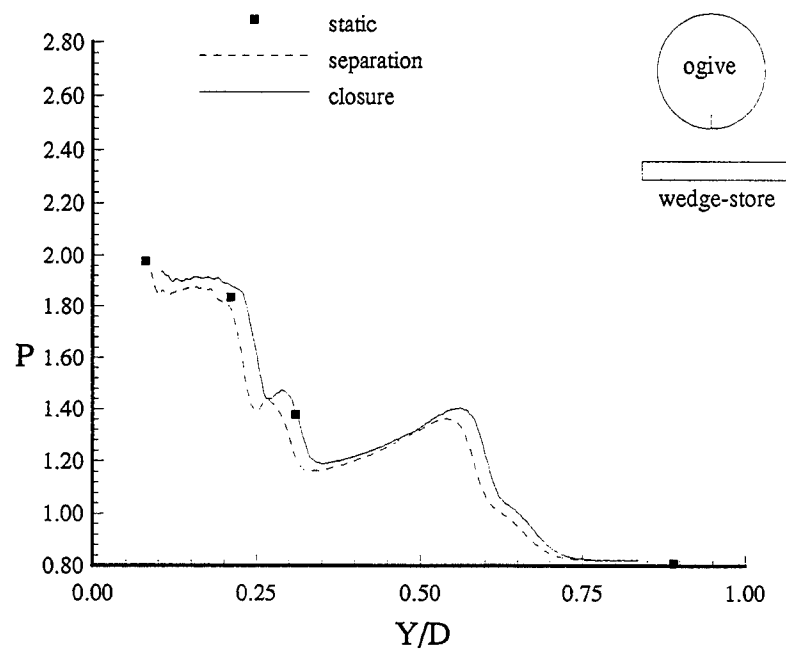
Figure B.7.   Ogive surface pressure at X/YE=3.37 and $\psi = 0°$ (6.1° wedge-store, M = 1.9).
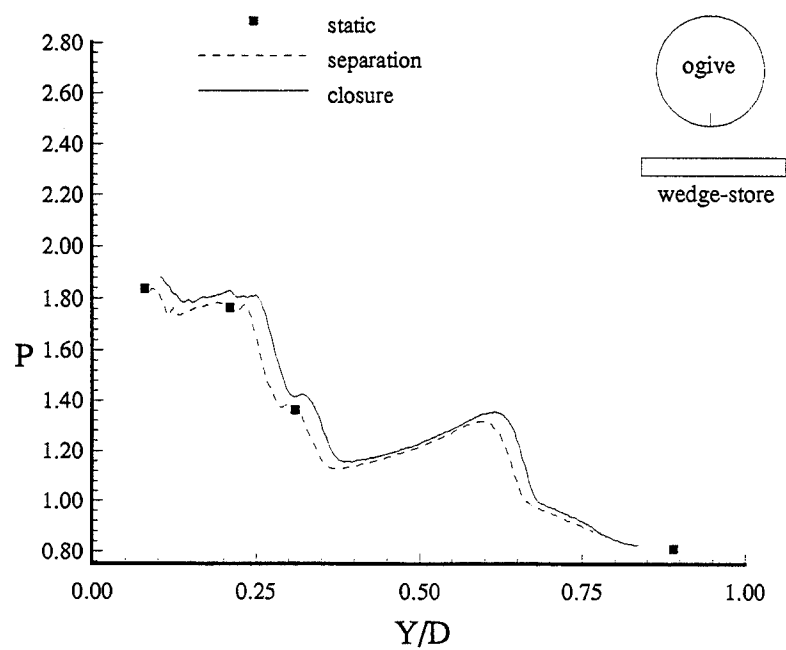
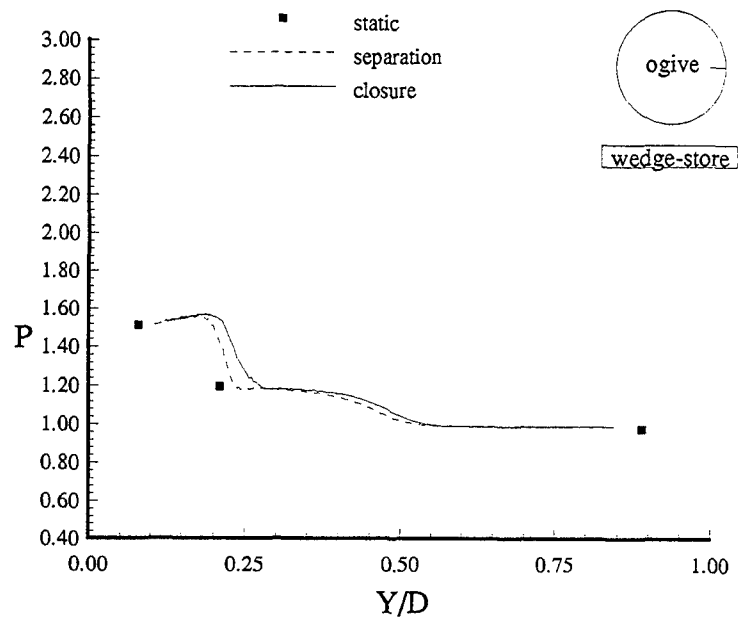Figure B.8.   Ogive surface pressure at X/YE=3.64 and $\psi = 0°$ (6.1° wedge-store, M = 1.9).
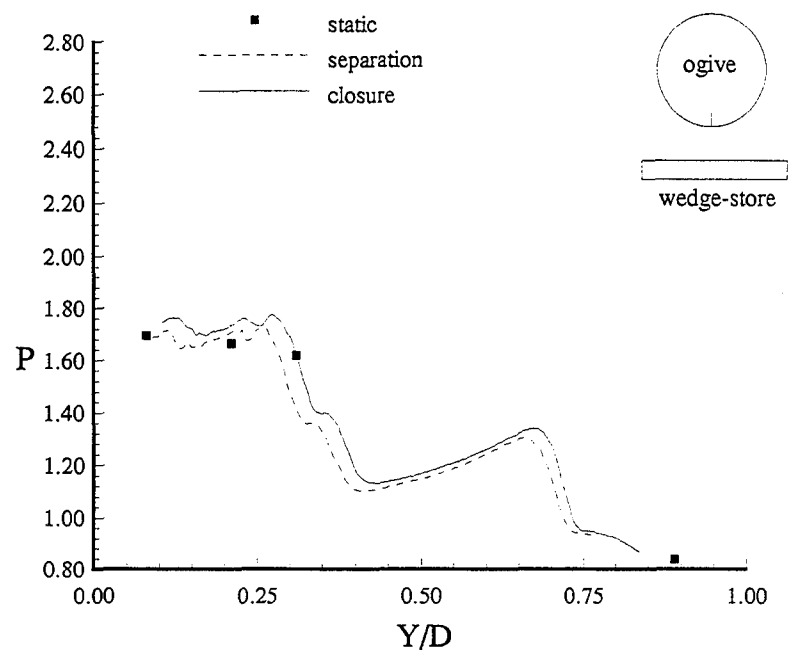
Figure B.9.   Ogive surface pressure at X/YE=3.90 and $\psi = 0°$ (6.1° wedge-store, M = 1.9).
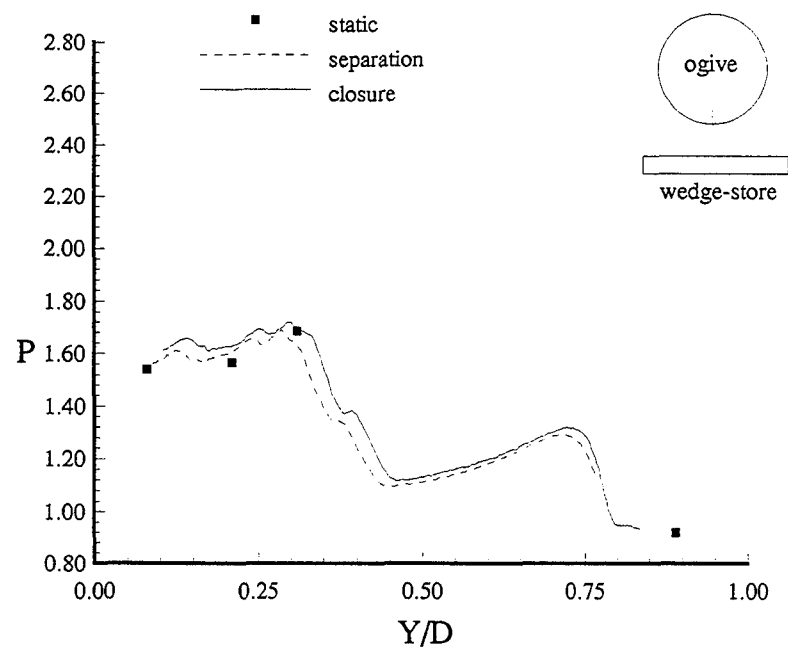
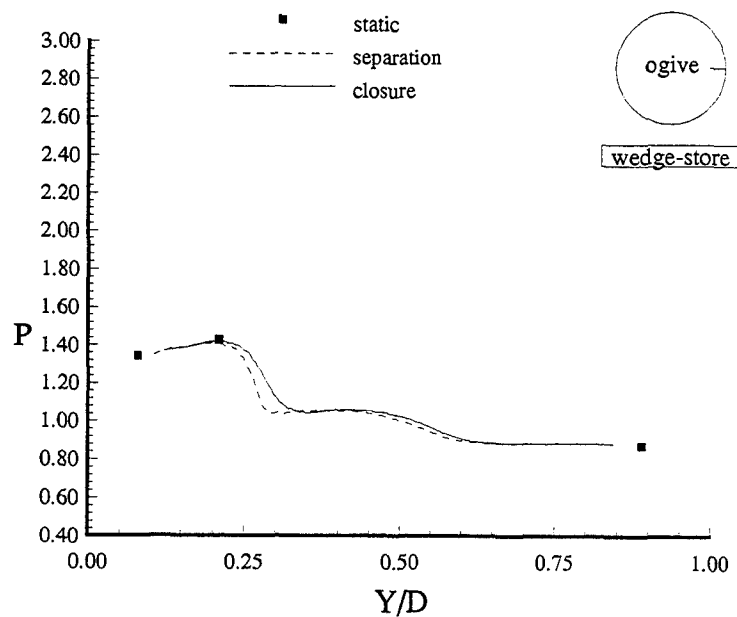

Figure B.10.   Ogive surface pressure at X/YE=4.17 and $\psi = 0°$ (6.1° wedge-store, M = 1.9).
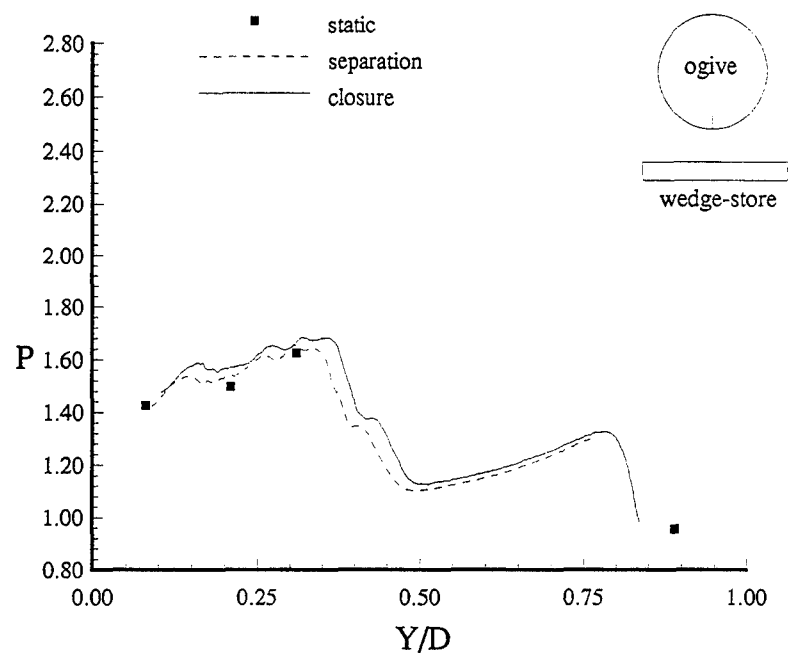
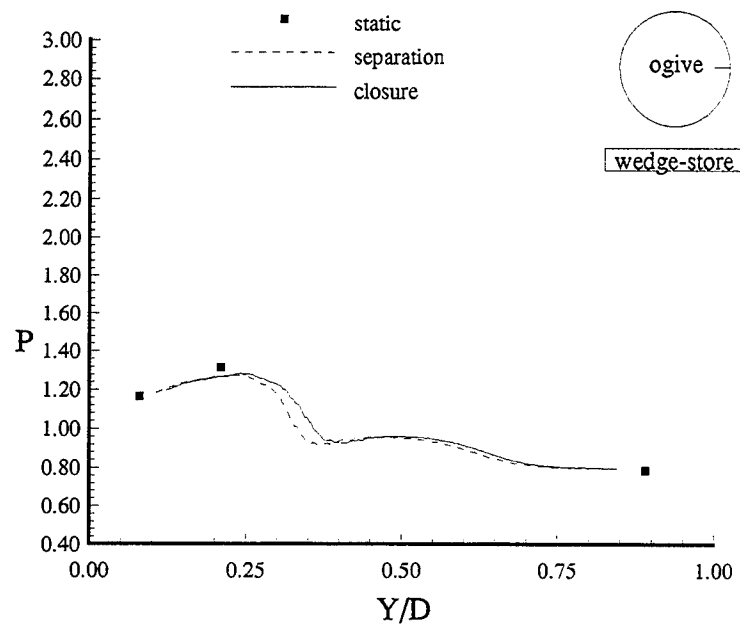Figure B.11.   Ogive surface pressure at X/YE=4.43 and $\psi = 0°$ (6.1° wedge-store, M = 1.9).
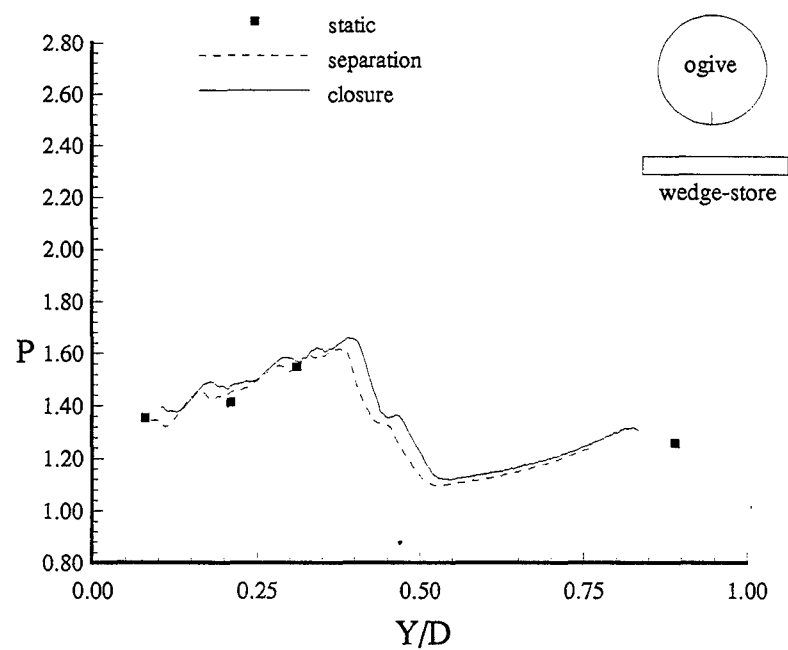
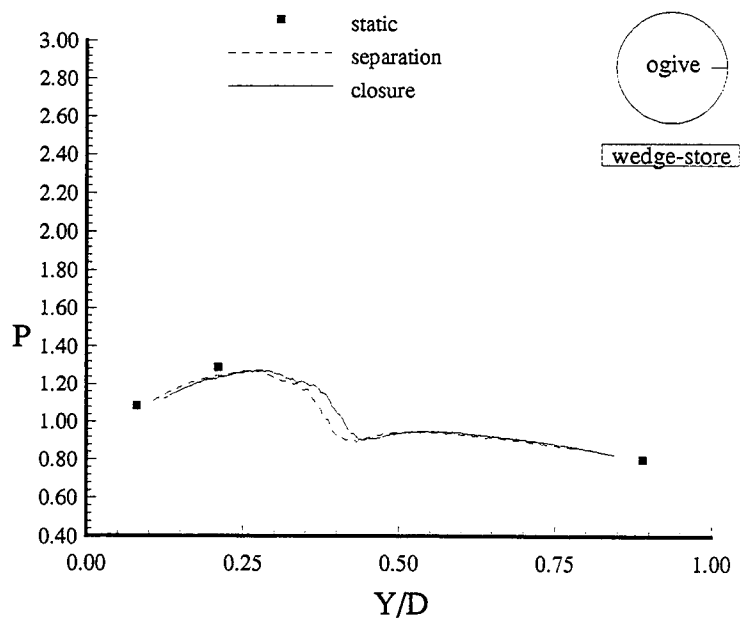

Figure B.12.   Ogive surface pressure at X/YE=4.70 and $\psi = 0°$ (6.1° wedge-store, M = 1.9).
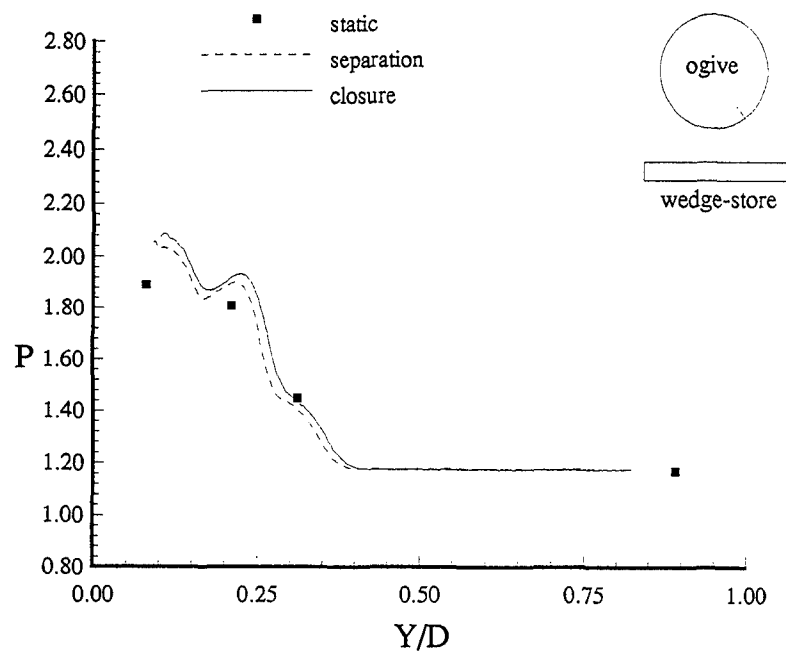
Figure B.13.   Ogive surface pressure at X/YE=2.31 and $\psi = 30°$ (6.1° wedge-store, M = 1.9).
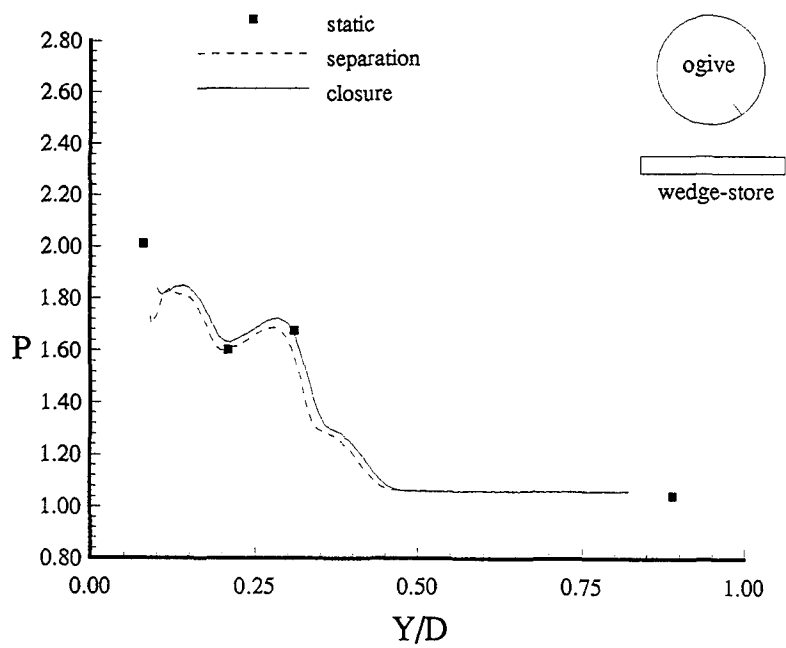
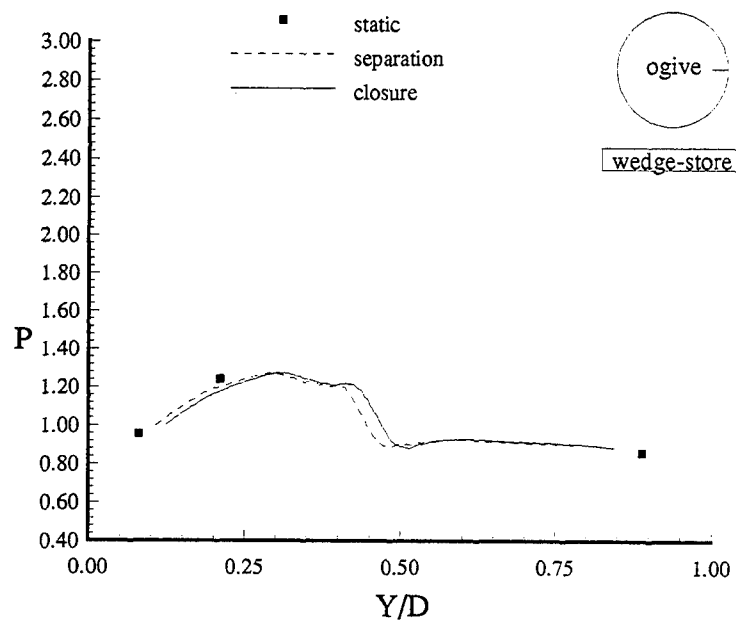
Figure B.14.   Ogive surface pressure at X/YE=2.57 and $\psi = 30°$ (6.1° wedge-store, M = 1.9).
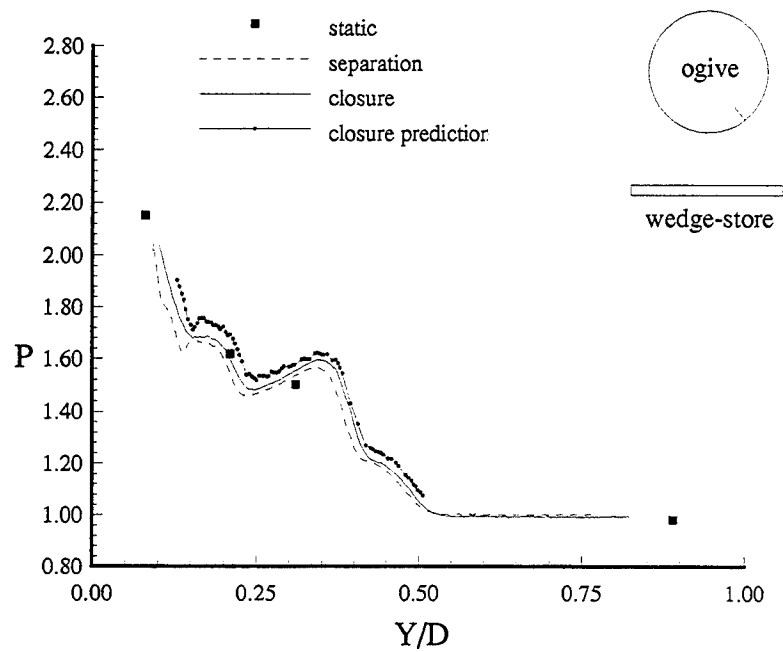
Figure B.15. Ogive surface pressure at X/YE=2.84 and $\psi = 30°$ (6.1° wedge-store, M = 1.9).
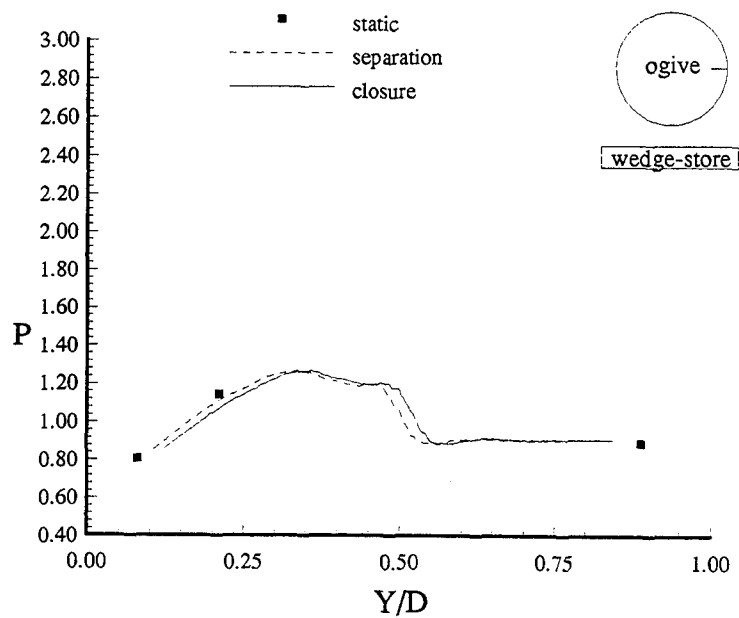

Figure B.16. Ogive surface pressure at X/YE=3.10 and $\psi = 30°$ (6.1° wedge-store, M = 1.9).

Figure B.17.   Ogive surface pressure at X/YE=3.37 and $\psi = 30°$ (6.1° wedge-store, M = 1.9).

Figure B.18.   Ogive surface pressure at X/YE=3.64 and $\psi = 30°$ (6.1° wedge-store, M = 1.9).

Figure B.19.   Ogive surface pressure at X/YE=3.90 and $\psi = 30°$ (6.1° wedge-store, M = 1.9).

Figure B.20.   Ogive surface pressure at X/YE=4.17 and $\psi = 30°$ (6.1° wedge-store, M = 1.9).
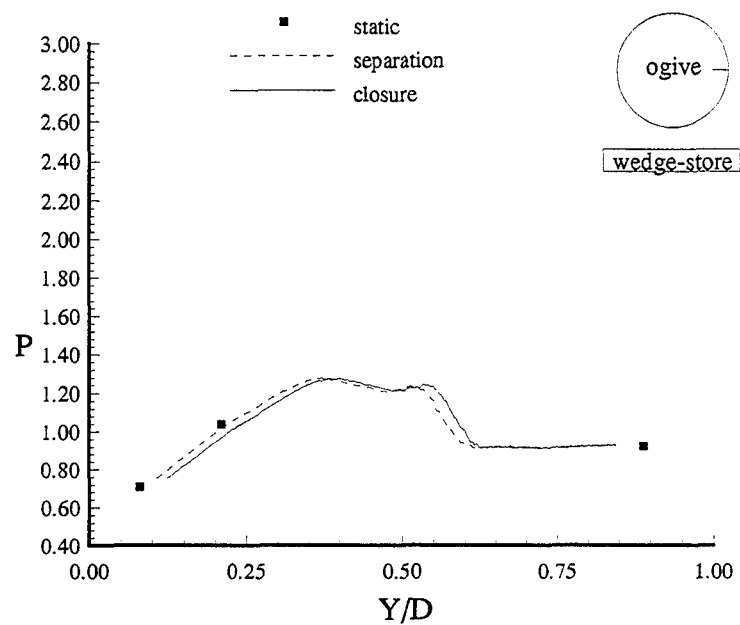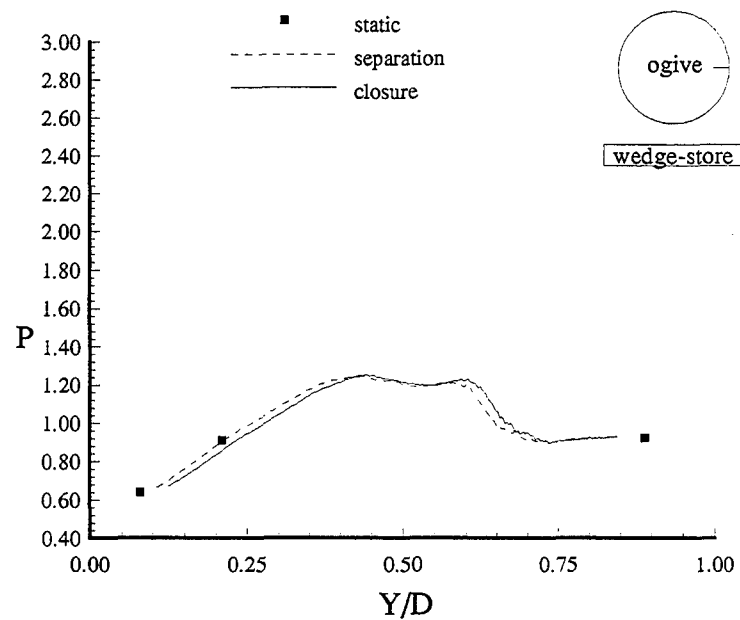
Figure B.21.　Ogive surface pressure at X/YE=4.43 and $\psi = 30°$ (6.1° wedge-store, M = 1.9).

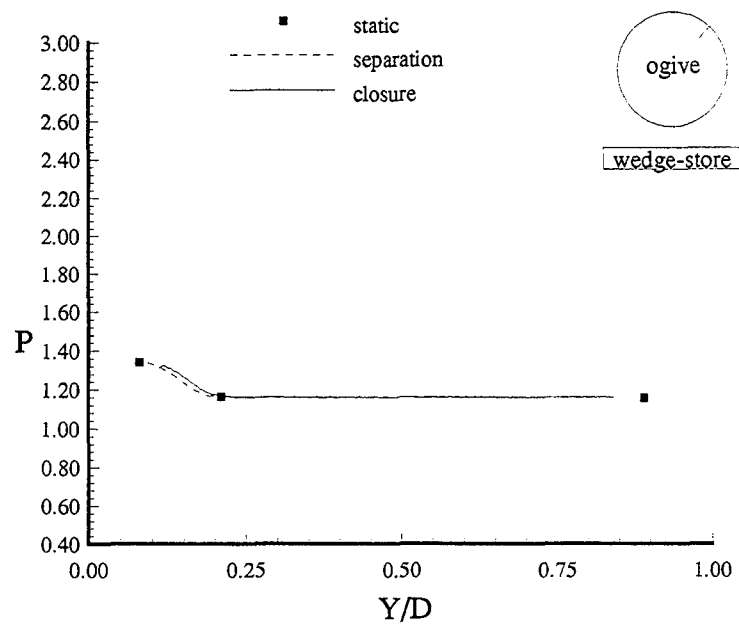Figure B.22.　Ogive surface pressure at X/YE=4.70 and $\psi = 30°$ (6.1° wedge-store, M = 1.9).

Figure B.23. Ogive surface pressure at X/YE=2.31 and $\psi = 60°$ (6.1° wedge-store, M = 1.9).
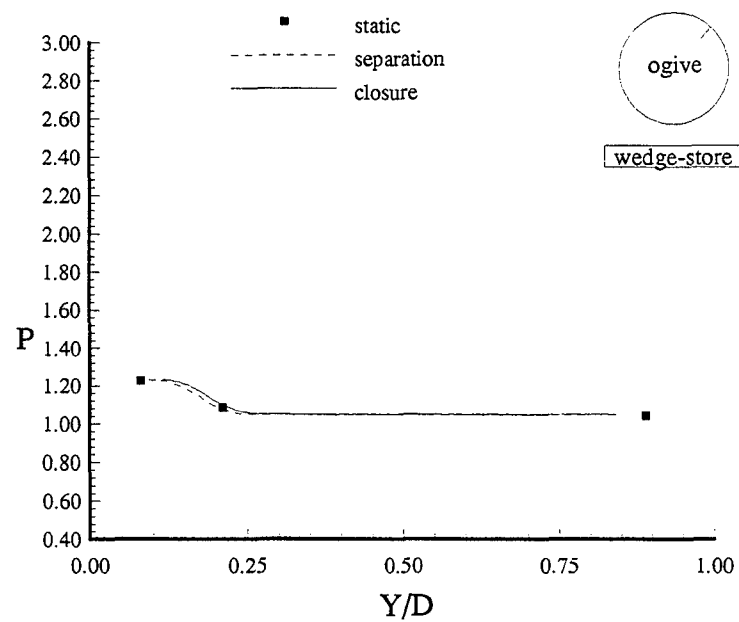

Figure B.24. Ogive surface pressure at X/YE=2.57 and $\psi = 60°$ (6.1° wedge-store, M = 1.9).

Figure B.25. Ogive surface pressure at X/YE=2.84 and $\psi = 60°$ (6.1° wedge-store, M = 1.9).

Figure B.26. Ogive surface pressure at X/YE=3.10 and $\psi = 60°$ (6.1° wedge-store, M = 1.9).

Figure B.27.   Ogive surface pressure at X/YE=3.37 and $\psi = 60°$ (6.1° wedge-store, M = 1.9).

Figure B.28.   Ogive surface pressure at X/YE=3.64 and $\psi = 60°$ (6.1° wedge-store, M = 1.9).

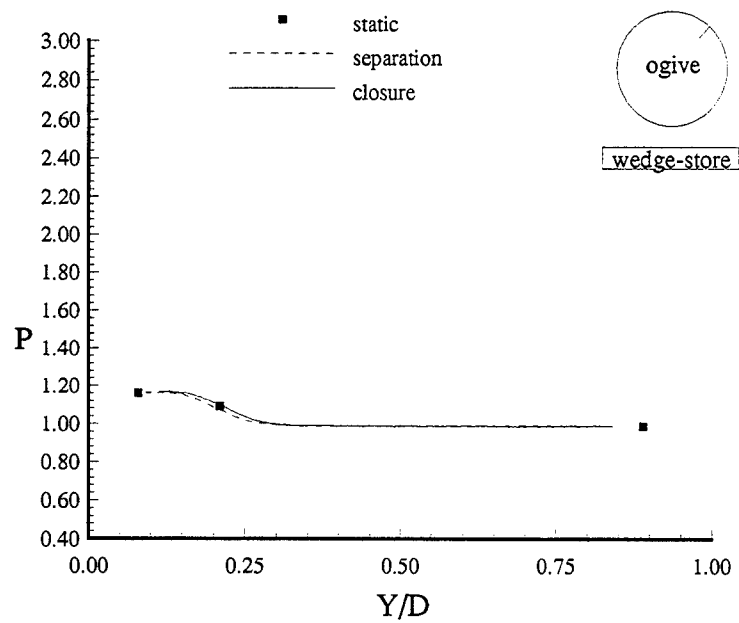Figure B.29. Ogive surface pressure at X/YE=3.90 and $\psi = 60°$ (6.1° wedge-store, $M = 1.9$).

Figure B.30. Ogive surface pressure at X/YE=4.17 and $\psi = 60°$ (6.1° wedge-store, $M = 1.9$).

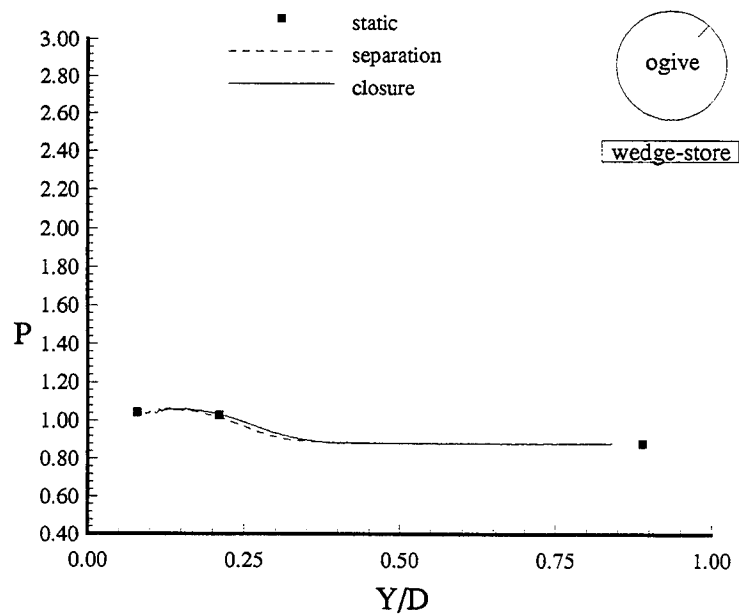Figure B.31. Ogive surface pressure at X/YE=4.43 and $\psi = 60°$ (6.1° wedge-store, $M = 1.9$).

Figure B.32. Ogive surface pressure at X/YE=4.70 and $\psi = 60°$ (6.1° wedge-store, $M = 1.9$).
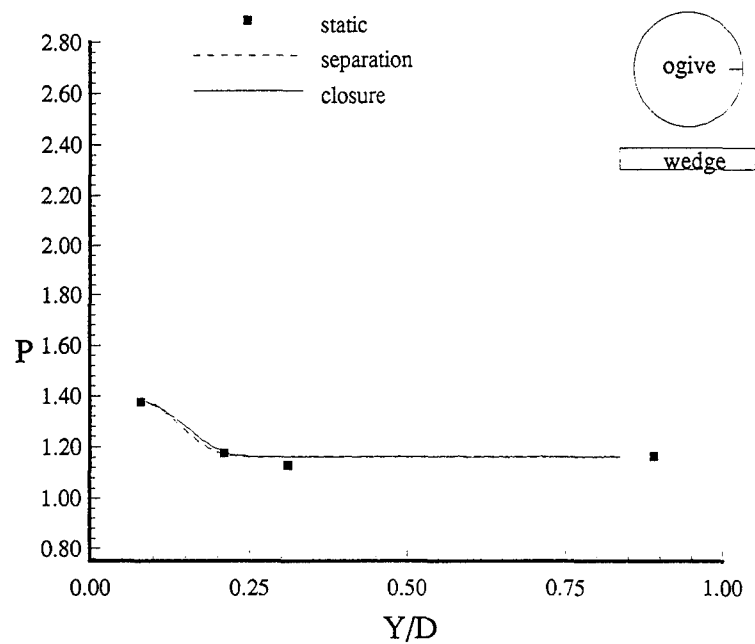
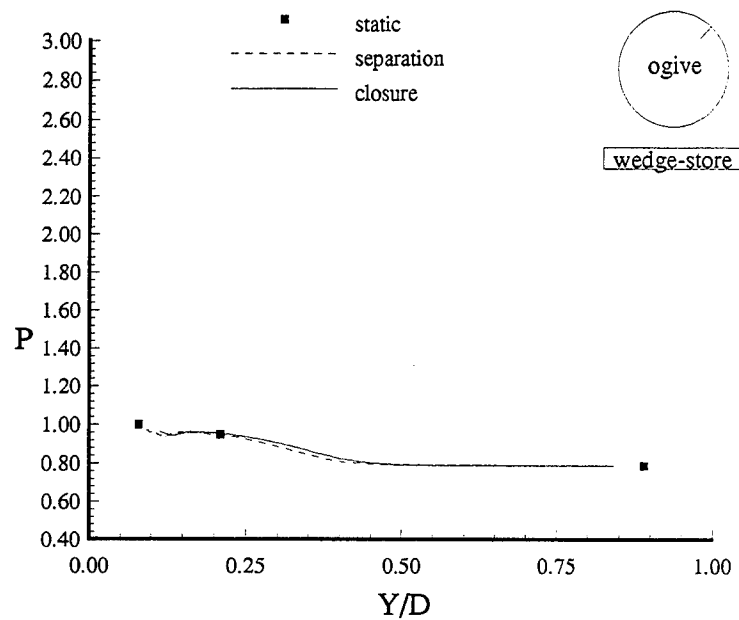Figure B.33. Ogive surface pressure at X/YE=2.31 and $\psi = 90°$ (6.1° wedge-store, M = 1.9).
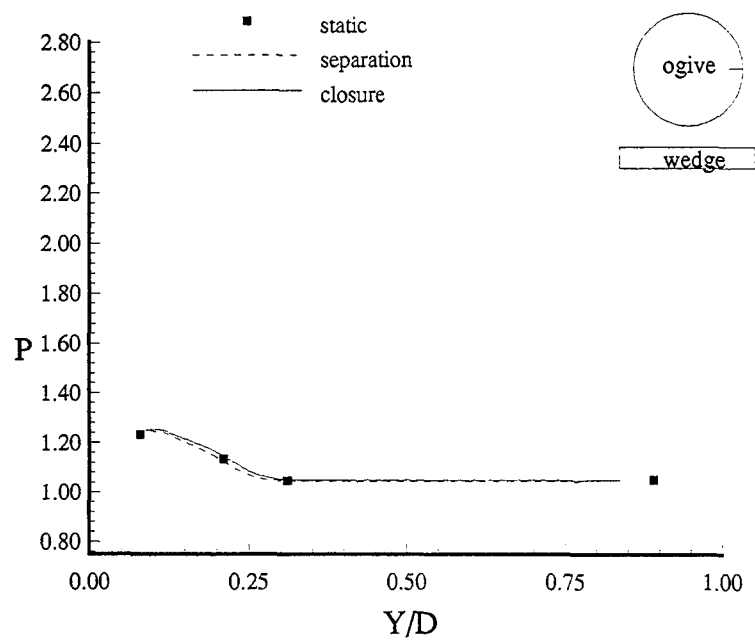
Figure B.34. Ogive surface pressure at X/YE=2.57 and $\psi = 90°$ (6.1° wedge-store, M = 1.9).
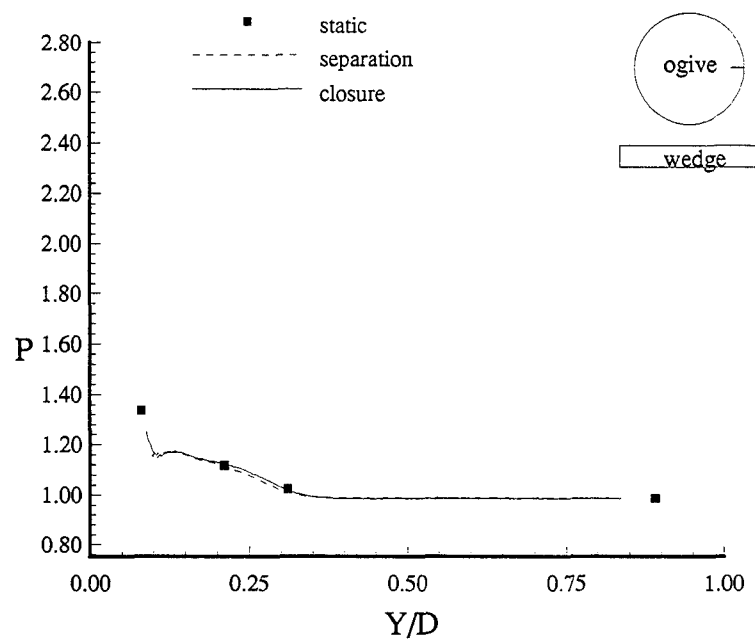
Figure B.35.   Ogive surface pressure at X/YE=2.84 and $\psi = 90°$ (6.1° wedge-store, M = 1.9).
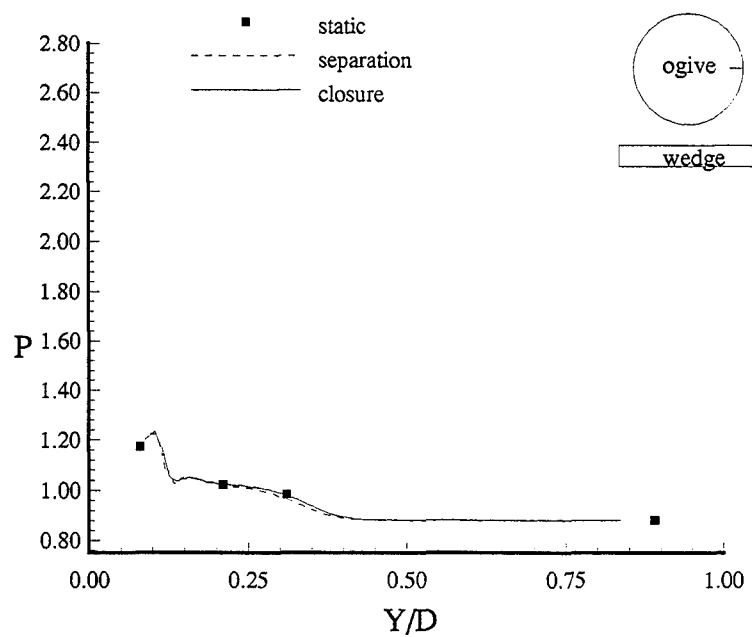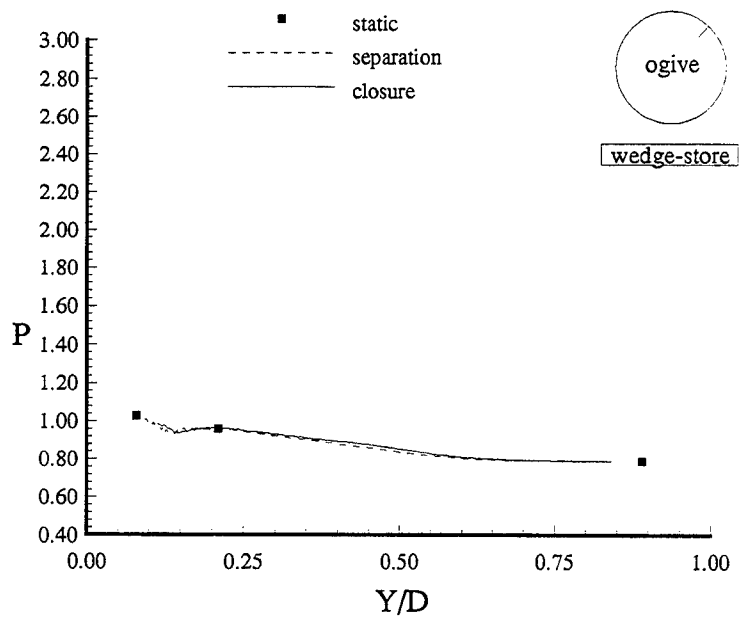

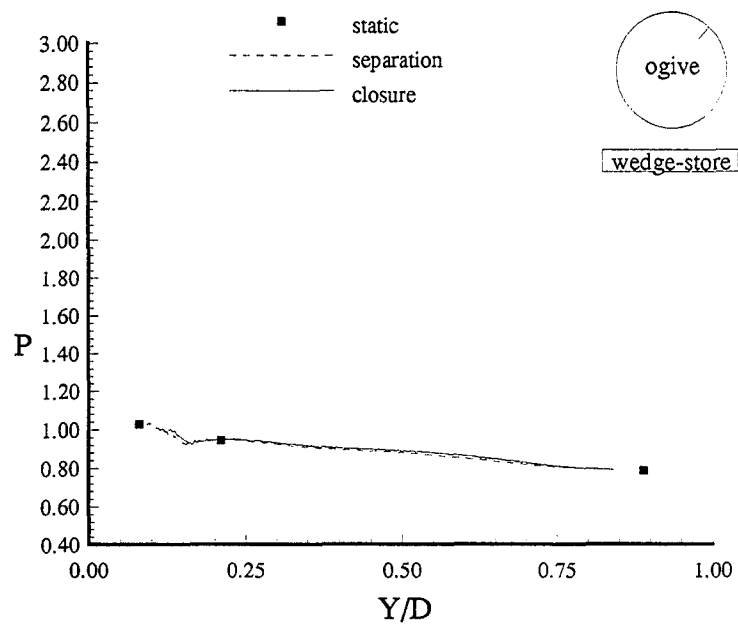
Figure B.36.   Ogive surface pressure at X/YE=3.10 and $\psi = 90°$ (6.1° wedge-store, M = 1.9).
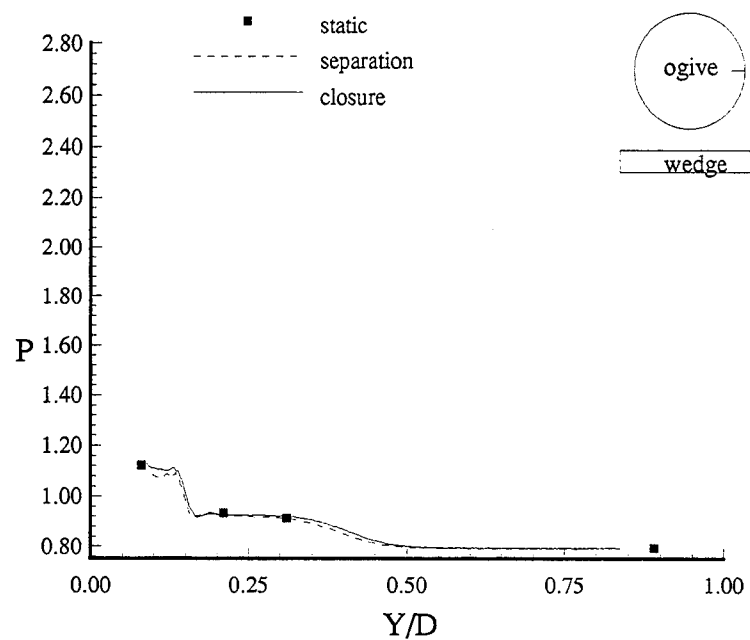
Figure B.37. Ogive surface pressure at X/YE=3.37 and $\psi = 90°$ (6.1° wedge-store, M = 1.9).
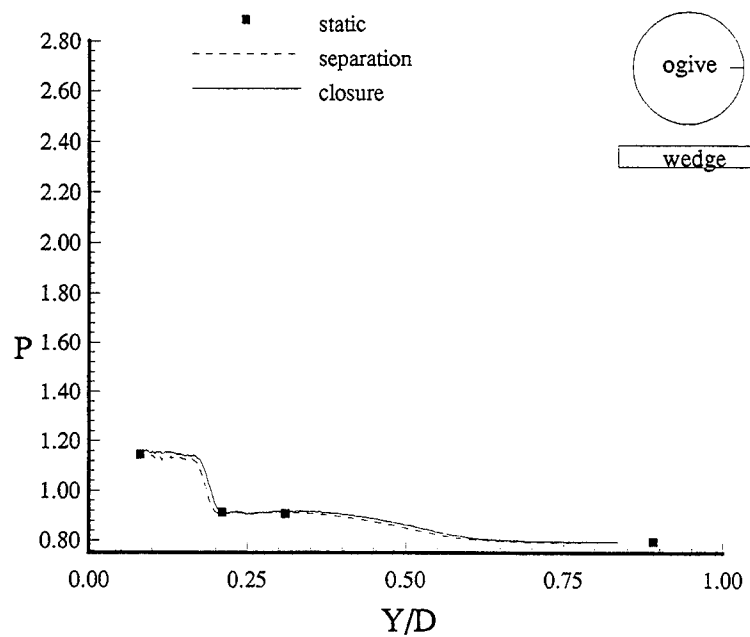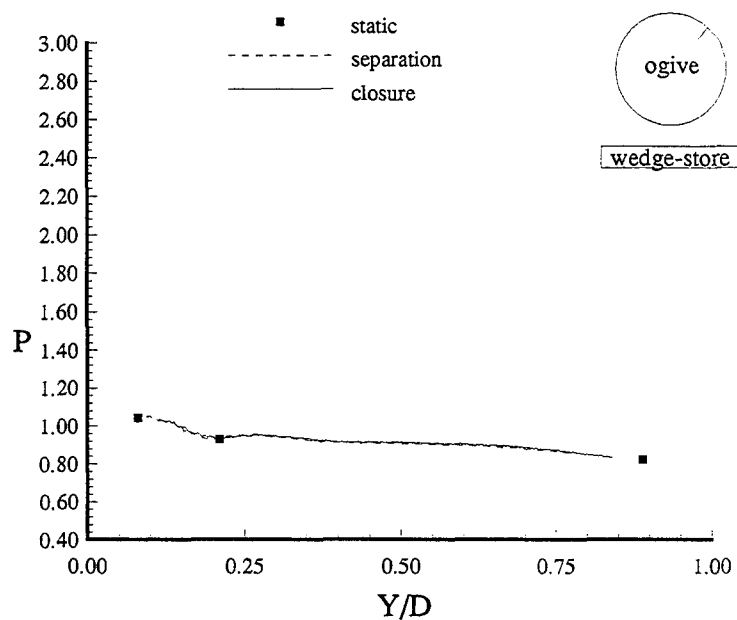

Figure B.38. Ogive surface pressure at X/YE=3.64 and $\psi = 90°$ (6.1° wedge-store, M = 1.9).
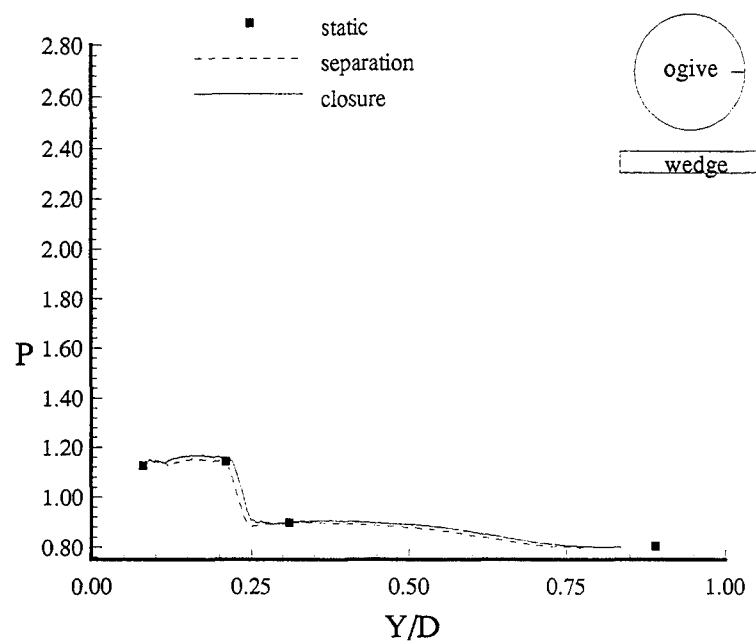
Figure B.39.   Ogive surface pressure at X/YE=3.90 and $\psi = 90°$ (6.1° wedge-store, M = 1.9).
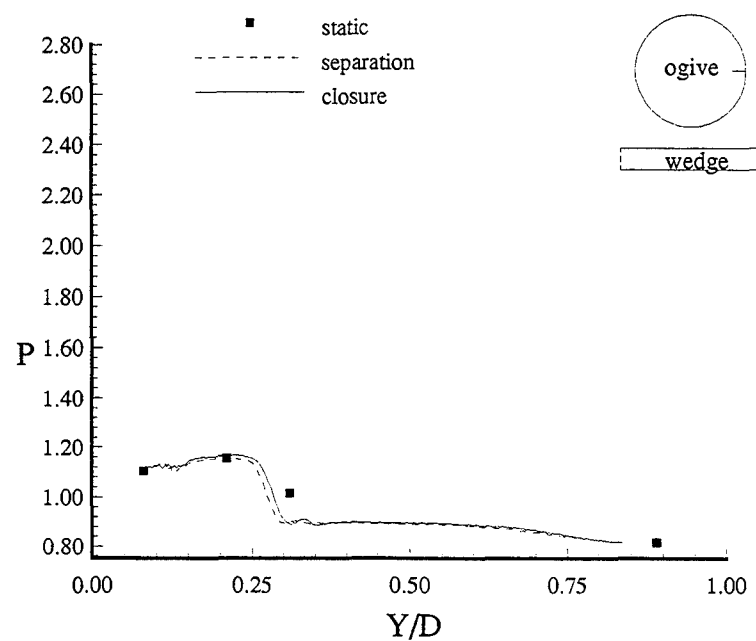
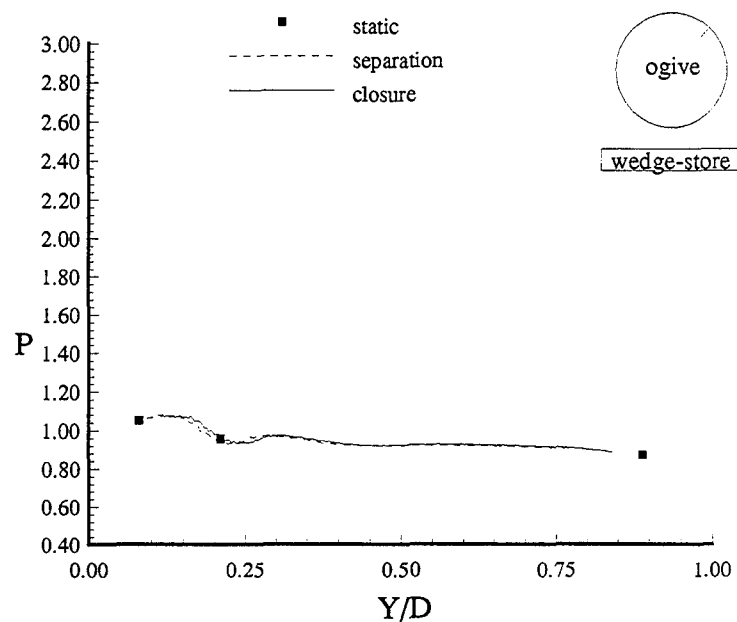Figure B.40.   Ogive surface pressure at X/YE=4.17 and $\psi = 90°$ (6.1° wedge-store, M = 1.9).
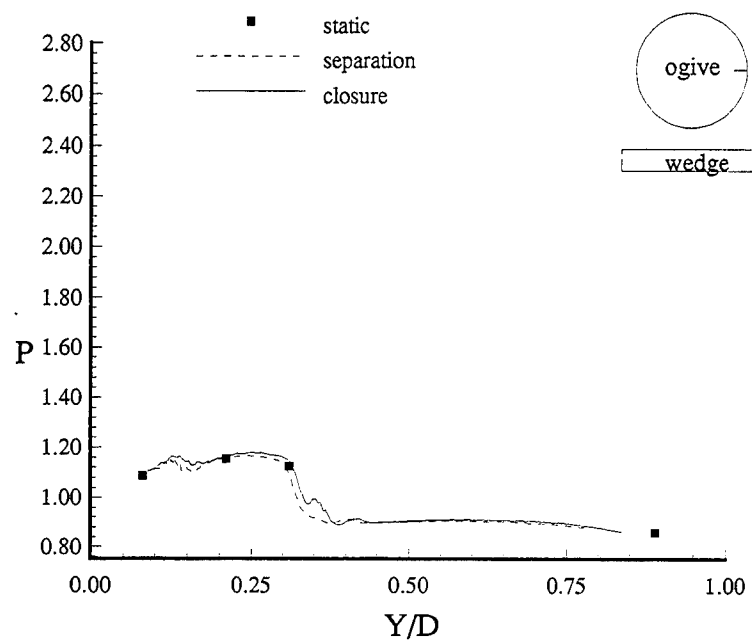
Figure B.41. Ogive surface pressure at X/YE=4.43 and $\psi = 90°$ (6.1° wedge-store, M = 1.9).
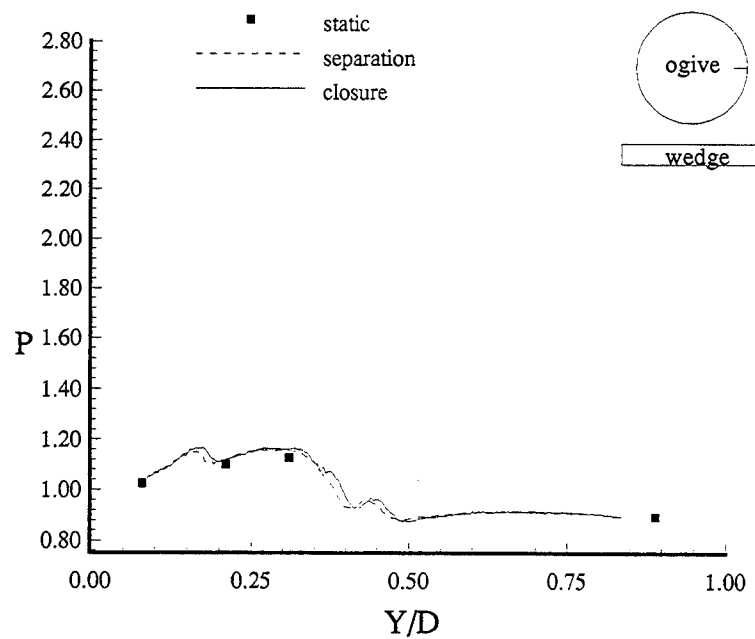
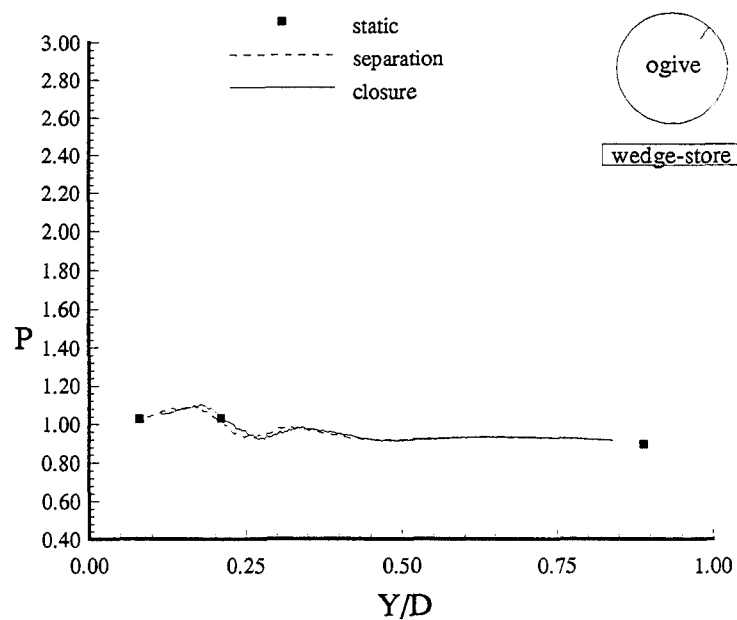

Figure B.42. Ogive surface pressure at X/YE=4.70 and $\psi = 90°$ (6.1° wedge-store, M = 1.9).
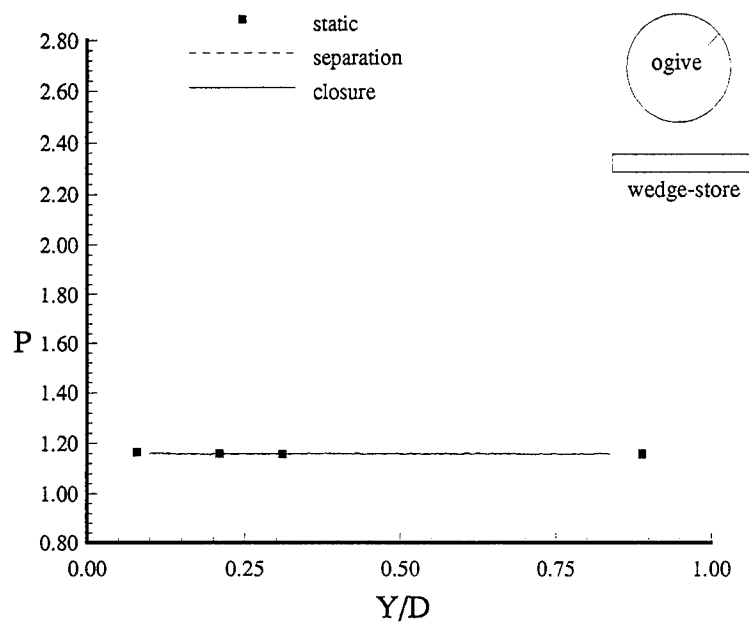
Figure B.43. Ogive surface pressure at X/YE=2.31 and $\psi = 135°$ (6.1° wedge-store, M = 1.9).
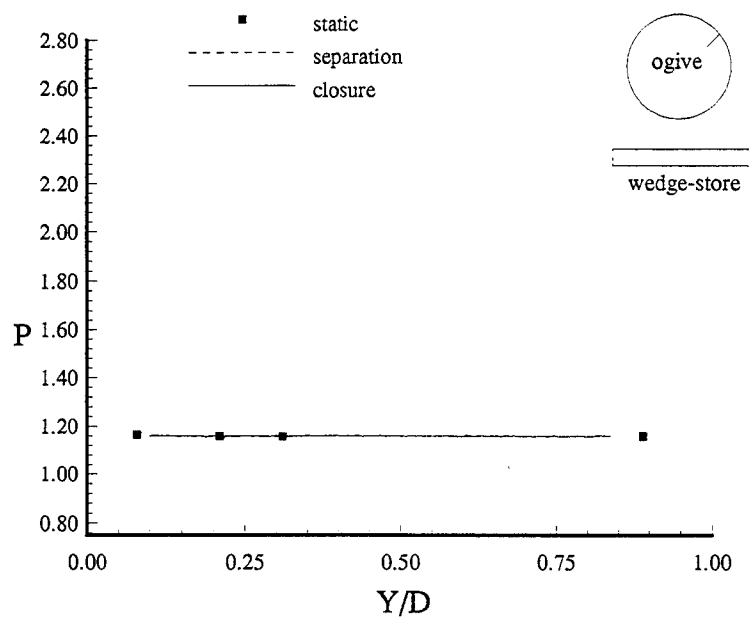
Figure B.44. Ogive surface pressure at X/YE=2.57 and $\psi = 135°$ (6.1° wedge-store, M = 1.9).
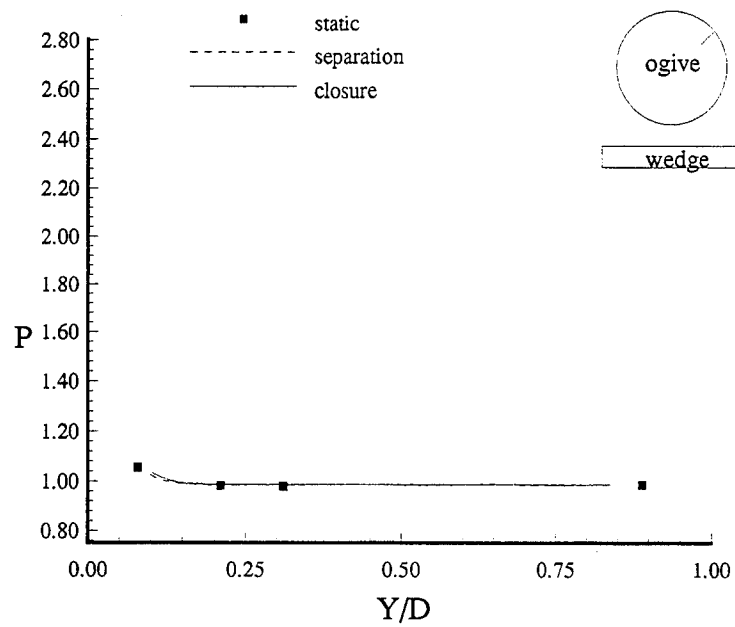
Figure B.45.   Ogive surface pressure at X/YE=2.84 and $\psi = 135°$ (6.1° wedge-store, M = 1.9).
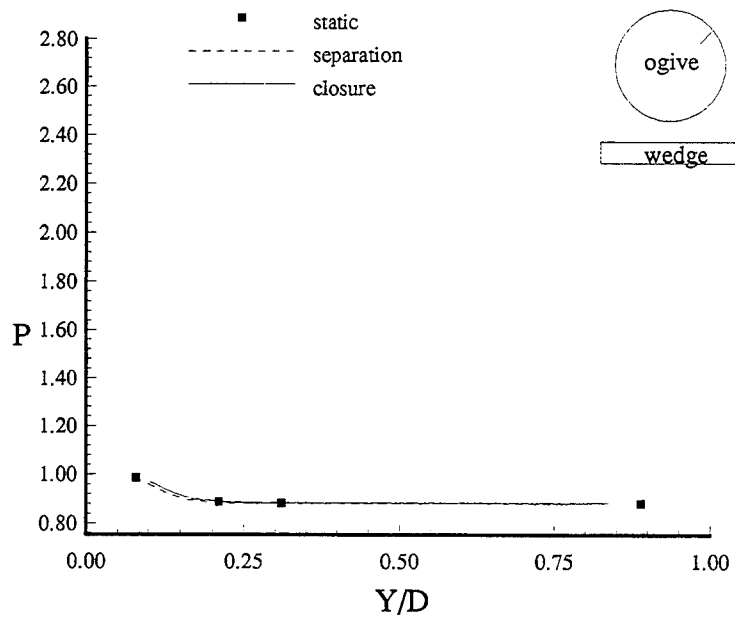
Figure B.46.   Ogive surface pressure at X/YE=3.10 and $\psi = 135°$ (6.1° wedge-store, M = 1.9).
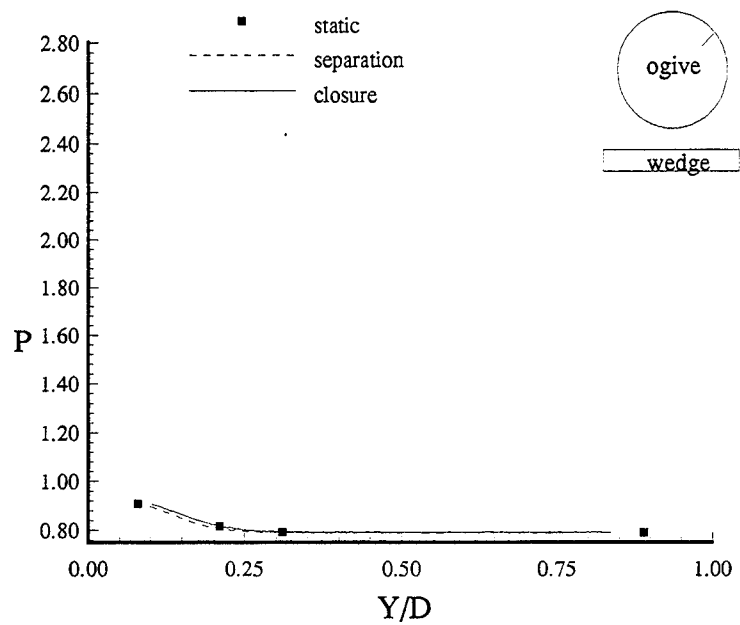
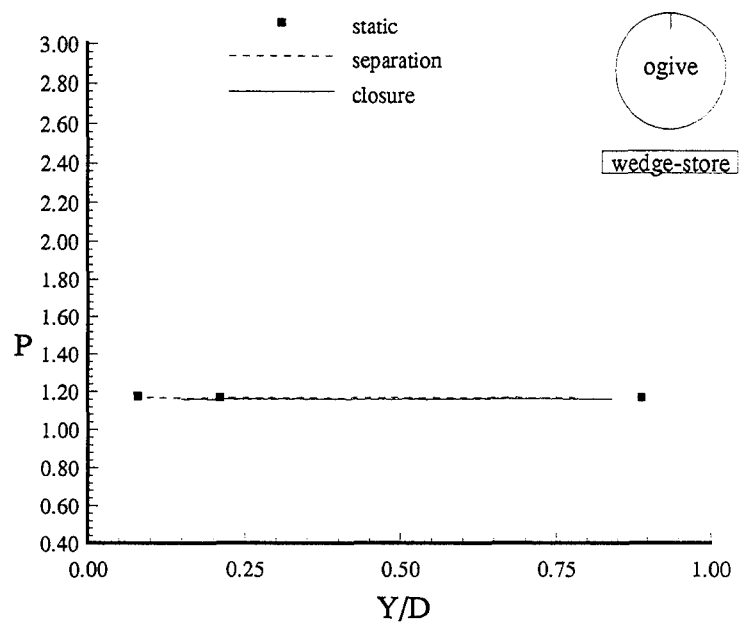Figure B.47.   Ogive surface pressure at X/YE=3.37 and $\psi = 135°$ (6.1° wedge-store, M = 1.9).
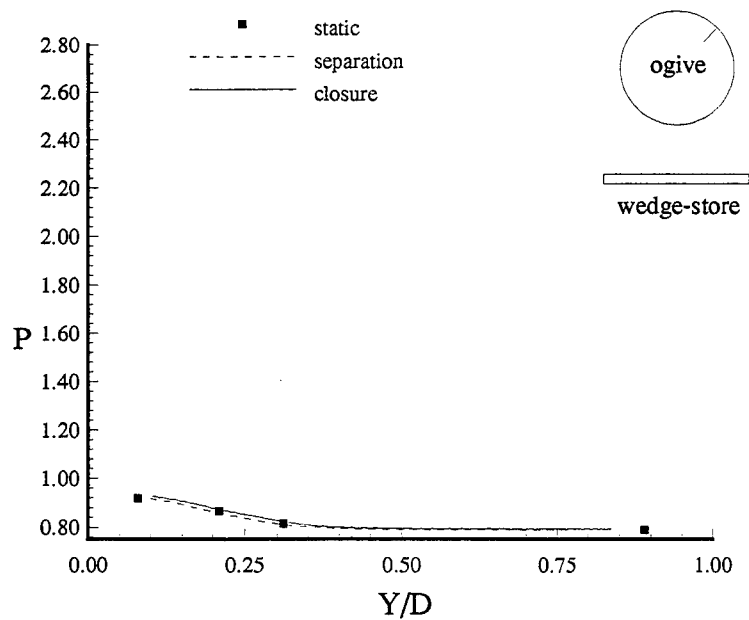
Figure B.48.   Ogive surface pressure at X/YE=3.64 and $\psi = 135°$ (6.1° wedge-store, M = 1.9).
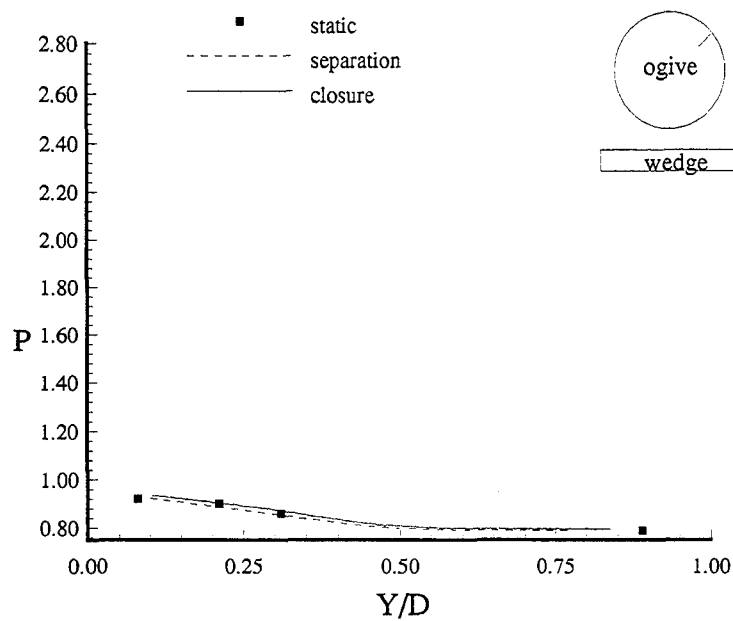
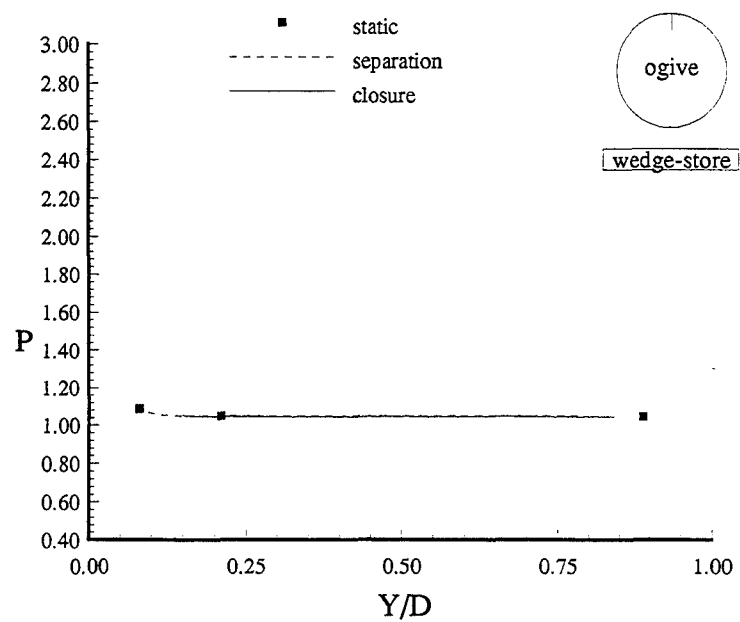Figure B.49. Ogive surface pressure at X/YE=3.90 and $\psi = 135°$ (6.1° wedge-store, M = 1.9).
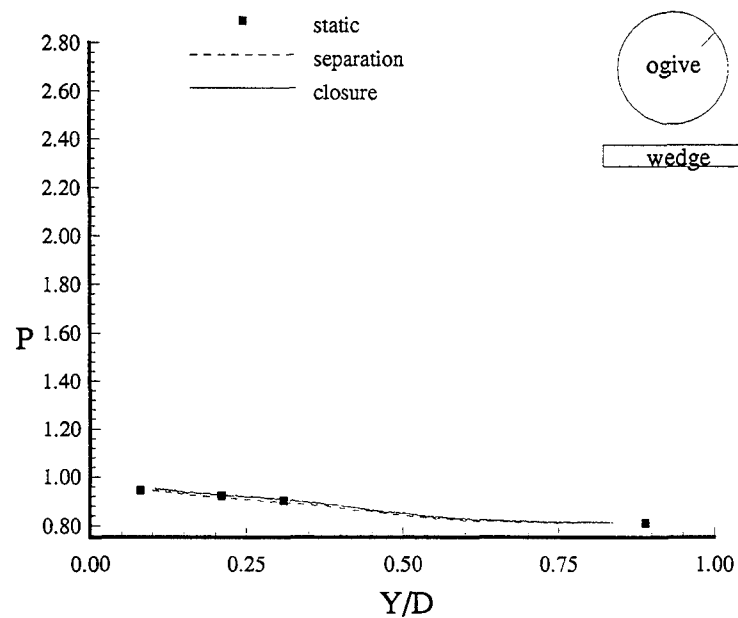
Figure B.50. Ogive surface pressure at X/YE=4.17 and $\psi = 135°$ (6.1° wedge-store, M = 1.9).
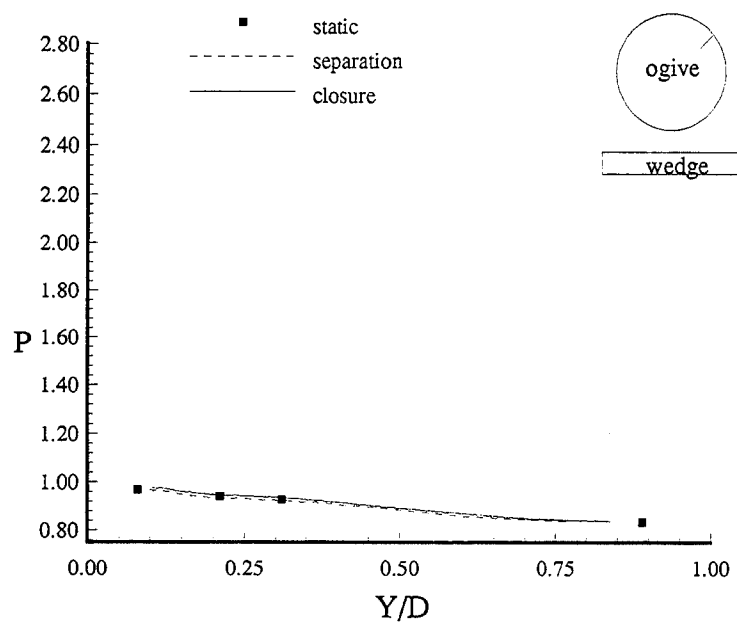
Figure B.51. Ogive surface pressure at X/YE=4.43 and $\psi = 135°$ (6.1° wedge-store, M = 1.9).
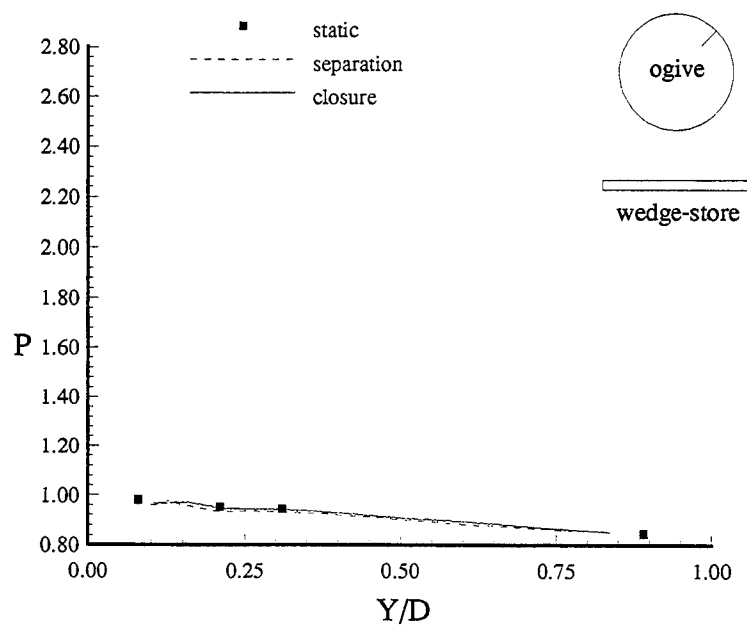
Figure B.52. Ogive surface pressure at X/YE=4.70 and $\psi = 135°$ (6.1° wedge-store, M = 1.9).
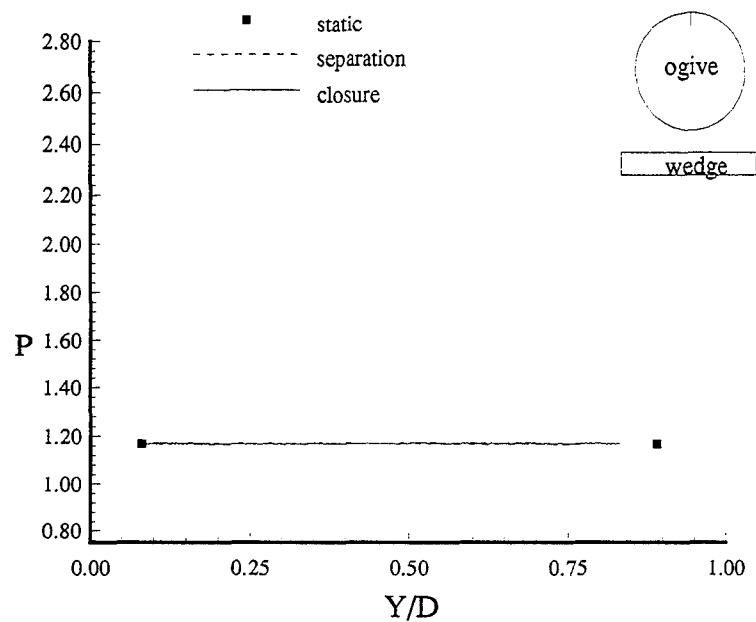
Figure B.53. Ogive surface pressure at X/YE=2.31 and $\psi = 180°$ (6.1° wedge-store, M = 1.9).
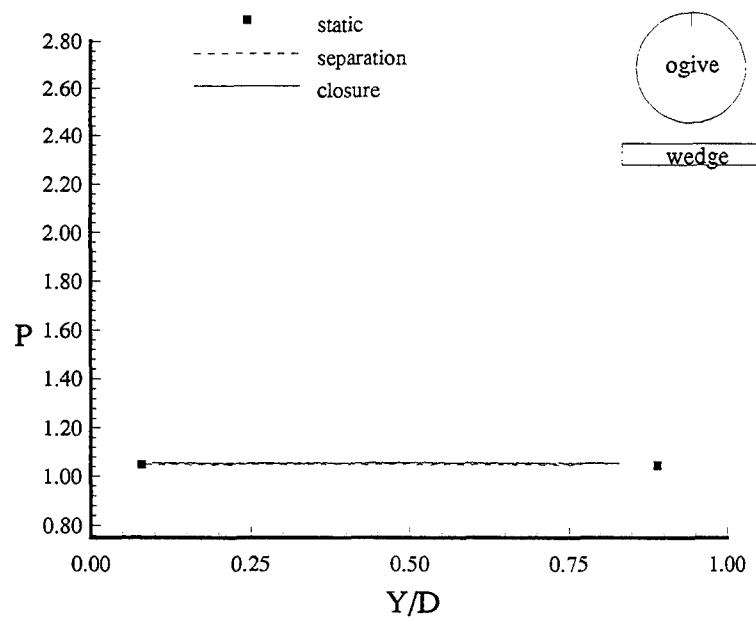
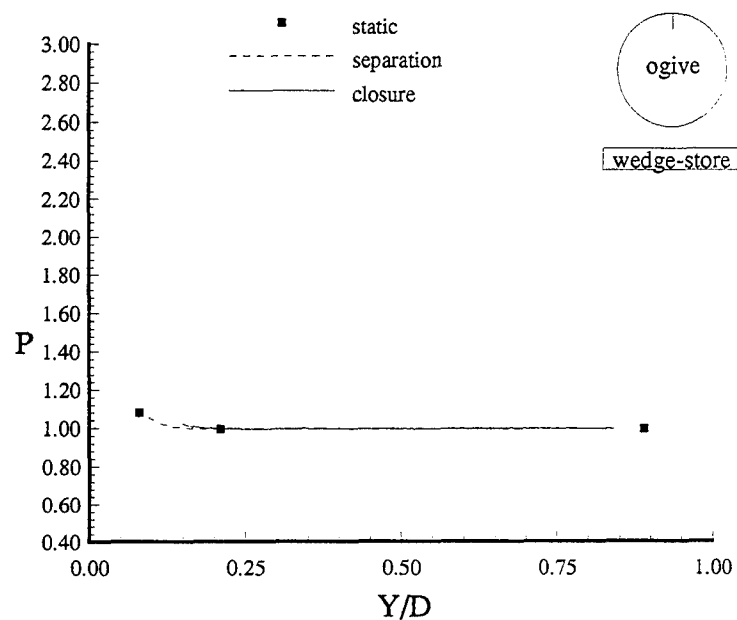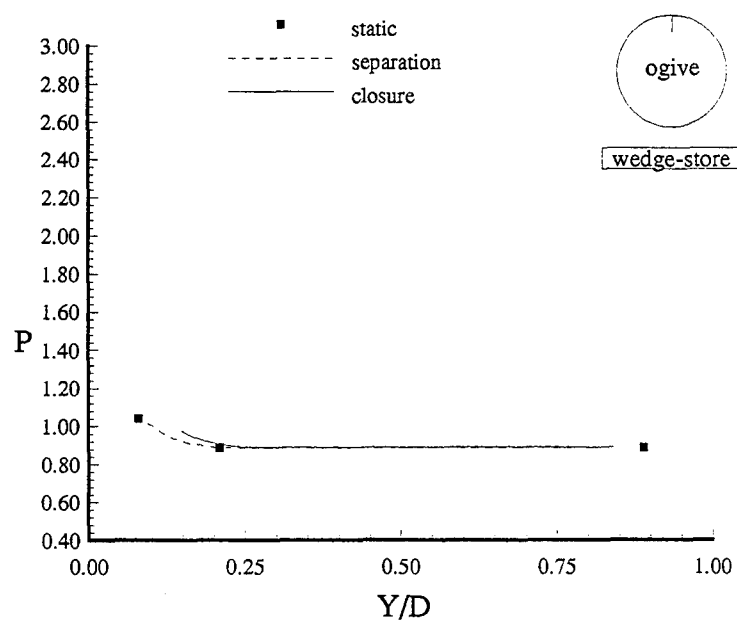Figure B.54. Ogive surface pressure at X/YE=2.57 and $\psi = 180°$ (6.1° wedge-store, M = 1.9).
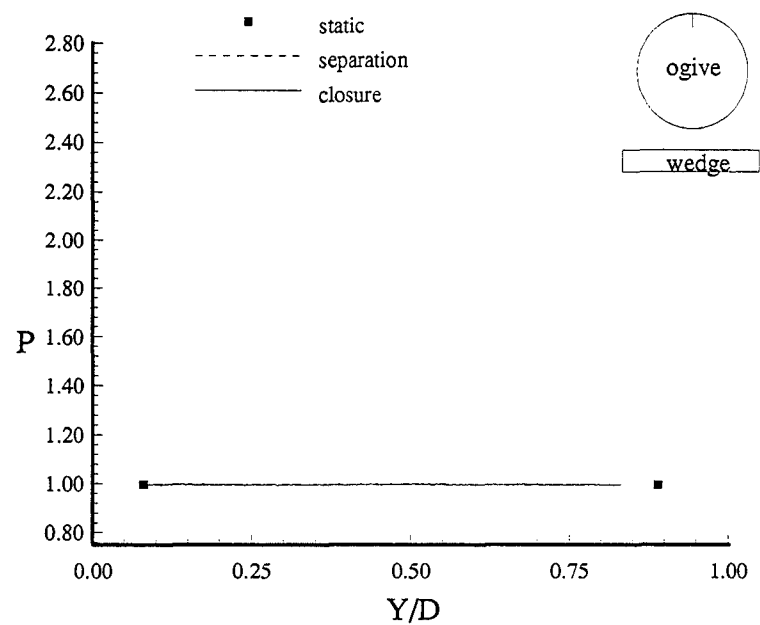
Figure B.55. Ogive surface pressure at X/YE=2.84 and $\psi = 180°$ (6.1° wedge-store, M = 1.9).
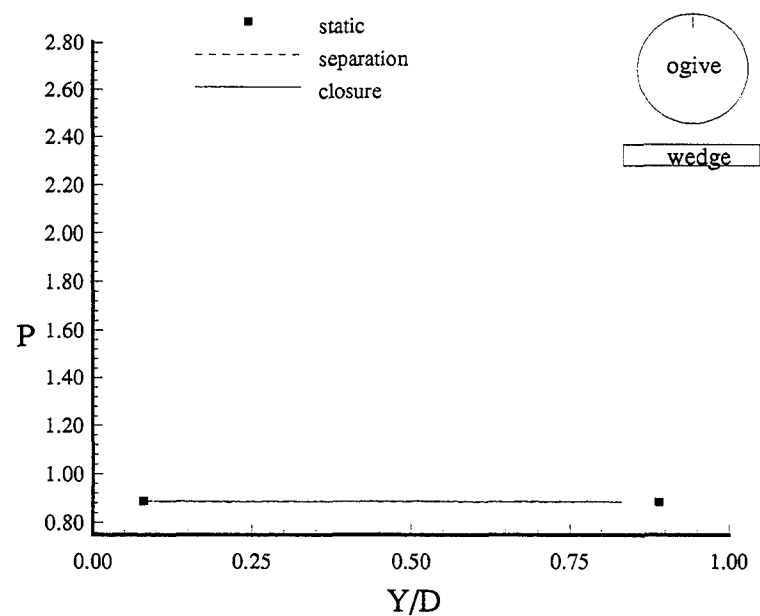
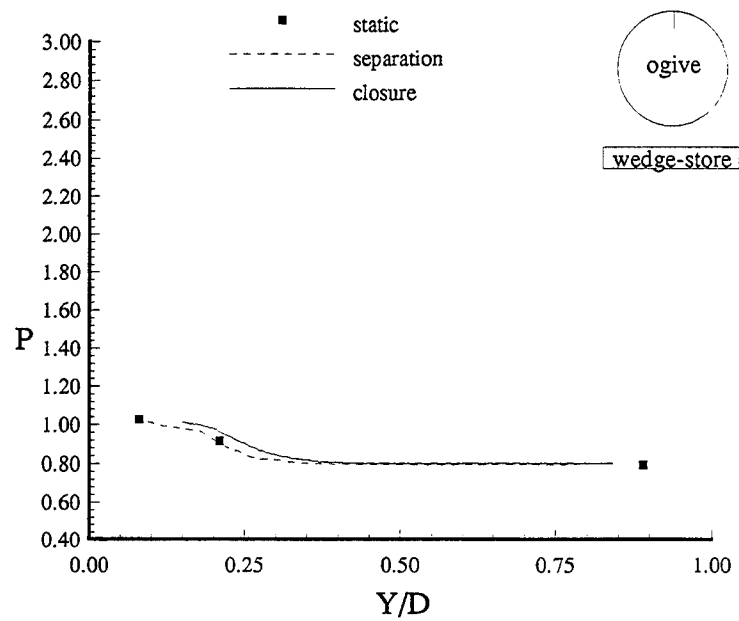Figure B.56. Ogive surface pressure at X/YE=3.10 and $\psi = 180°$ (6.1° wedge-store, M = 1.9).
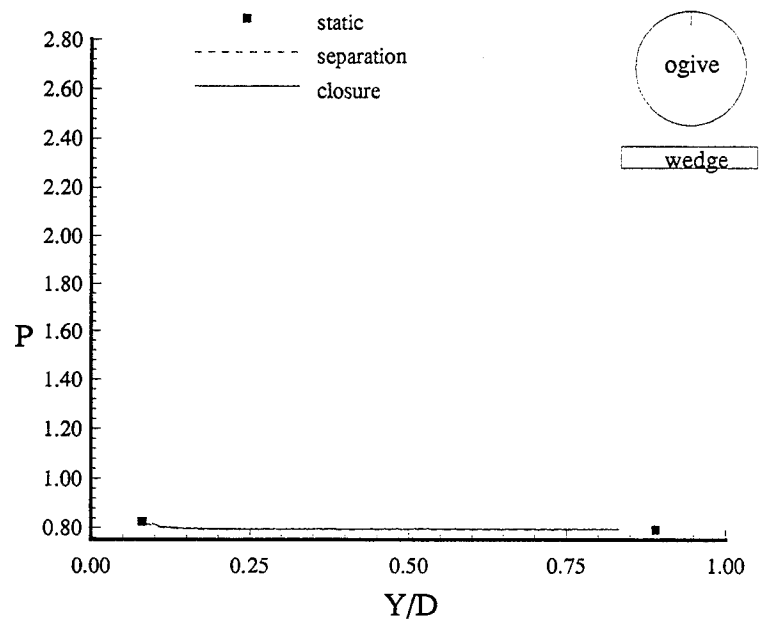
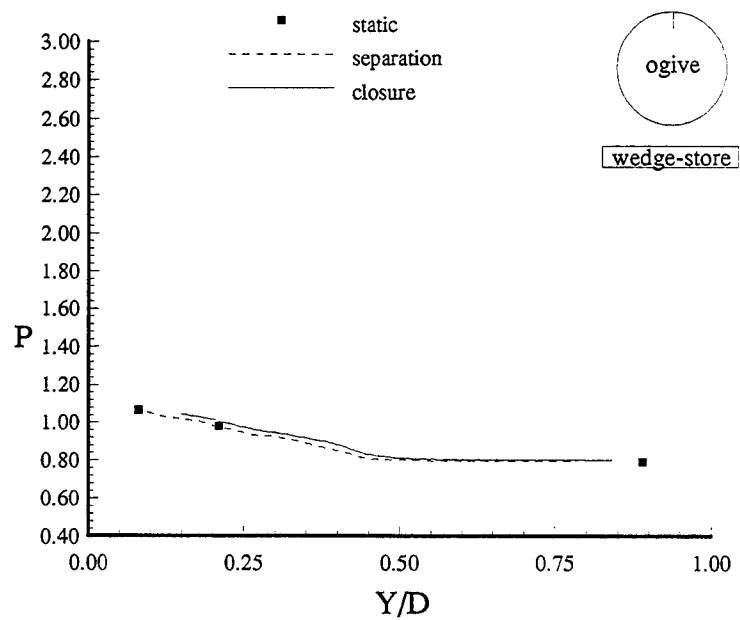Figure B.57. Ogive surface pressure at X/YE=3.37 and $\psi = 180°$ (6.1° wedge-store, M = 1.9).
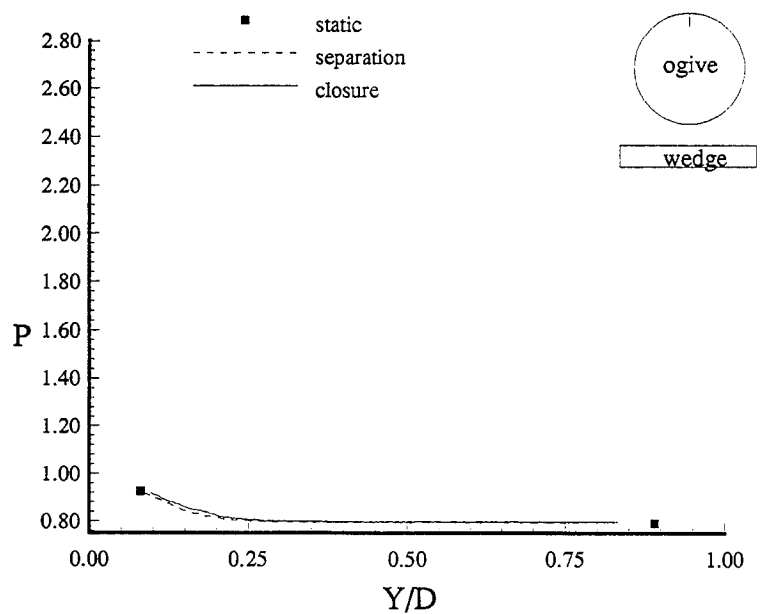
Figure B.58. Ogive surface pressure at X/YE=3.64 and $\psi = 180°$ (6.1° wedge-store, M = 1.9).
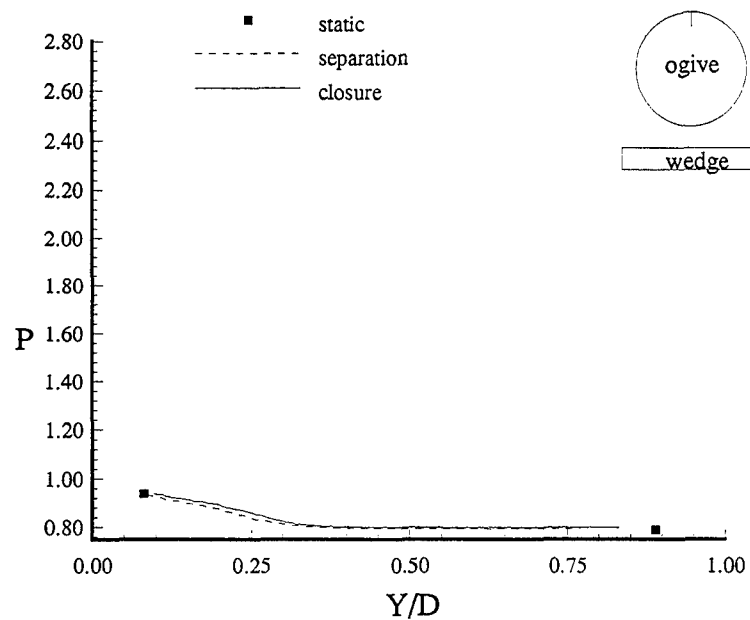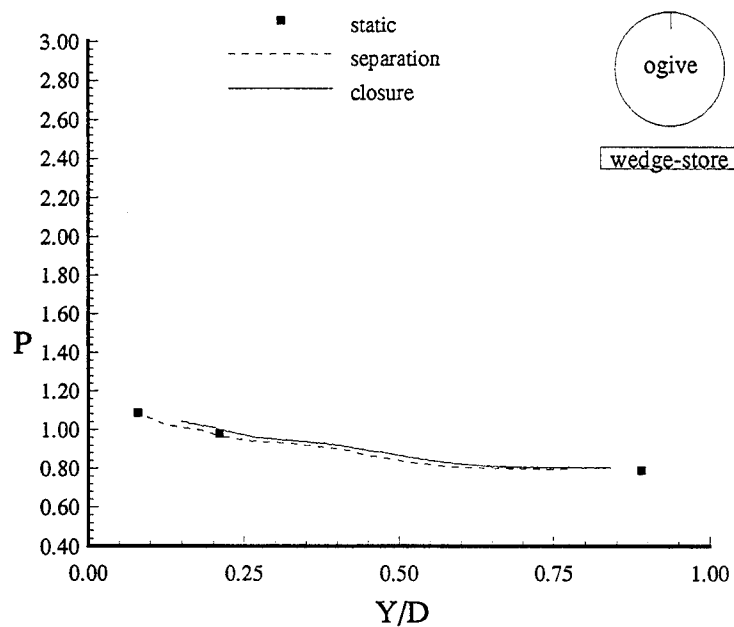
Figure B.59.   Ogive surface pressure at X/YE=3.90 and $\psi = 180°$ (6.1° wedge-store, M = 1.9).
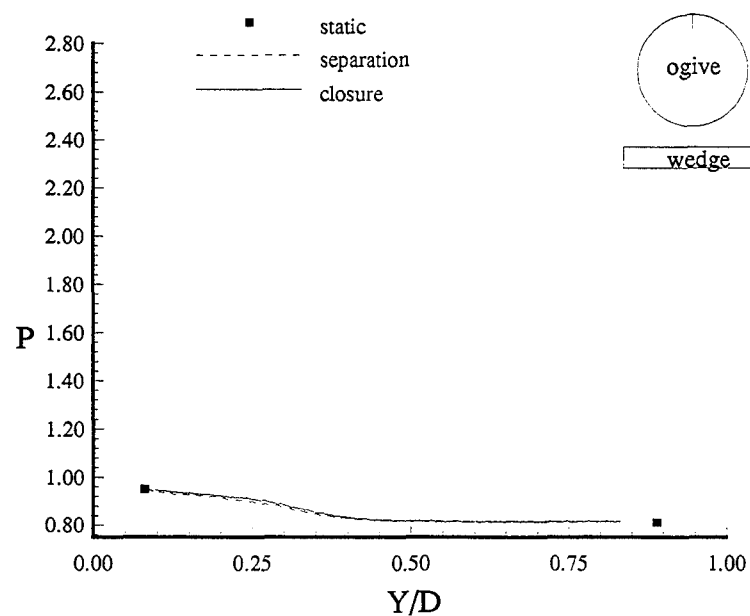
Figure B.60.   Ogive surface pressure at X/YE=4.17 and $\psi = 180°$ (6.1° wedge-store, M = 1.9).
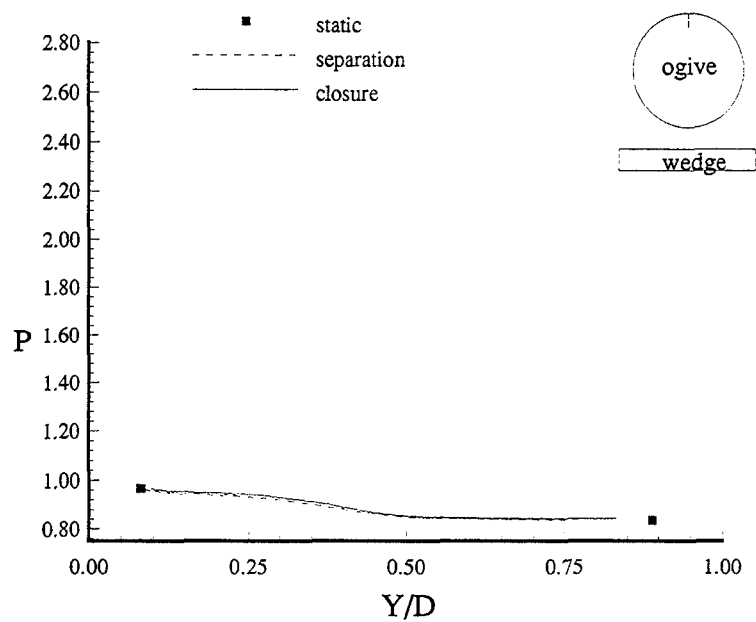
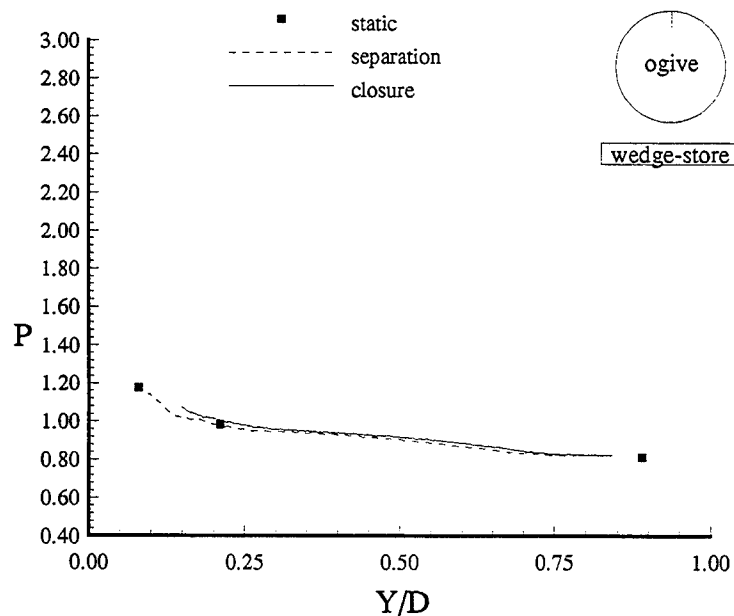Figure B.61.   Ogive surface pressure at X/YE=4.43 and $\psi = 180°$ (6.1° wedge-store, M = 1.9).
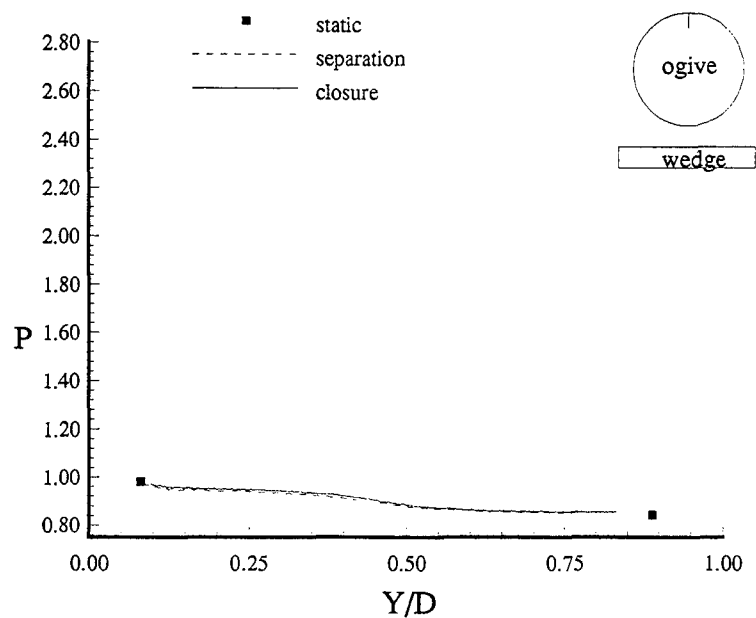
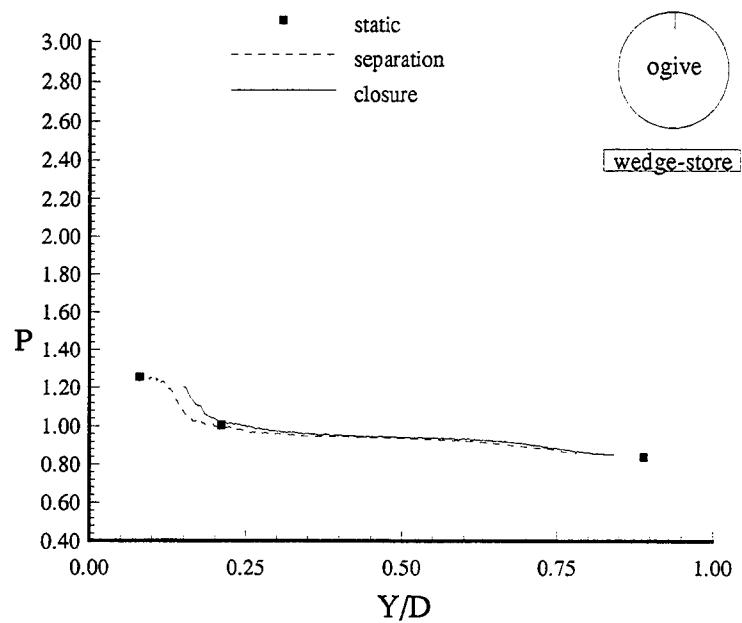Figure B.62.   Ogive surface pressure at X/YE=4.70 and $\psi = 180°$ (6.1° wedge-store, M = 1.9).
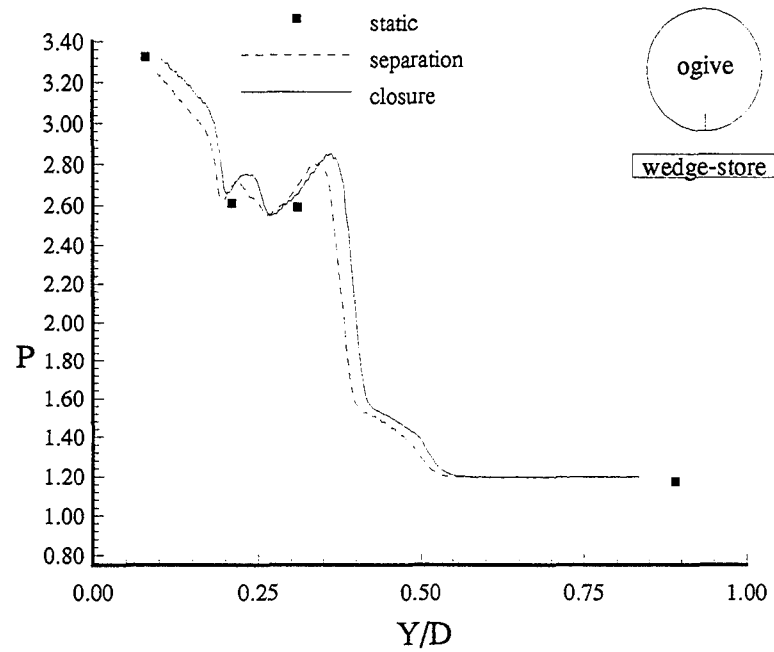
Figure B.63. Ogive surface pressure at X/YE=2.31 and $\psi = 0°$ (12.32° wedge-store, M = 1.9).
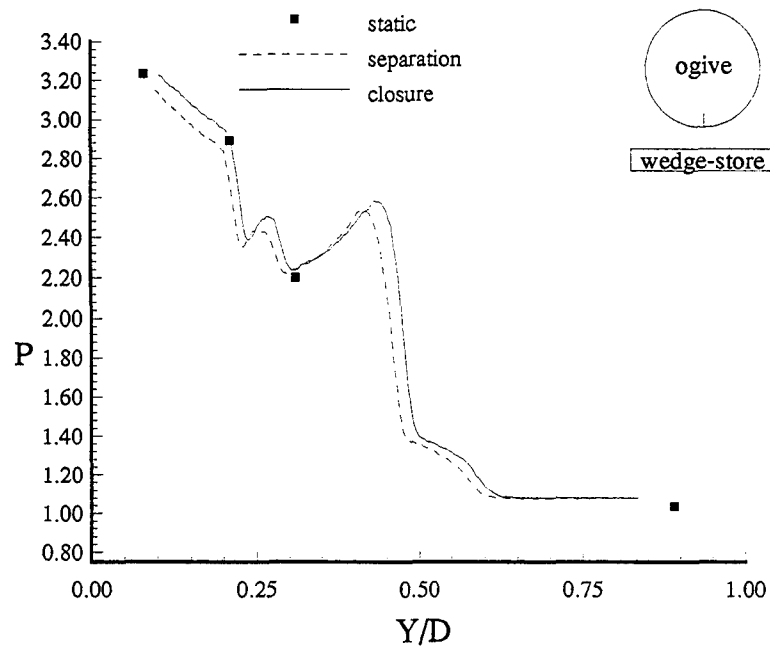
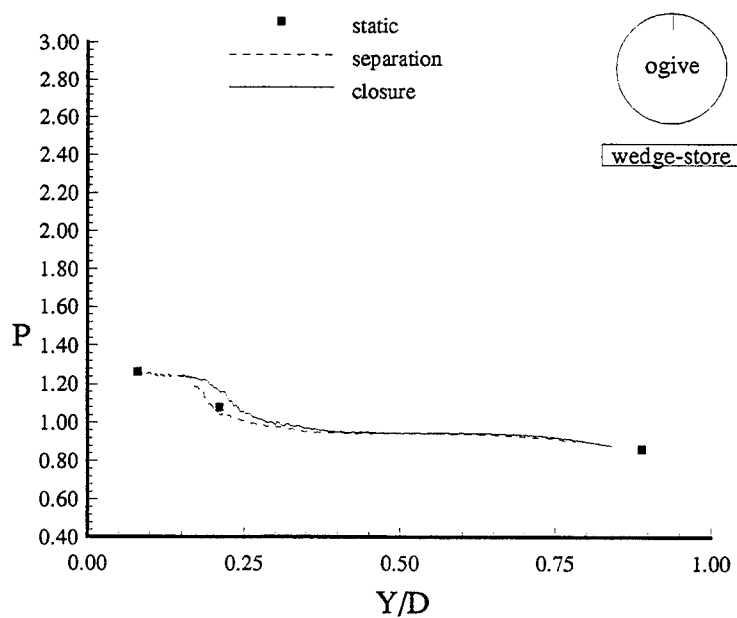
Figure B.64. Ogive surface pressure at X/YE=2.57 and $\psi = 0°$ (12.32° wedge-store, M = 1.9).
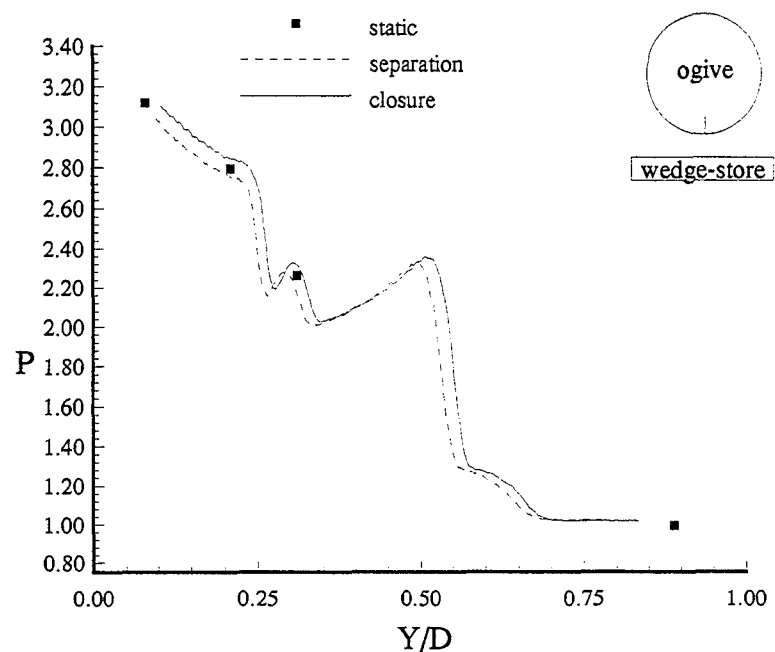
Figure B.65. Ogive surface pressure at X/YE=2.84 and $\psi = 0°$ (12.32° wedge-store, $M = 1.9$).
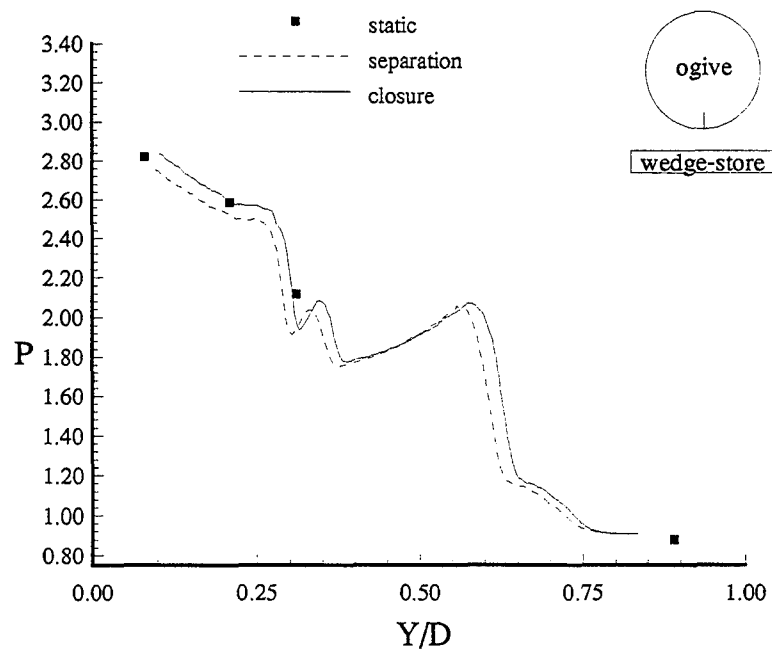
Figure B.66. Ogive surface pressure at X/YE=3.10 and $\psi = 0°$ (12.32° wedge-store, $M = 1.9$).
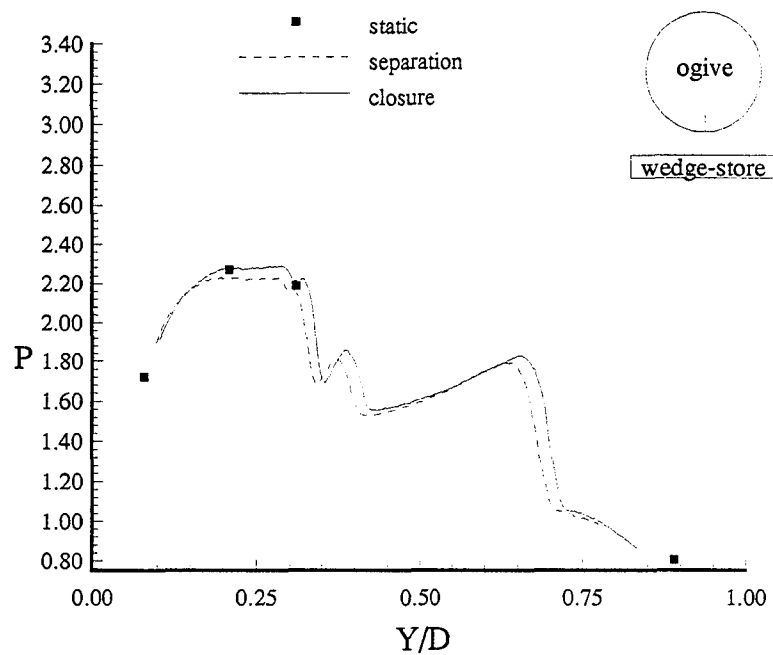
Figure B.67.   Ogive surface pressure at X/YE=3.37 and $\psi = 0°$ (12.32° wedge-store, M = 1.9).
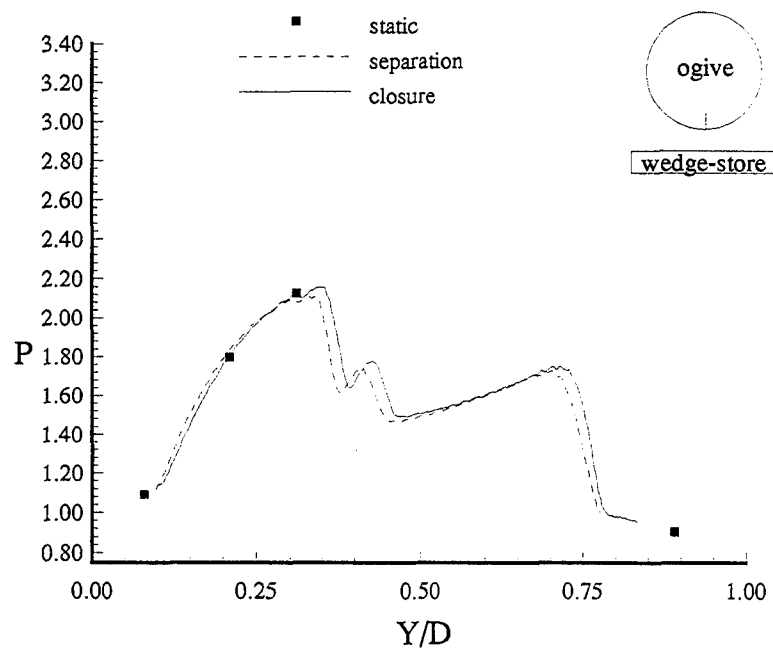
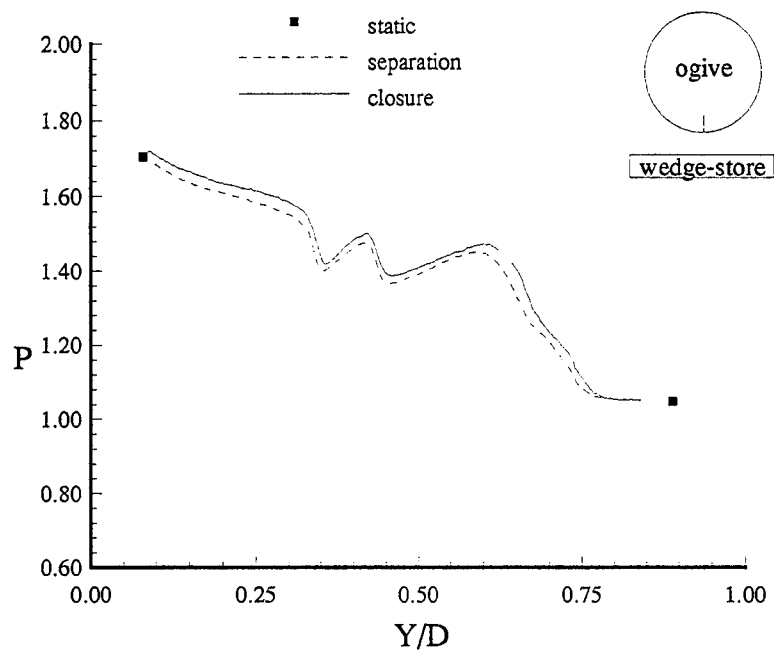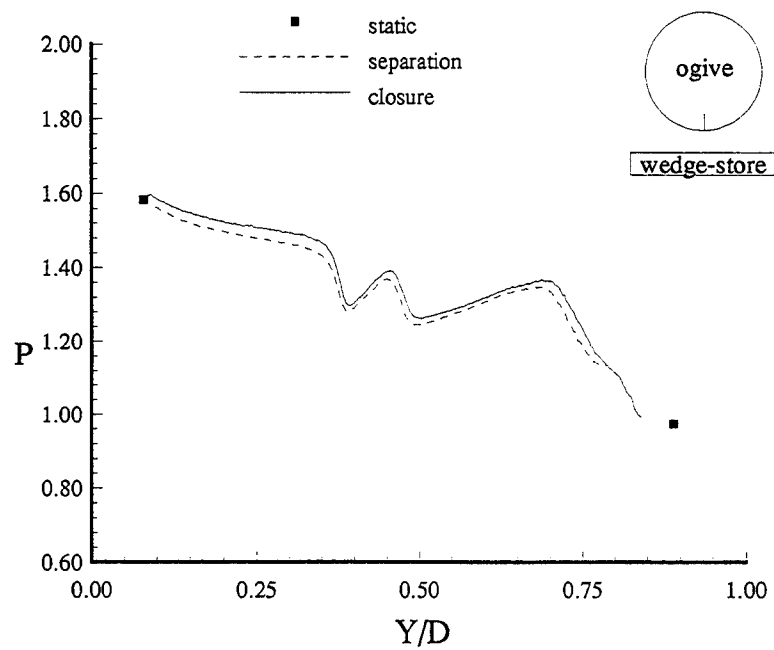Figure B.68.   Ogive surface pressure at X/YE=3.64 and $\psi = 0°$ (12.32° wedge-store, M = 1.9).
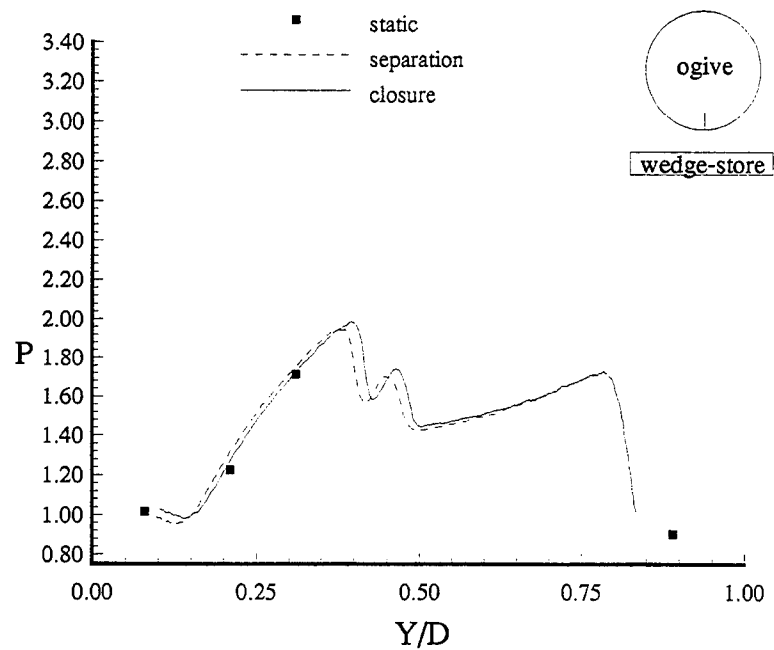
Figure B.69. Ogive surface pressure at X/YE=3.90 and $\psi = 0°$ (12.32° wedge-store, M = 1.9).
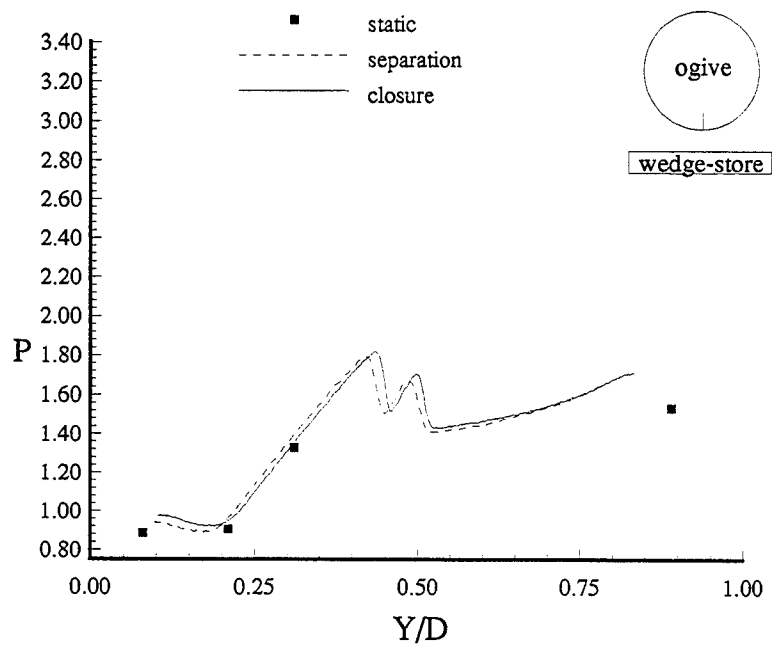
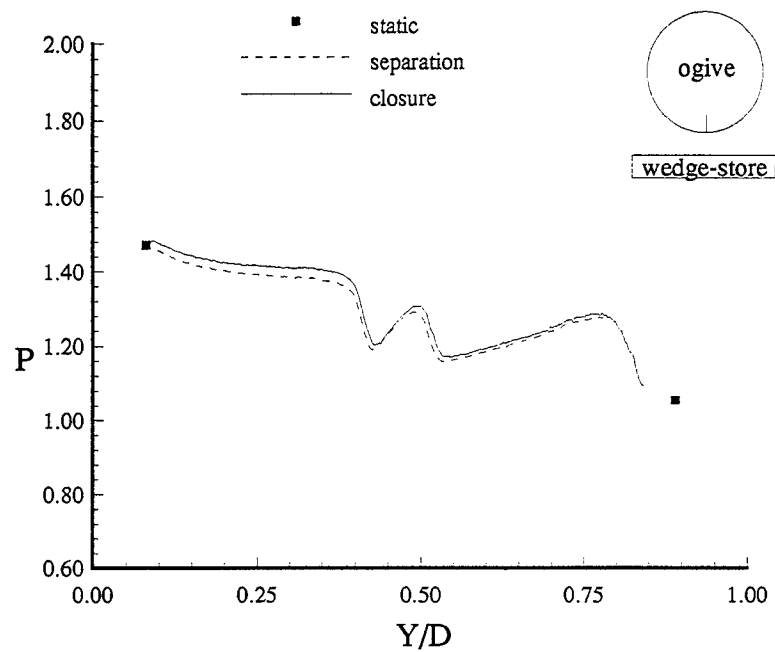Figure B.70. Ogive surface pressure at X/YE=4.17 and $\psi = 0°$ (12.32° wedge-store, M = 1.9).
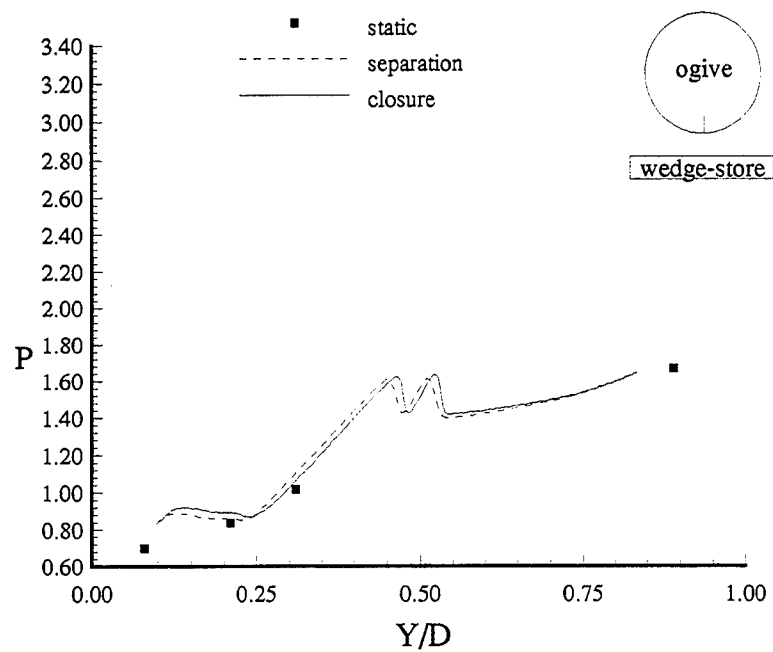
Figure B.71. Ogive surface pressure at X/YE=4.43 and $\psi = 0°$ (12.32° wedge-store, M = 1.9).
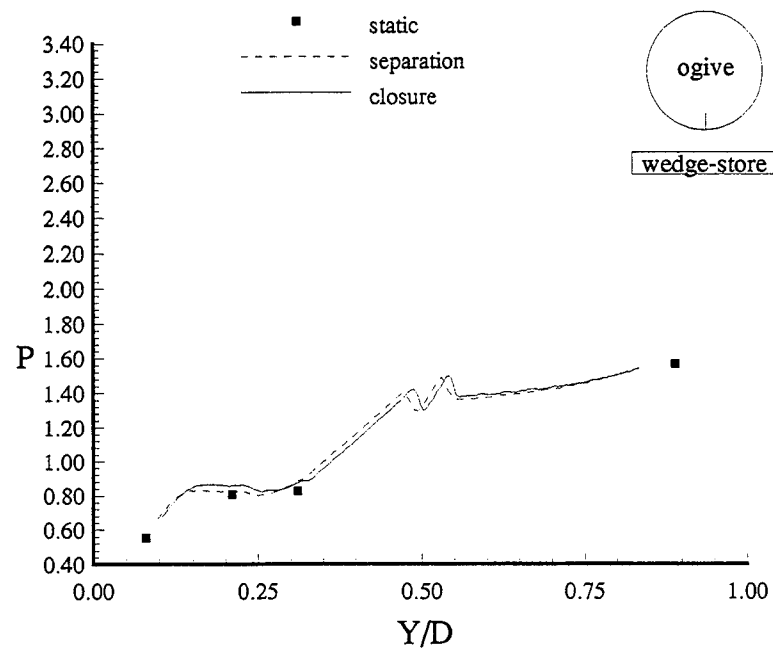
Figure B.72. Ogive surface pressure at X/YE=4.70 and $\psi = 0°$ (12.32° wedge-store, M = 1.9).
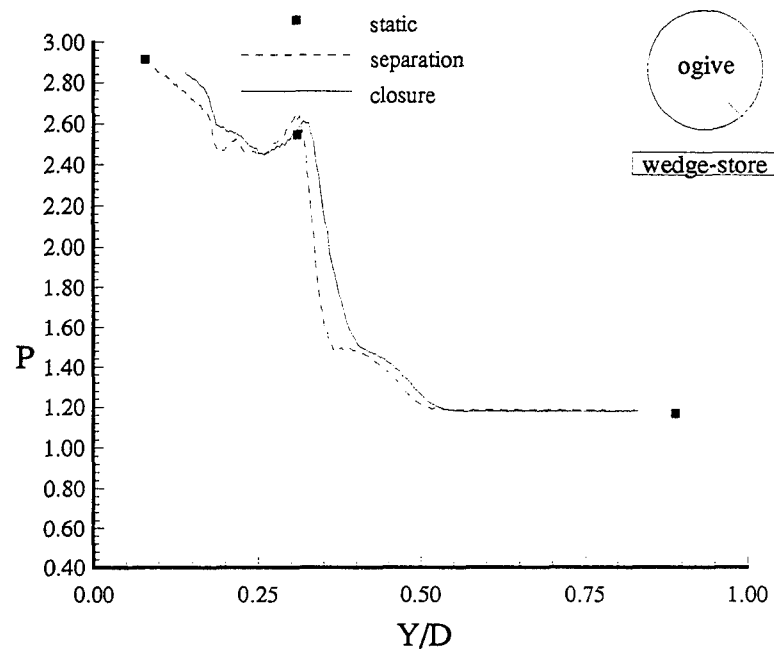
Figure B.73.   Ogive surface pressure at X/YE=2.31 and $\psi = 30°$ (12.32° wedge-store, M = 1.9).
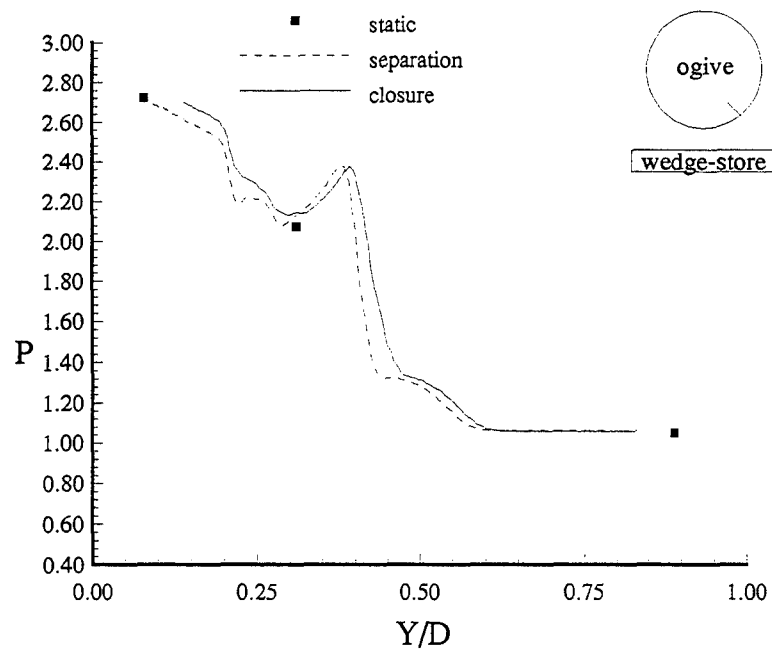
Figure B.74.   Ogive surface pressure at X/YE=2.57 and $\psi = 30°$ (12.32° wedge-store, M = 1.9).
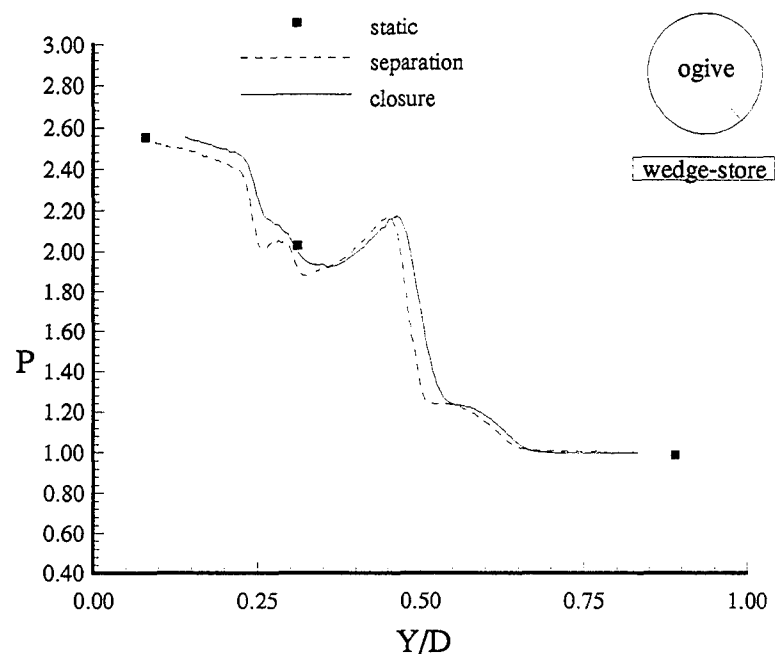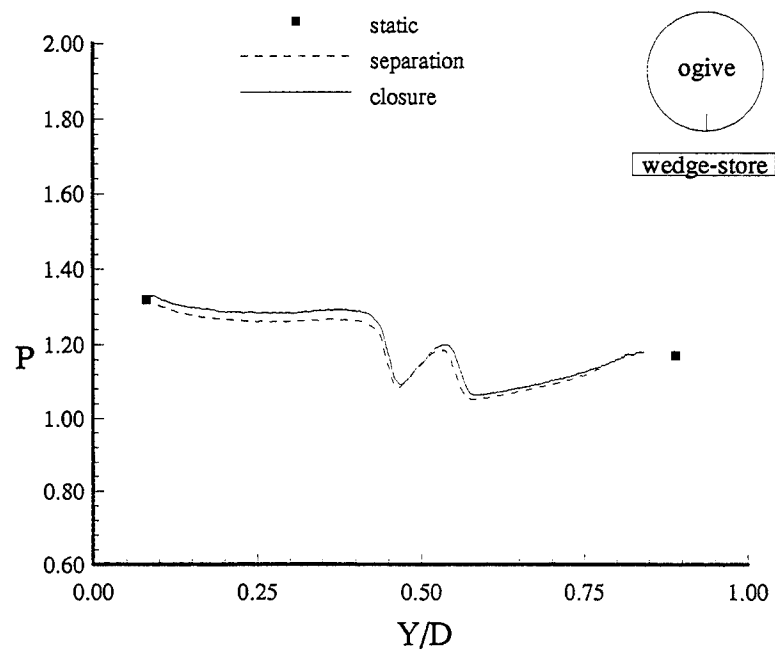
Figure B.75.   Ogive surface pressure at X/YE=2.84 and $\psi = 30°$ (12.32° wedge-store, M = 1.9).
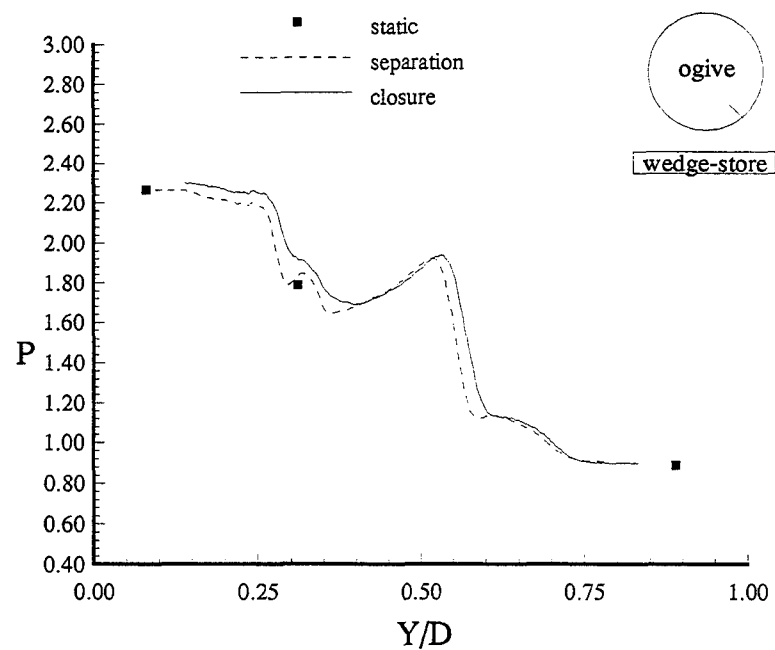
Figure B.76.   Ogive surface pressure at X/YE=3.10 and $\psi = 30°$ (12.32° wedge-store, M = 1.9).
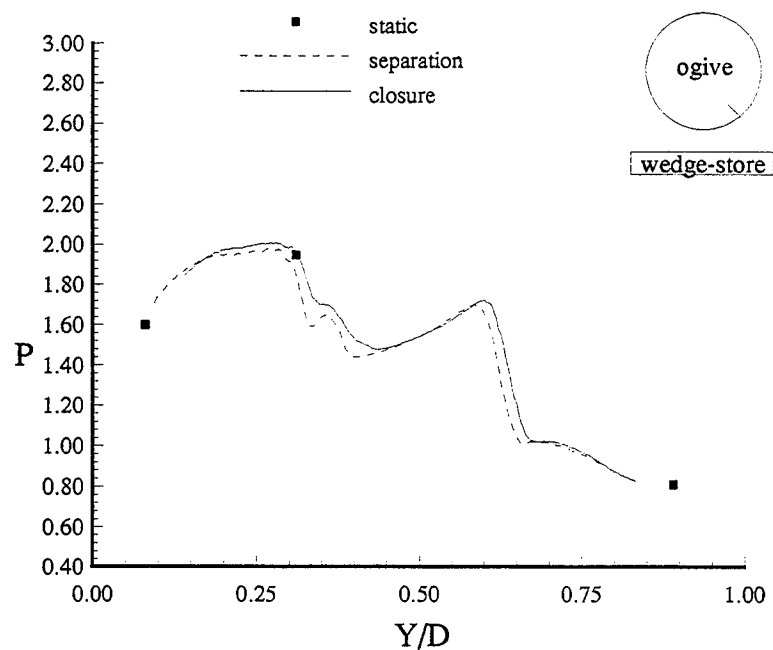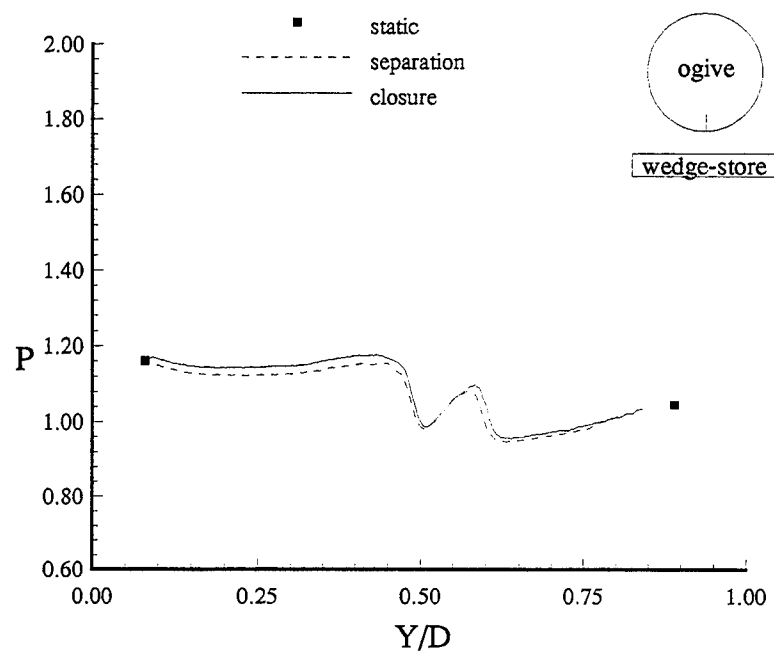
Figure B.77.   Ogive surface pressure at X/YE=3.37 and $\psi = 30°$ (12.32° wedge-store, M = 1.9).
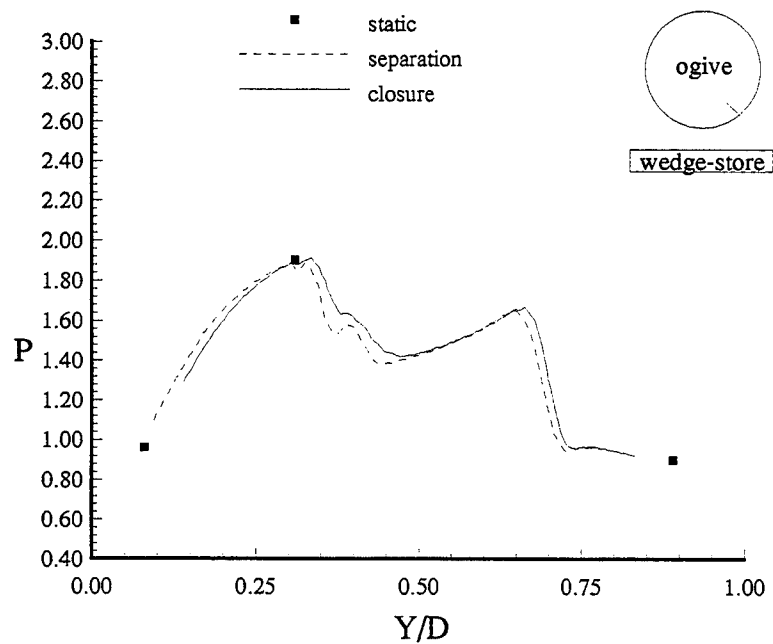
Figure B.78.   Ogive surface pressure at X/YE=3.64 and $\psi = 30°$ (12.32° wedge-store, M = 1.9).
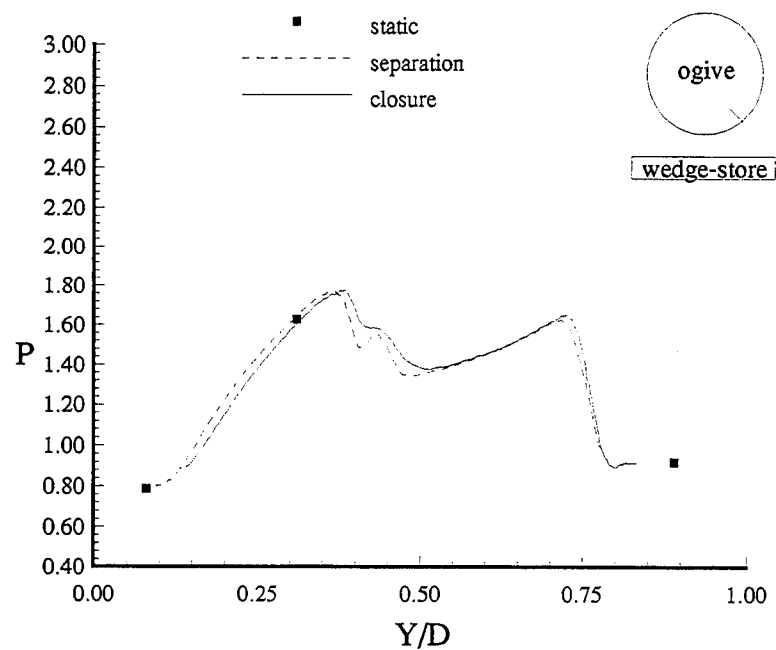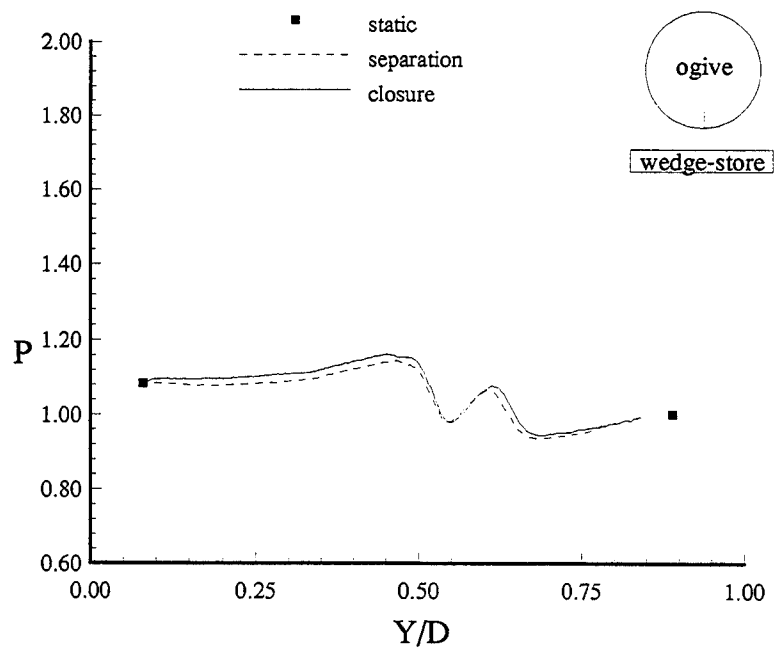
Figure B.79. Ogive surface pressure at X/YE=3.90 and $\psi = 30°$ (12.32° wedge-store, M = 1.9).
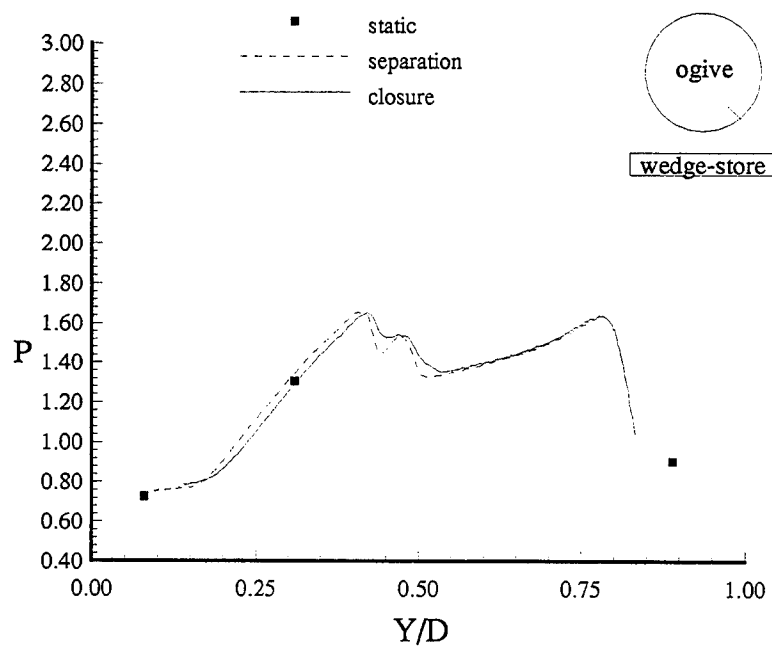
Figure B.80. Ogive surface pressure at X/YE=4.17 and $\psi = 30°$ (12.32° wedge-store, M = 1.9).
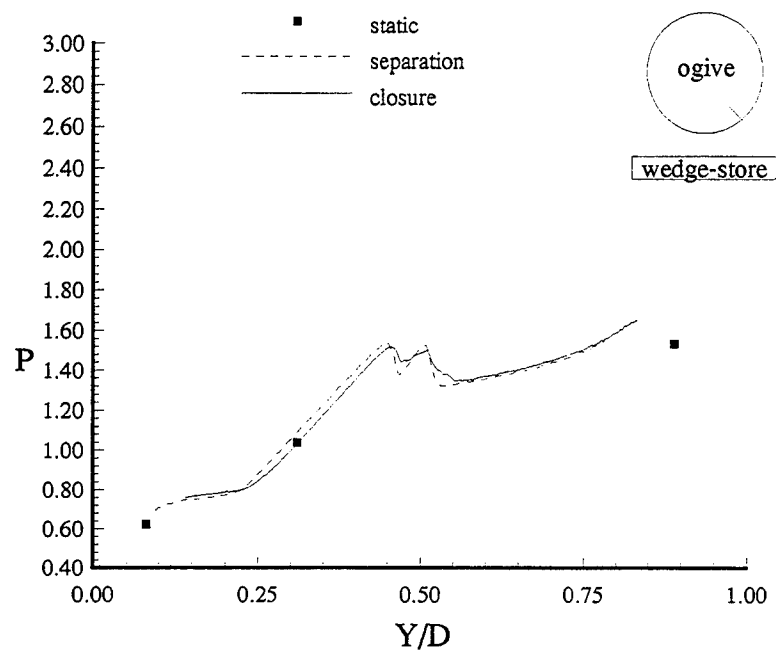
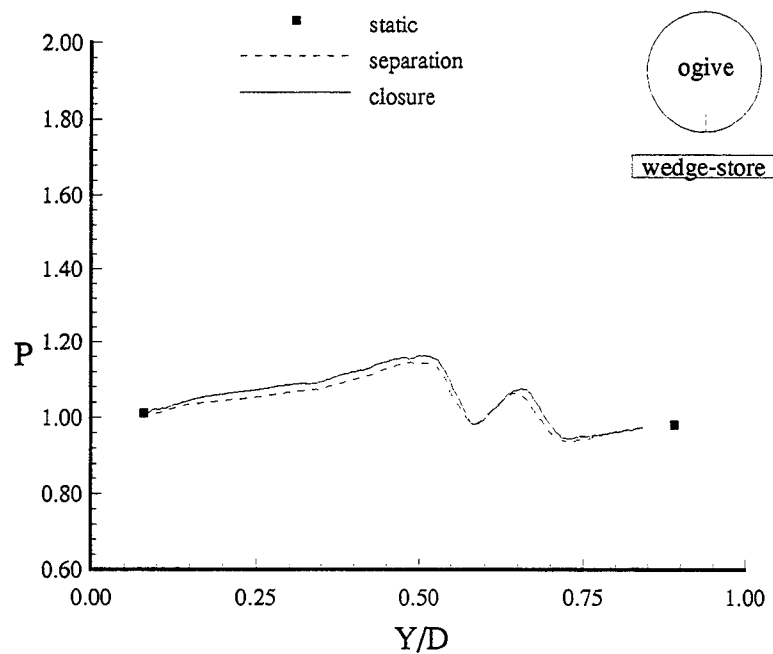Figure B.81. Ogive surface pressure at X/YE=4.43 and $\psi = 30°$ (12.32° wedge-store, M = 1.9).
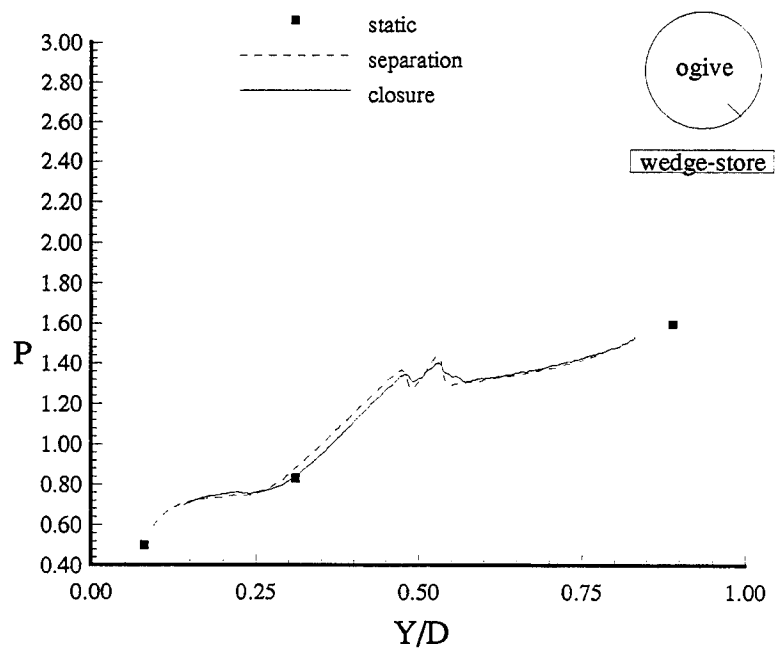
Figure B.82. Ogive surface pressure at X/YE=4.70 and $\psi = 30°$ (12.32° wedge-store, M = 1.9).
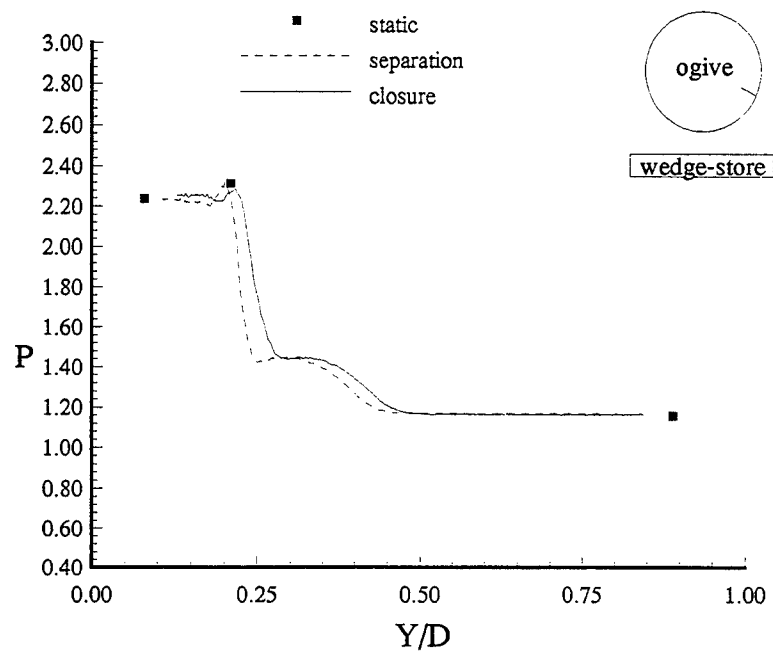
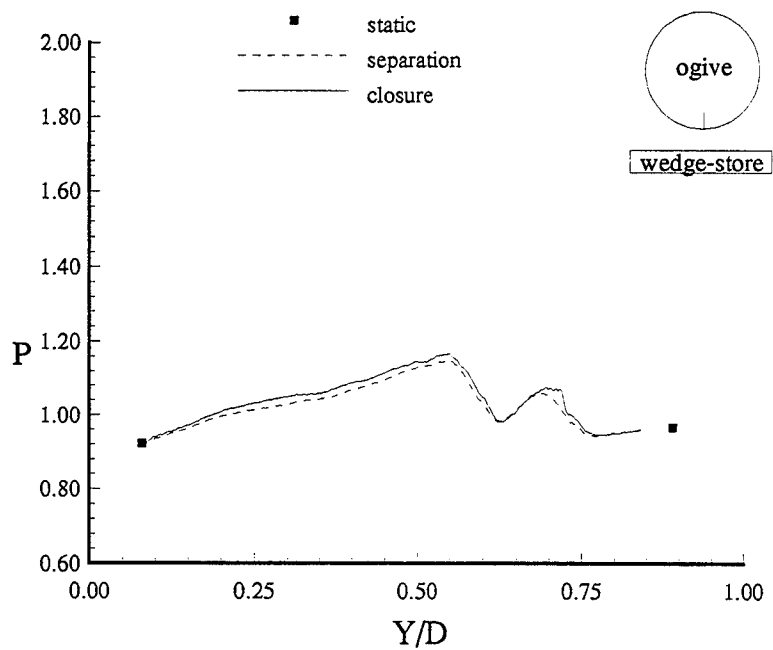Figure B.83. Ogive surface pressure at X/YE=2.31 and $\psi = 60°$ (12.32° wedge-store, M = 1.9).
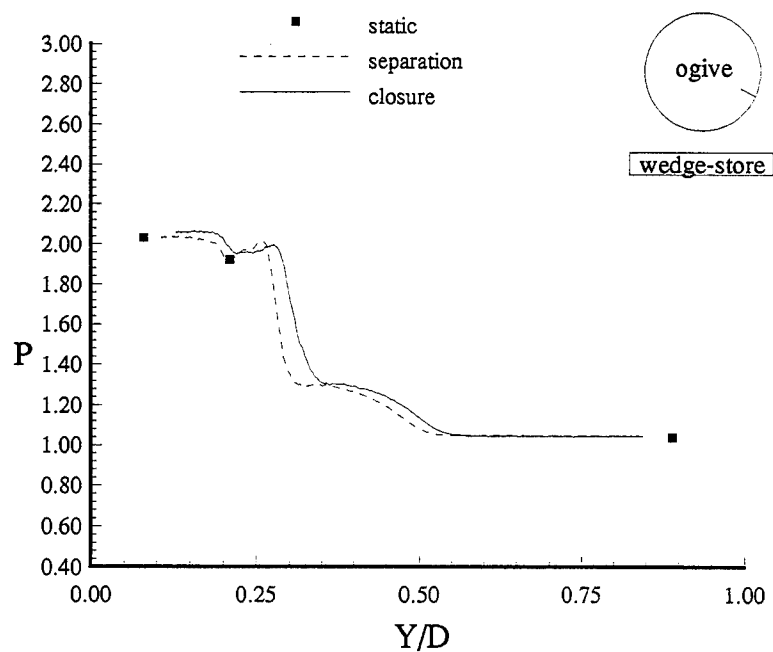
Figure B.84. Ogive surface pressure at X/YE=2.57 and $\psi = 60°$ (12.32° wedge-store, M = 1.9).
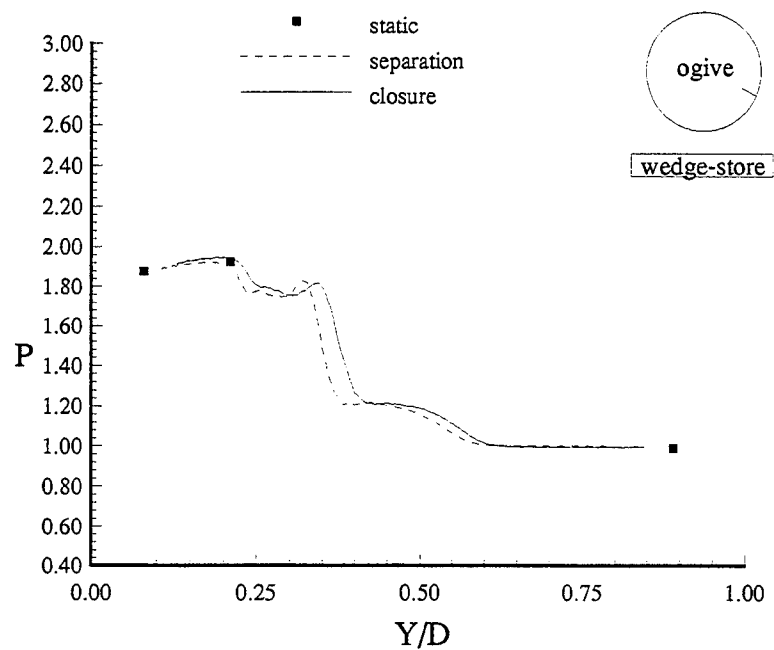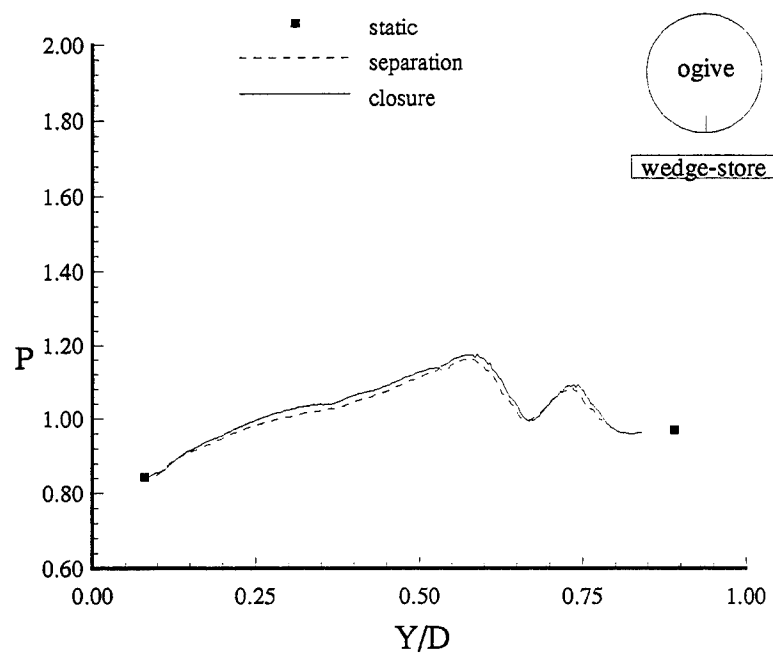
Figure B.85.   Ogive surface pressure at X/YE=2.84 and $\psi = 60°$ (12.32° wedge-store, M = 1.9).
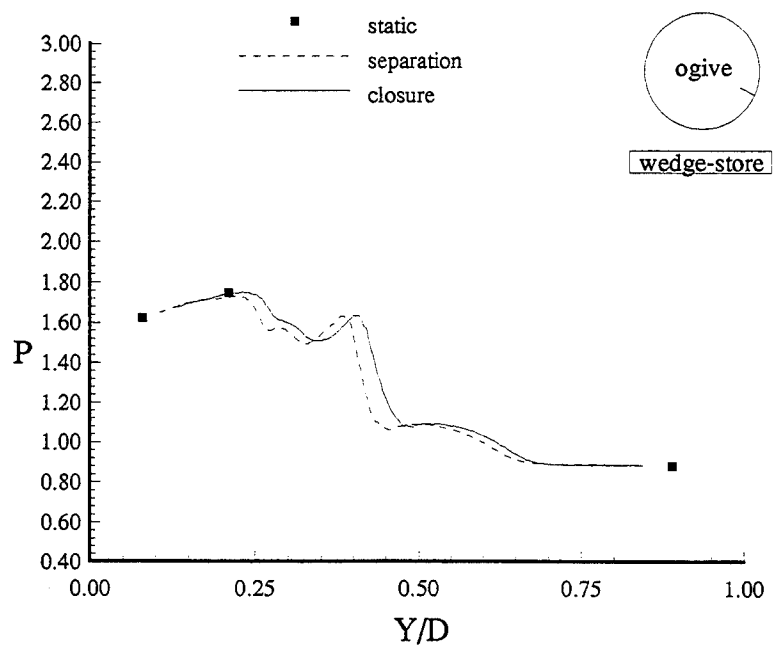
Figure B.86.   Ogive surface pressure at X/YE=3.10 and $\psi = 60°$ (12.32° wedge-store, M = 1.9).
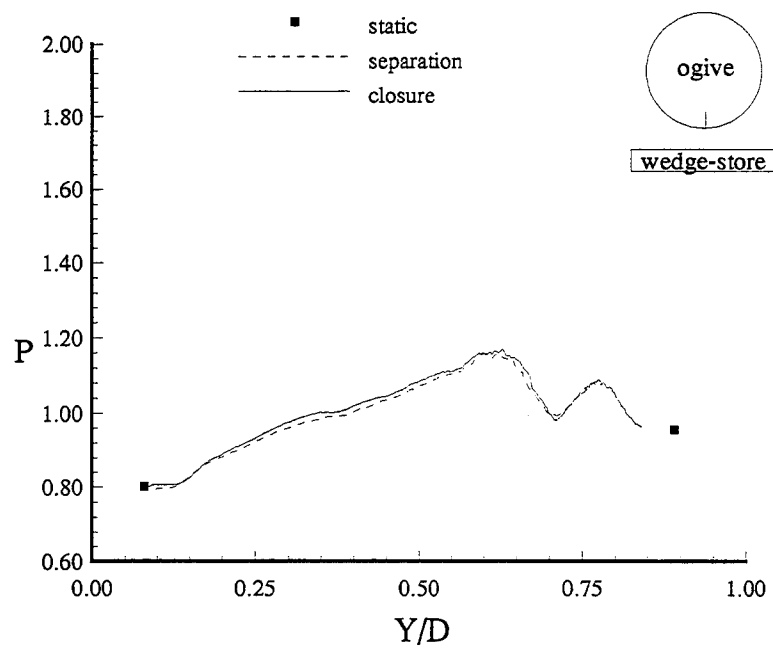
Figure B.87. Ogive surface pressure at X/YE=3.37 and $\psi = 60°$ (12.32° wedge-store, M = 1.9).

Figure B.88. Ogive surface pressure at X/YE=3.64 and $\psi = 60°$ (12.32° wedge-store, M = 1.9).

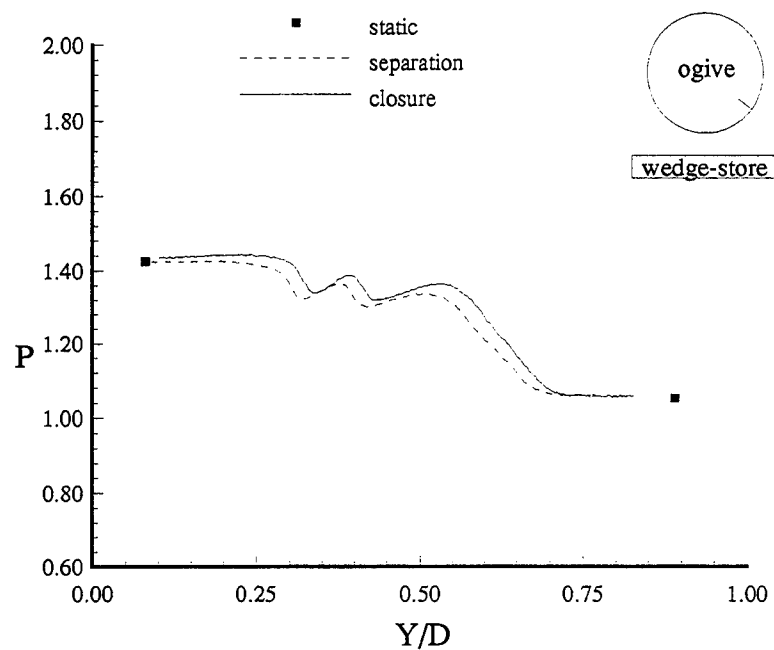Figure B.89. Ogive surface pressure at X/YE=3.90 and $\psi = 60°$ (12.32° wedge-store, M = 1.9).

Figure B.90. Ogive surface pressure at X/YE=4.17 and $\psi = 60°$ (12.32° wedge-store, M = 1.9).

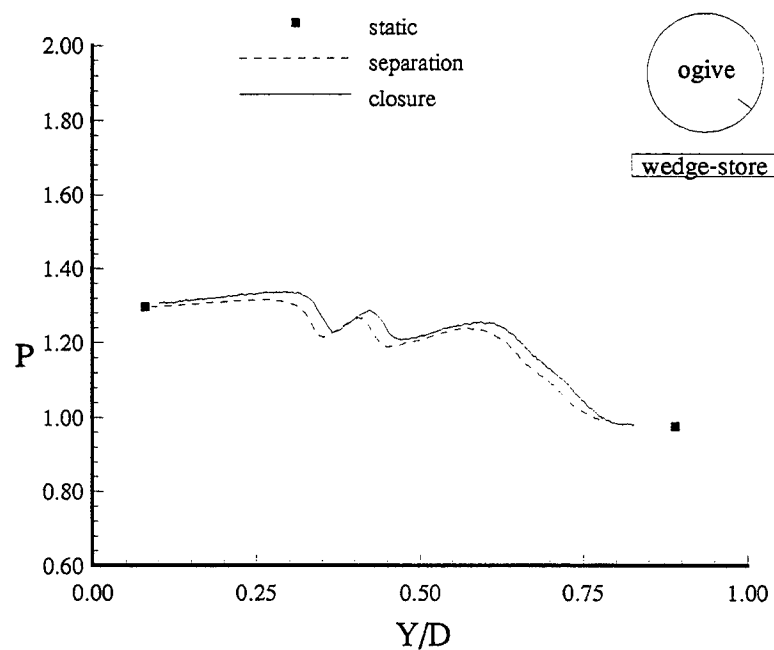Figure B.91. Ogive surface pressure at X/YE=4.43 and $\psi = 60°$ (12.32° wedge-store, M = 1.9).

Figure B.92. Ogive surface pressure at X/YE=4.70 and $\psi = 60°$ (12.32° wedge-store, M = 1.9).

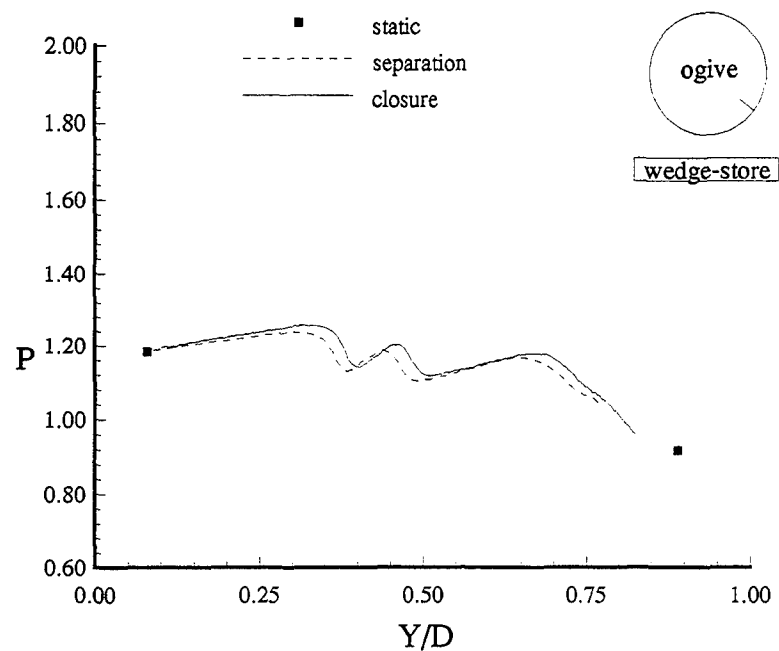Figure B.93. Ogive surface pressure at X/YE=2.31 and $\psi = 90°$ (12.32° wedge-store, M = 1.9).

Figure B.94. Ogive surface pressure at X/YE=2.57 and $\psi = 90°$ (12.32° wedge-store, M = 1.9).

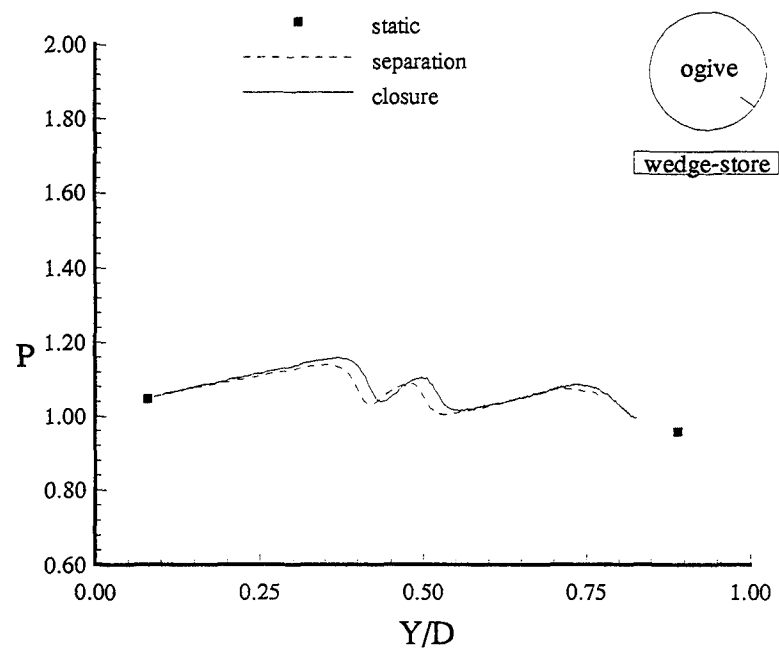Figure B.95. Ogive surface pressure at X/YE=2.84 and $\psi = 90°$ (12.32° wedge-store, M = 1.9).

Figure B.96. Ogive surface pressure at X/YE=3.10 and $\psi = 90°$ (12.32° wedge-store, M = 1.9).
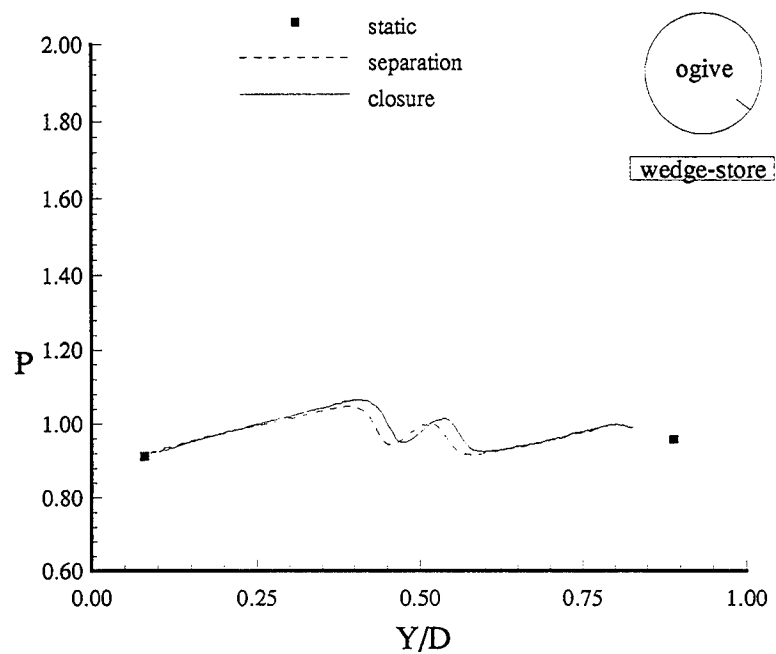
Figure B.97.   Ogive surface pressure at X/YE=3.37 and $\psi = 90°$ (12.32° wedge-store, M = 1.9).

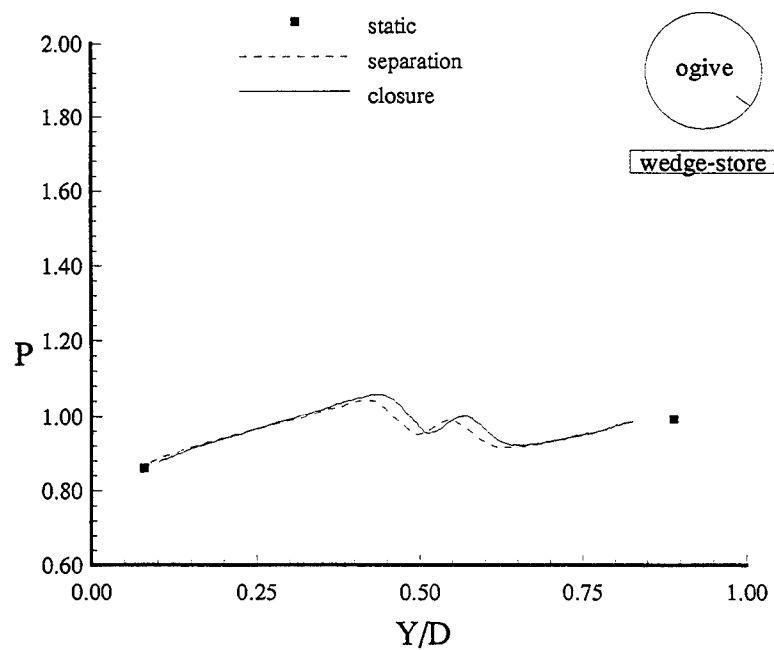Figure B.98.   Ogive surface pressure at X/YE=3.64 and $\psi = 90°$ (12.32° wedge-store, M = 1.9).

Figure B.99. Ogive surface pressure at X/YE=3.90 and $\psi = 90°$ (12.32° wedge-store, M = 1.9).

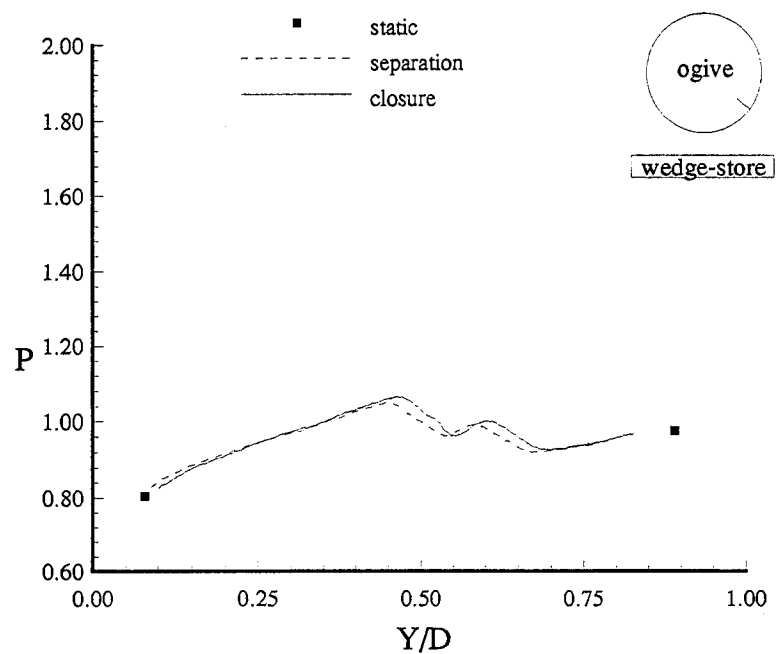Figure B.100. Ogive surface pressure at X/YE=4.17 and $\psi = 90°$ (12.32° wedge-store, M = 1.9).

Figure B.101. Ogive surface pressure at X/YE=4.43 and $\psi = 90°$ (12.32° wedge-store, M = 1.9).

Figure B.102. Ogive surface pressure at X/YE=4.70 and $\psi = 90°$ (12.32° wedge-store, M = 1.9).

Figure B.103.   Ogive surface pressure at X/YE=2.31 and $\psi = 135°$ (12.32° wedge-store, M = 1.9).

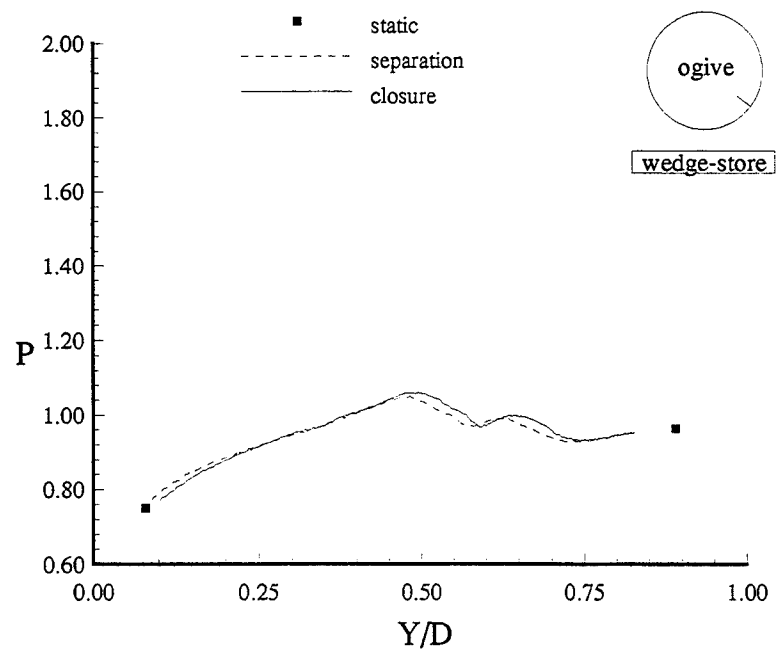Figure B.104.   Ogive surface pressure at X/YE=2.57 and $\psi = 135°$ (12.32° wedge-store, M = 1.9).

Figure B.105. Ogive surface pressure at X/YE=2.84 and $\psi = 135°$ (12.32° wedge-store, M = 1.9).

Figure B.106. Ogive surface pressure at X/YE=3.10 and $\psi = 135°$ (12.32° wedge-store, M = 1.9).
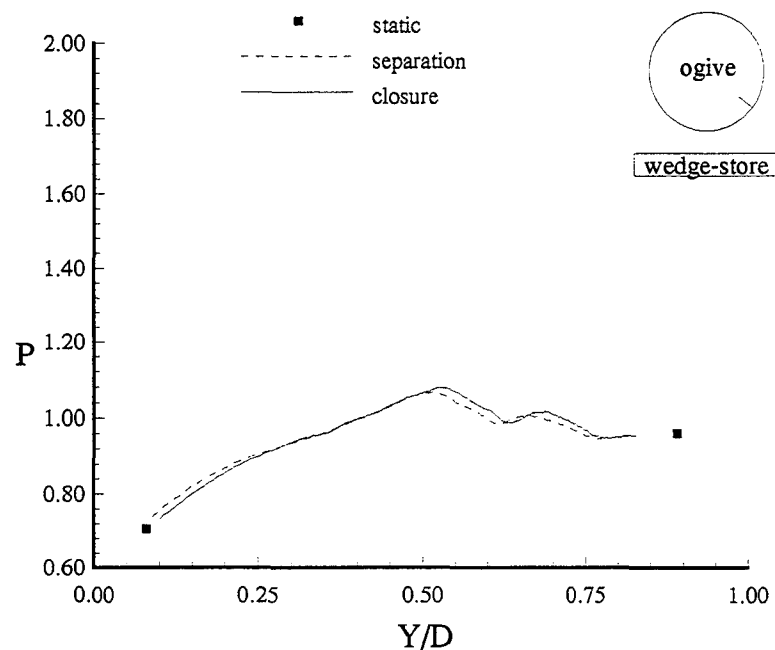
Figure B.107. Ogive surface pressure at X/YE=3.37 and $\psi = 135°$ (12.32° wedge-store, M = 1.9).

Figure B.108. Ogive surface pressure at X/YE=3.64 and $\psi = 135°$ (12.32° wedge-store, M = 1.9).
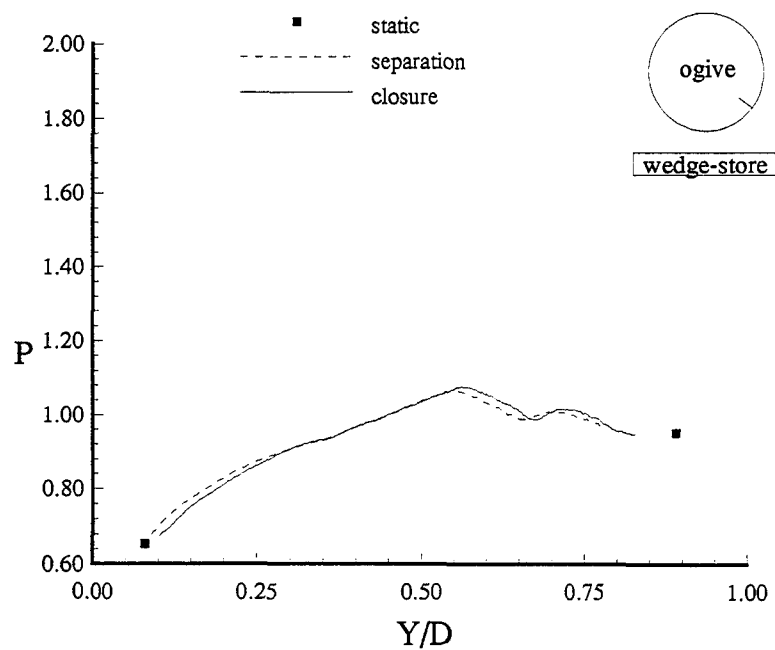
Figure B.109.   Ogive surface pressure at X/YE=3.90 and $\psi = 135°$ (12.32° wedge-store, M = 1.9).

Figure B.110.   Ogive surface pressure at X/YE=4.17 and $\psi = 135°$ (12.32° wedge-store, M = 1.9).

Figure B.111. Ogive surface pressure at X/YE=4.43 and $\psi = 135°$ (12.32° wedge-store, M = 1.9).

Figure B.112. Ogive surface pressure at X/YE=4.70 and $\psi = 135°$ (12.32° wedge-store, M = 1.9).

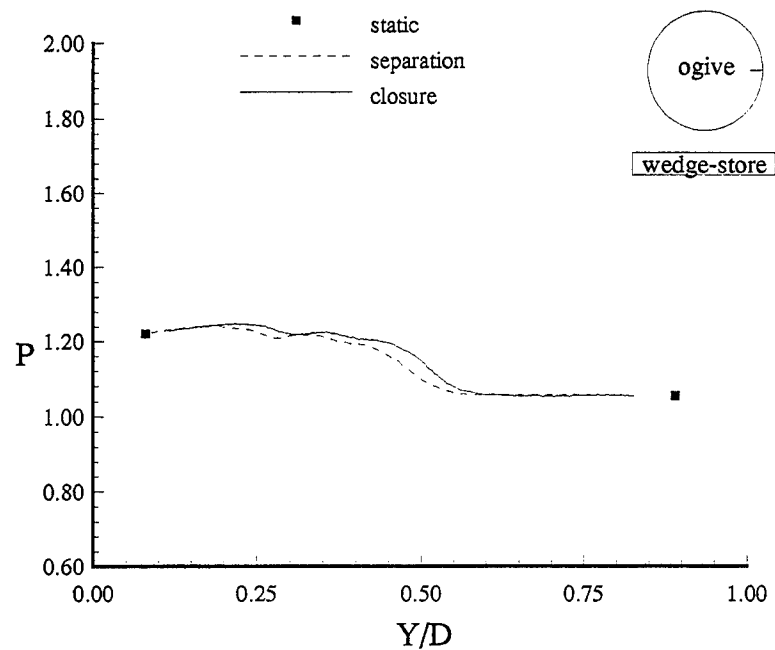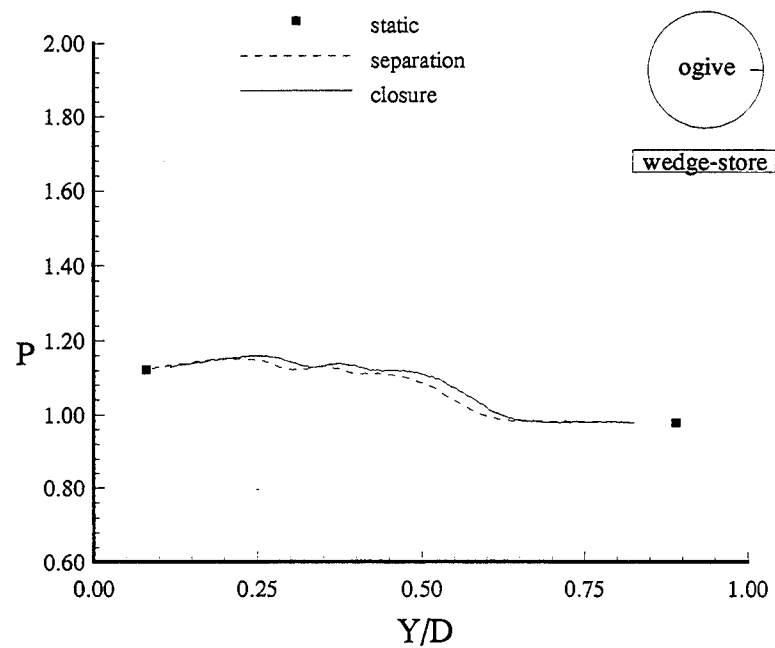Figure B.113. Ogive surface pressure at X/YE=2.31 and $\psi = 180°$ (12.32° wedge-store, M = 1.9).

Figure B.114. Ogive surface pressure at X/YE=2.57 and $\psi = 180°$ (12.32° wedge-store, M = 1.9).
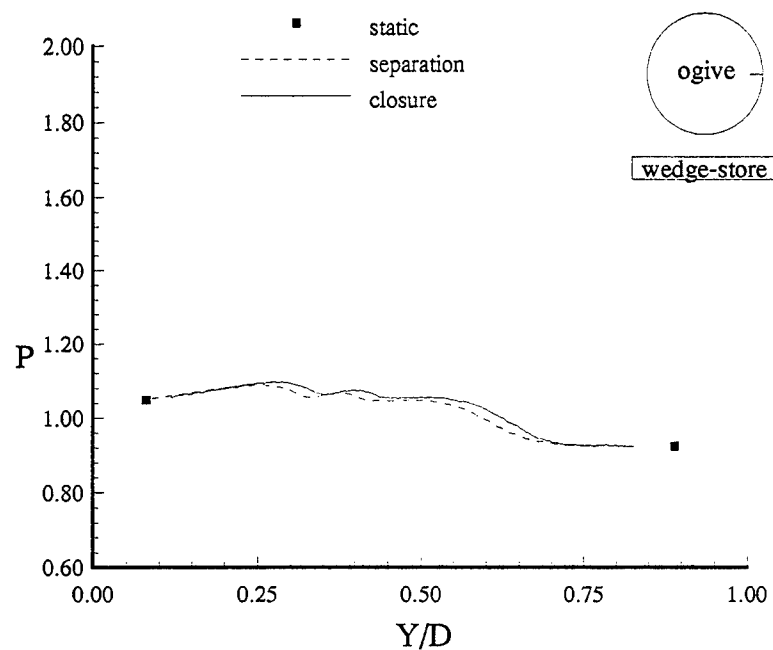
Figure B.115.   Ogive surface pressure at X/YE=2.84 and $\psi = 180°$ (12.32° wedge-store, M = 1.9).
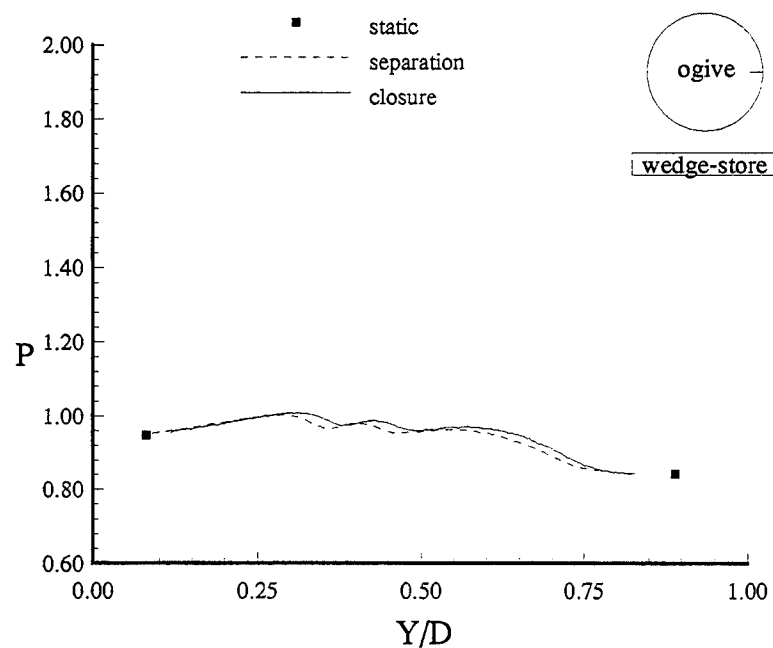

Figure B.116.   Ogive surface pressure at X/YE=3.10 and $\psi = 180°$ (12.32° wedge-store, M = 1.9).

Figure B.117. Ogive surface pressure at X/YE=3.37 and $\psi = 180°$ (12.32° wedge-store, M = 1.9).

Figure B.118. Ogive surface pressure at X/YE=3.64 and $\psi = 180°$ (12.32° wedge-store, M = 1.9).
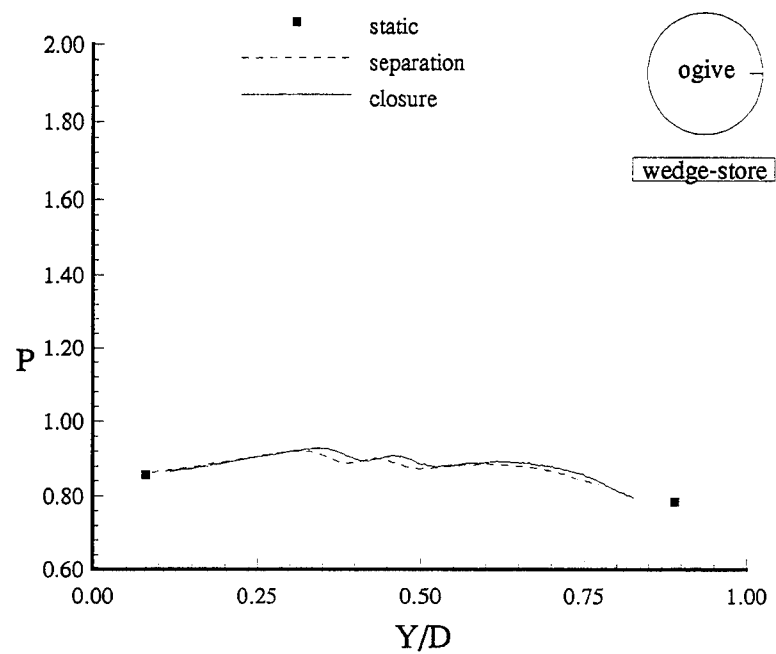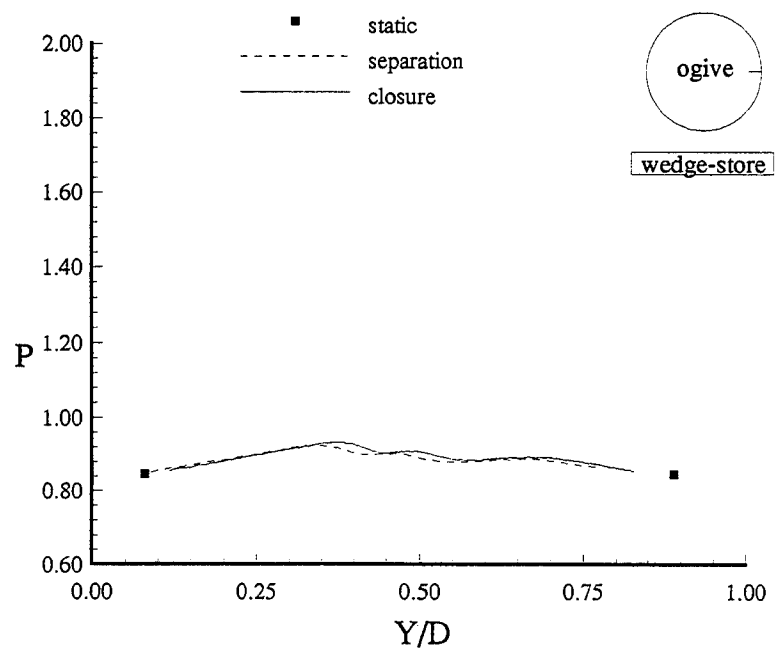
Figure B.119. Ogive surface pressure at X/YE=3.90 and $\psi = 180°$ (12.32° wedge-store, M = 1.9).

Figure B.120. Ogive surface pressure at X/YE=4.17 and $\psi = 180°$ (12.32° wedge-store, M = 1.9).

Figure B.121. Ogive surface pressure at X/YE=4.43 and $\psi = 180°$ (12.32° wedge-store, M = 1.9).

Figure B.122. Ogive surface pressure at X/YE=4.70 and $\psi = 180°$ (12.32° wedge-store, M = 1.9).

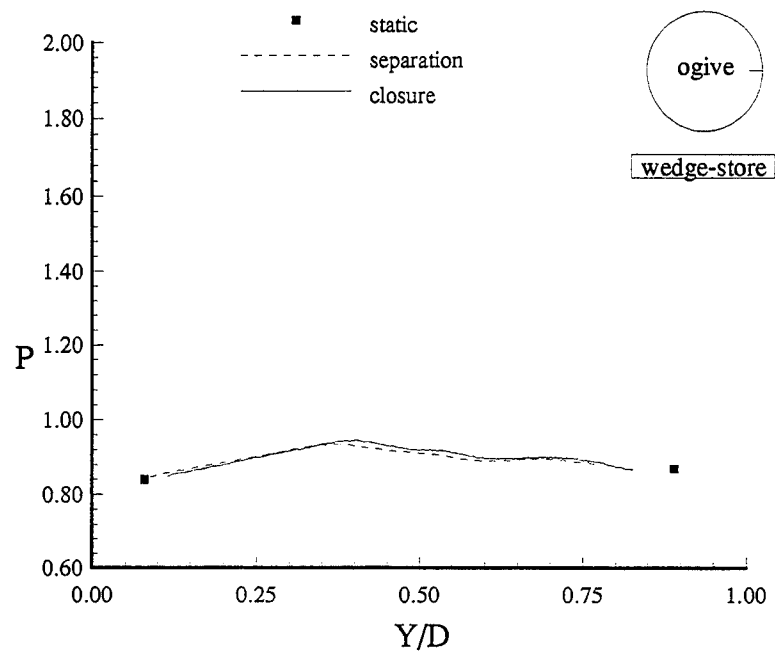Figure B.123. Ogive surface pressure at X/YE=2.31 and $\psi = 0°$ (6.1° wedge-store, M = 1.52).

Figure B.124. Ogive surface pressure at X/YE=2.57 and $\psi = 0°$ (6.1° wedge-store, M = 1.52).

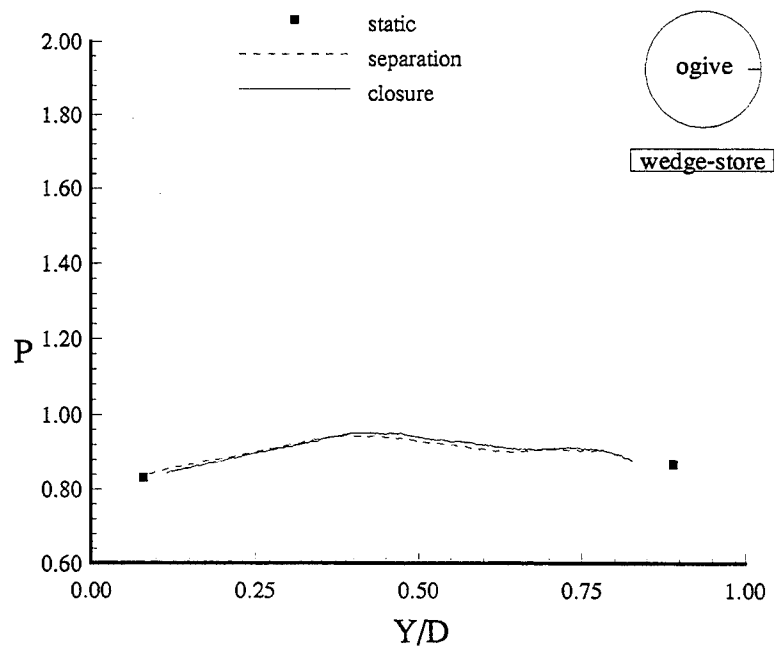Figure B.125. Ogive surface pressure at X/YE=2.84 and $\psi = 0°$ (6.1° wedge-store, M = 1.52).

Figure B.126. Ogive surface pressure at X/YE=3.10 and $\psi = 0°$ (6.1° wedge-store, M = 1.52).

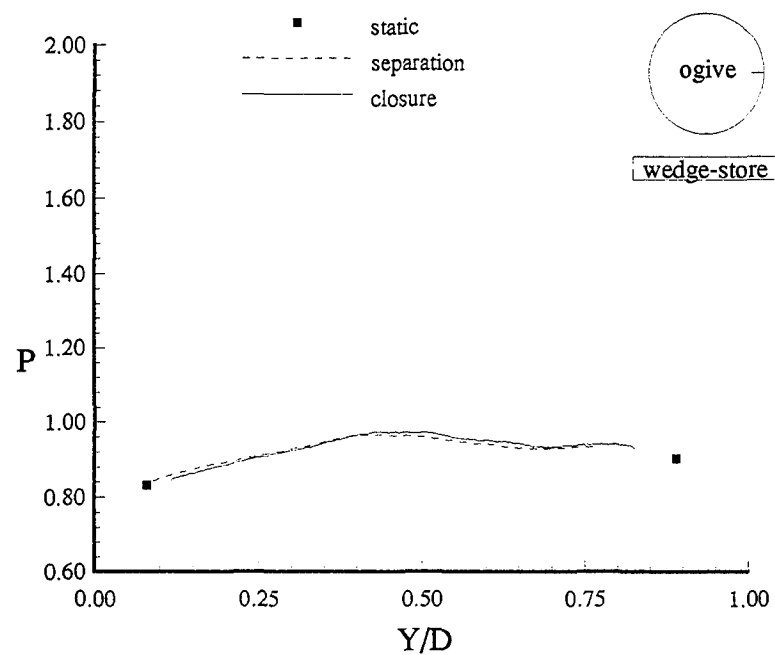Figure B.127.   Ogive surface pressure at X/YE=3.37 and $\psi = 0°$ (6.1° wedge-store, M = 1.52).

Figure B.128.   Ogive surface pressure at X/YE=3.64 and $\psi = 0°$ (6.1° wedge-store, M = 1.52).

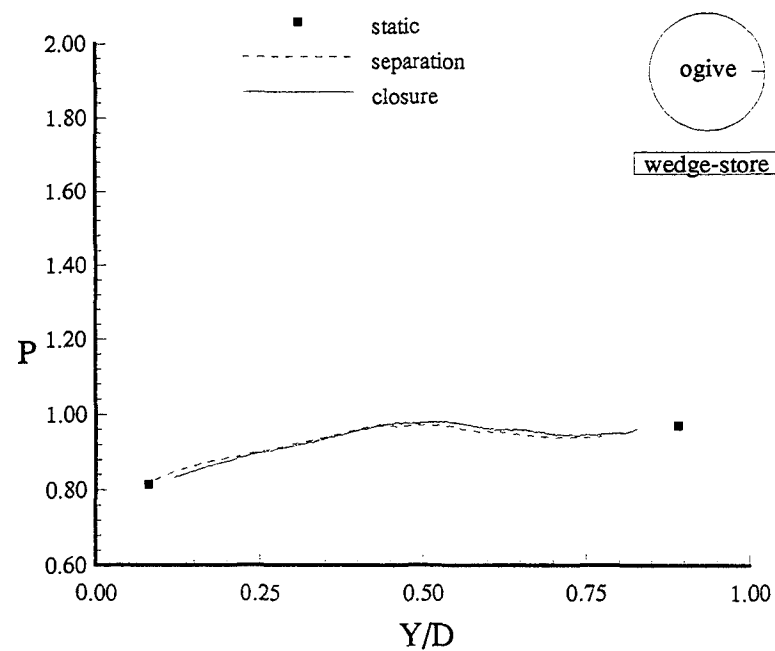Figure B.129. Ogive surface pressure at X/YE=3.90 and $\psi = 0°$ (6.1° wedge-store, M = 1.52).

Figure B.130. Ogive surface pressure at X/YE=4.17 and $\psi = 0°$ (6.1° wedge-store, M = 1.52).

Figure B.131.   Ogive surface pressure at X/YE=4.43 and $\psi = 0°$ (6.1° wedge-store, $M = 1.52$).

Figure B.132.   Ogive surface pressure at X/YE=4.70 and $\psi = 0°$ (6.1° wedge-store, $M = 1.52$).

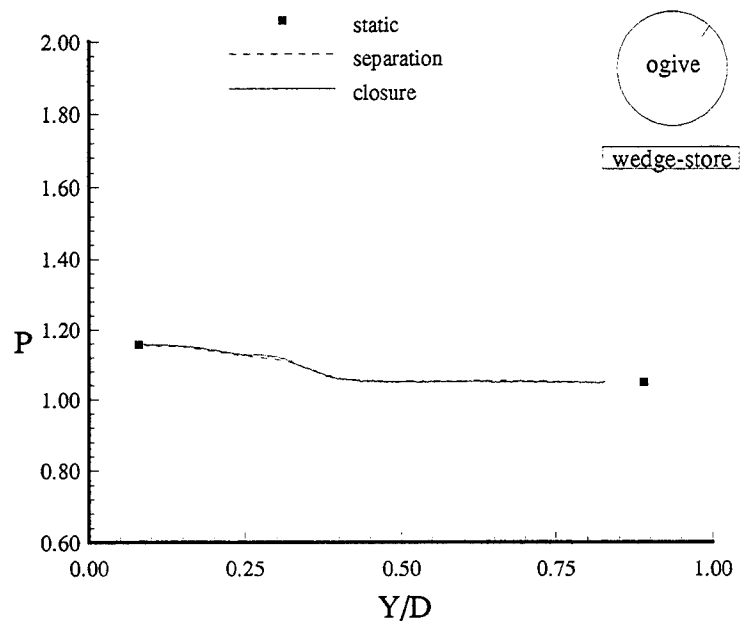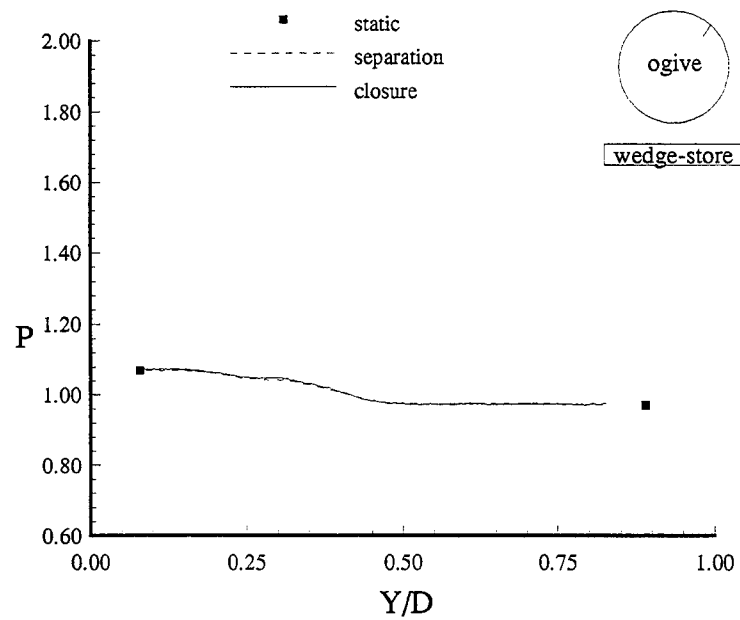Figure B.133. Ogive surface pressure at X/YE=2.31 and $\psi = 45°$ (6.1° wedge-store, M = 1.52).

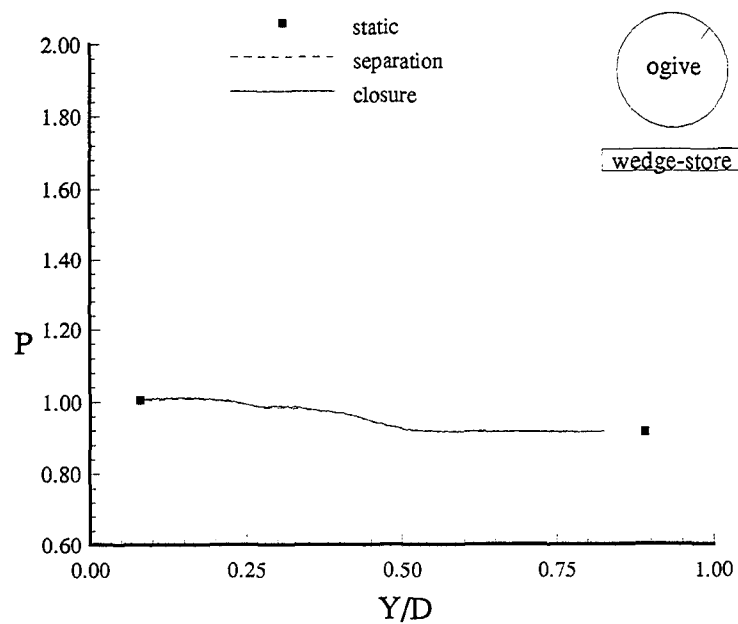Figure B.134. Ogive surface pressure at X/YE=2.57 and $\psi = 45°$ (6.1° wedge-store, M = 1.52).

Figure B.135. Ogive surface pressure at X/YE=2.84 and $\psi = 45°$ (6.1° wedge-store, M = 1.52).

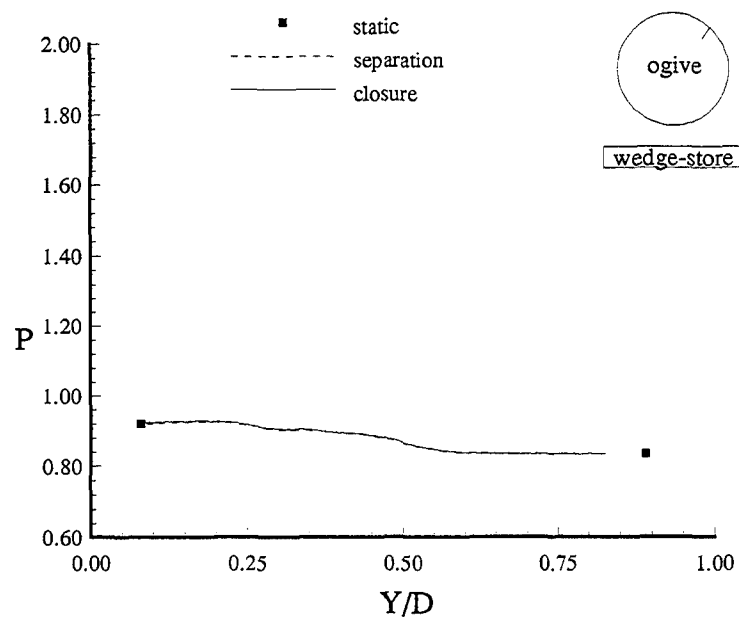Figure B.136. Ogive surface pressure at X/YE=3.10 and $\psi = 45°$ (6.1° wedge-store, M = 1.52).

Figure B.137. Ogive surface pressure at X/YE=3.37 and $\psi = 45°$ (6.1° wedge-store, M = 1.52).

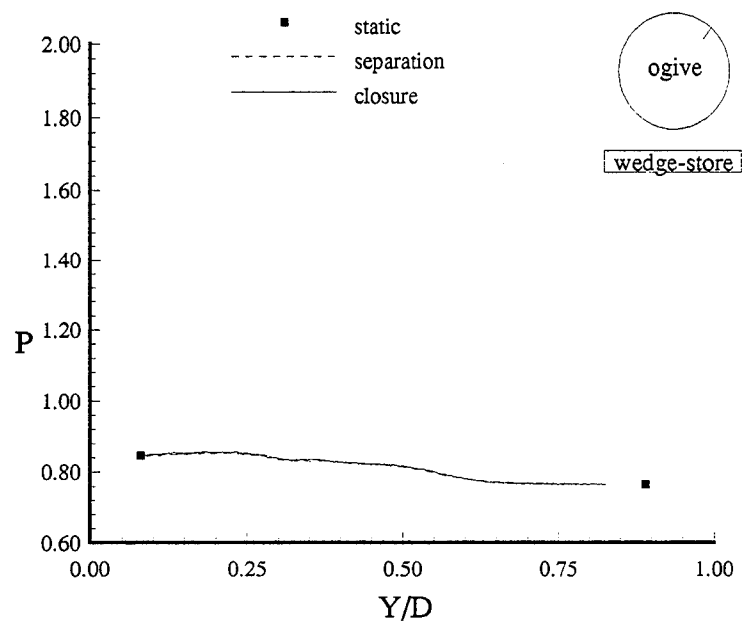Figure B.138. Ogive surface pressure at X/YE=3.64 and $\psi = 45°$ (6.1° wedge-store, M = 1.52).

Figure B.139. Ogive surface pressure at X/YE=3.90 and $\psi = 45°$ (6.1° wedge-store, M = 1.52).

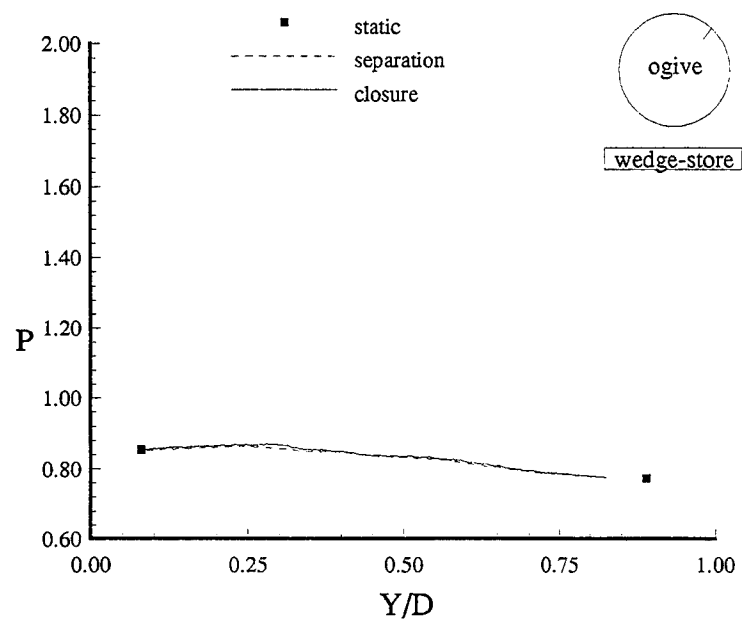Figure B.140. Ogive surface pressure at X/YE=4.17 and $\psi = 45°$ (6.1° wedge-store, M = 1.52).

Figure B.141. Ogive surface pressure at X/YE=4.43 and $\psi = 45°$ (6.1° wedge-store, M = 1.52).

Figure B.142. Ogive surface pressure at X/YE=4.70 and $\psi = 45°$ (6.1° wedge-store, M = 1.52).

Figure B.143.   Ogive surface pressure at X/YE=2.31 and $\psi = 90°$ (6.1° wedge-store, M = 1.52).

Figure B.144.   Ogive surface pressure at X/YE=2.57 and $\psi = 90°$ (6.1° wedge-store, M = 1.52).
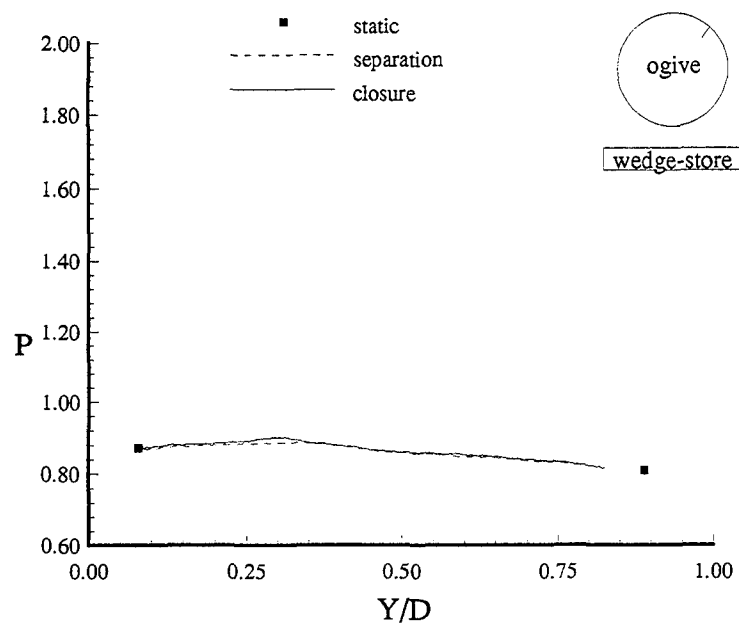
Figure B.145. Ogive surface pressure at X/YE=2.84 and $\psi = 90°$ (6.1° wedge-store, M = 1.52).

Figure B.146. Ogive surface pressure at X/YE=3.10 and $\psi = 90°$ (6.1° wedge-store, M = 1.52).

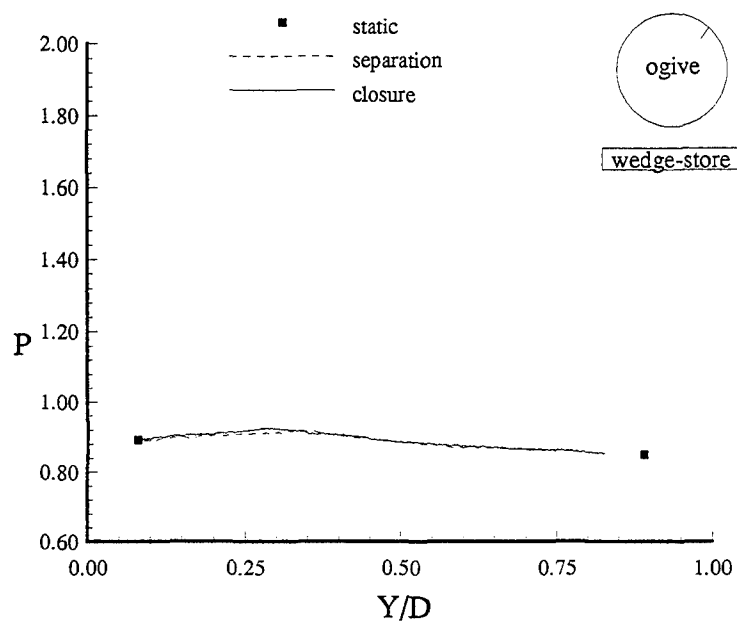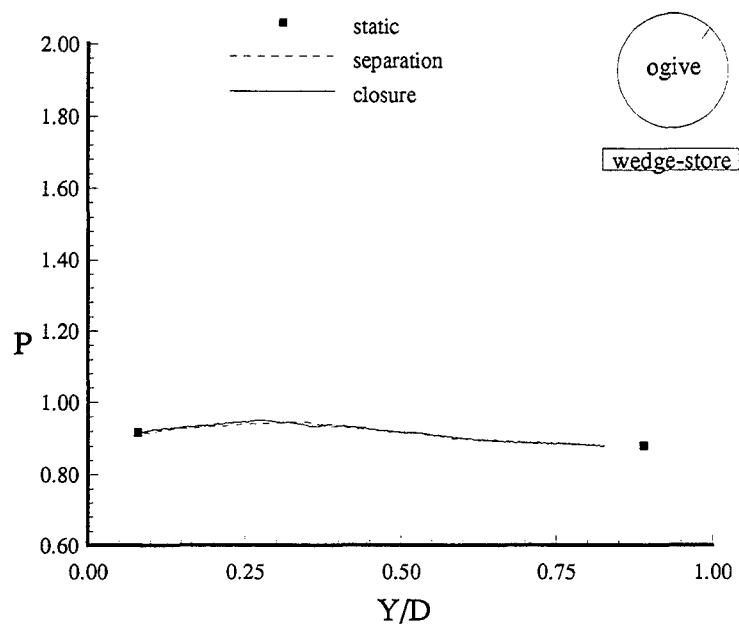Figure B.147. Ogive surface pressure at X/YE=3.37 and $\psi = 90°$ (6.1° wedge-store, M = 1.52).

Figure B.148. Ogive surface pressure at X/YE=3.64 and $\psi = 90°$ (6.1° wedge-store, M = 1.52).

Figure B.149.   Ogive surface pressure at X/YE=3.90 and $\psi = 90°$ (6.1° wedge-store, M = 1.52).

Figure B.150.   Ogive surface pressure at X/YE=4.17 and $\psi = 90°$ (6.1° wedge-store, M = 1.52).

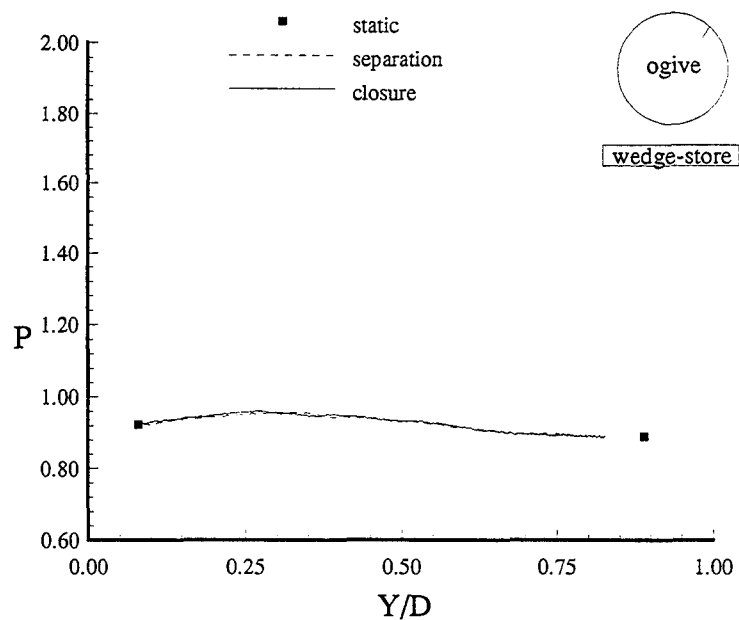Figure B.151.   Ogive surface pressure at X/YE=4.43 and $\psi = 90°$ (6.1° wedge-store, M = 1.52).

Figure B.152.   Ogive surface pressure at X/YE=4.70 and $\psi = 90°$ (6.1° wedge-store, M = 1.52).

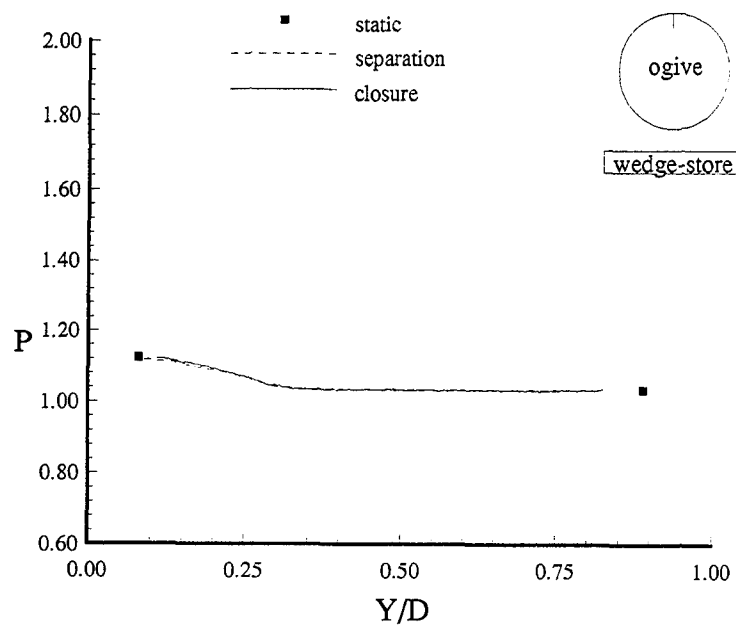Figure B.153. Ogive surface pressure at X/YE=2.31 and $\psi = 135°$ (6.1° wedge-store, M = 1.52).

Figure B.154. Ogive surface pressure at X/YE=2.57 and $\psi = 135°$ (6.1° wedge-store, M = 1.52).
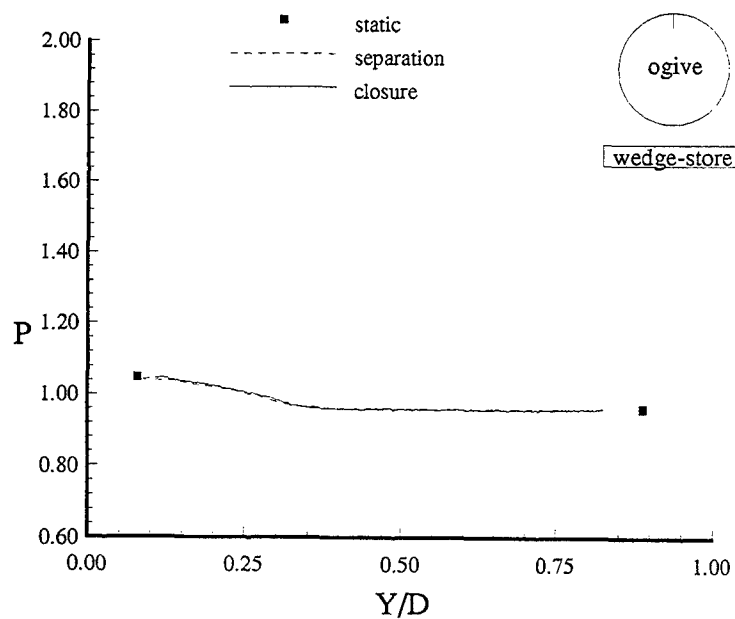
Figure B.155. Ogive surface pressure at X/YE=2.84 and $\psi = 135°$ (6.1° wedge-store, M = 1.52).

Figure B.156. Ogive surface pressure at X/YE=3.10 and $\psi = 135°$ (6.1° wedge-store, M = 1.52).

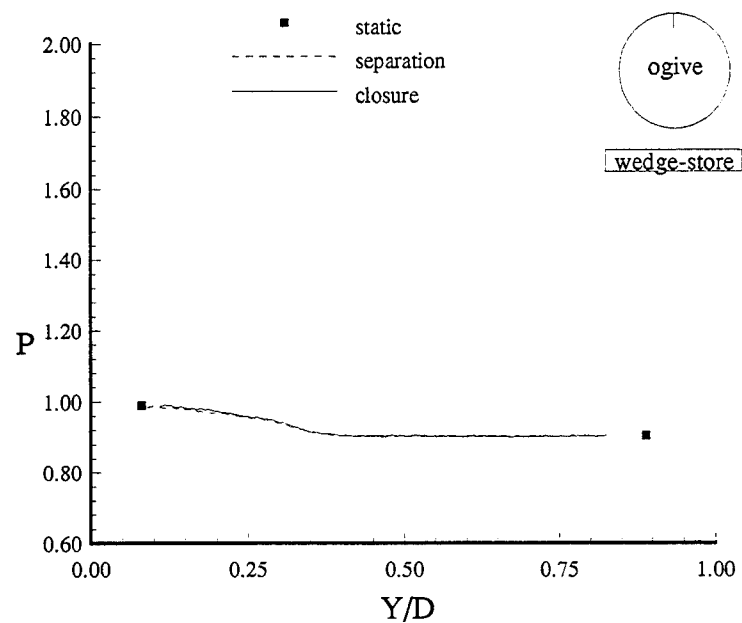Figure B.157. Ogive surface pressure at X/YE=3.37 and $\psi = 135°$ (6.1° wedge-store, M = 1.52).

Figure B.158. Ogive surface pressure at X/YE=3.64 and $\psi = 135°$ (6.1° wedge-store, M = 1.52).

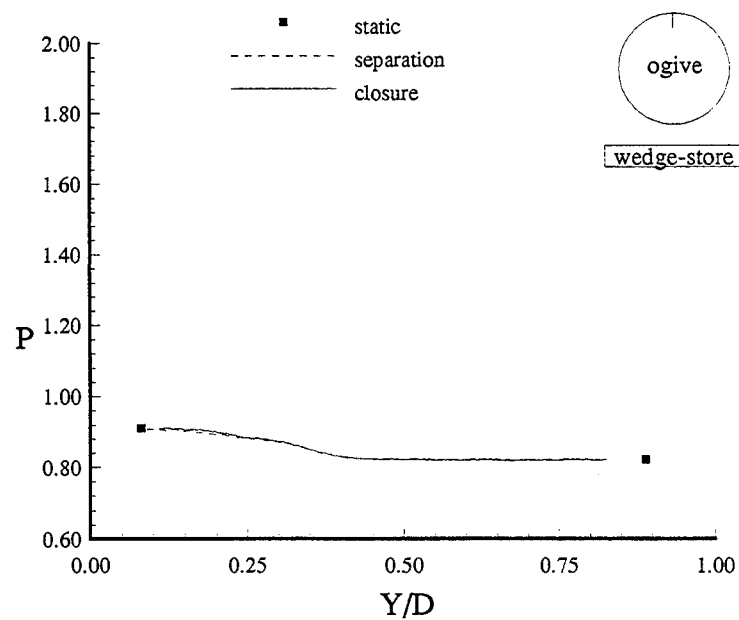Figure B.159. Ogive surface pressure at X/YE=3.90 and $\psi = 135°$ (6.1° wedge-store, M = 1.52).

Figure B.160. Ogive surface pressure at X/YE=4.17 and $\psi = 135°$ (6.1° wedge-store, M = 1.52).

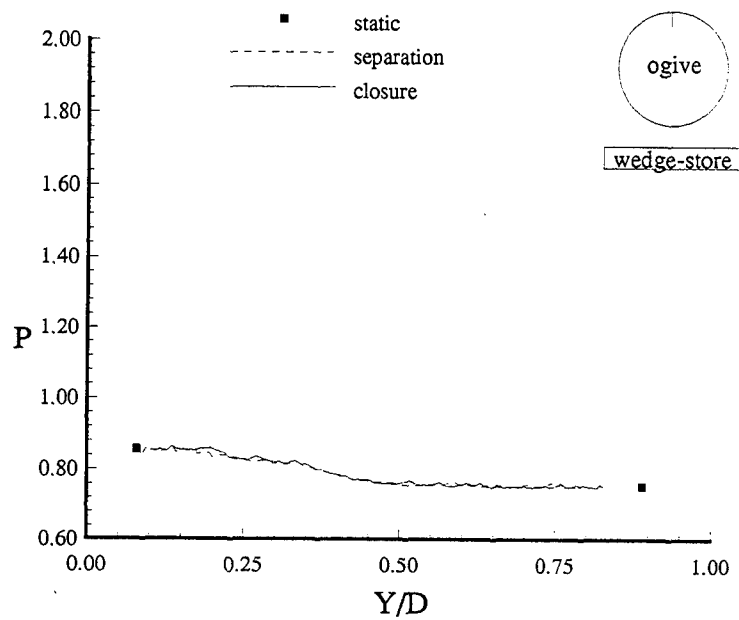Figure B.161. Ogive surface pressure at X/YE=4.43 and $\psi = 135°$ (6.1° wedge-store, M = 1.52).

Figure B.162. Ogive surface pressure at X/YE=4.70 and $\psi = 135°$ (6.1° wedge-store, M = 1.52).
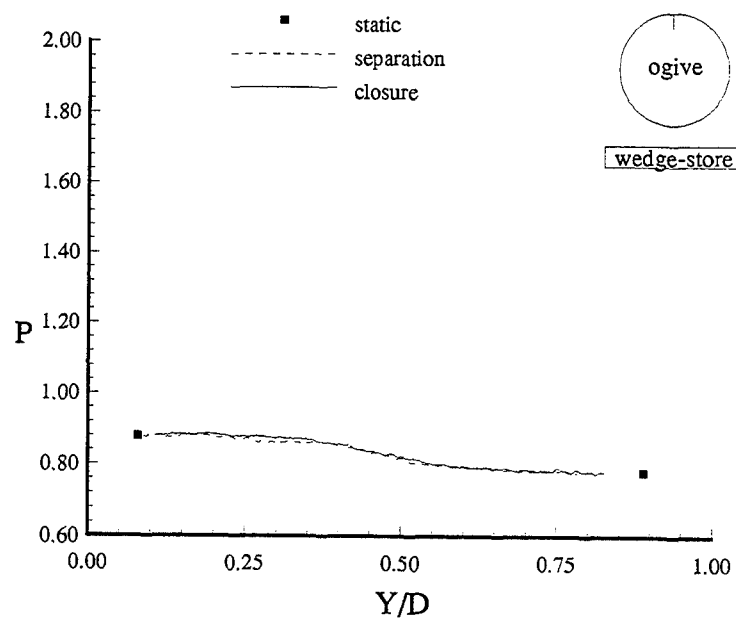
Figure B.163.   Ogive surface pressure at X/YE=2.31 and $\psi = 180°$ (6.1° wedge-store, M = 1.52).

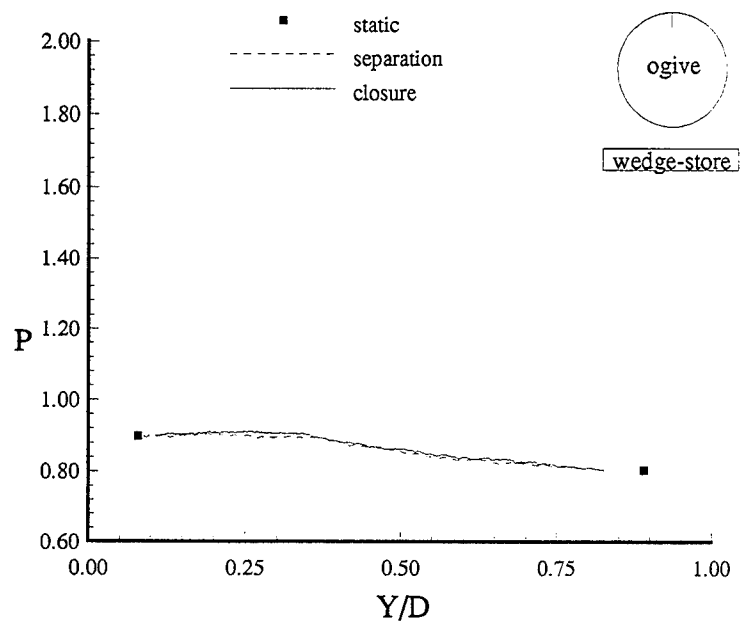Figure B.164.   Ogive surface pressure at X/YE=2.57 and $\psi = 180°$ (6.1° wedge-store, M = 1.52).

Figure B.165. Ogive surface pressure at X/YE=2.84 and $\psi = 180°$ (6.1° wedge-store, M = 1.52).

Figure B.166. Ogive surface pressure at X/YE=3.10 and $\psi = 180°$ (6.1° wedge-store, M = 1.52).

Figure B.167. Ogive surface pressure at X/YE=3.37 and $\psi = 180°$ (6.1° wedge-store, M = 1.52).

Figure B.168. Ogive surface pressure at X/YE=3.64 and $\psi = 180°$ (6.1° wedge-store, M = 1.52).

Figure B.169. Ogive surface pressure at X/YE=3.90 and $\psi = 180°$ (6.1° wedge-store, M = 1.52).

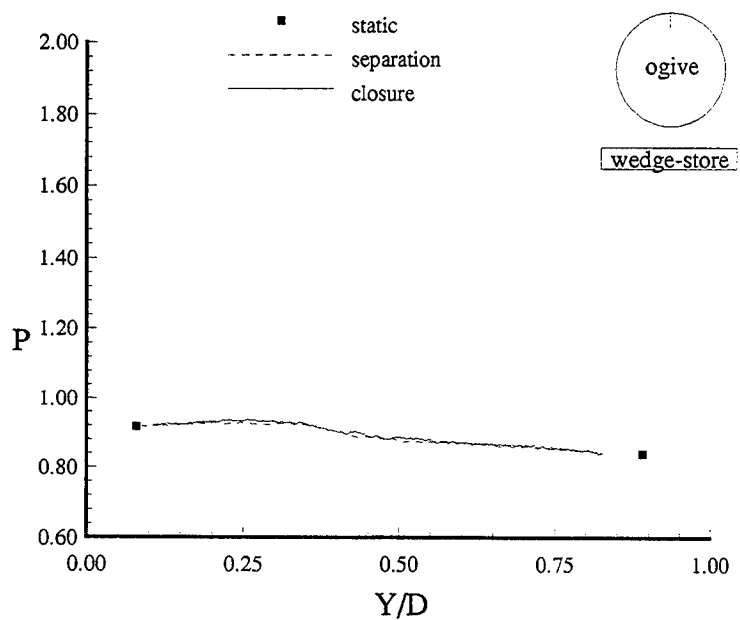Figure B.170. Ogive surface pressure at X/YE=4.17 and $\psi = 180°$ (6.1° wedge-store, M = 1.52).
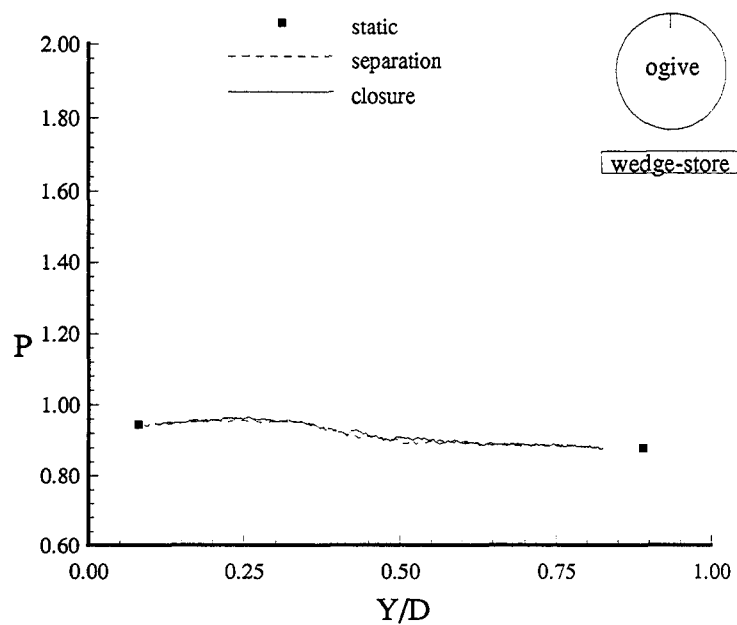
Figure B.171. Ogive surface pressure at X/YE=4.43 and $\psi = 180°$ (6.1° wedge-store, M = 1.52).

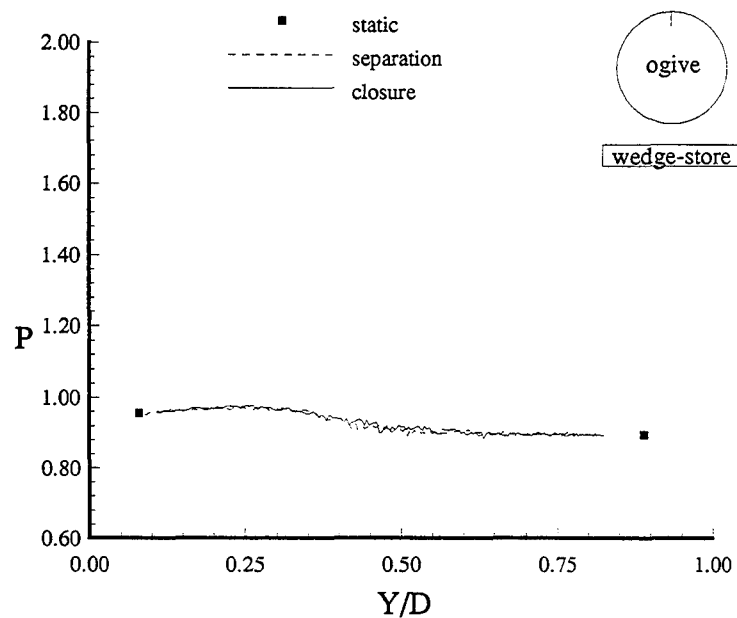Figure B.172. Ogive surface pressure at X/YE=4.70 and $\psi = 180°$ (6.1° wedge-store, M = 1.52).

REPORT DOCUMENTATION PAGE

1. AGENCY USE ONLY (leave blank)	2. REPORT DATE 1 Dec 1994	3. REPORT TYPE AND DATES COVERED Final

4. TITLE AND SUBTITLE
An Experimental Investigation of the Time-Dependent Separation of Tangent Bodies in Supersonic Flow

5. FUNDING NUMBERS

6. AUTHOR(S)
Neal A. Mosbarger, Captain, USAF

7. PERFORMING ORGANIZATION NAME(S) AND ADDRESS(ES)
Air Force Institute of Technology
Wright-Patterson AFB, OH 45433-7936

8. PERFORMING ORGANIZATION REPORT NUMBER

AFIT/DS/AA/94-7

9. SPONSORING / MONITORING AGENCY NAME(S) AND ADDRESS(ES)
Flight Dynamics Directorate
Wright Laboratory
Air Force Materiel Command
Wright-Patterson AFB, OH 45433-7562

10. SPONSORING / MONITORING AGENCY REPORT NUMBER

11. SUPPLEMENTARY NOTES

12a. DISTRIBUTION / AVAILABILITY STATEMENT

Approved for public release; distribution is unlimited.

12b. DISTRIBUTION CODE

13. ABSTRACT *(Maximum 200 words)*
An experimental, time-dependent separation of tangent bodies was performed in a supersonic wind tunnel (Mach 1.5 and 1.9) to investigate the significance of transient effects and the suitability of using steady-state assumptions to predict a dynamic event. The model configurations consisted of two bodies placed in a near tangent position. A stationary body, plate or ogive, was instrumented to obtain dynamic surface pressures, while a second body, a wedge attached to an air cylinder, was plunged in a constrained motion away from and towards the stationary model.

Three-dimensional flow expansion around the edge of the wedge reduced the strength of the shock waves and created a region of low pressure, near freestream static, on body surfaces between the incident and reflection shock waves. The dynamic motion of the wedge did not significantly affect the shock wave development between the bodies, and steady-state corrections that accounted for the motion-induced wedge angle were appropriate for predicting the time-dependent surface pressures induced by the incident shock wave.

14. SUBJECT TERMS store separation, time-dependent shock waves, three-dimensional flow, unsteady flow	15. NUMBER OF PAGES 295
	16. PRICE CODE

17. SECURITY CLASSIFICATION OF REPORT UNCLASSIFIED	18. SECURITY CLASSIFICATION OF THIS PAGE UNCLASSIFIED	19. SECURITY CLASSIFICATION OF ABSTRACT UNCLASSIFIED	20. LIMITATION OF ABSTRACT UNLIMITED